VNiVERSiDAD
Ð SALAMANCA
CAMPUS DE EXCELENCIA INTERNACIONAL

Formation and characterization of surface micro- and nanostructures in polymers and polymeric nanocomposites prepared by irradiation with pulsed nano- and femtosecond lasers

Javier Prada Rodrigo

Salamanca, May 2023.

A thesis submitted for the degree of
Doctor awarded by the University of Salamanca
In the Applied Physics and Technology doctorate program

Supervisors:
Esther Rebollar González (IQFR-CSIC)
Pablo Moreno Pedraz (ALF-USAL)

VNiVERSiDAD
Ð SALAMANCA
CAMPUS DE EXCELENCIA INTERNACIONAL

D. Pablo Moreno Pedraz, Catedrático de Ingeniería Mecánica de la Universidad de Salamanca y Dª. Esther Rebollar González, Investigadora del Instituto de Química Física Rocasolano (CSIC)

CERTIFICAN:

Que la presente memoria, "Formation and characterization of surface micro- and nanostructures in polymers and polymeric nanocomposites prepared by irradiation with pulsed nano- and femtosecond lasers / Formación y caracterización de micro- y nanoestructuras superficiales en polímeros y nanocompuestos poliméricos preparadas mediante irradiación con láseres pulsados de nano- y femtosegundos" ha sido realizada bajo su dirección en el Departamento de Ingeniería Mecánica de la Universidad de Salamanca por D. JAVIER PRADA RODRIGO y constituye su Tesis Doctoral para optar al grado de Doctor por la Universidad de Salamanca dentro del Programa de Doctorado en Física Aplicada y Tecnología con Mención Internacional.

En Salamanca, a 3 de mayo de 2023.

MORENO PEDRAZ PABLO MANUEL - 07878086B
Firmado digitalmente por MORENO PEDRAZ PABLO MANUEL - 07878086B
Fecha: 2023.05.03 11:43:28 +02'00'

REBOLLAR GONZALEZ ESTHER - DNI 50866326D
Firmado digitalmente por REBOLLAR GONZALEZ ESTHER - DNI 50866326D
Fecha: 2023.05.03 11:17:41 +02'00'

D. Pablo Moreno Pedraz

Dª. Esther Rebollar González

Acknowledgements

First of all, I would like to acknowledge all the help of my supervisors Esther Rebollar and Pablo Moreno. They have done a great job, knowing when to be patient and when to put pressure on me, to make sure I work the best I can. I would also like to thank all the members of the Aplicaciones de la Luz y la Fotónica (ALF) group, especially the experimental ones: Javi, Íñigo, Carolina, Nacho and Warein. They have always been ready to help with any problem I faced.

In the same vein, I would like to thank the members of the Lasers, nanostructures and materials processing (LANAMAP) group, especially Rebeca, Mikel and Mohamed, for taking me in as one of their own during my multiple stays at the Instituto de Química Física Rocasolano (IQFR-CSIC). I would also like to acknowledge the help received from the members of the Soft and Polymeric Matter group (Softmatpol), especially Tiberio and Aurora. Not only did they allow me to use their equipment and helped prepare samples and make measurements, but also, they tried to make sure I felt at home at the Instituto de Estructura de la Materia (IEM).

I would like to thank all of the members of the "Ablazione Laser con impulsi corti (nanosecondo) ed ultracorti (femtosecondo)" group of the Università degli Studi di Napoli Federico II, which I visited for 3 months. Specially professor Salvatore Amoruso and Dr. Jijil JJ Nivas for welcoming me and kindly and patiently helping me with anything I needed. I would also like to thank Dr. Manjot Singh and Dr. Meilin Hu for their hospitality and all the great food.

For the same reasons, I would like to express my gratitude to the division 6.2 of the Bundesanstalt für Materialforschung und -prüfung (BAM) Berlin, where I stayed for three months. Specially professor Jörn Bonse, Dr. Heike Voss and Karsten Wasmuth. Their willingness to help and make sure I was having a good time kept me warm in the German winter.

I cannot forget my friends and colleagues that shared the experience of working at the university with me: Elsa, Pablo, Alba, Laura, Ana, Miguel, Elena, Aurora, Roberto, Victor and Rodrigo. Being able to support each other and struggle together has been one of the greatest pleasures of this thesis and one of the reasons that kept me going in the worst days.

I would like to thank all the members of OSAL student Chapter that I have yet to mention. Being in this association is the thing that has made me more passionate not only about science outreach, but also about science in general.

To all my friends outside the University: Adry, Eloy, Félix, Jesús, Luna, Nacho, Pimen, Vero, Victor, I feel so incredibly lucky to have you. All of you helped me relax and disconnect from writing this thesis. You were an inexhaustible battery that helped me recharge and go back to work energized. Special thanks to Dani, Cuque, Mario and Sara, our adventures in the tomb and outside of it are and always will be one of the best memories of this period. Thank you for being there.

Finally, I would like to acknowledge the immense help given by my family. My mother Mª Belén and my father Antonio and my brother Luis. You have always supported me and made sure that I know if anything went wrong, I could always fall back on you. Although I have worked hard in this thesis, having your support behind me was a privilege that allowed me to focus on it and not need to worry about much else. I could not have done it without you.

Resumen

En este trabajo de tesis doctoral se estudió la formación de estructuras superficiales periódicas inducidas por láser (LIPSS, siglas del inglés *Laser Induced Periodic Surface Structures*) en polímeros y compuestos de matriz polimérica en forma de películas delgadas, ya sean autosoportadas o soportadas en diferentes substratos como son silicio, vidrio, acero, oro y poli(etileno tereftalato) (PET). Los polímeros y compuestos estudiados son PET, poli(trimetileno tereftalato) (PTT), un nanocomposite compuesto por PTT y nanotubos de disulfuro de wolframio (WS_2) (PTT-WS_2) y poli(3-hexiltiofeno) (P3HT).

En el caso de películas delgadas de PET depositadas sobre distintos substratos, las irradiamos con pulsos laser Gaussianos de femtosegundo en el infrarrojo (795 nm, 64 fs, 5 kHz) para estudiar la influencia del espesor de la película de polímero, y el material y la rugosidad del substrato en la formación de LIPSS. Demostramos que el espesor condiciona la formación de LIPSS, de hecho, éstas no se formaron para películas con espesores mayores de 1300 nm. Además, la irradiación produjo LIPSS perpendiculares a la polarización del láser en muestras depositadas sobre substratos de oro de baja rugosidad, y LIPSS paralelas a la polarización en muestras sobre substratos de silicio o vidrio. Sin embargo, no aparecieron LIPSS en las muestras sobre substratos de PET, ni sobre oro de rugosidad alta, ni tampoco sobre de acero de rugosidad alta. El periodo, que en general es cercano a la longitud de onda del láser, y profundidad de las estructuras, medidos con microscopía de fuerzas atómicas (AFM), adquieren valores que están condicionados por el material del substrato y el espesor de la película delgada.

A partir de estos resultados, propusimos un mecanismo de formación adicional a los ya conocidos, que se activa debido a la excitación de una onda electromagnética superficial generada por dispersión (SSW) en la interfaz película delgada-substrato. El caso de las LIPSS formadas en polímeros sobre substratos de oro, las cuales aparecen orientadas en la dirección perpendicular a la esperada, decidimos estudiarlo más a fondo con la ayuda de simulaciones numéricas del campo eléctrico. La concordancia entre las simulaciones y las medidas experimentales nos llevó a postular que la SSW que activa el mecanismo de formación de LIPSS en este caso es un plasmón polaritón superficial (SPP).

Además del trabajo que acabamos de describir, también estudiamos el efecto de las LIPSS en la modificación de distintas propiedades de nuestras muestras.

En el caso de las películas autosoportadas de PTT y PTT-WS_2, las irradiamos con haces Gaussianos de femtosegundo en el ultravioleta (265 nm, 260 fs, 1 kHz), resultando en la

formación de LIPSS paralelas a la polarización con un periodo similar a la longitud de onda del láser. En las muestras con nanoaditivo la energía necesaria para la aparición de LIPSS fue ligeramente mayor, efecto que achacamos a su mayor porcentaje de cristalinidad y mayor disipación térmica. En cuanto al efecto de las LIPSS en las propiedades micromecánicas de las muestras, fue determinado con la técnica de mapeo nanomecánico cuantitativo de fuerza máxima (PF-QNM) y fue similar para ambos materiales. El módulo de Young se mantuvo constante, pero las fuerzas de adhesión disminuyeron aproximadamente en un factor cuatro tras el nanoestructurado, lo que atribuimos a un cambio en la química superficial. Respecto a la mojabilidad, la caracterizamos utilizando la técnica de la gota sésil para medir el ángulo de contacto del agua, glicerol y aceite de parafina en las dos muestras. En ambas muestras la mojabilidad aumentó con la formación de LIPSS y la energía superficial total permaneció constante. Sin embargo, su componente polar negativa aumentó considerablemente. También achacamos este fenómeno a un cambio en la química superficial.

Por otro lado, irradiamos películas delgadas de PET depositadas sobre distintos substratos con haces vectoriales de femtosegundo en el visible (515 nm, 180 fs, 3 kHz). La irradiación con haces vectoriales sobre películas delgadas de PET provocó la formación de LIPSS paralelas a la polarización en las muestras depositadas sobre substratos de silicio o de vidrio, consiguiendo estructuras en forma de radios de bicicleta, anillos concéntricos y en espiral. En cuanto a las muestras depositadas sobre substratos de oro, aparecieron estructuras perpendiculares a la polarización del láser, pero demasiado desordenadas para poder llamarlas LIPSS.

También utilizamos estos haces para irradiar P3HT, consiguiendo LIPSS con las mismas direcciones paralelas a la polarización del láser. Además, utilizamos haces vectoriales y de vórtice óptico de nanosegundo en el visible (532 nm, 5 ns, 20 Hz), induciendo la formación de LIPSS en el mismo rango que se reportó previamente para haces Gaussianos con la misma longitud de onda. Esto permitió la generación de estructuras circulares, radiales y espirales. Medimos el cambio en la conductividad encontrando una disminución muy acusada en la parte superior de las estructuras en comparación con lo que ocurre en la parte inferior. Este cambio fue causado por una pérdida de cristalinidad. También caracterizamos el cambio en la mojabilidad utilizando el método de la gota sésil para medir el ángulo de contacto del agua antes y después de la irradiación. No encontramos diferencias para las diferentes polarizaciones del haz. Para todas ellas, la muestra se volvió más hidrófila después de la irradiación. Explicamos este fenómeno teniendo en cuenta los cambios químicos causados por la oxidación inducida por la irradiación láser.

Finalmente, irradiamos películas delgadas de (6,6)fenil-C_{71}-ácido butírico metil ester ($PC_{71}BM$) con esos mismos haces de nanosegundo produciendo LIPSS paralelas a la polarización del láser de un período menor que las encontradas en P3HT y en un rango de fluencia mucho más estrecho. Sus periodos y profundidades evolucionaron con los parámetros de irradiación igual que las estructuras encontradas en P3HT.

Abstract

In this doctoral thesis, the formation of Laser Induced Periodic Surface Structures (LIPSS) was studied in polymers and polymer matrix compounds. The samples were studied in the form of thin films, either self-standing or deposited on different substrates such as silicon, glass, steel, gold, and poly(ethylene terephthalate) (PET). The polymers and compounds studied are PET, poly(trimethylene terephthalate) (PTT), a nanocomposite made of PTT and tungsten disulfide (WS_2) nanotubes (PTT-WS_2), and poly(3-hexyl thiophene) (P3HT).

PET thin films deposited on different substrates were irradiated with femtosecond Gaussian laser pulses in the infrared (795 nm, 64 fs, 5 kHz) to study the influence of the thickness of the polymer film and the material and roughness of the substrate on the formation of LIPSS. We showed that the thickness of the thin film conditioned the formation of LIPSS, in fact, LIPSS were not formed for films with thicknesses greater than 1300 nm. In addition, the irradiation produced LIPSS perpendicular to the laser polarization in samples deposited on low roughness gold substrates, and LIPSS parallel to polarization in samples on silicon or glass substrates. However, LIPSS did not appear in samples on PET, high roughness gold, or high roughness steel substrates. The period, which in general was found to be close to the laser wavelength, and depth of the structures, measured with Atomic Force Microscopy (AFM), acquired values affected by the material of the substrate and the thickness of the thin film.

To explain these results, we proposed an additional formation mechanism to the already known ones, which was activated due to the excitation of a surface scattered wave (SSW) at the thin film-substrate interface. The LIPSS formed in polymer samples on gold substrates appear in a perpendicular direction to the expected one. Because of this, we decided to study it further with the help of numerical simulations of the electric field. The agreement between the simulations and the experiment led us to postulate that the SSW that activates the LIPSS formation mechanism in this case is a Surface Plasmon Polariton (SPP).

In addition to the work that we just described, we also studied the effect of LIPSS formation on the modification of different surface properties of our samples.

In the case of self-standing PTT and PTT-WS_2 films, we irradiated them with femtosecond Gaussian beams in the ultraviolet (265 nm, 260 fs, 1 kHz), resulting in the formation of LIPSS parallel to the polarization with a period similar to the wavelength of the laser. In the samples with the nanoadditive, the energy required for the appearance of LIPSS was slightly higher, an effect that we attribute to its higher percentage of crystallinity and thermal dissipation.

Regarding the effect of LIPSS on the micromechanical properties of the samples, it was determined with the technique of Peak-Force Quantitative Nanomechanical Mapping (PF-QNM) and was similar for both materials. The Young's modulus remained constant, but the adhesion force decreased by a factor of four after irradiation, which we attributed to a change in surface chemistry. Regarding the wettability of the samples, we characterized it using the sessile drop technique to measure the contact angle of water, glycerol, and paraffin oil in the two materials. In both, the wettability increased with the formation of LIPSS, and the total surface energy remained constant. However, its negative polar component increased considerably. We also attribute this phenomenon to a change in surface chemistry.

Besides, we irradiated PET thin films deposited on different substrates with femtosecond vector beams (515 nm, 180 fs, 3 kHz). Irradiation with vector beams in thin PET films provoked the formation of LIPSS parallel to the polarization of the laser in the samples deposited on silicon or glass substrates, achieving structures in the form of wheel-spokes, concentric rings, and spirals. As for the samples deposited on gold substrates, structures perpendicular to the polarization of the laser appeared, but they were too disordered to be called LIPSS.

We also used these beams to irradiate P3HT, achieving LIPSS in the same directions parallel to the polarization of the laser. Moreover, we used nanosecond vector and optical vortex beams (532 nm, 5 ns, 20 Hz), which induced the formation of LIPSS in the same range that was previously reported for Gaussian beams with the same wavelength. This allowed the generation of radial, circular, and spiral structures. We measured the change in conductivity, finding a marked decrease at the top of the structures compared to what happens at the bottom. This change was caused by a loss of crystallinity. We also characterized the change in wettability using the sessile drop method to measure the contact angle of water before and after irradiation. We found no differences for the different beam polarizations. For all of them, the sample became more hydrophilic after irradiation. We explained this phenomenon considering the chemical changes caused by oxidation induced by laser irradiation.

Finally, we irradiated thin films of (6,6)phenyl-C 71-butyric acid methyl ester ($PC_{71}BM$) with those same nanosecond beams producing LIPSS parallel to the laser polarization of a shorter period than those found in P3HT and in a much narrower fluence range. Their periods and depths evolved with the irradiation parameters like the structures found in P3HT.

List of publications

Derived from the thesis

- **Prada-Rodrigo, J.**; Rodríguez-Beltrán, R.I.; Paszkiewicz, S.; Szymczyk, A.; Ezquerra, T.A.; Moreno, P.; Rebollar, E. Laser-Induced Periodic Surface Structuring of Poly(trimethylene terephthalate) Films Containing Tungsten Disulfide Nanotubes. Polymers 2020, 12, 1090. https://doi.org/10.3390/polym12051090.
- Rodríguez-Beltrán, R.I.; **Prada-Rodrigo, J.**; Crespo, A.; Ezquerra, T.A.; Moreno, P.; Rebollar, E. Physicochemical Modifications on Thin Films of Poly(Ethylene Terephthalate) and Its Nanocomposite with Expanded Graphite Nanostructured by Ultraviolet and Infrared Femtosecond Laser Irradiation. Polymers 2022, 14, 5243. https://doi.org/10.3390/polym14235243.
- **Prada-Rodrigo, J.**; Rodríguez-Beltrán, R.I.; Ezquerra, T.A.; Moreno, P.; Rebollar, E. Influence of Film Thickness and Substrate Roughness on the Formation of Laser Induced Periodic Surface Structures in Poly(ethylene terephthalate) Films Deposited Over Gold Substrates. Optics & Laser Technology 2023, 159, 109007. https://doi.org/10.1016/j.optlastec.2022.109007.
- **Prada-Rodrigo, J.**, Nivas, J.J.; Hu,M; Salvatore, M; Oscurato, S; Ezquerra, T.A.; Amoruso, S; Moreno, P; Rebollar,E. Laser Induced Periodic Surface Structures Generated with Nanosecond Structured Beams in Organic Semiconducting Films. In preparation.
- **Prada-Rodrigo, J.**; Voss, H; Wasmuth, K; Bonse, J; Moreno, P; Rebollar, E. Influence of Femtosecond Laser Repetition Rate on The Formation of Laser Induced Periodic Surface Structures on Thin Films of Poly (ethylene terephthalate)-Expanded Graphite Nanocomposite. In preparation.

Others

- Ortiz-Membrado, L.; Liu, C.; **Prada-Rodrigo, J.;** Jiménez-Piqué, E.; Lin, L.L.; Moreno, P.; Wang, M.S.; Llanes, L. Assessment of Fracture Toughness of Cemented Carbides by Using a Shallow Notch Produced by Ultrashort Pulsed Laser Ablation, and a Comparative Study with Tests Employing Precracked Specimens. International Journal of Refractory Metals and Hard Materials 2022, 108, 105949. https://doi.org/10.1016/j.ijrmhm.2022.105949.

- López-Pernía, C.; Muñoz-Ferreiro, C.; **Prada-Rodrigo, J.;** Moreno, P.; Reveron, H.; Chevalier, J.; Morales-Rodríguez, A.; Poyato, R.; Gallardo-López, Á. R-Curve Evaluation of 3YTZP/Graphene Composites by Indirect Compliance Method. Journal of the European Ceramic Society, 2023, 43, 3486. https://doi.org/10.1016/j.jeurceramsoc.2023.02.002.

Contents

Chapter 1

Introduction

In this doctoral thesis, we investigate Laser Induced Periodic Surface Structures (LIPSS) generated with different kinds of laser beams in several polymeric materials. We study the role of the materials in the formation of LIPSS, *i.e.*, their optical properties and whether the laser processing is done to the material in bulk or in a thin film deposited on different substrates. Moreover, we use three kinds of laser beams, namely Gaussian, vector, and optical vortex beams, to produce nanostructures with different characteristics.

In this section, we introduce the theoretical background and state of the art concerning this research field. Afterwards, we discuss the properties of polymers relevant to our studies, as well as functional polymers and ways to add functionality to polymers. Subsequently, we go into detail about surface micro- and nanostructuring methods, focusing mainly on laser methods. Among them, the most relevant in this research, LIPSS, so we present the advantages, history, and state of the art of this technique. Finally, we present the structure of this thesis.

1.1. General concepts of polymer materials

A polymer is a macromolecule made up of repeated smaller units called monomers via covalent links [1–3]. The chemical process by which monomers join to form a polymer is called polymerization [1].

The number of monomers in a polymer is affected by random events in the polymerization process [1,2]. Therefore, the products of polymerization cannot have a defined molecular weight. To circumvent that, a statistical treatment is needed, which calculates a characteristic molecular weight. The most commonly used characteristic molecular weights are the numerical average molecular weight (M_n) and the weight average molecular weight (M_w) (see Figure 1.1) [1–3]. Assuming a number of molecules N_i for each molecular weight M_i with a total weight associated with that molecular weight $W_\mathrm{i} = N_\mathrm{i} \cdot M_\mathrm{i}$, we can define M_n as:

$$M_\mathrm{n} = \sum N_\mathrm{i} M_\mathrm{i} \,/ \sum N_\mathrm{i} \tag{1.1}$$

and M_w as:

$$M_\mathrm{w} = \sum W_\mathrm{i} M_\mathrm{i} \,/ \sum W_\mathrm{i} = \sum N_\mathrm{i} M_\mathrm{i}^2 \,/ \sum N_\mathrm{i}\, M_\mathrm{i} \tag{1.2}$$

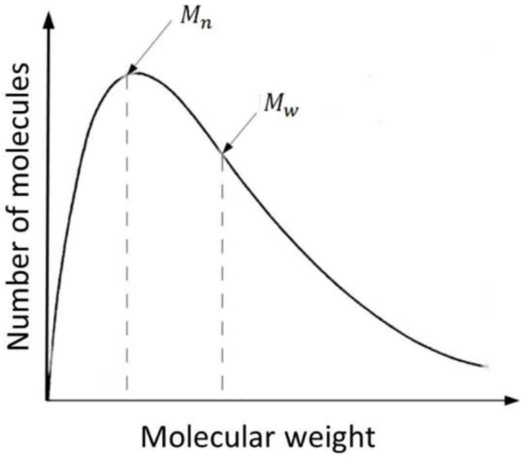

Figure 1.1. *Typical distribution of the molecular weights of a polymer. Figure modified from [4].*

Another important property of polymers is their molecular structure. According to it, polymers are classified as amorphous and semicrystalline [1–3]. An amorphous polymer has its chains randomly distributed, while a semicrystalline polymer has disorganized and organized regions. In practice, it is impossible to find a completely crystalline polymer, only semicrystalline polymers with different degrees of crystallinity [1,2]. The hierarchical organization of atoms in semicrystalline polymers is shown in Figure 1.2.

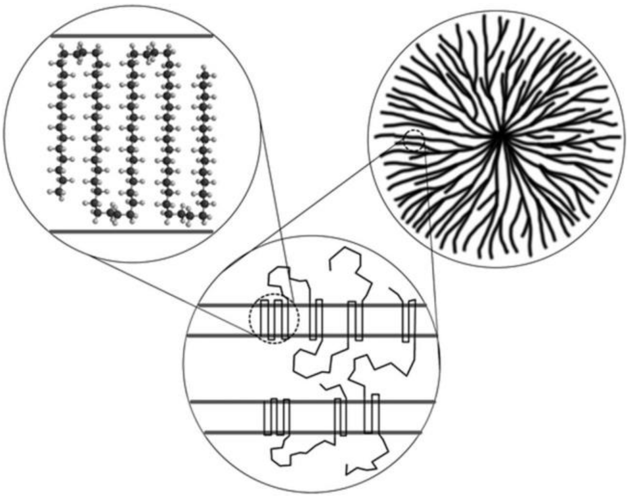

Figure 1.2. *Hierarchical structure of a semicrystalline polymer [5].*

In our work, a relevant parameter is the temperature at which the polymer chains can flow, as we will use a predominantly thermal process to nanostructure the polymeric samples. For amorphous polymers, that temperature is called glass transition temperature (T_g) [1,2]. Its value is specific to each polymer and depends on multiple factors such as molecular weight and chemical interactions. Regarding semicrystalline polymers, their amorphous regions will be able to flow at T_g, but their crystalline regions will need a higher temperature to break the crystalline structure. This temperature is called melting temperature (T_m) [2,3].

Polymers by themselves can have interesting unique properties that are often determined by the presence of chemical functional groups in their structure [6]. Besides, it is possible to give polymers added functionality with strategies such as including nanoadditives to a polymer matrix to create a nanocomposite [7,8] or creating micro- and nanostructures on the polymer surface [9,10]. In this research, we mainly investigated this last method, and we applied it to a semiconductive polymer *i.e.*, poly(3-hexylthiophene) (P3HT), as a representative of functional polymers; a nanocomposite —poly(trimethylene terephthalate) (PTT) doped with tungsten disulfide (WS_2) nanotubes (PTT-WS_2)—; and a commodity polymer *i.e.*, poly(ethylene terephthalate) (PET).

1.1.1. Semiconductive polymers

Polymers have been traditionally considered insulator materials. However, some polymers like P3HT, Poly(2,5-bis(3-tetradecylthiophen-2-yl)thieno[3,2-b]thiophene) (PBTTT), and Poly (p-phenylene vinylene) (PPV), are intrinsically conducting due to their particular molecular structure. They all share either having conjugated bonds, *i.e.,* alternating single and double bonds, along the polymer backbone; or being composed of aromatic rings joined by carbon-carbon single bonds [11]. The conductivity of conjugated polymers is due to the delocalization of π electrons that act like the conduction band in a metal [11]. Therefore, it is affected by the regioregularity of the polymer since the disposition of the atoms in each monomer must be the same to keep the chains of alternating bonds uninterrupted [12]. The name used for this “conduction band” is Lowest Unoccupied Molecular Orbital (LUMO) and the corresponding “valence band” is called Highest Occupied Molecular Orbital (HOMO). The difference in the energy levels HOMO-LUMO is the equivalent of the GAP in a semiconductor [11]. Besides this intrinsic conductivity, chemical doping and mechanical alignment of the polymer chains can increase the conductivity of a polymer by many orders of magnitude [11].

The interest in the study of semiconducting polymers has risen due to their potential applications in electronics, like PBTTT used in field effect transistors [13] and PPV in polymeric LEDs [14]; and in photovoltaics, such as P3HT used as a light absorber/electron donor material [15].

1.1.2. Nanocomposites

Nanocomposites are created by introducing some percentage of a nanometric material, called additive, into a polymeric matrix. Nanomaterials can have excellent mechanical, electrical and thermal properties that can be partially passed on to the nanomaterial even for ratios of nanomaterial to polymer matrix smaller than 1%. Its properties can be tailored by changing the two materials, the diffusion of the additive in the matrix, and the percentage of additive introduced [16]. These capabilities have popularized their use in biomaterials [17], protective coatings [18], thin film technology [19] and many others:

- Biomaterials for bone tissue regeneration [17]: a wide array of biocompatible polymeric matrices such as chitosan, collagen, cellulose, polyethylene glycol, poly (lactic acid), and polyurethane are used. Regarding nanofillers, nano-hydroxyapatite [20], nano-zirconia [21], nano-silica [22], silver nanoparticles [23], nano-titanium dioxide [24], and graphene oxide [25] are frequently employed to render important properties, such as large surface area, improved mechanical strength, stability, improved cell adhesion, proliferation, and cell differentiation.
- Protective coatings [18]: given the large number of different properties that nanocomposites can have it is possible to engineer different systems for different applications. Some examples are nano-silica in a poly (methyl methacrylate) (PMMA) matrix, used for anticorrosion [26] and halloysite nanotubes in an epoxy matrix, used as flame retardant [27].
- Thin film technology [19]: polyamide matrices with a multitude of different fillers such as zeolite nanoparticles, nano-silica, Ag nanoparticles, and carbon nanotubes have been investigated for water filtering.

1.2. Surface micro- and nanostructuring of polymers

Surface nanostructuring is a common strategy consisting of changing the surface of a material at the nanoscale to improve some of its mechanical, chemical or any other properties. In polymers, this strategy is useful to improve their surface mechanical properties or to give the material added functionality [9,10], in some cases imitating nature creating the so-called biomimetic surfaces [28]. Some examples of their applications are:

- Wettability: The creation of nanostructures on a surface can be engineered to create superhydrophilic or superhydrophobic surfaces, for instance to provide self-cleaning surfaces [29]. The control of wettability in a wider sense can apply to any liquid and has applications in biomaterials as for instance for the control of protein absorption [9].
- Anti-bacterial: Nanostructuring surfaces with features few times smaller than bacterial size prevents proliferation, either because it diminishes adhesion, or the nanostructures puncture the bacteria, killing it [30,31].
- Cell growth: Creating surfaces with features on the scale of cells size can improve cell growth. Moreover, cell growth may be guided through suitable design of the nanostructures [32]. This has been applied in fields such as dental implantology [33].
- Tribology: Nanostructuring a surface reduces its contact area and, therefore, its adhesion and friction properties [34].
- Organic photovoltaics: The electrons and holes are generated in the donor-acceptor interface. Thus, increasing the area of this interface would improve the performance of the device. This can be done without enlarging the device by increasing the interface roughness. Besides, surface nanostructures can also improve light absorption as a result of scattering and surface plasmon excitation [35].
- Sensors: In the same way they improve photovoltaics performance, nanostructures can increase the signal of sensors due to field confinement effects [36] or due to the increase in surface area [37].

Bearing in mind how different all these possibilities are, there is an interest in developing the nanostructuring techniques adequate for each application. Presently, the most common techniques for surface nanostructuring are lithographic techniques [38,39]. These techniques have the advantage of high reproducibility and low cost, but they are generally complex many-step techniques and require access to a controlled atmosphere facility, like a clean room.

Besides, their resolution, nanostructured area and versatility are quite limited. For these reasons, laser processing techniques [40–43] have been rising as a strong alternative.

1.3. Laser surface structuring of polymers

Laser processing techniques take advantage of the ability of the laser to accurately concentrate energy in a very small area. They are divided into two groups:

- Bottom-up approaches: They are based on the deposit of a controlled amount of material on a substrate until the desired structure is created. Some examples are Laser Induced Forward Transfer (LIFT) [40] —useful to deposit a thin layer of a material on a transparent substrate— and Matrix-Assisted Pulsed Laser Evaporation (MAPLE) [44] —which uses the mediation of a solvent to efficiently transfer soft materials to a substrate. Moreover, there are techniques, derived from these, for special cases, like MAPLE direct writing [44] —for materials sensitive to temperature elevation— and Laser Induced Thermal Imaging (LITI) [44] —for plastic microelectronic applications.
- Top-down approaches: They start from a bulk material and remove or rearrange parts of it to create the structures. Some examples are Laser Ablation [42,45] —which uses the laser beam directly to ablate the material— and Laser Interference Lithography (LIL) [41] —which uses the interference pattern of two or more laser beams to ablate the material, creating micro- and nanostructures. The technique that we study in this thesis —LIPSS—, is also a top-down technique. LIPSS are periodic ripples that form when irradiating a material with a laser in a particular intensity range. This technique can create nanostructures with periods from hundreds of nanometers to several microns and depths that can go from less than ten nanometers up to several hundreds. Its main advantages are a large processing area, simplicity of operation, and relatively low equipment requirements [46–48]. We will discuss this method in detail in the next section.

1.3.1. Laser Induced Periodic Surface Structures

Laser Induced Periodic Surface Structures are periodic ripples that are formed when irradiating a material with a laser in a particular intensity range. They were discovered by Birnbaum [49] at the bottom of an ablation crater. Sipe *et al*. explained them as the result of the interference of the incident wave with a surface scattered wave [50–52], which in the case of metals can be a Surface Plasmon Polariton (SPP), resulting in an inhomogeneous rise in temperature on the material surface. They even found a formula for their period (⍰):

$$\Lambda = \frac{\mathrm{A}}{\mathrm{n_{eff}\pm sin}} \tag{1.3}$$

where λ is the wavelength of the laser, θ is its incidence angle and n_{eff} is the effective refractive index close to the surface, also called the selvedge region [53].

Since then, the formation of LIPSS has been reported for laser pulses with different durations from ns [54] through ps [55] right up to fs [56] in all kinds of materials [57–60], with an orientation either parallel or perpendicular to the polarization of the laser depending on the material. Moreover, strategies have been developed that allow for the nanostructuring of large areas with high regularity and speed [61–63] as well as methods to use LIPSS to create different nanostructures like linear gratings, grids and arrays of nanodots [54]. The physicochemical modifications brought by LIPSS formation have also been studied using different methods [64–67].

The technique to generate LIPSS with femtosecond laser pulses offers some advantages related to the particular features of laser-matter interaction in this time regime. Those being that the linear optical absorption of the material is less critical, and a better control of the area affected by irradiation, since the interaction time is shorter than the thermal relaxation times resulting in a much smaller thermally affected area [68]. However, it is not fully understood yet. Bonse *et al*. [69] adapted Sipe's theory to consider changes in the refractive index due to the intensity of the laser following the Drude model, but it cannot explain LIPSS formation in full.

In particular, when using femtosecond pulses, there are two kinds of LIPSS: the already presented above LIPSS with a period given by eq. 1.3, called Low Spatial Frequency LIPSS (LSFL), and the so called High Spatial Frequency LIPSS (HSFL), with periods smaller than half the wavelength of the laser. Depending on the material, HSFL can appear parallel or perpendicular to the polarization of the laser (see Table 1.1). Although this classification has not been widely adopted, Bonse et al. [46] further subdivided them in two types: Type 1 HSFL, often observed in dielectrics and semiconductors, with a period of only a few tens of nanometers and a depth that can reach the hundreds of nanometers; and type 2 HSFL, often observed in metals, with periods of a few hundred nanometers and depths of only a few tens of nanometers.

Table 1.1. *Orientation and period of HSFL found in different materials.*

Material	Orientation	Period (Λ)	Reference
Si	Parallel	$\Lambda \leq 0.25\,\lambda$	[70]
Fused silica	Perpendicular	$\Lambda \leq 0.25\,\lambda$	[71]
Quartz	Perpendicular	$\Lambda \leq 0.21\,\lambda$	[71]
Ti	Parallel	$0.08 \leq \Lambda / \lambda \leq 0.12$	[72]
TiN	Perpendicular	$\Lambda \leq 0.16\,\lambda$	[73]
Steel (800H)	Parallel	$0.15 \leq \Lambda / \lambda \leq 0.24$	[74]
InP	Perpendicular	$\Lambda \leq 0.24\,\lambda$	[75]
Diamond	Parallel	$\Lambda \leq 0.26\,\lambda$	[76]
ZnO	Perpendicular	$0.25 \leq \Lambda / \lambda \leq 0.35$	[75,77]
ZnSe	Parallel	$\Lambda \sim \lambda / 2n$	[78]
Sapphire	Perpendicular	$\Lambda \leq 0.34\,\lambda$	[75]

The formation mechanism of HSFL continues being controversial today [79]. New theoretical models have been proposed to explain these phenomena, including a model based on self-organization from highly electrostatic instabilities originated by the laser [80], one based on thin-films hydrodynamics [81], another one based on the analysis of an electronic excitation when short-lived plasma is created [82,83] or another model that uses Finite Differences Time Domain methods to solve Maxwell’s curl equations for linear, isotropic, dispersive materials with no magnetic losses [84]. Moreover, the appearance of another kind of larger structures, both in depth and period, at higher fluences and number of pulses than LSFL and HSFL has been reported in semiconductors and metals [85]. The scope of this thesis is almost exclusively the study of LSFL, so from now on we will refer to them as LIPSS.

For both ns and fs pulses, LIPSS in bulk polymers appear parallel to polarization. They can form not only because of material removal [86] but also, for lower fluences, they appear due to a rearrangement of the material [47,56]. For this rearrangement to happen, the polymer must be heated above a temperature at which its polymer chains can flow. As discussed in Section 1.1, this temperature is T_g for amorphous polymers and T_m for crystalline polymers [4,87].

The influence of laser parameters in the formation of LIPSS has been studied quite extensively both for ns and fs lasers showing similar behaviors [69,88,89]. These studies demonstrated that the period and depth of LIPSS are influenced not only by the wavelength and the material (as shown in eq. 1.3) but also by the intensity and the number of pulses used. In general, both the depth and period of the structures grow with fluence until they reach a plateau. They have the same relation with the number of pulses, which is attributed to incubation effects [47,90–92].

Additionally, since the structures are parallel to polarization, the kind of beam we use changes the direction of the structures. We will explore this using Gaussian, vector, and vortex beams.

1.3.1.1. Types of beams for LIPSS formation

Any beam can be represented by eq. 1.4.

$$\vec{E}(\vec{r},t) = \vec{A}(\vec{r},t)e^{i\,(\vec{\ },\ )} \tag{1.4}$$

where $\vec{E}$ is the electric field, $\vec{r}$ is the position vector, t is time, the argument of the exponential (ϕ) is the state of oscillation of the electric field, called phase, the module of $\vec{A}$ is the amplitude of the electric field, and its direction is the direction of the electric field, which, taking its dependence with $\vec{r}$ and t into account, gives the so called polarization of the beam. The locus of the points where the phase is constant is called wavefront.

For linearly polarized plane harmonic waves [93], that is, waves with only one frequency (*f*), constant amplitude, with a direction of the electric field independent of $\vec{r}$ and t, and a plane wavefront, that equation becomes eq. 1.5.

$$\vec{E}(\vec{r},t) = \vec{A}\,e^{i(-\vec{k}\cdot\vec{\ }-w+\ 0)} \tag{1.5}$$

where $\omega = 2\pi f$ is the radial frequency, $\vec{k}$ is called wavevector, its module $k = \frac{wn}{e} = \frac{2rr}{\ }$ wavenumber, and its direction is the direction of propagation of the wave, n is the refractive index, c is the speed of light in vacuum, and ϕ_0 is the initial phase at $t = 0$ and $\vec{r} = 0$.

Gaussian Beams

Laser beams can usually be approximated by Gaussian beams [94]. The field can be represented by eq. 1.6, if it is linearly polarized, with *z* being the direction of propagation and *x* the direction of polarization, with the coordinate origin in the point where the radius of the beam is minimum.

$$\vec{E}(\rho,z,t) = A_0\vec{u}\,\frac{w_0}{w(z)}\,e^{-\frac{p^2}{(z)^2}}\,e^{i\,kz+k\frac{p^2}{2R(z)}-1/(z)-w\ )} \tag{1.6}$$

where A_0 is the peak amplitude of the electric field, w_0 is the minimum radius of the beam called beam waist, $w(z) = w_0\sqrt{1+\left(\frac{z}{z_R}\right)^2}$ is the radius of the beam, $z_R = \frac{rrw_0^2n}{\ }$ is the distance along the propagation direction from the waist of the beam to the point at which the area of the beam is doubled $(w(z_R) = \sqrt{2}\, w_0)$ called the Rayleigh range, $R(z) = \frac{z^2+z_R^2}{z}$ is the radius of curvature of the wavefront, $\rho = \sqrt{x^2 + y^2}$ is the cylindrical coordinate of radius, $\psi(z) = arctan\left(\frac{z}{z_R}\right)$ is the phase advance acquired by the beam around the focal region called Gouy phase and $\vec{u}$ is the unit vector in the x direction.

Vector Beams

Vector beams [95], also called beams carrying spin, are beams where the phase behaves like that of a Gaussian beam, but the polarization varies with the azimuth $\beta = arctan\left(\frac{y}{}\right)$. This variation in polarization forces a zero in intensity at the center of the beam to avoid a singularity, giving them an annular intensity spatial profile that can be approximated by the Laguerre-Gauss polynomial LG_{0l} [96]. An important property of these beams is their topological charge l, defined as the number of rotations in the azimuthal variation of the polarization. A vector beam propagating in the z direction can be described by eq. 1.7:

$$\vec{E} = A_0\, LG_{0l}(x, y)\, e^{-iw} \left(cos\,(|l|\beta)\vec{u} - sin(|l|\beta)\,\vec{u}_y\right) \tag{1.7}$$

where $\vec{u}_y$ is the unit vector in the y direction.

These beams have been used to create complex nanostructures in metals [97], semiconductors [98], and dielectrics [99].

Optical vortex Beams

Optical vortex beams [100], also referred to as beams carrying orbital angular momentum are beams with the same intensity spatial profile as vector beams but their polarization is circular and spatially constant, and their phase varies azimuthally. These beams also have an important property called topological charge l, but here it is defined as the number of rotations in the azimuthal variation of the phase.

A vortex beam propagating in the z direction can be described by eq. 1.8:

$$\vec{E} = A_0\, LG_{0l}(x, y)\, e^{-iw}\, cos(|l|\beta)\,(\vec{u} + e^{irr/2}\vec{u}_y) \tag{1.8}$$

These beams have been used to create complex nanostructures in materials such as silicon [101] and metallic alloys [102]. As for polymers, they have been used to create complex microstructures via ablation in azo-polymers [103].

We show the main characteristics of Gaussian, vector, and optical vortex beams in Figure 1.3.

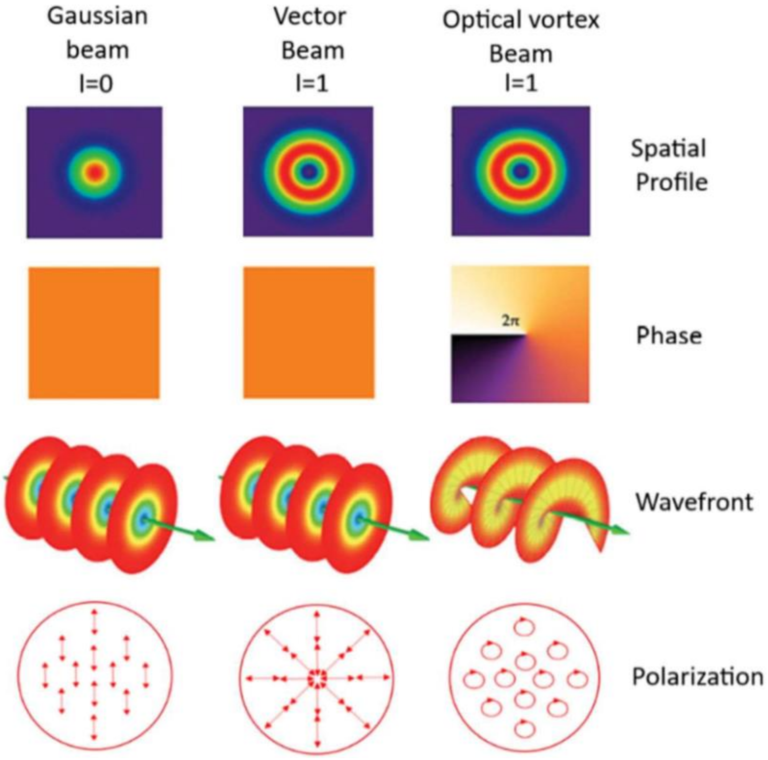

Figure 1.3. *Characteristics of Gaussian, vector, and optical vortex beams. (Image modified, credit: E-karimi, Creative Commons Attribution-Share Alike 3.0 unported).*

1.3.1.2. LIPSS in thin films

There has been growing interest in the investigation of LIPSS on thin films of different materials due to their potential applications [47,56,104–108]. For the formation of LIPSS, we need to bear in mind additional considerations, that is, the influence of different substrate properties and film thicknesses. Cui *et al*. [107] reported that the thermal conductivity of the substrate affects the threshold for LIPSS formation in the polymer thin film covering it and linked the LIPSS organization to the polymer film thickness. Besides, P. Nürberger *et al*. [108] observed a change in the orientation of the LIPSS formed on a SiO_2/Si layered system by varying the thickness of the dielectric SiO_2 on the semiconducting Si substrate. They explained it as a competition between two mechanisms, the SPP excited in the thin film-substrate boundary, which would produce LIPSS perpendicular to the polarization of the laser, and the surface scattered wave produced on the surface of the oxide thin film, which would result in the generation of LIPSS parallel to it. Moreover, some recent works in which LIPSS are formed on the surface of thin films of dielectric materials have remarkable interest, as it is the case of some oxides [59,109–112] in which LSFL are formed without any plasmonic interface. Regarding polymer thin films, there are studies showing the influence of the material of the substrate in the generation of LIPSS for UV nanosecond and femtosecond pulses [91,107], where the different heat transfer properties of the substrate change the intensity range for LIPSS formation. In addition, some other works using near-IR femtosecond pulses [113] revealed that LIPSS formation only happened for some types of substrates.

1.3.1.3. Surface Plasmon Polaritons and LIPSS formation

As we have briefly mentioned in the last sections, for metallic samples, the interference of the incident wave with a SPP excited on the surface of the sample is the mechanism that triggers LIPSS formation and P. Nürberger *et al.* [108] proposed SPP as one of the contributing mechanisms in LIPSS formation in a thin film of SiO_2 deposited on Si, a semiconductor. As long as we are studying thin films of polymers deposited on different substrates, some of which are metallic and semiconductors, it is worth introducing SPP and their properties in more detail.

SPP is a surface scattered wave that can be excited in the interface between a metal and a dielectric [114]. Solving Maxwell equations for the geometric conditions of SPP excitation gives as a result a transverse magnetic (TM) evanescent wave. For a plane interface at $y = 0$, the x axis can be chosen so the SPP field is described by eq. 1.9:

$$E_{\mathrm{d,m}} = (E\ \ , E_{\mathrm{yd,ym}}, 0)\ exp(-k_{\mathrm{yd,ym}}y)\ exp\ [i(k_{\mathrm{SPP}}x - \omega t)] \tag{1.9}$$

where $k_{\mathrm{SPP}} = \frac{\mathrm{w}}{\mathrm{e}}\sqrt{\frac{\mathrm{E_dE_m}}{\mathrm{E_d+E_m}}}$ is the modulus of the SPP wavevector for plane interfaces and media with thickness much larger than the penetration distance of the SPP, ε is the electric permittivity, the subindexes d and m correspond to the field in the dielectric and the metal respectively, $k^2_{\mathrm{yd,ym}} = k^2_{\mathrm{SPP}} - \varepsilon_{\mathrm{d,m}}\left(\frac{\mathrm{w}}{\mathrm{e}}\right)^2$ and $E_{\mathrm{yd,ym}} = i\frac{\mathrm{k_{SPP}}}{\mathrm{k_{yd,ym}}}E$.

The properties relevant to our case are the spatial period Λ and the penetration length in the metal P_{m} and in the dielectric P_{d}. The spatial period is defined as usual, and the penetration length is defined as the distance from the interface at which the SPP field amplitude decays $1/e$ times. These properties can be obtained from the wavevector modulus k_{SPP} as [114]:

$$\Lambda = 2\pi/k_{\mathrm{SPP}} \quad ; \quad P_{\mathrm{d}} = 1/Re(k_{\mathrm{yd}}) \quad ; \quad P_{\mathrm{m}} = 1/Re(k_{\mathrm{ym}}) \tag{1.10}$$

SPP is a TM wave, hence the direction of its wavevector is parallel to the projection of the laser polarization on the interface. As seen in the definition of k_{SPP}, since $\varepsilon_{\mathrm{d}} > 1$ and $Re(\varepsilon_{\mathrm{m}}) < 0$, the SPP wavevector is larger than the one of the incident light (ω/c), so to excite SPP we need to increase this wavevector. There are many irradiation setups to achieve this reported in the bibliography [115]. In this work, SPPs should be eventually excited just as a result of scattering due to substrate roughness.

Regarding the influence of the different parameters on SPP, there are theoretical works about the influence of the properties of a thin film deposited on a substrate and the SPP generated. According to the theory [116], the thickness of the thin film changes the SPP wavevector and, therefore, the LIPSS period, following eq. 1.11:

$$e^{-4k_{tf}d} = \frac{k_{tf}/E_{tf}+k_s/E_s}{k_{tf}/E_{tf}-k_s/E_s}\,\frac{k_{tf}/E_{tf}+k_{air}/E_{air}}{k_{tf}/E_{tf}-k_{air}/E_{air}} \tag{1.11}$$

where k is the wavevector modulus and the subindexes $tf,\ s,$ and air refer to the thin film, substrate, and air respectively. As it can be observed in [116], for small thickness eq. 1.11 can be approximated as:

$$k_{\mathrm{SPP-}} = k_{\mathrm{SPP}} + k_{\mathrm{a}} + k_{\mathrm{b}} \tag{1.12}$$

with k_{a} and k_{b}:

$$k_{\mathrm{a}} = \frac{2rr}{\ }\ \frac{E_{tf}-E_{air}}{E_{tf}})\left(\frac{E_{air}Re(E_s)}{E_{air}+Re(E_s)}\right)^{2}\left(\frac{E_{tf}-Re(E_s)}{E_{air}-Re(E_s)}\right)\left(-Re(\varepsilon_S)\varepsilon_{ai}\ \right)^{-\frac{1}{2}}\left(\frac{2rr}{\ }d\right) \tag{1.13}$$

$$k_{\mathrm{b}} = k_{\mathrm{a}}\ \frac{1\quad k_a}{2\ Re(k_{SPP})}\left(\frac{2(2E_{air}^2-E_{tf}^2)}{E_{air}(E_{air}-E_{tf})}+\frac{Re(E_s)+E_{air}}{-E_{air}}\right)-\frac{1}{2}\ \frac{/m(E_s)}{Re(E_s)} \tag{1.14}$$

As for the effect of roughness, there are also studies about its influence on the formation of SPP [117–120] and its impact on LIPSS properties [121]. These studies are focused on the influence of two roughness parameters. The root mean square roughness (R_{q}),

$$R_{\mathrm{q}} = \left[\frac{1}{LA}\int_0^L\int_0^A Z(x,y)^2dxdy\right]^{1/2} \tag{1.15}$$

with $Z(x,\ y)$ being the surface height function, which is an indication of the height or depth of the surface features; and the autocorrelation length (σ), defined as the horizontal distance at which the autocorrelation function (eq. 1.16) decreases to 0.2 at the highest rate, which is an indication of their width.

$$ACF(t\ \ ,t_y) = \frac{\int_0^L\int_0^A Z(\ \ ,y)Z((\ \ -\ \ _x),(y-\ \ _y))d\ \ dy}{\int_0^L\int_0^A Z(\ \ ,y)Z(\ \ ,y)d\ \ dy} \tag{1.16}$$

For more information about their mathematical definition see reference [122].

Getting back to the matter at hand, in the appendix of reference [117], it was shown that for $\varepsilon_{\mathrm{S}} = \varepsilon_{\mathrm{S}} + i\ \varepsilon_{\mathrm{Si}}$ with $|\varepsilon_{\mathrm{S}}| \gg |\varepsilon_{\mathrm{Si}}|$, R_{q} and σ cause a change in the wavevector of the SPP, provided R_{q} is much smaller than the incident laser wavelength, that follows eq. 1.17:

$$\Delta k_{\mathrm{SPP}} = \frac{R_{\mathrm{q}}^2\sigma^2}{2}\frac{|\varepsilon_{\mathrm{sr}}\varepsilon_{\mathrm{tf}}|^{1/2}}{(\varepsilon_{\mathrm{sr}}+\varepsilon_{\mathrm{tf}})^2}\, e^{-k_{\mathrm{SPP}}^2\sigma^2/4}\, F(k_{\mathrm{SPP}},\ k,\sigma) \qquad (1.17)$$

where $F(k_{\mathrm{SPP}},\ k,\ \sigma)$ is a function independent of R_{q}. From eq. 1.17 and eq. 1.10 follows that the period and penetration length of the SPP decrease monotonically with R_{q} and have a more complex dependence with σ.

No need to mention the importance of the material of the substrate itself, since SPP can only be generated in metal-dielectric interfaces, and their properties are heavily influenced by the electric permittivity of the materials on both sides of the interface [114].

1.4. Structure of this thesis

This thesis is organized into seven chapters. In this first chapter, we have introduced the theoretical background and state of the art concerning this research field.

In Chapter 2, we will describe the properties of the materials we worked with and the methods to prepare our samples, as well as the different irradiation schemes and characterization techniques used for each sample. Finally, we will explain the numerical simulation methods used to better understand the changes in some of the samples after irradiation.

In Chapters 3 to 6, we will show the results of our investigations as well as a discussion of these results. In Chapter 3, we will explore the formation of LIPSS in PET thin films of different thickness on different substrates. In Chapter 4, we will study the formation mechanism of LIPSS in the samples with gold substrates with the help of numerical simulations. In Chapter 5, we will get into the characterization of LIPSS properties that can be interesting for potential applications, such us the change in micromechanical properties, topography, surface energy, and wettability induced by LIPSS formation in the nanocomposite PTT-WS_2. In Chapter 6, we will study the changes in conductivity after generating LIPSS with vector beams in P3HT and (6,6)-Phenyl C_{71} butyric acid methyl ester ($PC_{71}BM$).

Finally, in Chapter 7, we will summarize the main results of this thesis and possible lines for future investigations.

1.5. References

[1] C.A. Harper, Modern Plastics Handbook, McGraw-Hill, 2000. https://www.accessengineeringlibrary.com/content/book/9780070267145 (accessed March 31, 2020).

[2] J.M.G. Cowie, V. (Valeria) Arrighi, Polymers Chemistry and Physics of Modern Materials, Third Edition., CRC Press, 2007.

[3] W. Hu, Polymer physics: A molecular approach, 1st ed., Springer Vienna, 2013. https://doi.org/10.1007/978-3-7091-0670-9.

[4] G. Strobl, The physics of polymers: Concepts for understanding their structures and behavior, 3rd ed., Springer Berlin Heidelberg, 2007. https://doi.org/10.1007/978-3-540-68411-4.

[5] S.T. Milner, Polymer crystal-melt interfaces and nucleation in polyethylene, Soft Matter. 7 (2011) 2909–2917. https://doi.org/10.1039/c0sm00070a.

[6] K. Wang, K. Amin, Z. An, Z. Cai, H. Chen, H. Chen, Y. Dong, X. Feng, W. Fu, J. Gu, Y. Han, D. Hu, R. Hu, D. Huang, F. Huang, F. Huang, Y. Huang, J. Jin, X. Jin, Q. Li, T. Li, Z. Li, Z. Li, J. Liu, J. Liu, S. Liu, H. Peng, A. Qin, X. Qing, Y. Shen, J. Shi, X. Sun, B. Tong, B. Wang, H. Wang, L. Wang, S. Wang, Z. Wei, T. Xie, C. Xu, H. Xu, Z.K. Xu, B. Yang, Y. Yu, X. Zeng, X. Zhan, G. Zhang, J. Zhang, M.Q. Zhang, X.Z. Zhang, X. Zhang, Y. Zhang, Y. Zhang, C. Zhao, W. Zhao, Y. Zhou, Z. Zhou, J. Zhu, X. Zhu, B.Z. Tang, Advanced functional polymer materials, Materials Chemistry Frontiers 4 (2020) 1803–1915. https://doi.org/10.1039/D0QM00025F.

[7] G. Mittal, V. Dhand, K.Y. Rhee, S.J. Park, W.R. Lee, A review on carbon nanotubes and graphene as fillers in reinforced polymer nanocomposites, Journal of Industrial and Engineering Chemistry 21 (2015) 11–25. https://doi.org/10.1016/J.JIEC.2014.03.022.

[8] S. Paszkiewicz, A. Szymczyk, R. Pilawka, B. Przybyszewski, A. Czulak, Z. Rosłaniec, Improved Thermal Conductivity of Poly(trimethylene terephthalate- *block* -poly(tetramethylene oxide) Based Nanocomposites Containing Hybrid Single-Walled Carbon Nanotubes/Graphene Nanoplatelets Fillers, Advances in Polymer Technology 36 (2017) 236–242. https://doi.org/10.1002/adv.21611.

[9] I. Firkowska-Boden, X. Zhang, K.D. Jandt, Controlling Protein Adsorption through Nanostructured Polymeric Surfaces, Advanced Healthcare Materials 7 (2018) 1700995. https://doi.org/10.1002/ADHM.201700995.

[10] J.C. Arango, L.O. Williams, A. Shi, A. Singh, E.K. Nava, R. v. Fisher, J.A. Garfield, S.A. Claridge, Nanostructured Surface Functionalization of Polyacrylamide Hydrogels Below the Length Scale of Hydrogel Heterogeneity, ACS Applied Materials & Interfaces 14 (2022) 43937–43945. https://doi.org/10.1021/acsami.2c12034.

[11] M.C. Scharber, N.S. Sariciftci, Low Band Gap Conjugated Semiconducting Polymers, Advanced Materials Technology 6 (2021) 2000857. https://doi.org/10.1002/admt.202000857.

[12] B. de Boer, A. Facchetti, Semiconducting polymeric materials, Polymer Reviews 48 (2008) 423–431. https://doi.org/10.1080/15583720802231718.

[13] I. McCulloch, M. Heeney, C. Bailey, K. Genevicius, I. MacDonald, M. Shkunov, D. Sparrowe, S. Tierney, R. Wagner, W. Zhang, M.L. Chabinyc, R.J. Kline, M.D. McGehee, M.F. Toney, Liquid-crystalline semiconducting polymers with high charge-carrier mobility, Nature Materials 5 (2006) 328–333. https://doi.org/10.1038/nmat1612.

[14] M.T. Bernius, M. Inbasekaran, J. O'brien, W. Wu, Progress with Light-Emitting Polymers, Advanced Materials 12 (2000) 1737–1750. https://doi.org/10.1002/1521-4095.

[15] K. Xian, Y. Liu, J. Liu, J. Yu, Y. Xing, Z. Peng, K. Zhou, M. Gao, W. Zhao, G. Lu, J. Zhang, J. Hou, Y. Geng, L. Ye, Delicate crystallinity control enables high-efficiency P3HT organic photovoltaic cells, Journal of Materials Chemistry A 10 (2022) 3418–3429. https://doi.org/10.1039/D1TA10161G.

[16] F. Hussain, M. Hojjati, M. Okamoto, R.E. Gorga, Review article: Polymer-matrix nanocomposites, processing, manufacturing, and application: An overview, Journal of Composite Materials 40 (2006) 1511–1575. https://doi.org/10.1177/0021998306067321.

[17] A. Bharadwaz, A.C. Jayasuriya, Recent trends in the application of widely used natural and synthetic polymer nanocomposites in bone tissue regeneration, Materials Science and Engineering: C 110 (2020) 110698. https://doi.org/10.1016/J.MSEC.2020.110698.

[18] C.I. Idumah, C.M. Obele, E.O. Emmanuel, A. Hassan, Recently Emerging Nanotechnological Advancements in Polymer Nanocomposite Coatings for Anti-corrosion, Anti-fouling and Self-healing, Surfaces and Interfaces 21 (2020) 100734. https://doi.org/10.1016/j.surfin.2020.100734.

[19] Z. Yang, P.F. Sun, X. Li, B. Gan, L. Wang, X. Song, H.D. Park, C.Y. Tang, A Critical Review on Thin-Film Nanocomposite Membranes with Interlayered Structure: Mechanisms, Recent Developments, and Environmental Applications, Environmental Science & Technology 54 (2020) 15563–15583. https://doi.org/10.1021/acs.est.0c05377.

[20] W. Bonfield, M.D. Grynpas, A.E. Tully, J. Bowman, J. Abram, Hydroxyapatite reinforced polyethylene — a mechanically compatible implant material for bone replacement, Biomaterials 2 (1981) 185–186. https://doi.org/10.1016/0142-9612(81)90050-8.

[21] B. Gaihre, A.C. Jayasuriya, Comparative investigation of porous nano-hydroxyapaptite/chitosan, nano-zirconia/chitosan and novel nano-calcium zirconate/chitosan composite scaffolds for their potential applications in bone regeneration, Materials Science and Engineering: C 91 (2018) 330–339. https://doi.org/10.1016/J.MSEC.2018.05.060.

[22] M. Mehrasa, M.A. Asadollahi, K. Ghaedi, H. Salehi, A. Arpanaei, Electrospun aligned PLGA and PLGA/gelatin nanofibers embedded with silica nanoparticles for tissue engineering, International Journal of Biological Macromolecules 79 (2015) 687–695. https://doi.org/10.1016/J.IJBIOMAC.2015.05.050.

[23] A. Hasan, G. Waibhaw, V. Saxena, L.M. Pandey, Nano-biocomposite scaffolds of chitosan, carboxymethyl cellulose and silver nanoparticle modified cellulose nanowhiskers for bone tissue engineering applications, International Journal of Biological Macromolecules 111 (2018) 923–934. https://doi.org/10.1016/J.IJBIOMAC.2018.01.089.

[24] Z. Chen, Y. Wang, T. Ba, Y. Li, J. Pu, T. Chen, Y. Song, Y. Gu, Q. Qian, J. Yang, G. Jia, Genotoxic evaluation of titanium dioxide nanoparticles in vivo and in vitro, Toxicology Letters 226 (2014) 314–319. https://doi.org/10.1016/J.TOXLET.2014.02.020.

[25] W. Shao, J. He, F. Sang, Q. Wang, L. Chen, S. Cui, B. Ding, Enhanced bone formation in electrospun poly(l-lactic-co-glycolic acid)–tussah silk fibroin ultrafine nanofiber scaffolds incorporated with graphene oxide, Materials Science and Engineering: C 62 (2016) 823–834. https://doi.org/10.1016/J.MSEC.2016.01.078.

[26] N. Saba, M. Jawaid, O.Y. Alothman, M.T. Paridah, A. Hassan, Recent advances in epoxy resin, natural fiber-reinforced epoxy composites and their applications, Journal of Reinforced Plastics and Composites. 35 (2015) 447–470. https://doi.org/10.1177/0731684415618459.

[27] N. Misra, V. Kumar, J. Bahadur, S. Bhattacharya, S. Mazumder, L. Varshney, Layered silicate-polymer nanocomposite coatings via radiation curing process for flame retardant applications, Progress in Organic Coatings 77 (2014) 1443–1451. https://doi.org/10.1016/J.PORGCOAT.2014.04.027.

[28] E. Stratakis, J. Bonse, J. Heitz, J. Siegel, G.D. Tsibidis, E. Skoulas, A. Papadopoulos, A. Mimidis, A.C. Joel, P. Comanns, J. Krüger, C. Florian, Y. Fuentes-Edfuf, J. Solis, W. Baumgartner, Laser engineering of biomimetic surfaces, Materials Science and Engineering: R: Reports 141 (2020) 100562. https://doi.org/10.1016/J.MSER.2020.100562.

[29] S. K. Samal, S. Mohanty, S.K. Nayak, eds., Superhydrophobic Polymer Coatings, Elsevier, 2019. https://doi.org/10.1016/c2018-0-00746-x.

[30] D.P. Linklater, V.A. Baulin, S. Juodkazis, R.J. Crawford, P. Stoodley, E.P. Ivanova, Mechano-bactericidal actions of nanostructured surfaces, Nature Reviews Microbiology 19 (2021) 8–22. https://doi.org/10.1038/s41579-020-0414-z.

[31] A.M. Richter, G. Buchberger, D. Stifter, J. Duchoslav, A. Hertwig, J. Bonse, J. Heitz, K. Schwibbert, Spatial period of laser-induced surface nanoripples on pet determines escherichia coli repellence, Nanomaterials 11 (2021) 3000. https://doi.org/10.3390/NANO11113000/S1.

[32] E. Rebollar, I. Frischauf, M. Olbrich, T. Peterbauer, S. Hering, J. Preiner, P. Hinterdorfer, C. Romanin, J. Heitz, Proliferation of aligned mammalian cells on laser-nanostructured polystyrene, Biomaterials 29 (2008) 1796–1806. https://doi.org/10.1016/J.BIOMATERIALS.2007.12.039.

[33] R. Rasouli, A. Barhoum, H. Uludag, A review of nanostructured surfaces and materials for dental implants: Surface coating, patterning and functionalization for improved performance, Biomaterials Science 6 (2018) 1312–1338. https://doi.org/10.1039/c8bm00021b.

[34] P. Lan, E.E. Nunez, A.A. Polycarpou, Advanced Polymeric Coatings and Their Applications: Green Tribology, in: S. Hashmi, I.A. Choudhury (Eds.), Encyclopedia of Renewable and Sustainable Materials, Elsevier, 2020: pp. 345–358. https://doi.org/10.1016/b978-0-12-803581-8.11466-3.

[35] T. Putnin, S. Nootchanat, C. Lertvachirapaiboon, K. Shinbo, K. Kato, K. Ounnunkad, A. Baba, Effect of Micro/Nanostructured P3HT:PCBM Surfaces on the Performance of Organic Photovoltaic Devices, Molecular Crystals and Liquid Crystals 688 (2019) 89–97. https://doi.org/10.1080/15421406.2019.1651073.

[36] R.A. Surmenev, R. V. Chernozem, I.O. Pariy, M.A. Surmeneva, A review on piezo- and pyroelectric responses of flexible nano- and micropatterned polymer surfaces for biomedical sensing and

energy harvesting applications, Nano Energy 79 (2021) 105442. https://doi.org/10.1016/j.nanoen.2020.105442.

[37] E.D. Diebold, N.H. Mack, S.K. Doom, E. Mazur, Femtosecond Laser-Nanostructured substrates for Surface-Enhanced Raman scattering, Langmuir 25 (2009) 1790–1794. https://doi.org/10.1021/la803357q.

[38] M.A. Rose, J.J. Bowen, S.A. Morin, Emergent Soft Lithographic Tools for the Fabrication of Functional Polymeric Microstructures, ChemPhysChem 20 (2019) 909–925. https://doi.org/10.1002/CPHC.201801140.

[39] L.M. Cox, A.M. Martinez, A.K. Blevins, N. Sowan, Y. Ding, C.N. Bowman, Nanoimprint lithography: Emergent materials and methods of actuation, Nano Today 31 (2020) 100838. https://doi.org/10.1016/J.NANTOD.2019.100838.

[40] B. Thomas, A.P. Alloncle, P. Delaporte, M. Sentis, S. Sanaur, M. Barret, P. Collot, Experimental investigations of laser-induced forward transfer process of organic thin films, Applied Surface Science 254 (2007) 1206–1210. https://doi.org/10.1016/J.APSUSC.2007.09.042.

[41] F. Yu, P. Li, H. Shen, S. Mathur, C.-M. Lehr, U. Bakowsky, F. Mücklich, Laser interference lithography as a new and efficient technique for micropatterning of biopolymer surface, Biomaterials 26 (2005) 2307–2312. https://doi.org/10.1016/J.BIOMATERIALS.2004.07.021.

[42] S. Lazare, V. Tokarev, A. Sionkowska, M. Wiśniewski, Surface foaming of collagen, chitosan and other biopolymer films by KrF excimer laser ablation in the photomechanical regime, Applied Physics A 81 (2005) 465–470. https://doi.org/10.1007/s00339-005-3260-y.

[43] M. Sirajuddin, P.J. Reddy, Pyroelectric behaviour of laser-evaporated poly(vinyl fluoride) films, Thin Solid Films 124 (1985) 149–154. https://doi.org/10.1016/0040-6090(85)90257-3.

[44] A.P. Caricato, A. Luches, Applications of the matrix-assisted pulsed laser evaporation method for the deposition of organic, biological and nanoparticle thin films: a review, Applied Physics A 2011 105:3 105 (2011) 565–582. https://doi.org/10.1007/S00339-011-6600-0.

[45] P.E. Dyer, Excimer laser polymer ablation: twenty years on, Applied Physics A 77 (2003) 167–173. https://doi.org/10.1007/S00339-003-2137-1.

[46] J. Bonse, S. Hohm, S. V. Kirner, A. Rosenfeld, J. Kruger, Laser-Induced Periodic Surface Structures-A Scientific Evergreen, IEEE Journal on Selected Topics in Quantum Electronics 23 (2017) 9000615. https://doi.org/10.1109/JSTQE.2016.2614183.

[47] E. Rebollar, M. Castillejo, T.A. Ezquerra, Laser induced periodic surface structures on polymer films: From fundamentals to applications, European Polymer Journal 73 (2015) 162–174. https://doi.org/10.1016/j.eurpolymj.2015.10.012.

[48] J. Bonse, S. v Kirner, S. Höhm, N. Epperlein, D. Spaltmann, A. Rosenfeld, J. Krüger, Applications of laser-induced periodic surface structures (LIPSS), in: U. Klotzbach, K. Washio, R. Kling (Eds.), Laser-Based Micro- and Nanoprocessing XI, SPIE, 2017: pp. 114–122. https://doi.org/10.1117/12.2250919.

[49] M. Birnbaum, Semiconductor Surface Damage Produced by Ruby Lasers, Journal of Applied Physics 36 (1965) 3688–3689. https://doi.org/10.1063/1.1703071.

[50] J.E. Sipe, J.F. Young, J.S. Preston, H.M. van Driel, Laser-induced periodic surface structure. I. Theory, Physical Reviews B 27 (1983) 1141–1154. https://doi.org/10.1103/PhysRevB.27.1141.

[51] J.F. Young, J.S. Preston, H.M. van Driel, J.E. Sipe, Laser induced periodic surface structure. II. Experiments on Ge, Si, Al and brass, Physical Review B 27 (1983) 1155–1172. https://doi.org/10.1103/PhysRevB.27.1155.

[52] J.F. Young, J.E. Sipe, H.M. van Driel, Laser-induced periodic surface structure. III. Fluence regimes, the role of feedback, and details of the induced topography in germanium, Physical Review B 30 (1984) 2001–2015. https://doi.org/10.1103/PhysRevB.30.2001.

[53] J.E. Sipe, Bulk-selvedge coupling theory for the optical properties of surfaces, Physical Review B 22 (1980) 1589–1599. https://doi.org/10.1103/PhysRevB.22.1589.

[54] E. Gutiérrez-Fernández, T.A. Ezquerra, A. Nogales, E. Rebollar, Straightforward patterning of functional polymers by sequential nanosecond pulsed laser irradiation, Nanomaterials 11 (2021). https://doi.org/10.3390/nano11051123.

[55] M. Mezera, M. van Drongelen, G.R.B.E. Römer, Laser-Induced Periodic Surface Structures (LIPSS) on Polymers Processed with Picosecond Laser Pulses, Journal of Laser Micro/Nanoengineering 13 (2018) 105–116. https://doi.org/10.2961/jlmn.2018.02.0010.

[56] E. Rebollar, J.R. Vázquez De Aldana, I. Martín-Fabiani, M. Hernández, D.R. Rueda, T.A. Ezquerra, C. Domingo, P. Moreno, M. Castillejo, Assessment of femtosecond laser induced periodic surface structures on polymer films, Physical Chemistry Chemical Physics 15 (2013) 11287–11298. https://doi.org/10.1039/c3cp51523k.

[57] S.I. Kudryashov, T. Pflug, N.I. Busleev, M. Olbrich, A. Horn, M.S. Kovalev, N.G. Stsepuro, Topological transition from deeply sub- to near-wavelength ripples during multi-shot mid-IR femtosecond laser exposure of a silicon surface, Optical Materials Express 11 (2021) 1. https://doi.org/10.1364/ome.412790.

[58] G.D. Tsibidis, E. Stratakis, Ionisation processes and laser induced periodic surface structures in dielectrics with mid-infrared femtosecond laser pulses, Scientific Reports 10 (2020). https://doi.org/10.1038/s41598-020-65613-w.

[59] C. Florian, J.L. Déziel, S. v. Kirner, J. Siegel, J. Bonse, The role of the laser-induced oxide layer in the formation of laser-induced periodic surface structures, Nanomaterials 10 (2020). https://doi.org/10.3390/nano10010147.

[60] O. Shavdina, H. Rabat, M. Vayer, A. Petit, C. Sinturel, N. Semmar, Polystyrene thin films nanostructuring by UV femtosecond laser beam: From one spot to large surface, Nanomaterials 11 (2021). https://doi.org/10.3390/nano11051060.

[61] A. San-Blas, M. Martinez-Calderon, E. Granados, M. Gómez-Aranzadi, A. Rodríguez, S.M. Olaizola, LIPSS manufacturing with regularity control through laser wavefront curvature, Surfaces and Interfaces 25 (2021) 101205. https://doi.org/10.1016/J.SURFIN.2021.101205.

[62] C. Kunz, S. Engel, F.A. Müller, S. Gräf, Large-Area Fabrication of Laser-Induced Periodic Surface Structures on Fused Silica Using Thin Gold Layers, Nanomaterials 10 (2020) 1187. https://doi.org/10.3390/NANO10061187.[63] J. Reif, C. Martens, S. Uhlig, M. Ratzke, O. Varlamova, S. Valette, S. Benayoun, On large area LIPSS coverage by multiple pulses, Applied Surface Science 336 (2015) 249–254. https://doi.org/10.1016/J.APSUSC.2014.11.153.

[63] J. Reif, C. Martens, S. Uhlig, M. Ratzke, O. Varlamova, S. Valette, S. Benayoun, On large area LIPSS coverage by multiple pulses, Applied Surface Science 336 (2015) 249–254. https://doi.org/10.1016/J.APSUSC.2014.11.153.

[64] E. Rebollar, S. Pérez, M. Hernández, C. Domingo, M. Martín, T.A. Ezquerra, J.P. García-Ruiz, M. Castillejo, Physicochemical modifications accompanying UV laser induced surface structures on poly(ethylene terephthalate) and their effect on adhesion of mesenchymal cells, Physical Chemistry Chemical Physics 16 (2014) 17551–17559. https://doi.org/10.1039/c4cp02434f.

[65] R.I. Rodríguez-Beltrán, D.E. Martínez-Tong, A. Reyes-Contreras, S. Paszkiewicz, A. Szymczyk, T.A. Ezquerra, P. Moreno, E. Rebollar, Laterally-resolved mechanical and tribological properties of laser-structured polymer nanocomposites, Polymer 168 (2019) 178–184. https://doi.org/10.1016/j.polymer.2019.02.034.

[66] S. Pérez, E. Rebollar, M. Oujja, M. Martín, M. Castillejo, Laser-induced periodic surface structuring of biopolymers, Applied Physics A 110 (2013) 683–690. https://doi.org/10.1007/s00339-012-7186-x.

[67] J. Prada-Rodrigo, R.I. Rodríguez-Beltrán, S. Paszkiewicz, A. Szymczyk, T.A. Ezquerra, P. Moreno, E. Rebollar, Laser-induced periodic surface structuring of poly(trimethylene terephthalate) films containing tungsten disulfide nanotubes, Polymers 12 (2020) 1090. https://doi.org/10.3390/POLYM12051090.

[68] B.N. Chichkov, C. Momma, S. Nolte, F. Von Alvensleben, A. Tünnermann, Femtosecond, picosecond and nanosecond laser ablation of solids, Applied Physics A 63 (1996) 109–115. https://doi.org/10.1007/BF01567637.

[69] J. Bonse, A. Rosenfeld, J. Krüger, On the role of surface plasmon polaritons in the formation of laser-induced periodic surface structures upon irradiation of silicon by femtosecond-laser pulses, Journal of Applied Physics 106 (2009) 104910. https://doi.org/10.1063/1.3261734.

[70] F. Costache, S. Kouteva-Arguirova, J. Reif, Sub-damage-threshold femtosecond laser ablation from crystalline Si: Surface nanostructures and phase transformation, Applied Physics A 79 (2004) 1429–1432. https://doi.org/10.1007/s00339-004-2803-y.

[71] S. Höhm, A. Rosenfeld, J. Krüger, J. Bonse, Femtosecond laser-induced periodic surface structures on silica, Journal of Applied Physics 112 (2012) 014901. https://doi.org/10.1063/1.4730902.

[72] J. Bonse, S. Höhm, A. Rosenfeld, J. Krüger, Sub-100-nm laser-induced periodic surface structures upon irradiation of titanium by Ti:sapphire femtosecond laser pulses in air, Applied Physics A 110 (2013) 547–551. https://doi.org/10.1007/s00339-012-7140-y.

[73] N. Yasumaru, K. Miyazaki, J. Kiuchi, Femtosecond-laser-induced nanostructure formed on hard thin films of TiN and DLC, Applied Physics A 76 (2003) 983–985. https://doi.org/10.1007/S00339-002-1979-2.

[74] B. Huis in ’t Veld, H. van der Veer, Initiation of femtosecond laser machined ripples in steel observed by scanning helium ion microscopy (SHIM), Journal of Laser Micro Nanoengineering 5 (2010) 28–34. https://doi.org/10.2961/JLMN.2010.01.0007.

[75] A. Borowiec, H.K. Haugen, Subwavelength ripple formation on the surfaces of compound semiconductors irradiated with femtosecond laser pulses, Applied Physics Letters 82 (2003) 4462. https://doi.org/10.1063/1.1586457.

[76] Q. Wu, Y. Ma, R. Fang, Y. Liao, Q. Yu, X. Chen, K. Wang, Femtosecond laser-induced periodic surface structure on diamond film, Applied Physics Letters 82 (2003) 1703–1705. https://doi.org/10.1063/1.1561581.

[77] D. Dufft, A. Rosenfeld, S.K. Das, R. Grunwald, J. Bonse, Femtosecond laser-induced periodic surface structures revisited: A comparative study on ZnO, Journal of Applied Physics 105 (2009) 034908. https://doi.org/10.1063/1.3074106.

[78] T.Q. Jia, H.X. Chen, M. Huang, F.L. Zhao, J.R. Qiu, R.X. Li, Z.Z. Xu, X.K. He, J. Zhang, H. Kuroda, Formation of nanogratings on the surface of a ZnSe crystal irradiated by femtosecond laser pulses, Physicl Review B 72 (2005) 125429. https://doi.org/10.1103/PhysRevB.72.125429.

[79] A. Sarracino, A.R. Ansari, B. Torralva, S. Yalisove, Sub-100 nm high spatial frequency periodic structures driven by femtosecond laser induced desorption in GaAs, Applied Physics Letters 118 (2021) 242106. https://doi.org/10.1063/5.0053037.

[80] O. Varlamova, J. Reif, S. Varlamov, M. Bestehorn, Self-organized Surface Patterns Originating from Laser-Induced Instability, in: S. Sakabe, C. Lienau, R. Grunwald (Eds.), Progress in Nonlinear Nano-Optics. Nano-Optics and Nanophotonics, Springer, Cham, 2015: pp. 3–29. https://doi.org/10.1007/978-3-319-12217-5_1.

[81] G.D. Tsibidis, C. Fotakis, E. Stratakis, From ripples to spikes: A hydrodynamical mechanism to interpret femtosecond laser-induced self-assembled structures, Physical Review B 92 (2015) 041405. https://doi.org/10.1103/PhysRevB.92.041405.

[82] R. Buividas, M. Mikutis, S. Juodkazis, Surface and bulk structuring of materials by ripples with long and short laser pulses: Recent advances, Progress in Quantum Electronics 38 (2014) 119–156. https://doi.org/10.1016/J.PQUANTELEC.2014.03.002.

[83] L. Wang, B. Bin Xu, X.W. Cao, Q.K. Li, W.J. Tian, Q.D. Chen, S. Juodkazis, H.B. Sun, Competition between subwavelength and deep-subwavelength structures ablated by ultrashort laser pulses, Optica 4 (2017) 637–642. https://doi.org/10.1364/OPTICA.4.000637.

[84] G.R.B.E. Römer, J.Z.P. Skolski, J.V. Oboňa, A.J. Huis In ’t Veld, Finite-difference time-domain modeling of laser-induced periodic surface structures, in: Physics Procedia, 2014: pp. 1325–1333. https://doi.org/10.1016/j.phpro.2014.08.058.

[85] G.D. Tsibidis, E. Skoulas, A. Papadopoulos, E. Stratakis, Convection roll-driven generation of supra-wavelength periodic surface structures on dielectrics upon irradiation with femtosecond pulsed lasers, Physical Review B 94 (2016) 081305. https://doi.org/10.1103/PhysRevB.94.081305.

[86] J. Heitz, B. Reisinger, M. Fahrner, C. Romanin, J. Siegel, V. Svorcik, Laser-induced periodic surface structures (LIPSS) on polymer surfaces, in: International Conference on Transparent Optical Networks, 2012. https://doi.org/10.1109/ICTON.2012.6253723.

[87] I. Martín-Fabiani, M.-C. García-Gutiérrez, D.R. Rueda, A. Linares, J.J. Hernández, T.A. Ezquerra, M. Reynolds, Crystallization under One-Dimensional Confinement in Alumina Nanopores of

Poly(trimethylene terephthalate) and Its Composites with Single Wall Carbon Nanotubes, ACS Applied Materials & Interfaces 5 (2013) 5324–5329. https://doi.org/10.1021/am401194p.

[88] M. Csete, Z. Bor, Laser-induced periodic surface structure formation on polyethylene-terephthalate, Applied Surface Science 133 (1998) 5–16. https://doi.org/10.1016/S0169-4332(98)00192-5.

[89] M. Hashida, Y. Ikuta, Y. Miyasaka, S. Tokita, S. Sakabe, Simple formula for the interspaces of periodic grating structures self-organized on metal surfaces by femtosecond laser ablation, ersApplied Physics Lett 102 (2013) 174106. https://doi.org/10.1063/1.4803940.

[90] M. Castillejo, T.A. Ezquerra, M. Martín, M. Oujja, S. Pérez, E. Rebollar, Laser nanostructuring of polymers: Ripples and applications, AIP Conference Procedings 1464 (2012) 372. https://doi.org/10.1063/1.4739891.

[91] E. Rebollar, T.A. Ezquerra, A. Nogales, Laser-induced periodic surface structures (Lipss) on polymer surfaces, in: Wrinkled Polymer Surfaces: Strategies, Methods and Applications, 2019: pp. 143–155. https://doi.org/10.1007/978-3-030-05123-5.

[92] I. Martín-Fabiani, E. Rebollar, S. Pérez, D.R. Rueda, M.C. García-Gutiérrez, A. Szymczyk, Z. Roslaniec, M. Castillejo, T.A. Ezquerra, Laser-Induced Periodic Surface Structures Nanofabricated on Poly(trimethylene terephthalate) Spin-Coated Films, Langmuir 28 (2012) 7938–7945. https://doi.org/10.1021/la300833x.

[93] R. Freeman, J. King, G. Lafyatis, Essentials of Electricity and Magnetism, in: Electromagnetic Radiation, Oxford University Press, 2019: pp. 3–42. https://doi.org/10.1093/oso/9780198726500.003.0001.

[94] O. Svelto, Principles of lasers, 5th ed., Springer US, Milan, 2010. https://doi.org/10.1007/978-1-4419-1302-9.

[95] D.G. Hall, Vector-beam solutions of Maxwell's wave equation, Optics Letters 21 (1996) 9–11. https://doi.org/10.1364/OL.21.000009.

[96] Q. Zhan, Cylindrical vector beams: from mathematical concepts to applications, Advances in Optics and Photonics 1 (2009) 1–57. https://doi.org/10.1364/AOP.1.000001.

[97] O.J. Allegre, W. Perrie, S.P. Edwardson, G. Dearden, K.G. Watkins, Laser microprocessing of steel with radially and azimuthally polarized femtosecond vortex pulses, Journal of Optics 14 (2012) 085601. https://doi.org/10.1088/2040-8978/14/8/085601.

[98] J. JJ Nivas, E. Allahyari, F. Cardano, A. Rubano, R. Fittipaldi, A. Vecchione, D. Paparo, L. Marrucci, R. Bruzzese, S. Amoruso, Vector vortex beams generated by q-plates as a versatile route to direct fs laser surface structuring, Applied Surface Science 471 (2019) 1028–1033. https://doi.org/10.1016/j.apsusc.2018.12.091.

[99] A. Papadopoulos, E. Skoulas, G.D. Tsibidis, E. Stratakis, Formation of periodic surface structures on dielectrics after irradiation with laser beams of spatially variant polarisation: a comparative study, Applied Physics A 124 (2018) 1–12. https://doi.org/10.1007/S00339-018-1573-X.

[100] P. Coullet, L. Gil, F. Rocca, Optical vortices, Optics Communications 73 (1989) 403–408. https://doi.org/10.1016/0030-4018(89)90180-6.

[101] K.K. Anoop, A. Rubano, R. Fittipaldi, X. Wang, D. Paparo, A. Vecchione, L. Marrucci, R. Bruzzese, S. Amoruso, Femtosecond laser surface structuring of silicon using optical vortex beams generated by a q-plate, Applied Physics Letters 104 (2014) 241604. https://doi.org/10.1063/1.4884116.

[102] L.L. Ran, S.L. Qu, Z.Y. Guo, Surface mico-structures on amorphous alloys induced by vortex femtosecond laser pulses, Chinese Physics B 19 (2010) 034204. https://doi.org/10.1088/1674-1056/19/3/034204.

[103] A. Ambrosio, L. Marrucci, F. Borbone, A. Roviello, P. Maddalena, Light-induced spiral mass transport in azo-polymer films under vortex-beam illumination, Nature Communications 2012 3:1. 3 (2012) 1–9. https://doi.org/10.1038/ncomms1996.

[104] R. Santillan, A. Wong, P. Segovia, M. Camacho-Lopez, S. Camacho-Lopez, Femtosecond laser-induced periodic surface structures formation on bismuth thin films upon irradiation in ambient air, Optical Materials Express 10 (2020) 674. https://doi.org/10.1364/ome.384019.

[105] D.A. Belousov, K.A. Bronnikov, K.A. Okotrub, S.L. Mikerin, V.P. Korolkov, V.S. Terentyev, A. V. Dostovalov, Thermochemical laser-induced periodic surface structures formation by femtosecond laser on hf thin films in air and vacuum, Materials 14 (2021) 6714. https://doi.org/10.3390/ma14216714.

[106] S.M. Petrović, B. Gaković, D. Peruško, E. Stratakis, I. Bogdanović-Radović, M. Čekada, C. Fotakis, B. Jelenković, Femtosecond laser-induced periodic surface structure on the Ti-based nanolayered thin films, Journal of Applied Physics 114 (2013) 233108. https://doi.org/10.1063/1.4848016.

[107] J. Cui, A. Nogales, T.A. Ezquerra, E. Rebollar, Influence of substrate and film thickness on polymer LIPSS formation, Applied Surface Science 394 (2017) 125–131. https://doi.org/10.1016/j.apsusc.2016.10.045.

[108] P. Nürnberger, H.M. Reinhardt, H.C. Kim, E. Pfeifer, M. Kroll, S. Müller, F. Yang, N.A. Hampp, Orthogonally superimposed laser-induced periodic surface structures (LIPSS) upon nanosecond laser pulse irradiation of SiO 2 /Si layered systems, Applied Surface Science 425 (2017) 682–688. https://doi.org/10.1016/j.apsusc.2017.06.316.

[109] A. Talbi, C.T. Tameko, A. Stolz, E. Millon, C. Boulmer-Leborgne, N. Semmar, Nanostructuring of titanium oxide thin film by UV femtosecond laser beam: From one spot to large surfaces, Applied Surface Science 418 (2017) 425–429. https://doi.org/10.1016/J.APSUSC.2017.02.033.

[110] A. Talbi, P. Coddet, M. Tabbal, A.L. Thomann, E. Millon, A. Stolz, C. Boulmer-Leborgne, G.M. O'Connor, N. Semmar, Comparative study of laser induced periodic surface structures formed on pulsed laser deposited and magnetron sputtered titanium oxide films, Applied Surface Science 476 (2019) 303–307. https://doi.org/10.1016/J.APSUSC.2019.01.069.

[111] M. Zamfirescu, A. Dinescu, M. Danila, G. Socol, C. Radu, The role of the substrate material type in formation of laser induced periodical surface structures on ZnO thin films, Applied Surface Science 258 (2012) 9385–9388. https://doi.org/10.1016/J.APSUSC.2012.01.089.

[112] M. Hashida, Y. Miyasaka, Y. Ikuta, S. Tokita, S. Sakabe, Crystal structures on a copper thin film with a surface of periodic self-organized nanostructures induced by femtosecond laser pulses, Physical Review B 83 (2011) 235413. https://doi.org/10.1103/PhysRevB.83.235413.

[113] R.I.R. Beltrán, Nanoestructurado de composites de matriz polimérica y aditivos de base carbono con láseres pulsados de nano- y femtosegundos, Universidad de Salamanca, 2018. https://doi.org/10.14201/GREDOS.137359.

[114] A. v. Zayats, I.I. Smolyaninov, A.A. Maradudin, Nano-optics of surface plasmon polaritons, Physics Reports 408 (2005) 131–314. https://doi.org/10.1016/J.PHYSREP.2004.11.001.

[115] H. Raether, Surface Plasmons on Smooth and Rough Surfaces and on Gratings, in: Springer Tracts in Modern Physics, 1st ed., Springer, Berlin, 1988: pp. 58–70. https://doi.org/10.1007/BFb0048317.

[116] I. Pockrand, Surface plasma oscillations at silver surfaces with thin transparent and absorbing coatings, Surface Science 72 (1978) 577–588. https://doi.org/10.1016/0039-6028(78)90371-0.

[117] E. Fontana, R.H. Pantell, Characterization of multilayer rough surfaces by use of surface-plasmon spectroscopy, Physical Review B 37 (1988) 3164–3182. https://doi.org/10.1103/PhysRevB.37.3164.

[118] F. Toigo, A. Marvin, V. Celli, N.R. Hill, Optical properties of rough surfaces: General theory and the small roughness limit, Physical Review B 15 (1977) 5618–5626. https://doi.org/10.1103/PhysRevB.15.5618.

[119] S. Schröder, A. Duparré, L. Coriand, A. Tünnermann, D.H. Penalver, J.E. Harvey, Modeling of light scattering in different regimes of surface roughness, Optics Express 19 (2011) 9820. https://doi.org/10.1364/OE.19.009820.

[120] K. Arya, Z.B. Su, J.L. Birman, Localization of the Surface Plasmon Polariton Caused by Random Roughness and its Role in Surface-Enhanced Optical Phenomena, Physical Review Letters 54 (1985). https://doi.org/10.1103/PhysRevLett.54.1559.

[121] Y. Fuentes-Edfuf, J.A. Sánchez-Gil, C. Florian, V. Giannini, J. Solis, J. Siegel, Surface Plasmon Polaritons on Rough Metal Surfaces: Role in the Formation of Laser-Induced Periodic Surface Structures, ACS Omega 4 (2019) 6939–6946. https://doi.org/10.1021/acsomega.9b00546.

[122] P. Sahoo, Surface topography, in: J.P. Davim (Ed.), Tribology for Engineers, Woodhead Publishing, 2011: pp. 1–32. https://doi.org/10.1533/9780857091444.1.

Chapter 2

Materials and methods

In this chapter, we explain the methodology followed in this research. First, we briefly present the properties of the materials we worked with. Then, we detail the methods by which we prepared our samples. Afterwards, we describe the different irradiation schemes used on each sample and the characterization techniques that allowed the measurement of the relevant properties of the samples and the study of how they changed after irradiation. Finally, we explain the methods to obtain the surface energy of the different samples from contact angle measurements and the numerical simulation methods we used to better understand LIPSS formation.

2.1. Materials

2.1.1. PET

Poly(ethylene terephthalate) (PET) is a polymer of the polyesters family synthesized in the 1940s [1]. It is a thermoplastic polymer usually synthesized by condensation polymerization, often called polycondensation. This method involves ethylene glycol reacting with dimethyl terephthalate (DMT) [2]. From this reaction, PET is obtained in an amorphous state with the chemical structure shown in Figure 2.1.

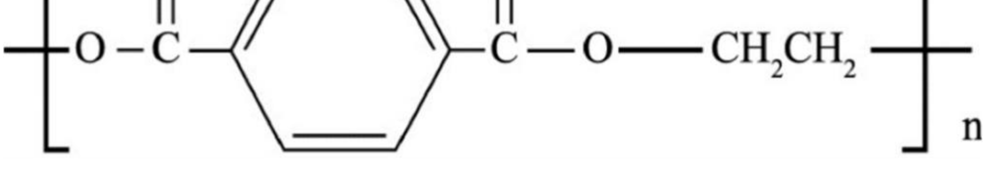

Figure 2.1. *PET chemical structure [9].*

Its excellent mechanical properties, chemical resistance, thermal stability, gas barrier, and resistance to wear and corrosion, have made PET one of the most used polymers both in daily life and in science [3–6]. The PET used in this work was synthesized and characterized by our colleagues at the West Pomeranian University of Technology (Poland) [7,8]. Its relevant properties for laser processing are shown in Table 2.1 as well as optical absorption spectrum in Figure 2.2.

Table 2.1: *Properties of PET used in our experiments: T_m [8], T_g [8], crystallization temperature (T_c) [8], crystallization percentage (X_c) [7], heat capacity (ΔC_p) [10], thermal conductivity (K) [10], thermal diffusivity ($\alpha = K/\Delta C_p \rho$) [10].*

	T_m (°C)	**T_g (°C)**	**ΔC_p (J/g°C)**	**T_c (°C)**	**X_c (%)**	**K (W(m K)$^{-1}$)**	**α (m^{2}s^{-1})**
PET	257	85	1.16	214	12	0.258	$1.67 \cdot 10^{-7}$

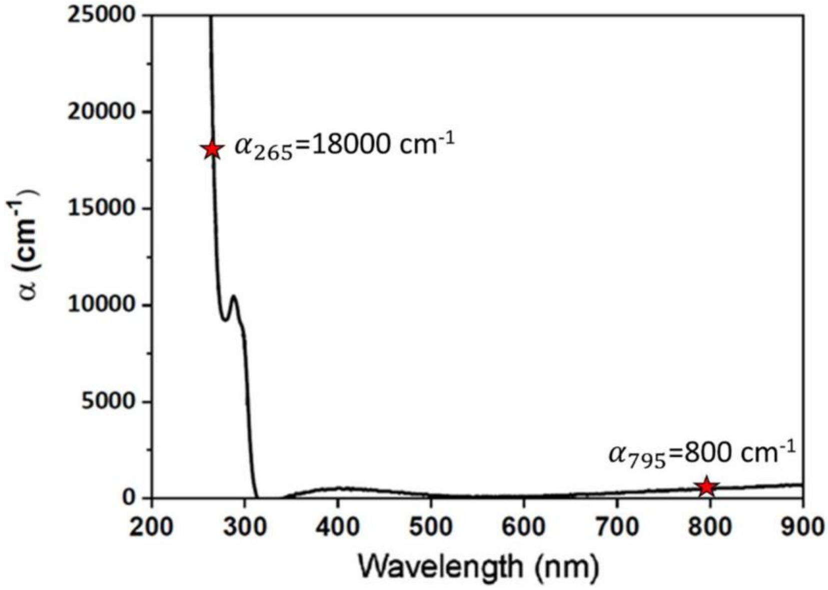

Figure 2.2. *Optical absorption coefficient (α) of PET. Its values at 265 nm and 795 nm [11] are highlighted on the figure.*

2.1.2. PTT and PTT-WS_2 nanotubes nanocomposite

Poly(trimethylene terephthalate) (PTT) is a polymer synthesized in the 1940s [1] belonging to the terephthalate polyesters family that combines the good properties of PET, the ease of processing of Poly (Butylene Terephthalate), and a higher elasticity provided by the three methylenes in its monomer chemical structure (Figure 2.3) [12,13]. This polymer is commonly found in a semicrystalline state. It can be prepared via *in situ* polymerization from 1,3-propanediol and DMT [14], using tetrabutyl orthotitanate as a catalyst and Irganox 1010 as an antioxidant.

PTT is an interesting material by virtue of its particular crystalline structure and crystallization rate which allow for processing in many different ways (injection molding, film casting, and film spinning) [15]. Moreover, it can be fabricated out of a high percentage of renewable materials [14] and has good mechanical, chemical, and thermal properties [16,17].

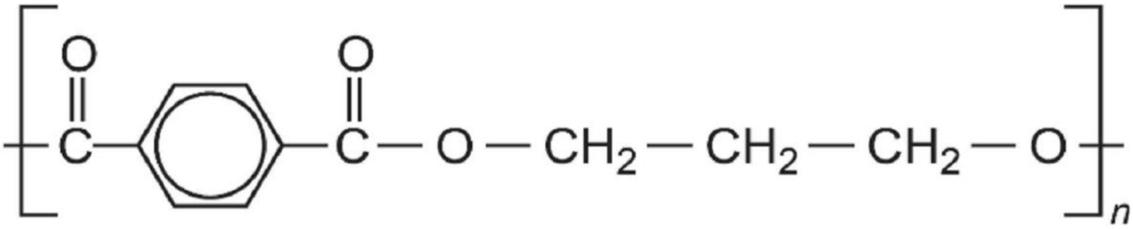

Figure 2.3. *PTT chemical structure [18].*

Tungsten disulfide (WS_2) inorganic nanotubes (see Figure 2.4) are an appreciated alternative to carbon nanotubes due to their high impact resistance and good tribological behavior as well as relatively low fabrication costs, as the precursors are relatively inexpensive [19]. It is because of these properties that they have applications in high energy absorptive materials [20], biosensors and nanomedicine [21], and antiballistic and impact resisting materials [22,23], among many others.

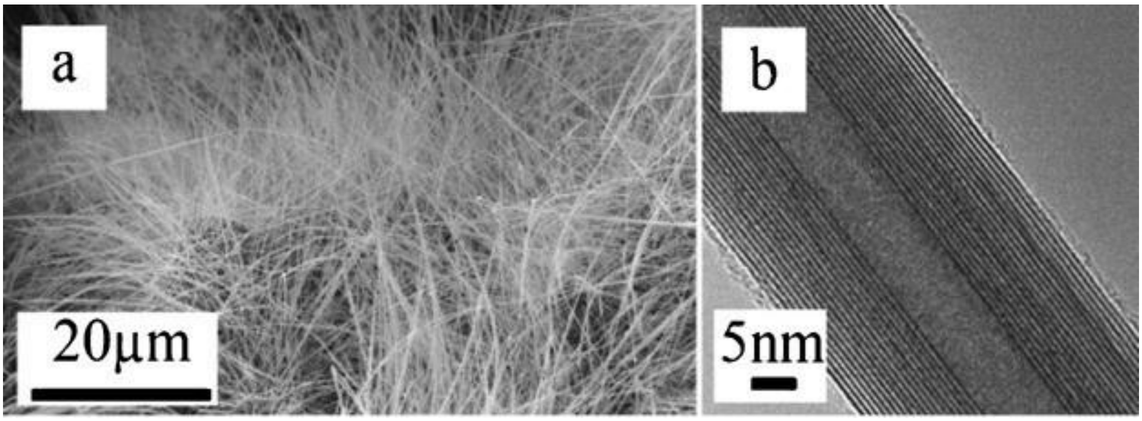

Figure 2.4. *a) Scanning Electron Microscopy and b) Transmission Electron Microscopy micrographs of WS_2 inorganic nanotubes [24].*

We have worked with a nanocomposite made of a PTT matrix reinforced with WS_2 inorganic nanotubes (0.5% in weight). The nanotubes have 2-20 mm length, 40-120 nm diameter and are disposed randomly in the PTT matrix. The synthesis of the nanocomposite and its characterization and comparison with simple PTT was detailed in a previous work by our colleagues in the West Pomeranian University of Technology (Poland) [14]. The more relevant properties for our work are presented in Table 2.2 and the UV-Vis absorption spectrum of PTT is shown in Figure 2.5.

Table 2.2. *Relevant properties of PTT and PTT-WS_2.* T_m*,* T_g*,* ΔC_p*,* T_c *and* X_c *obtained from [14]; K, and* α*, obtained from the PTT data [25].* The values for *PTT-WS_2 have been obtained from the ones of PTT and the properties of WS_2 nanotubes applying the rule of mixtures, an approach that has proven to be effective for other nanocomposites [26].*

Sample	**T_m (ºC)**	**T_g (ºC)**	**ΔC_p (J/gºC)**	**T_c (ºC)**	**X_c (%)**	**K (W(m K)$^{-1}$)**	**α (m^{2}s^{-1})**
PTT	229	53	0.17	171	30.1	0.22	$9.6\cdot10^{-7}$
PTT-WS_2	228	53	0.16	177	32.1	0.23	$10.6\cdot10^{-7}$

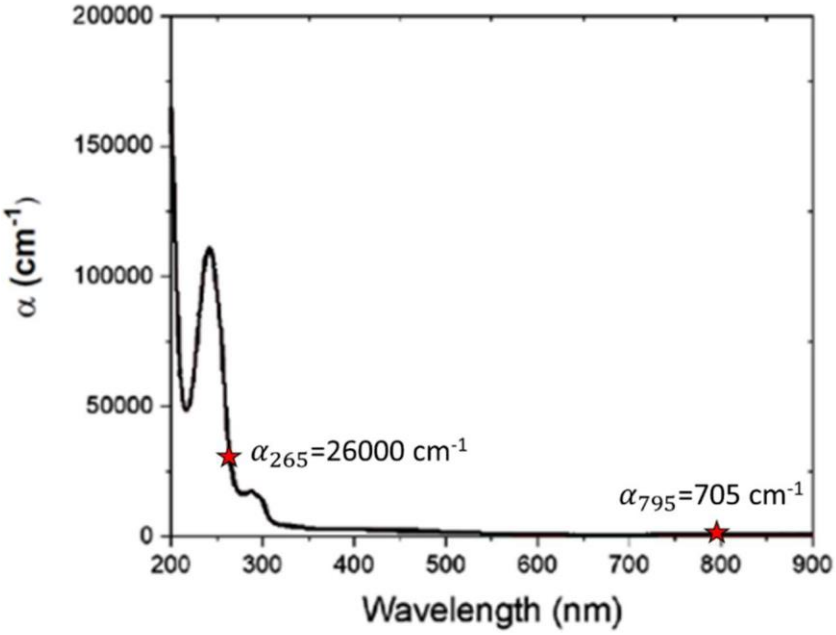

Figure 2.5. *Optical absorption coefficient of PTT. Its values at 265 nm and 795 nm [25] are highlighted on the figure.*

2.1.3. P3HT

Poly(3-hexylthiophene-2,5-diyl) (P3HT) is a semiconducting semicrystalline polymer of the family of polythiophenes. More specifically, it belongs to the group of poly(alkyl-thiophenes). It has applications as the active layer in organic field-effect transistors (OFET) [27] and organic solar cells [28] due to its high optical absorption in the visible range.

As we mentioned in Section 1.1 the intrinsic conductivity of P3HT is due to its molecular structure as a conjugated polymer providing delocalized electrons [29]. However, this conductivity is affected by the crystallinity of the polymer. The well-ordered structures with strong intermolecular interactions found in crystalline structures result in efficient charge pathways on a macroscopic level [30].

The P3HT used in this thesis was bought from Ossila (UK) (batch M106). See its properties in Table 2.3. and its chemical structure in Figure 2.6.

Table 2.3. *Relevant properties of P3HT as given by the manufacturer (Ossila).*

Sample	M_w (g/mol)	M_n (g/mol)	Poly Dispersity Index	Regioregularity (%)	HOMO (eV)	LUMO (eV)
P3HT	34100	19500	1.75	94.7	-5.2	-3.2

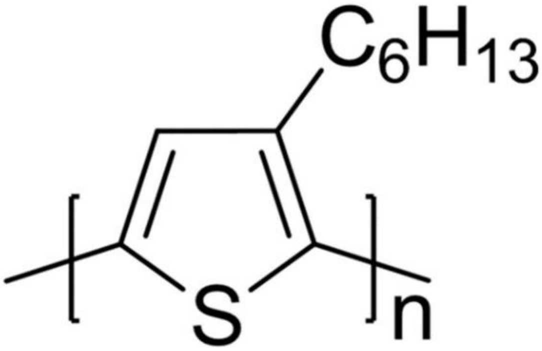

Figure 2.6. *P3HT chemical structure* [31].

2.1.4. $PC_{71}BM$

$PC_{71}BM$ is a n-conductor C_{70} fullerene derivative that is frequently used in organic photovoltaics along with P3HT. It has replaced $PC_{61}BM$, a C_{60} fullerene derivative, due to its stronger optical absorption in the visible range [32]. C_{70} fullerene is the most stable fullerene excluding C_{60}. It presents a less symmetrical structure, which gives it more reactive links than C_{60}. The $PC_{71}BM$ used in this thesis was bought from Ossila (UK) >99% purity (<1% $PC_{61}BM$), HOMO=-5.9 eV, LUMO=-3.9 eV. See its chemical structure in Figure 2.7.

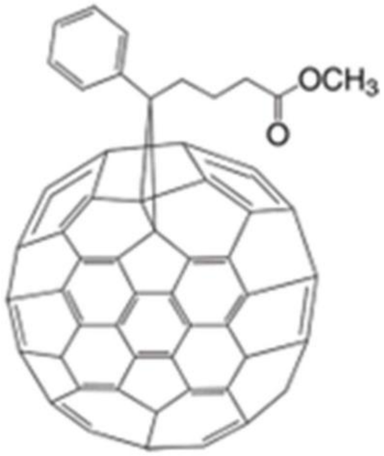

Figure 2.7. *$PC_{71}BM$ chemical structure [33].*

2.2. Sample preparation

2.2.1. Thin films

2.2.1.1. Substrates

PET, P3HT and $PC_{71}BM$ were deposited as thin films on different substrates.

In the case of PET, thin films were deposited on the following substrates:

- Cover glass (microscope slides, Thermo Scientific).
- Silicon (1 0 0) from Wafer World Inc.
- PET from 3M®.
- Steel Atomic Force Microscopy holder.
- Low R_q gold substrate obtained by sputtering 6 min with Sputter coater S150B (Edwards) on silicon wafers (1 0 0) polished on both sides.
- High R_q gold substrate prepared from a bulk sample increasing its roughness mechanically with Buehler MetaDi II® monocrystalline diamond paste of 1 µm and ¼ µm, as well as Struers® deagglomerated alpha alumina powder of 0.3 µm as abrasive.

As for the P3HT and $PC_{71}BM$ thin films, we deposited them on n-silicon (1 0 0) doped with arsenic from ACM (France). See the roughness parameters of the substrates measured by AFM in Table 2.4.

Before thin film deposition, the substrates were cleaned by 3 minutes of sonication in acetone (Sigma-Aldrich® 99.5%), followed by 3 minutes of sonication in isopropyl alcohol (Sigma-Aldrich® 98%), both in an ultrasound bath (J.P. Selecta 3000513, Instituto de Estructura de la Materia (IEM-CSIC)), and dried at room temperature.

Table 2.4. *R_q, σ and thickness of the substrates.*

Substrate	**R_q (nm)**	**σ (nm)**	**Thickness (mm)**
Low R_q Gold	2.4±0.5	30±9	$(90\pm6)\cdot10^{-6}$
High R_q Gold	52±2	770±30	1.08±0.04
Silicon	0.4±0.05	440±6	0.50±0.01
Doped Silicon	0.4±0.05	40±6	0.50±0.01
PET	6.0±0.7	220±80	0.10±0.01
Steel	90±40	490±50	1.0±0.1
Cover Glass	1.1±0.4	117±14	1.0±0.1

2.2.1.2. Drop cast

The technique of drop casting requires the polymer to be solved in a solvent and a droplet of the solution to be poured on a substrate, leaving it to dry. See the scheme in Figure 2.8.

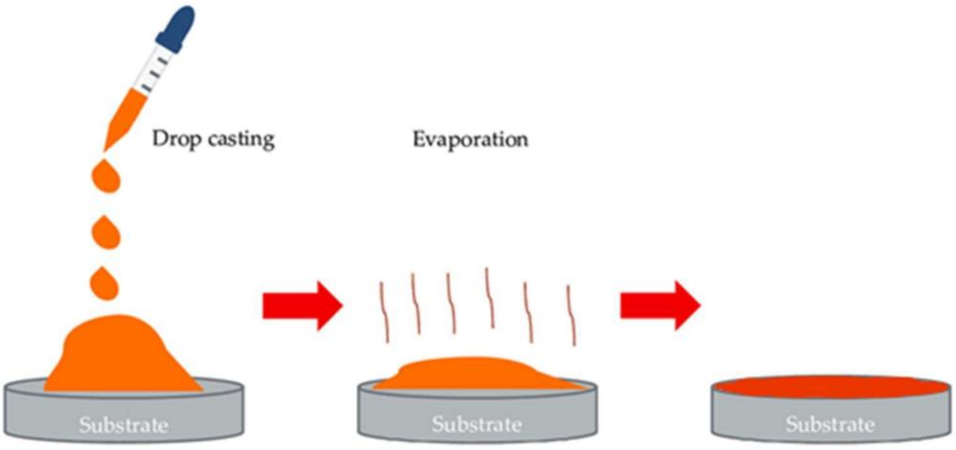

Figure 2.8. *Drop casting scheme [34].*

In our case, we employed this technique to create films of PET. We dissolved PET at room temperature for 2 hours in trifluoroacetic acid (Sigma-Aldrich®, reagent ≥ 99 %) with a concentration of 60 g/L. Afterwards, we dropped it on one of our substrates and left it to dry at room temperature in a vertical laminar flow chamber. The thickness of the film and roughness parameters of each sample prepared this way can be seen in Table 2.5.

***Table 2.5**. Thickness and roughness parameters of the PET samples prepared by drop-cast.*

Substrate	R_q **(nm)**	σ **(nm)**	**Thickness (µm)**
Low R_q Gold	80±30	840±90	16.0±0.5
Silicon	250±20	1200±200	16.0±0.5
Glass	101±3	1280±120	16.0±0.5

2.2.1.3. Spin coating

In this technique, we also need to prepare a solution, but instead of just dropping it on a still substrate, the substrate spins at thousands of rpm. The centrifugal force makes the drop expand and evenly coat the substrate and, once the solvent evaporates, we obtain thin films with low roughness —see the scheme in Figure 2.9. We employed this technique to create thin films of PET, P3HT and $PC_{71}BM$.

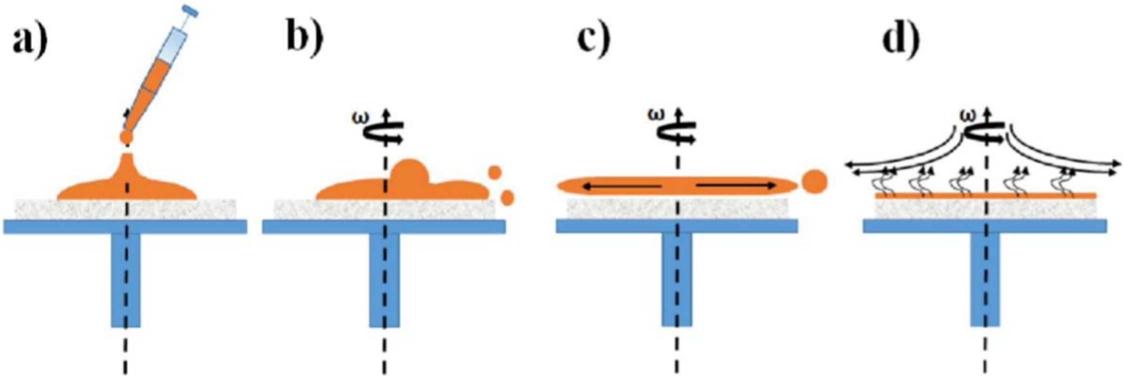

***Figure 2.9.** Spin coating scheme [35].*

We dissolved PET, at room temperature for two hours in trifluoroacetic acid (Sigma-Aldrich®, reagent ≥ 99%) and P3HT and $PC_{71}BM$ at room temperature for one hour in chlorobenzene

(Sigma-Aldrich®, Anhydrous, 99.8%). We spun the solutions for 120 seconds at 2380 rpm using a spin processor (Laurell WS-650 Series (IEM-CSIC)). We varied the concentrations of the solutions to get different thicknesses. The thickness and roughness parameters of the PET samples obtained in this way, measured by AFM, are shown in Table 2.6; and those of $PC_{71}BM$ and P3HT are shown in Table 2.7.

Table 2.6. *Thickness and roughness parameters of the PET thin films deposited on different substrates.*

Substrate	PET concentration (g/L)	Thickness (nm)	Roughness R_q | σ (nm)
Low R_q gold	7	90±3	61±3 | 260±70
Low R_q gold	10	102±2	0.5±0.1 | 104±8
Low R_q gold	15	150±5	0.5±0.1 | 174±60
Low R_q gold	25	1300±10	1.0±0.1 | 110±20
High R_q gold	15	165±7	13±1| 900±100
Silicon	10	79±3	0.3±0.1| 320±60
Silicon	15	120±20	0.4±0.1 | 300±90
Silicon	25	441±14	0.3±0.1 | 690±70
Steel	10	210±28	24±7 | 340±20
Steel	15	298±58	46±16 | 524±142
Glass	15	115±14	0.4±0.1 | 160±21
Glass	30	205±25	0.6±0.1 | 160±20
PET	10	243±22	13±2 | 550±60
PET	15	318±36	5±1 | 300±90

Table 2.7. *Thickness and roughness parameters of the $PC_{71}BM$ and P3HT samples. The substrate was doped Si in all cases.*

Sample	Concentration (g/L)	Thickness (nm)	Roughness R_q | σ (nm)
$PC_{71}BM$	40	65±7	0.51±0.04|170±70
P3HT	20	275±21	4.7±0.2|176±13

2.2.2 Free standing films

Our colleagues in the West Pomeranian University of Technology (Poland) [14] prepared PTT and PTT-WS_2 free-standing amorphous films of about 200±10 µm thickness by press molding using a Collin P 200E molding press at 245°C and 15 bar for 2 min and subsequently quenched in ice water (250°C/min). We show their roughness parameters in Table 2.8.

Table 2.8. *Roughness parameters of the PTT and PTT-WS_2 samples.*

Sample	R_q |σ (nm)
PTT	4.3±1.6 | 140±30
PTT-WS_2	12±1 | 250±40

2.3. Laser irradiation set-up

Here we describe the various laser systems used to modify the surfaces of the different samples. All the irradiations were done at normal incidence in air at room temperature and pressure.

2.3.1. Gaussian beams

We used two different ultrashort pulsed laser systems with two different wavelengths, one in the infrared and the other one in the ultraviolet range.

The infrared ultrashort laser pulses were delivered from a Spectra Physics® system (Facultad de Ciencias, Universidad de Salamanca) composed of a Ti:Sa oscillator (MaiTai, Spectra Physics®), which provides seed pulses of 35 fs FWHM (Full Width Half Maximum) and a maximum pulse energy of 5 nJ at a repetition rate of 84 MHz, and a Spitfire ACE regenerative amplifier (Spectra Physics®). The ACE turns them into linearly polarized pulses of 64 fs FWHM, centered at $\lambda = 798$ nm with a repetition rate of 5 kHz and a maximum pulse energy of 1.2 mJ.

The ultraviolet ultrashort laser pulses were achieved generating the third harmonic of the fundamental wavelength (795 nm) of the emission of another system (Facultad de Ciencias, Universidad de Salamanca) consisting of a Ti:Sa oscillator (Tsunami, Spectra Physics®) that generates seed pulses of 100 fs FWHM at a repetition rate of 80 MHz and a maximum pulse energy of 9 nJ. A Spitfire regenerative amplifier (Spectra Physics®) increases the energy of some of the seed pulses using CPA (Chirped Pulse Amplification) technique. The amplified pulses have 120 fs FWHM, 1 kHz repetition rate, and 1 mJ/pulse as a maximum. To generate the third harmonic, we used the set-up in Figure 2.10, designed and characterized in [36]. At the exit of the third harmonic set-up, the pulses have 260 fs FWHM, a wavelength of 265 nm, 1 kHz repetition rate, a maximum pulse energy of 50 µJ and linear polarization.

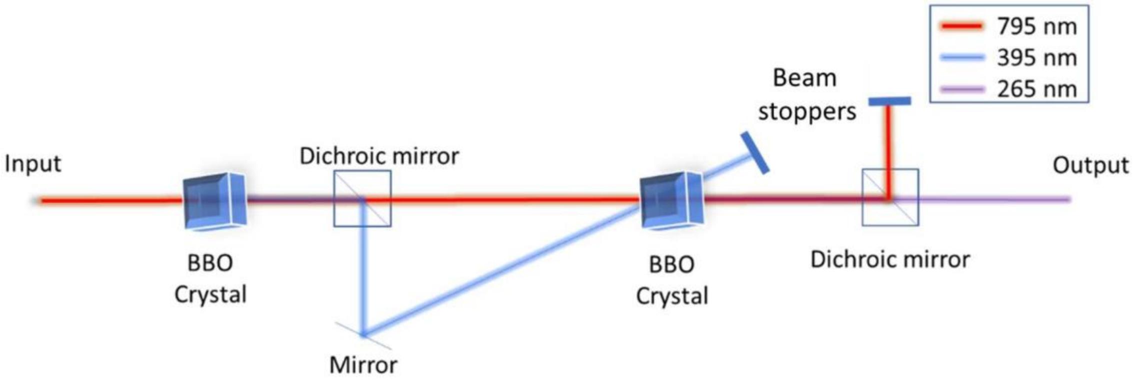

Figure 2.10. *Scheme of the third harmonic generation module.*

Once generated, the irradiation set-up is the same regardless of the ultrashort pulses selected (Figure 2.11). In this set-up, we used a shutter to control the irradiation time, which is related to the number of pulses by the repetition rate. To control the energy of the pulses, we used a motorized λ/2 plate and a linear polarizer. In addition, we moved the sample closer or further from the focal plane for fine tuning, so we deposited the required energy on the surface of the sample.

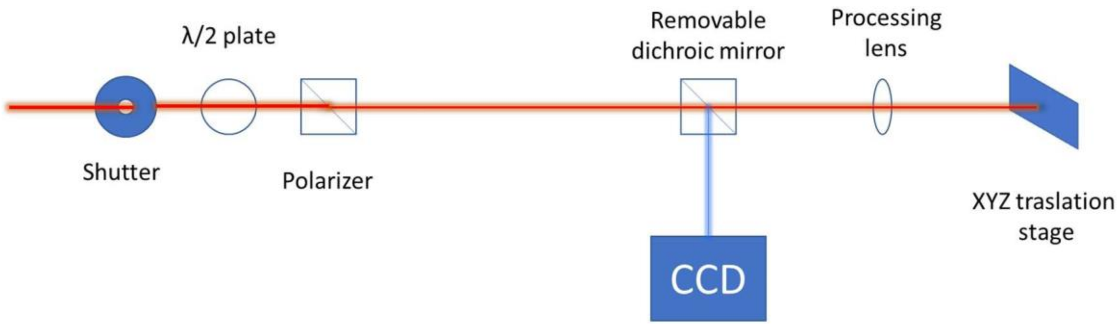

Figure 2.11. *Scheme of the experimental set-up for sample irradiation.*

The pulses were guided by means of mirrors to impinge perpendicular to the samples. The samples rested on a XYZ motorized translation stage (PI miCos®), controlled by LABVIEW. An achromatic doublet lens ($f = 100$ mm, G063201000, CVI Laser Optics® for IR pulses; and $f = 100$ mm, LA4380-UV, Thorlabs® for UV pulses) focused the pulses on the surface of the samples. We used a CCD camera (IDS uEye CP INFAIMON®) to help focus and position the samples.

As mentioned in Section 1.3, previous studies proved that LIPSS morphology depends on the irradiation parameters. Because of that, we have irradiated our samples with different number of pulses at different fluences. To decide the fluence and number of pulses range, we made some irradiations to assess at which fluence range each of the samples was modified without ablation.

2.3.2. Vector and optical vortex beams

As shown in Section 1.3, vector beams, also called beams carrying spin, are beams where the phase behaves like that of a Gaussian beam, but the polarization varies azimuthally. On the other hand, optical vortex beams, also referred to as beams carrying orbital angular momentum, are beams with the same intensity spatial profile as vector beams but their polarization is circular and spatially constant, and their phase varies azimuthally.

To produce this kind of beams we used a commercial Thorlabs zero order $m = 1$ vortex half-wave plate. These plates are designed to affect the radial and azimuthal polarization of light beams. They can be understood as a half-wave plate where the fast axis rotates continuously around its center (see Figure 2.12).

Viewed through crossed polarizers with a white light source, these retarders produce an intensity profile with two modulations. Thus, when used with a linearly polarized light source, these retarders will generate a polarization pattern with two nodes. The plate turns linearly polarized Gaussian beams into different vector beams of topological charge 1, according to the angle of the incident polarization and the 0° fast axis of the vortex plate. See Figure 2.13.

We used vector beams with radial, azimuthal, and spiral polarization, which were generated with angles between the polarization and the 0° fast axis of 0°, 90° and 45° respectively. This plate also turns circularly polarized Gaussian beams into optical vortex beams of topological charge ± 1 [37].

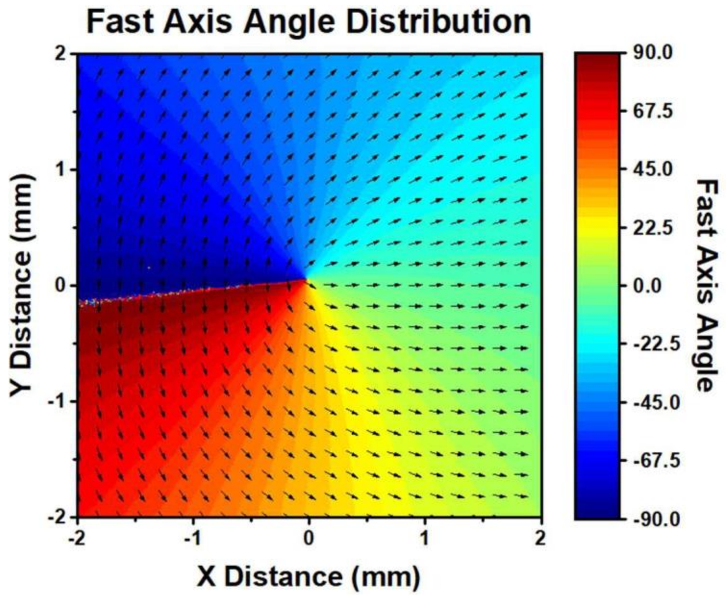

Figure 2.12. *Vortex half-wave plate* $m = 1$.

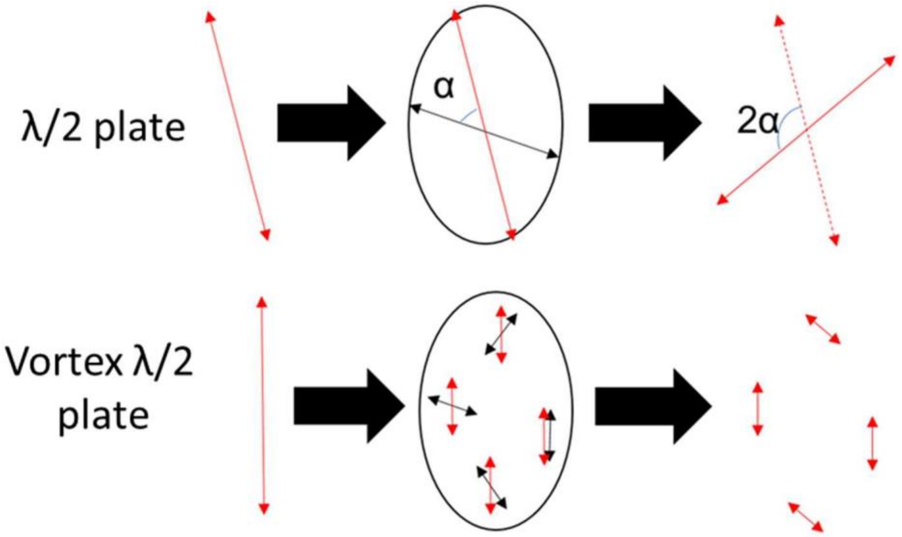

Figure 2.13. *Scheme of how a vortex halfwave plate works.*

The laser used to generate vector beams in the nanosecond range is a Nd:YAG laser Brilliant-b (Quantel®) with a frequency doubling module, which gives linearly polarized pulses with a wavelength of 532 nm, 5 ns FWHM, at a repetition rate of 20 Hz (Dipartimento di Fisica 'Ettore Pancini' Università degli Studi di Napoli Federico II). Since the output power of the laser was enough to induce LIPSS formation, it was not necessary to use focused beams, and this allowed us to nanostructure larger areas. We used a pinhole to obtain a more homogeneous spatial profile with a spot diameter of around 1 mm. See a scheme of the set-up in Figure 2.14.

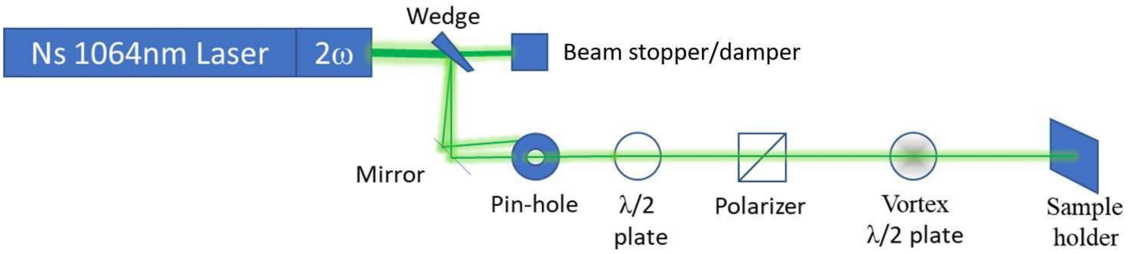

Figure 2.14. *Irradiation scheme for ns vector beams.*

The laser used to generate vector beams in the femtosecond range was a diode pumped Yb:KGW fiber laser Pharos PH 2 s/n I211804 (Light Conversion®) with a harmonic generation module Hiro s/n h21124 (Light Conversion®), which delivers linearly polarized laser pulses centered at 515 nm and 180 fs FWHM with a customizable repetition rate up to 3 kHz and a maximum optical power of 6 W (Dipartimento di Fisica 'Ettore Pancini' Università degli Studi di Napoli Federico II). See a scheme of the set-up in Figure 2.15.

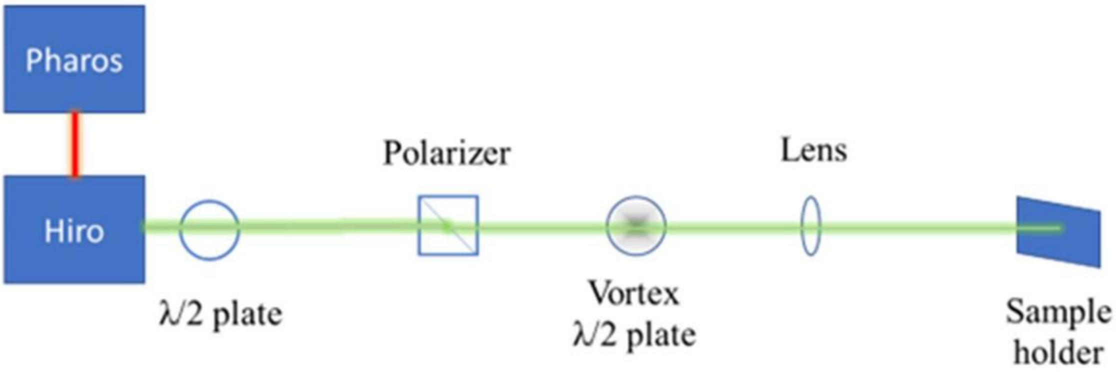

Figure 2.15. *Irradiation scheme for fs vector beams.*

The fluence of the vector beams was determined by measuring the power of the laser beam with a Gentec-e Maestro power-meter and calculating the area of the laser beam section with the method shown by Allahyari *et al.* [38]. In this method, both the size of the inner and outer radii of the annular ablation crater created on the target surface are measured. They are a function of the fluence, and numerical fitting is used to find the threshold fluence and the waist of the laser beam. For beams $m = 1$, as it was our case, the fitting equation was eq. 2.1:

$$E(r) = \frac{\mathrm{ae}^{\mathrm{r}^2\mathrm{b}}}{2} \tag{2.1}$$

where $a = F_{th} w_0^4 \pi/4$ and $b = 2/w_0^2$ are the fitting parameters, r is the distance to the center of the spot, E is the energy deposited, F_{th} is the threshold fluence and w_0 is the beam waist.

2.4. Sample characterization techniques

2.4.1. Scanning Probe Microscopy

Scanning Probe Microscopy (SPM) [39] is a branch of microscopy that is used to characterize different properties at the nanoscale. The first kind of SPM was Tunnel Effect Microscopy, invented in IBM Zurich in 1981 by Gerd Binning and Heinrich Rohrer [40], for which they were awarded the Nobel Prize in Physics.

SPM involves scanning a surface with a probe. The probe consists of a nanotip mounted at the end of a cantilever, which can have different characteristics depending on the kind of interaction intended to be explored. When the tip approaches the surface, they interact through different forces according to the tip properties and the distance between the tip and the surface, causing the deflection of the cantilever. This deflection is measured by shining a laser on the cantilever, which is reflected to different positions in a photodiode array depending on the bend of the cantilever. By using this data as feedback, a piezoelectric tries to either keep the force constant and measure the deflection, or keep the deflection constant and measure the force. The result is a matrix of deflections or forces for each position of the tip, which can be translated to a mapping of some property of the surface of the sample at the nanometric scale. The basic scheme of a SPM system is shown in Figure 2.16.

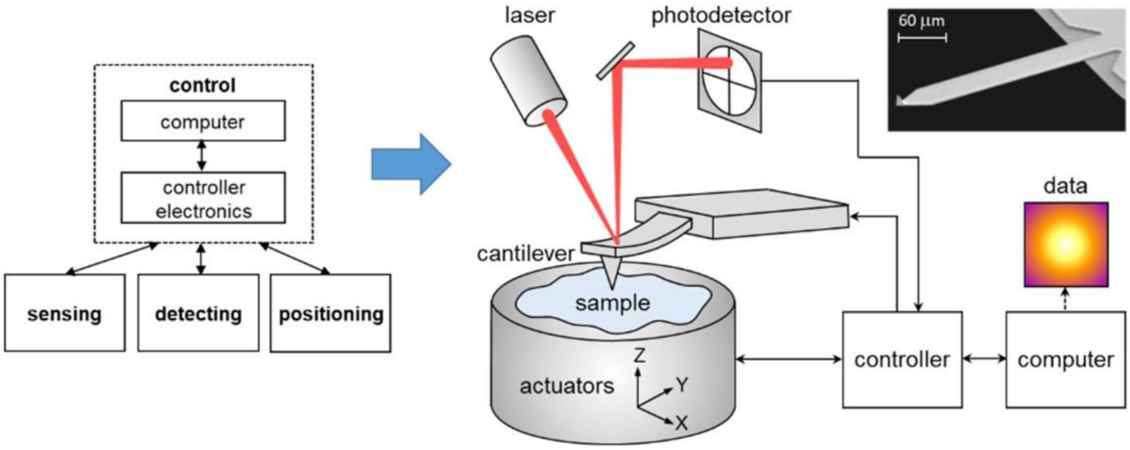

***Figure 2.16**. Basic elements of any SPM system [41].*

All our measurements were done with AFM Multimode 8 (Bruker®) (IEM-CSIC) with the Nanoscope V (Bruker®) controller. The data were further analyzed with Nanoscope Analysis 1.50 (Bruker®) software.

We have used three different SPM techniques:

2.4.1.1. Atomic Force Microscopy (AFM)

The forces scanned by this technique are interatomic interactions, such as electronic interactions and Van der Waals forces. These interactions are attractive at long distances and repulsive at short distances (mechanical contact), see force distance curve in Figure 2.17. This originates three different regimes which translate to three different measurement modes: contact mode, non-contact mode, and tapping mode. Contact and non-contact are self-explanatory and in tapping mode, the cantilever vibrates at its resonant frequency lightly tapping the sample at maximum deflection.

We used AFM to measure the topography of the samples. We equipped it with silicon tips (NT-MDT®) with a typical radius of approximately 6 nm, a nominal resonant frequency of 320 kHz, and a spring constant of 40 N/m. We chose the tapping mode due to the soft nature of our samples.

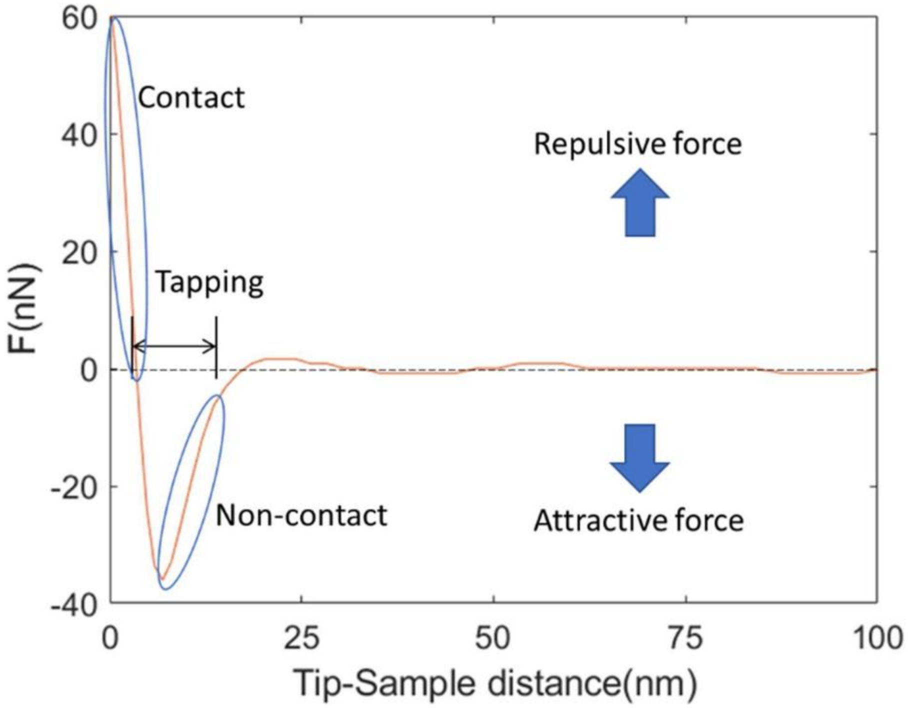

Figure 2.17. *AFM force distance curve. The three different regimes are shown [42].*

2.4.1.2. Peak Force-Quantitative Nanomechanical Mapping (PF-QNM)

PF-QNM [43] is a contact mode AFM based protocol, developed by Bruker®. It is based on making a matrix of indentations on the sample to map the mechanical properties and topology of the surface at the same time. For each indentation, we measured the peak force as a function of the cantilever deflection. From that data, the system extracts a force-distance curve and from it, the values of the elastic modulus, adhesion, and deformation in each point, as seen in Figure 2.18.

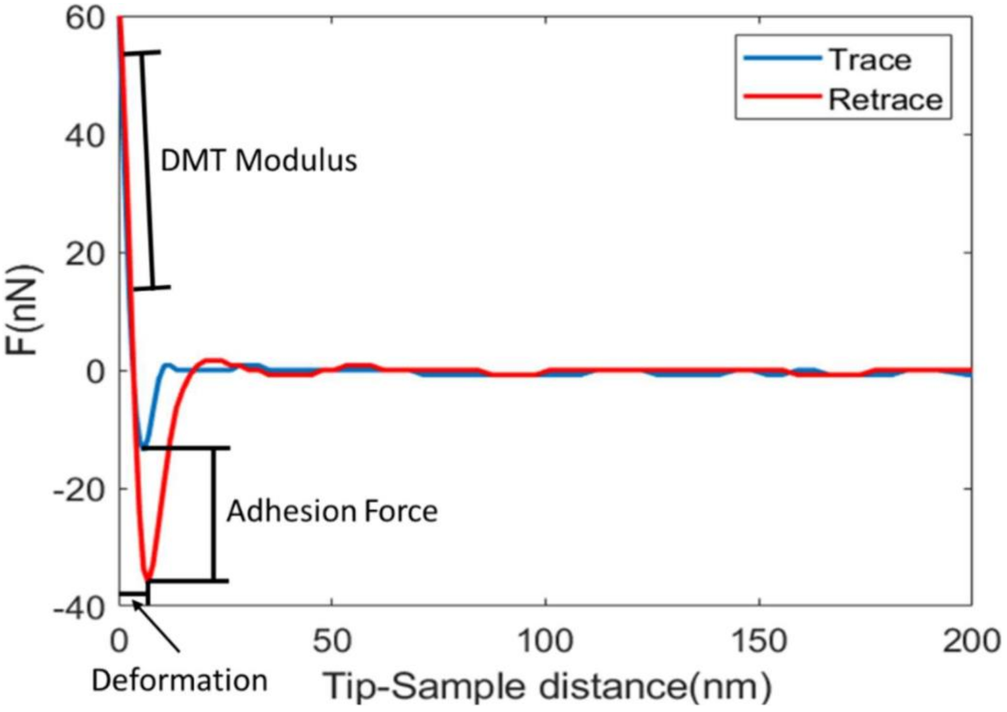

Figure 2.18. *Force-distance curve of PF-QNM measurement. The difference between the approach curve or trace (red) and the minimum of the retraction curve or retrace (blue) gives the adhesion force. The elastic modulus is given by the slope of the F-Tip-Sample distance line in the retraction curve.*

Specifically, the surface elastic modulus was obtained by application of the Derjaguin-Müller-Toporov (DMT) model [44]:

$$F - F_{\mathrm{adh}} = \frac{4}{3} E^{*} R^{1/2} d^{3/2} \tag{2.2}$$

Where F is the force, F_{adh} the adhesion force, R the tip radius, and d the deformation, *i.e.,* a parameter related to the tip penetration into the sample. E^{*} is the so-called reduced modulus, and it was measured using the retraction force curve. We choose the fit boundary parameters as 90% and 20% of the peak force for the maximum and minimum values, respectively. In this fitting range, both load/unload curves superimposed (see Figure 2.18), indicating an elastic response and validating the use of the DMT model. E^* is related to the elastic or Young's modulus of the sample by:

$$\frac{1}{\mathrm{E}^*} = \frac{1-\mathrm{v}^2_{\mathrm{sample}}}{\mathrm{E}_{\mathrm{sample}}} + \frac{1-\mathrm{v}^2_{\mathrm{probe}}}{\mathrm{E}_{\mathrm{probe}}} \tag{2.3}$$

where ν_{Sample} and ν_{probe} are the Poisson's ratios of the sample and probe, respectively. If the probe Young's modulus (E_{probe}) is much higher than that of the sample (E_{Sample}), as it is the case for most polymeric samples including ours, the second term in the right side of eq. 2.3 can be approximated to zero and the elastic modulus of the sample relates to the reduced modulus measured by PF-QNM as:

$$E_{\mathrm{Sample}} = (1 - \nu^2_{\mathrm{Sample}})E^* \tag{2.4}$$

To extract information, we must know the spring constant of the cantilever, the radius of the tip, and the deflection sensitivity of the cantilever. We obtained this information according to the following protocol. First, we used Bruker software to calculate the deflection sensitivity by making an indentation in a standardized sapphire sample. Afterwards, we used Sader’s method [45] to calculate the spring constant. The spring constant can be related with the length (L) and width (b) of the cantilever, its fundamental resonant frequency ω_{f}, Reynolds number, and the quality factor (Q_{f}) through eq. 2.5.

$$k = 0.1906\rho_{\mathrm{f}} b^2 L\, Q_{\mathrm{f}} \Gamma_{\mathrm{i}}(\omega_{\mathrm{f}})\omega^2{}_{\mathbf{f}} \tag{2.5}$$

where Γ_{i} is the imaginary part of the hydrodynamic function which only depends on the Reynolds number and ω_{f}. Everything is easily measurable except Q_{f} and ω_{f}, which Sader obtained by measuring the frequency response of the cantilevers at a range of frequencies in the neighborhood of its fundamental resonance peak. With our set-up, this can be easily achieved using the software controller.

Finally, to adjust the tip radius, we made indentations in a standardized polystyrene sample, and adjusted the tip radius until we measured 2.7 GPa as its elastic modulus.

Once the system was calibrated, we measured 2 x 2 μm^2 squares made of 256 x 256 spots.

We used RTESPA-300 (Bruker®) tips with a typical radius of 13 nm and an elastic constant and nominal resonant frequency of 40 N/m and 300 kHz, respectively.

2.4.1.3. Conductive AFM (C-AFM)

We used C-AFM to measure the change in conductivity after irradiation and its relationship with the change in topography, which was measured simultaneously. In C-AFM a voltage is applied between the tip and the sample holder. By scanning with a conductive tip, a preamplifier can measure the current that goes through the tip for each point of the scan. Since the voltage is applied between the holder and the sample, the holder and the tape used to fix the sample to it must be conductive. Usually, a Faraday cage isolates the sample and improves the signal/noise ratio of the measurements. See Figure 2.19 for the scheme.

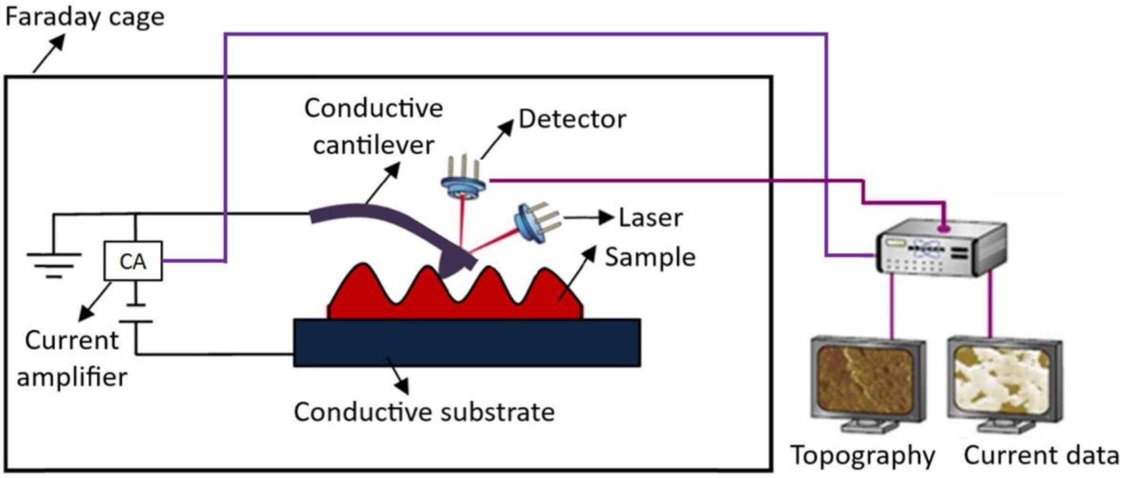

***Figure 2.19**. C-AFM scheme. (Original image with elements from [46,47]).*

In our case, the tips were conductive Pt−Ir covered Si probes with a low spring constant, k = 0.2 N/m, SCM-PIC by Bruker®.

2.4.2. Contact angle (CA)

The contact angle is the angle between the air-liquid interface and the liquid-solid interface formed when we deposit a drop of a liquid on a solid. From that angle, we can get information about the wettability and the surface energy. Wettability defines to what extent a liquid can keep contact with the surface of a solid. If the contact angle is less than 90° the sample has high wettability, and, if the liquid is water, we say the sample is hydrophilic. On the other hand, if the contact angle is more than 90°, the sample has low wettability, and, if the liquid is water, we say the sample is hydrophobic.

We used the sessile drop technique to measure the contact angles, at ambient temperature and humidity, using a pocket goniometer PG2 (FIBRO system) (Instituto de Química Física Rocasolano (IQFR-CSIC)). This instrument has a built-in camera that captures a picture of the liquid droplet applied on the surface of the sample. In Figure 2.20 we show an example of the measurements.

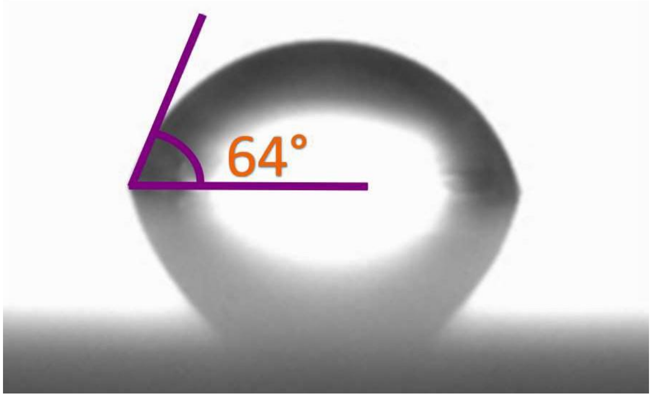

Figure 2.20. *Picture of a drop of water on the surface of a PTT sample. The measurement of the contact angle is shown.*

2.4.3. Confocal microscopy

A confocal microscope [48,49] selects a small volume to image by using a set-up that only collects light from spots very close to the focal point. This selection can be done easier if the source that illuminates the sample is a point source such as a laser. As long as only a single point image is needed, the requirements on the lenses and the optical system in general are not very demanding. The whole picture is then built by scanning. As the system only gets light from a point in the focal plane, it can measure 3D images instead of just 2D ones. Figure 2.21 shows the set-up used to select only the light close to the focal point. It is based on filtering the reflected light with the use of a pinhole and the microscope objective.

A system Alpha300 RAS (WITec, Ulm, Germany) (Dipartimento di Fisica "Ettore Pancini", Università degli Studi di Napoli “Federico II”), which uses an optical fiber with a diameter of 25 µm as pinhole and a He-Ne laser (633 nm) as the illumination source, was used. The system microscope objective has 50x magnification and a numerical aperture of 0.75, ensuring a diffraction-limited focused spot in the objective focal plane with a FWHM of approximately 320 nm.

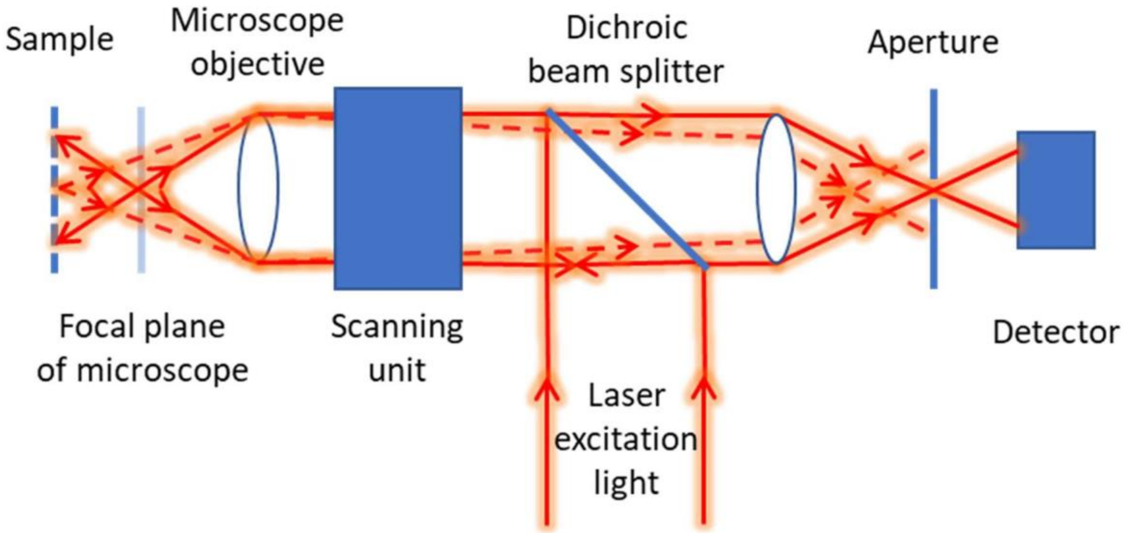

Figure 2.21. *Ray paths in a confocal microscope scanner. Light from sections of the sample located out of focus will largely fall outside the aperture and is thus strongly attenuated.*

2.4.4. Micro-Raman Spectroscopy

Micro-Raman spectroscopy is a non-destructive and non-invasive technique that allows the chemical and structural characterization of a material. The analyzed samples do not need special preparation and may exist in any physical state: solid, liquid, or gas.

This technique is based on the Raman scattering phenomenon [50,51]. When a photon from a monochromatic light beam strikes a molecule, it will interact with the electron cloud of the system, transiently taking the molecule from an allowed vibrational-rotational energy state to a higher transient energy state. After the interaction, the molecule will decay to one of the allowed energy levels, re-emitting a photon. The photon can be elastically scattered by the material, keeping the same frequency as the incident photon (Rayleigh scattering), which means that the molecule returns to the same state before the interaction and there is no energy exchange between it and the incident photon. On the other hand, if the photon is scattered inelastically, there is energy transfer, and its frequency is modified (Raman scattering). When the photon gains energy, we speak of an anti-Stokes process, while when it loses energy, we speak of Stokes scattering. An energy diagram, explaining the process, is shown in Figure 2.22.

The inelastic components give information about the rotational and vibrational motion of the atomic bonds, atoms and ions that make up the molecules and crystal lattices [52,53]. Such rotational and vibrational motion occurs at a certain value of energy or at a well-defined frequency. The representation of the Raman bands is made based on the normalized wave number $\bar{\nu}$, which is defined as

$$\bar{\nu} = \frac{\mathrm{v}}{\mathrm{e}} = \frac{1}{\ } \tag{2.6}$$

In this work, micro-Raman spectroscopy was conducted to detect possible chemical changes in the samples after being irradiated. Spectra were obtained using a micro-Raman spectrometer (Renishaw In Via 0310-02) (IEM-CSIC), equipped with an excitation laser source, operating at a power of 5 mW and a wavelength of 785 nm, and a CCD camera. Raman spectra were acquired with a spectral resolution of 2 cm^{-1} using a microscope objective with 50x magnification which gives a beam size < 1 µm in diameter.

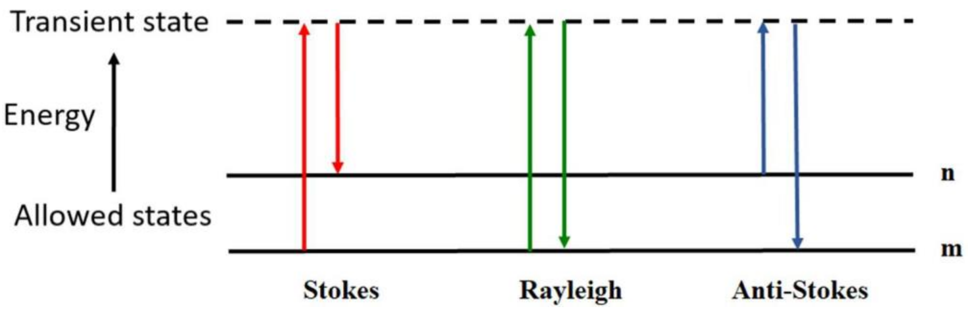

Figure 2.22. *Schematic of the Raman and Rayleigh dispersion process [35].*

2.5. Surface energy calculation

The surface energy is defined as the work necessary to produce a new surface of the material. In the bulk form of a material, atoms are generally stable and have a balanced set of interactions. However, the surface atoms will have an incomplete, unbalanced set of interactions and therefore have unrealized bonding energy. Surface energy is a relative measurement of the energy at the surface, which is a result of this incomplete bonding [54].

We used two different models to calculate different contributions to the surface energy of the samples.

2.5.1. Owens, Wendt, Rabel and Kaeble model (OWRK)

This model [55,56] considers the dispersive (γ^{d}) and polar (γ^{p}) contributions of the surface energy. It uses Young’s equation (eq. 2.7) to relate the measured contact angle of a drop of liquid resting on the surface of a solid (θ), the surface energy of the liquid (γ_l), the interfacial tension between the liquid and the solid (γ_{Sl}), and the surface energy of the solid (γ_S):

$$\gamma_S = \gamma_l cos\theta + \gamma_{Sl} \tag{2.7}$$

The interfacial tension is the sum of the surface energies of the liquid and the solid plus their interaction energy. This interaction is interpreted in this model as the geometric mean of a dispersive part (due to Van der Waals forces) and a polar part (for the electric interaction between polar molecules), as shown in eq. 2.8.

$$\gamma_{Sl} = \gamma_S + \gamma_l - 2\left[(\gamma_S^d\gamma_l^d)^{1/2} + (\gamma_S^p\gamma_l^p)^{1/2}\right] \tag{2.8}$$

Operating with eq. 2.7 and eq. 2.8 we obtain eq. 2.9.

$$\frac{y_l(1+eoS0)}{2(y_l^d)^{1/2}} = (\gamma_S^p)^{1/2}\left(\frac{y_l^p}{y_l^d}\right)^{1/2} + (\gamma_S^d)^{1/2} \tag{2.9}$$

In eq. 2.8 all the terms are known but γ_S^p and γ_S^d. We can interpret it as the equation of a line $y = ax + b$ where $y = \gamma_l(1 + cos\theta)/2(\gamma_l^d)^{1/2}$ and $x = (\gamma_l^p/\gamma_l^d)^{1/2}$. For each sample, we measured the contact angle of three different liquids with known surface energies, so we had three points of the line, and we could simply calculate the linear regression to obtain the polar and dispersive components of the surface energy of the sample.

2.5.2. Van Oss, Chaudhury and Good method based on Young-Dupré's theory

This method [57] calculates two contributions to the polar component of the surface energy: a polar negative component (γ^-, associated with electron-donor species) and a polar positive one (γ^+, associated with electron-acceptor species). However, it has a requirement, at least three liquids of different natures (polar and apolar) must be used. Since we used this method as well as WORK method, our liquids were chosen to meet all their requirements, as shown in Table 2.9.

The components of the surface energy of the liquids, already known, can be related to those of the solid with eq. 2.10, based on Young-Dupré's theory.

$$\gamma_l^{TOT}(1 + cos\theta) = 2(\gamma_S^d\gamma_l^d)^{1/2} + 2(\gamma_S^+\gamma_l^-)^{1/2} + 2(\gamma_l^+\gamma_S^-)^{1/2} \tag{2.10}$$

For the apolar liquid, we can get γ_S^d by directly substituting the values of the components of its surface energy in eq. 2.10 obtaining:

$$\gamma_S^{d} = \gamma_l^{TOT}(1 + cos\theta)^2/4 \tag{2.11}$$

Once γ_s^d is known, we can obtain γ_s^+ and γ_s^- using the contact angle measurements obtained for the polar liquids in eq. 2.10, and from them $\gamma_S^p = 2(\gamma_S^+\gamma_S^-)^{1/2}$ and $\gamma_S^{TOT} = \gamma_S^d + \gamma_S^p$.

Table 2.9. *Components of the surface energy of the liquids used in the contact angle measurements (mJ/m²) [57].*

Liquid	γ_l^d	γ_l^-	γ_l^+	γ_l^p	γ_l^{TOT}
Deionized Water	21.8	25.5	25.5	51.0	72.8
Glycerol	34.0	57.4	3.92	30.0	64.0
Paraffin oil	28.9	0	0	0	28.9

2.6. Numerical simulations

While conducting experiments where we irradiated PET on different substrates, we found that LIPSS formation was particularly difficult to understand when PET was deposited on a gold substrate. In particular, the direction of the structures was perpendicular to the polarization instead of parallel. We will explain this in more detail in Chapters 3 and 4. This discovery led us to assume that a particular electromagnetic mode called a Surface Plasmon Polariton was being excited and mediated the process. The properties of this mode and the influence of different parameters in its properties were discussed in Section 1.3.

We simulated this system to try to understand the underlying principles behind it and shed light on the aforementioned assumption. We simulated the electromagnetic field resulting of propagation and dispersion of the laser incident wave inside our samples and we compared the results to the experimental measurements.

2.6.1. Theoretical background

To simplify the problem, we used a plane wave approximation for the incident field $\vec{E}(\vec{r},t) = \vec{E}(\vec{r})e^{-iw}$. With this approximation, since we only consider linear optics, the electric field can be separated into a time-independent part and a part that oscillates at the frequency of the incident radiation.

For linear polarization, which is our case of study, LIPSS are longitudinal structures, therefore, it is enough to study the problem in 2D where the x direction is parallel to the sample surface and the direction of laser polarization, and the y direction is normal to the surface (see Figure 2.23). We can now further simplify the electric field as $\vec{E}(\vec{r})e^{-iw} = \vec{E}(x, y)e^{-i(k_z z+w)}$, which alongside eq. 2.12:

$$\nabla \times \mu^{-1}(\nabla \times \vec{E}) - k_0^2\left(\varepsilon - \frac{i}{wE_0}\right)\vec{E} = 0 \tag{2.12}$$

with μ the relative magnetic permeability, Φ the electric conductivity and i the imaginary unit, are the simplified Maxwell equations whose solution should be provided by numerical methods.

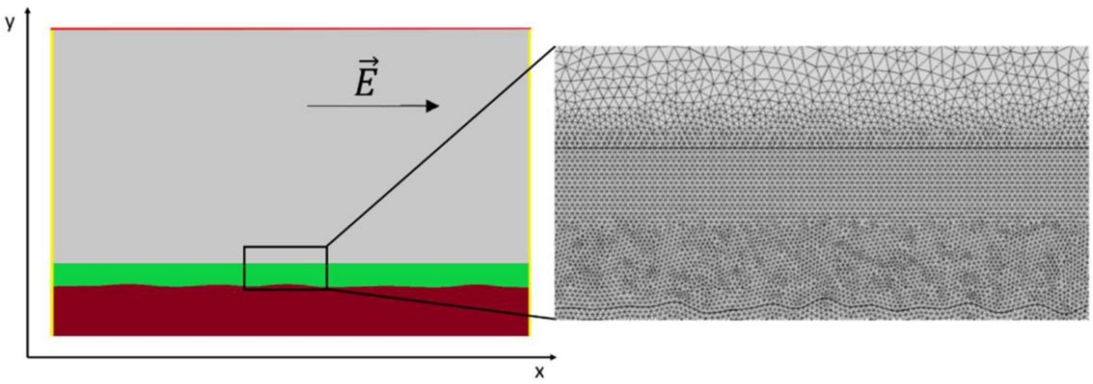

Figure 2.23. *Diagram of the geometry of our simulations and close-up to show the mesh. Gray represents air, green is PET, and maroon is gold. The periodic conditions are used for the yellow boundary and the periodic Port in the red boundary.*

We chose these directions since we knew the SPP wavevector should be parallel to the laser polarization as it corresponds to a TM wave. Information about the behavior of the SPP out of the plane XY is lost, but we assume there will only be small variations of the field, whose influence in LIPSS has to do with slight lack of linearity of the nanostructures.

2.6.2. Numerical simulation method

To perform the simulations, we used COMSOL Multiphysics Wave Optics Module, a software that solves Maxwell equations with finite element methods. In this method, the area of the problem is divided into subdomains, and in each subdomain, we apply an approximated equation of the physics of the problem. This allows for the approximation of the complicated solution of the problem by a set of simple polynomials. The method also forces the continuity of the solution and its derivatives up to a chosen order between subdomains. The key features of this method are:

- The complex region of the problem is modelled by simple subdomains called finite elements. These finite elements must have a shape that allows the derivation of the approximation functions.
- In each finite element, the equations that govern them are solved using the relations imposed by the physics of the problem and some approximation method.
- The equations of all the finite elements are assembled forcing continuity.

In our case, we subdivided the area of the problem into triangular elements of sizes between 1 and 50 nm. The lower limit allowed us to accurately model small roughness, whereas the upper was applied to the zones far from the surfaces, so we could save computing time but still be able to model our electric field at 16 elements per wavelength (see Figure 2.23). This number of elements should be more than enough to model the variation of the field in a plane wave, which would be a good approximation of the expected field far from the interface.

As for the magnitude of the area of the problem shown in Figure 2.23, we chose to simulate a region of 8 wavelengths in the x direction, which we found was a good compromise between the computing time and the quantity of data provided. In the y direction, we simulated the whole thin film, a distance of three wavelengths in air —to have enough space to observe both the incident wave and the plasmon—, and half a wavelength inside the gold substrate —which is more than enough, since the penetration distance of the electric field in gold, that was calculated according to eq. 1.10, is much smaller. This is also why we did not need to simulate the whole experimental substrate, *i.e.*, a thin layer of gold on silicon, as shown in Section 2.2, since the plasmon would not feel the silicon presence behind the gold layer.

2.6.2.1. Boundary conditions

In the *y* direction we used a periodic Port to introduce the plane wave and absorb it. The periodic Port boundary condition is used when modelling plane waves incident upon diffraction gratings and similar cases where we know that all waves getting out or going into the boundary must be plane waves. We checked the differences taking into consideration other scattering possibilities as the so-called Perfectly Matched Layers (PMLs) [58] or using just periodic Ports. We found them insignificant for the sake of our study. Given that the computing times needed for PMLs are much longer than for periodic Ports, we decided to discard PMLs.

As for the *x* direction, we used Floquet periodic boundary conditions to avoid edge effects. This periodic boundary condition —instead of the standard $\vec{E}(\text{-}r_0\vec{\ }) = \vec{E}(\text{-}r_1\vec{\ })$— adds a change in the field given by $\vec{E}(\text{-}r_0\vec{\ }) = \vec{E}(\text{-}r_1\vec{\ })e^{\text{-i-k}\vec{\ }(\text{- }\vec{0}\text{ -- }1\vec{\ })}$, where $r\vec{\ }$ is the position vector and $\vec{k}$ is the wavevector of the plane wave introduced in the periodic port.

2.6.2.2. Materials and interfaces definition

We defined the different materials (air, PET, gold) by their relative electrical permittivity (ε), relative magnetic permeability (μ) and electrical conductivity (Φ). We show the ε used for each material in Table 2.9. We considered the electrical conductivity of all materials to be 0 since it would only be important to calculate the field in gold and this does not affect the features of interest. As for their relative magnetic permeability, it was fixed at 1 since none of our materials have relevant magnetic properties.

Table 2.9. *Relative electric permittivity of the simulated materials.*

Material	ε_r
Air	1
PET	2.25
Gold	-24.061-i·1.5068

The roughness profile of the substrate was introduced using a MATLAB® random function which allowed us to establish *a priori* its R_q and σ, which now are defined for a line instead of a surface. To account for the fact that the electric field may depend on further features of the roughness function in addition to R_q and σ, we carried out three simulations with different roughness functions but the same R_q and σ for each measurement.

2.6.2.3. Data extraction

We took eight values per simulation of the SPP parameters relevant for LIPSS formation and gave the average as the result and the statistic deviation as the indetermination. These parameters are: (i) period, as it is assumed to match the period of the generated LIPSS; (ii) penetration distance, as it should be longer than the polymer film thickness in order to induce the process of LIPSS formation on the surface; and (iii) field amplitude, as it is required to be comparable to the incident field amplitude to induce any changes, although multiple pulse irradiation could give rise to comparable effects as far as accumulation is an important issue in LIPSS formation.

The evaluation of these parameters was carried out following the procedure shown in Figure 2.24, providing the mean value as well as the standard deviation. We used the parallel component (E) of the electric field to measure the period and intensity since it is much larger than the perpendicular component and will contribute the most. We used the perpendicular component of the electric field (E_y) to measure the penetration length as the SPP is the overwhelming contribution to this component while it is difficult to isolate the SPP contribution to E .

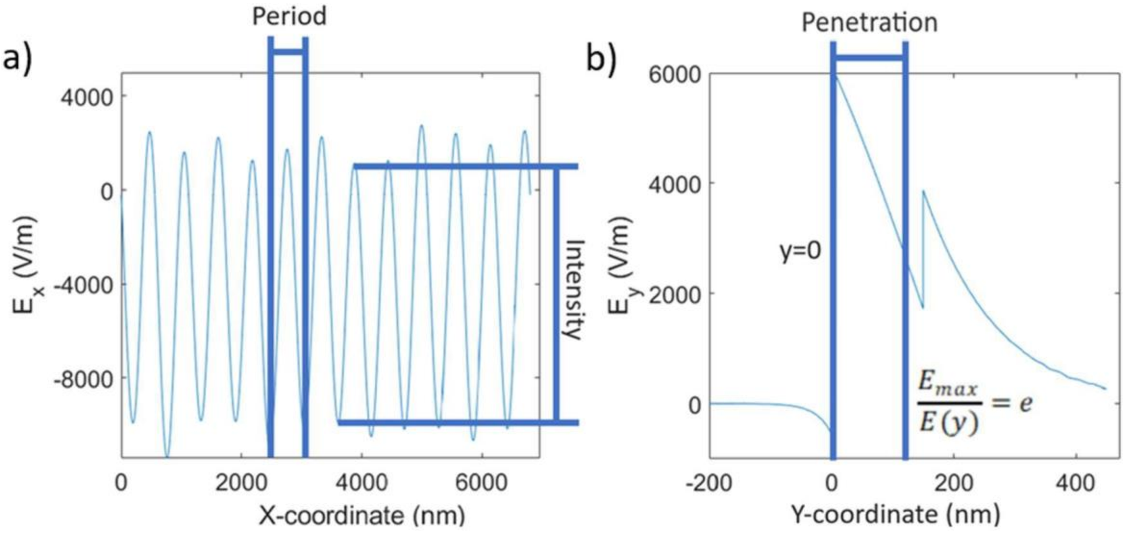

Figure 2.24. *a) X component of the simulated electric field across a horizontal cut at the surface of the thin film. The procedure to determine the period and intensity of the SPP is outlined. B) Y component of the simulated electric field across a perpendicular cut to the surface which allows the determination of the penetration length in the thin film.*

2.7. References

[1] J.R. Whinfield, J.T. Dickson, Improvements relating to the manufacture of highly polymeric substances, GB578079A, 1941.

[2] T. Rieckmann, S. Völker, Poly(Ethylene Terephthalate) Polymerization– Mechanism, Catalysis, Kinetics, Mass Transfer and Reactor Design, in: J. Scheirs, T.E. Long (Eds.), Modern Polyesters: Chemistry and Technology of Polyesters and Copolyesters, John Wiley & Sons, Ltd, 2004: pp. 29–115. https://doi.org/10.1002/0470090685.ch2.

[3] F. Welle, Twenty years of PET bottle to bottle recycling—An overview, Resources Conservation and Recycling 55 (2011) 865–875. https://doi.org/10.1016/J.RESCONREC.2011.04.009.

[4] R. Nisticò, Polyethylene terephthalate (PET) in the packaging industry, Polymer Testing 90 (2020) 106707. https://doi.org/10.1016/J.POLYMERTESTING.2020.106707.

[5] R.I. Umasabor, S.C. Daniel, The effect of using polyethylene terephthalate as an additive on the flexural and compressive strength of concrete, Heliyon. 6 (2020) e04700. https://doi.org/10.1016/J.HELIYON.2020.E04700.

[6] T. Çaykara, M.G. Sande, N. Azoia, L.R. Rodrigues, C.J. Silva, Exploring the potential of polyethylene terephthalate in the design of antibacterial surfaces, Medical Microbiology and Immunology 209 (2020) 363–372. https://doi.org/10.1007/S00430-020-00660-8/.

[7] S. Paszkiewicz, A. Szymczyk, Z. Spitalsky, M. Soccio, J. Mosnacek, T.A. Ezquerra, Z. Rosłaniec, Electrical conductivity of poly(ethylene terephthalate)/expanded graphite nanocomposites prepared by in situ polymerization, Journal of Polymer Science B 50 (2012) 1645–1652. https://doi.org/10.1002/polb.23176.

[8] S. Paszkiewicz, A. Szymczyk, Z. Spitalsky, J. Mosnacek, Z. Roslaniec, CHEMIK 66 (2012) 21–30.

[9] M.C. Feitor, C.A. Junior, C.M. Bezerra, R.R.M. De Sousa, T.H. De Carvalho Costa, Evaluation of Aging in Air of Poly (Ethylene Terephthalat) in Oxygen Plasma, Materials Research 18 (2015) 891–896. https://doi.org/10.1590/1516-1439.305814.

[10] Overview of materials for Polyethylene Terephthalate (PET), Unreinforced, (n.d.). https://www.matweb.com/search/DataSheet.aspx?MatGUID=a696bdcdff6f41dd98f8eec3599eaa20&ckck=1 (accessed December 21, 2022).

[11] M. Castillejo, T.A. Ezquerra, M. Oujja, E. Rebollar, Laser Nanofabrication of Soft Matter, in: M. Castillejo, P.M. Ossi, L. Zhigilei (Eds.), Lasers in Materials Science, Springer International Publishing, Cham, 2014: pp. 325–344. https://doi.org/10.1007/978-3-319-02898-9_13.

[12] M. Pyda, A. Boller, J. Grebowicz, H. Chuah, B. v Lebedev, B. Wunderlich, Heat Capacity of Poly(trimethylene terephthalate), Journal of Polymer Science B 36 (1998) 2499–2511. https://doi.org/10.1002/(SICI)1099-0488(199810)36:14.

[13] J.H. Chang, Comparison of Thermomechanical Properties and Morphologies of Polyester Nanocomposite Fibers: PBT, PET, and PTT, Polymer – Plastics Technology and Engineering 47 (2008) 791–801. https://doi.org/10.1080/03602550802188680.

[14] S. Paszkiewicz, A. Szymczyk, I. Janowska, R. Jedrzejewski, A. Linares, T.A. Ezquerra, H.D. Wagner, R. Tenne, Z. Rosłaniec, Comparative study on the properties of poly(trimethylene terephthalate)-based nanocomposites containing multi-walled carbon (MWCNT) and tungsten disulfide (INT-WS2) nanotubes, Polymers for Advanced Technologies 28 (2017) 645–657. https://doi.org/10.1002/pat.3964.

[15] H.A. Khonakdar, S.H. Jafari, A. Asadinezhad, A review on homopolymer, blends, and nanocomposites of poly(trimethylene terephtalate) as a new addition to the aromatic polyesters class, Iranian Polymer Journal 17 (2008) 19–38.

[16] Q. Xie, X. Hu, T. Hu, P. Xiao, Y. Xu, K.W. Leffew, Polytrimethylene Terephthalate: An Example of an Industrial Polymer Platform Development in China, Macromolecular Reaction Engineering 9 (2015) 401–408. https://doi.org/10.1002/MREN.201400070.

[17] J. Guo, H.X. Xiang, Q.Q. Wang, Rheological, Mechanical and Thermal Properties of Polytrimethylene Terephthalate, Polymer-Plastics Technology and Engineering 51 (2012) 199–207. https://doi.org/10.1080/03602559.2011.551979.

[18] C.A. Harper, Modern Plastics Handbook, McGraw-Hill, 2000. https://www.accessengineeringlibrary.com/content/book/9780070267145 (accessed March 31, 2020).

[19] A. Zak, L. Sallacan-Ecker, A. Margolin, M. Genut, R. Tenne, Insight into the growth mechanism of ws2 nanotubes in the scaled-up fluidized-bed reactor, Nano 4 (2009) 91–98. https://doi.org/10.1142/S1793292009001551.

[20] C.S. Reddy, A. Zak, E. Zussman, WS 2 nanotubes embedded in PMMA nanofibers as energy absorptive material, Journal of Materials Chemistry 21 (2011) 16086–16093. https://doi.org/10.1039/C1JM12700D.

[21] S. Niknam, S.A. Dehdast, O. Pourdakan, M. Shabani, M.K. Koohi, Tungsten Disulfide Nanomaterials (WS2 NM) Application in Biosensors and Nanomedicine: A review, Nanomedicine Research Journal 7 (2022) 214–226. https://doi.org/10.22034/NMRJ.2022.03.001.

[22] S. Ghosh, G. Otorgust, A. Idelevich, O. Regev, I. Lapsker, D.Y. Lewitus, A. Zak, Reinforcement of poly (methyl methacrylate) by WS2 nanotubes towards antiballistic applications, Composites Science and Technology 207 (2021) 108736. https://doi.org/10.1016/J.COMPSCITECH.2021.108736.

[23] D.M. Simić, D.B. Stojanović, M. Dimić, K. Mišković, M. Marjanović, Z. Burzić, P.S. Uskoković, A. Zak, R. Tenne, Impact resistant hybrid composites reinforced with inorganic nanoparticles and nanotubes of WS2, Composites B 176 (2019) 107222. https://doi.org/10.1016/J.COMPOSITESB.2019.107222.

[24] M. Shneider, L. Rapoport, A. Moshkovich, H. Dodiuk, S. Kenig, R. Tenne, A. Zak, Tribological performance of the epoxy-based composite reinforced by WS2 fullerene-like nanoparticles and nanotubes, Physica Status Solidi (a) 210 (2013) 2298–2306. https://doi.org/10.1002/PSSA.201329162.

[25] E. Rebollar, S. Pérez, J.J. Hernández, I. Martín-Fabiani, D.R. Rueda, T.A. Ezquerra, M. Castillejo, Assessment and formation mechanism of laser-induced periodic surface structures on polymer spin-coated films in real and reciprocal space, Langmuir 27 (2011) 5596–5606. https://doi.org/10.1021/la200451c.

[26] M. Naffakh, A.M. Díez-Pascual, Nanocomposite biomaterials based on poly(ether-ether-ketone) (PEEK) and WS2 inorganic nanotubes, Journal of Materials Chemistry B 2 (2014) 4509–4520. https://doi.org/10.1039/c4tb00557k.

[27] S.G. Sandeep Surya, K.N. Salama, C. Soc Rev, D. Kurouski, A. Dazzi, R. Zenobi, A. Centrone, S. Yuvaraja, A. Nawaz, bc Qian Liu, D. Dubal, de G. Sandeep Surya, P. Sonar, Organic field-effect transistor-based flexible sensors, Chemical Society Reviews 49 (2020) 3423–3460. https://doi.org/10.1039/C9CS00811J.

[28] Z. Hu, J. Wang, X. Ma, J. Gao, C. Xu, K. Yang, Z. Wang, J. Zhang, F. Zhang, A critical review on semitransparent organic solar cells, Nano Energy 78 (2020) 105376. https://doi.org/10.1016/J.NANOEN.2020.105376.

[29] T.H. Le, Y. Kim, H. Yoon, Electrical and Electrochemical Properties of Conducting Polymers, Polymers 9 (2017) 150. https://doi.org/10.3390/POLYM9040150.

[30] M.P. Bhatt, H.D. Magurudeniya, E.A. Rainbolt, P. Huang, D.S. Dissanayake, M.C. Biewer, M.C. Stefan, Poly(3-hexylthiophene) nanostructured materials for organic electronics applications, Journal of Nanoscience and Nanotechnology 14 (2014) 1033–1050. https://doi.org/10.1166/JNN.2014.8892.

[31] B.M. Omer, Optical properties of poly (3-hexylthiophene-2,5-diyl) and poly (3-hexylthiophene-2,5-diyl) / [6,6]-phenyl c61-butyric acid 3-ethylthiophene ester thin films, Journal of Nano- and Electronic Physics 5 (2013) 3010. https://jnep.sumdu.edu.ua/en/component/content/full_article/986 (accessed February 28, 2022).

[32] O. Inganäs, Organic Photovoltaics over Three Decades, Advanced Materials 30 (2018) 1800388. https://doi.org/10.1002/ADMA.201800388.

[33] PC71BM│609771-63-3 Luminescence technology corp., (n.d.). https://www.lumtec.com.tw/products-view.php?ID=679 (accessed February 28, 2022).

[34] E. Bormashenko, Y. Bormashenko, M. Frenkel, Formation of hierarchical porous films with breath-figures self-assembly performed on oil-lubricated substrates, Materials 12 (2019) 3051. https://doi.org/10.3390/ma12183051.

[35] R.I.R. Beltrán, Nanoestructurado de composites de matriz polimérica y aditivos de base carbono con láseres pulsados de nano- y femtosegundos, Universidad de Salamanca, 2018. https://doi.org/10.14201/GREDOS.137359.

[36] C. Romero Vázquez, Optical Parametric Processes with Femtosecond Pulses in Nonlinear Crystals: Novel Schemes and Applications, Universidad de Salamanca, 2012. https://doi.org/10.14201/gredos.115608.

[37] L. Marrucci, E. Karimi, S. Slussarenko, B. Piccirillo, E. Santamato, E. Nagali, F. Sciarrino, Spin-to-orbital conversion of the angular momentum of light and its classical and quantum applications, Journal of Optics 13 (2011) 064001. https://doi.org/10.1088/2040-8978/13/6/064001.

[38] E. Allahyari, J. Jj Nivas, F. Cardano, R. Bruzzese, R. Fittipaldi, L. Marrucci, D. Paparo, A. Rubano, A. Vecchione, S. Amoruso, Simple method for the characterization of intense Laguerre-Gauss vector vortex beams, Applied Physics Letters 112 (2018) 211103. https://doi.org/10.1063/1.5027661.

[39] R. Howland, L. Benatar, A practical guide to Scanning Probe Microscopy, First, ThermoMicroscopes, 1993.

[40] G. Binnig, H. Rohrer, Scanning tunneling microscopy, IBM Journal of Research and Development 30 (1986) 355–369. https://doi.org/10.5555/10869.10870.

[41] Atomic Force Microscopy An Overview from Asylum Research, (n.d.). https://afm.oxinst.com/outreach/atomic-force-microscopy (accessed September 23, 2022).

[42] C.C. Lai, J.M. Bell, N. Motta, Bovine Serum Albumin Adhesion Force Measurements Using an Atomic Force Microscopy, Advanced Materials Research 32 (2008) 49–52. https://doi.org/10.4028/www.scientific.net/amr.32.49.

[43] B. Pittenger, N. Erina, C. Su, Mechanical property mapping at the nanoscale using PeakForce QNM scanning probe technique, in: A. Tiwari (Ed.), Nanomechanical Analysis of High Performance Materials. Solid Mechanics and Its Applications, Vol 203., Springer, Dordrecht, 2014. https://doi.org/10.1007/978-94-007-6919-9_2.

[44] B.V. Derjaguin, V.M. Muller, Yu.P. Toporov, Effect of contact deformations on the adhesion of particles, Journal of Colloid and Interface Science 53 (1975) 314–326. https://doi.org/10.1016/0021-9797(75)90018-1.

[45] J.E. Sader, J.W.M. Chon, P. Mulvaney, Calibration of rectangular atomic force microscope cantilevers, Review of Scientific Instruments 70 (1999) 3967–3969. https://doi.org/10.1063/1.1150021.

[46] E. Gutiérrez Fernández, Nanostructuring Of Soft Matter For Organic Electronics, Universidad Complutense de Madrid, 2019. https://eprints.ucm.es/id/eprint/57833/ (accessed April 13, 2023)

[47] Á. Rodríguez Rodríguez, Propiedades físico-químicas de polímeros conjugados nanoestructurados y sus aplicaciones en células solares orgánicas, Universidad Complutense de Madrid, 2018. https://eprints.ucm.es/id/eprint/49017/ (accessed April 13, 2023)

[48] T. Wilson, Confocal Microscopy, Microanalysis of Solids (1994) 219–232. https://doi.org/10.1007/978-1-4899-1492-7_7.

[49] A. Liljeborg, K. Carlsson, L. Majlöf, N. Åslund, P.E. Danielsson, R. Lenz, Three-dimensional microscopy using a confocal laser scanning microscope, Optics Letters 10 (1985) 53–55. https://doi.org/10.1364/OL.10.000053.

[50] H.A. Szymanski, ed., Raman Spectroscopy. Theory and Practice., 1st ed., Springer New York, NY, Boston, MA, 1967. https://doi.org/10.1007/978-1-4684-3024-0.

[51] R.L. McCreery, Raman Spectroscopy for Chemical Analysis, Measurement Science and Technol 12 (2001) 653. https://doi.org/10.1088/0957-0233/12/5/704.

[52] I.M. Ward, M.A. Wilding, Infra-red and Raman spectra of poly(m-methylene terephthalate) polymers, Polymer 18 (1977) 327–335. https://doi.org/10.1016/0032-3861(77)90077-5.

[53] J. Štokr, B. Schneider, D. Doskočilová, J. Lövy, P. Sedláček, Conformational structure of poly(ethylene terephthalate). Infra-red, Raman and n.m.r. spectra, Polymer 23 (1982) 714–721. https://doi.org/10.1016/0032-3861(82)90057-X.

[54] E. Spooner, What is Surface Energy? Calculation Models and More Explained | Ossila, (n.d.). https://www.ossila.com/en-eu/pages/a-guide-to-surface-energy (accessed October 4, 2022).

[55] D.K. Owens, R.C. Wendt, Estimation of the surface free energy of polymers, Journal of Applied Polymer Science 13 (1969) 1741–1747. https://doi.org/10.1002/app.1969.070130815.

[56] D.H. Kaelble, Dispersion-Polar Surface Tension Properties of Organic Solids, The Journal of Adhesion 2 (1970) 66–81. https://doi.org/10.1080/0021846708544582.

[57] C.J. Van Oss, M.K. Chaudhury, R.J. Good, Interfacial Lifshitz-van der Waals and polar interactions in macroscopic systems, Chemical Reviews 88 (1988) 927–941. https://doi.org/10.1021/cr00088a006.

[58] J.P. Berenger, A perfectly matched layer for the absorption of electromagnetic waves, Journal of Computational Physics 114 (1994) 185–200. https://doi.org/10.1006/JCPH.1994.1159.

Chapter 3

Influence of film thickness and substrate nature on LIPSS formation in thin films of PET irradiated with fs Gaussian pulses

In Section 1.3, we mentioned the additional considerations one must bear in mind when trying to understand LIPSS formation in thin films. In this chapter, we study the influence of the material of the substrate as well as the thickness of the thin film. We deposited the thin films on substrates of different nature: a semiconductor (silicon), a dielectric (glass), a dielectric polymer (PET) and two metals (steel and gold). We expected this to make a difference since the optical properties (absorption, refractive index) and thermal properties of the substrates are extremely different, and so we expected the formation range of the LIPSS to change accordingly.

We tried to generate LIPSS in the PET samples described in Section 2.2. We used linearly polarized fs Gaussian pulses at a wavelength of 795 nm, for which PET has low linear optical absorption. We made systematic irradiations in a wide range of fluences and number of pulses. We characterized the spots as long as we observed appreciable changes and until the material was clearly ablated, insofar as we did not expect LIPSS outside that range.

This surface characterization of the nanostructured samples was done by AFM, as detailed in Section 2.4. We took one 10 x 10 μm^2 topography image of each spot, being careful to always choose the same zone. We made horizontal cuts to measure the period and height of the structures. We took ten measurements and gave the result as their average and the indetermination as their statistical deviation.

3.1. Thin films of PET on silicon substrates

We studied the formation of LIPSS on PET thin films of different thicknesses deposited on silicon substrates. As stated in Section 2.2, the thickness of these films ranges from 79 nm to 16 µm. We will now describe the surface structures found in each of the samples and their characteristics, starting from the one with the thinnest film.

The sample with the 79±3 nm thick film was irradiated with 1000 to 100000 pulses at fluences from 12 to 46 mJ/cm^2. LIPSS appeared parallel to the polarization of the laser at the spots that had been irradiated with 10000 to 100000 pulses at a fluence of 21 mJ/cm^2. For fluences ≥23 mJ/cm^2, the sample was ablated, and for fluences ≤18 mJ/cm^2, we did not observe any modifications. In Figure 3.1, we show an example of the evolution of the structures with the number of pulses, which was similar to their behavior with fluence. As it has been reported for other polymers [1–3], the roughness of the sample increased with laser irradiation, and increasing the number of pulses or fluence gave rise to LIPSS. A further increase brought about a loss of their periodicity, whereas the surface roughness still increased. The period of the structures was around 750 nm and their depth around 140 nm.

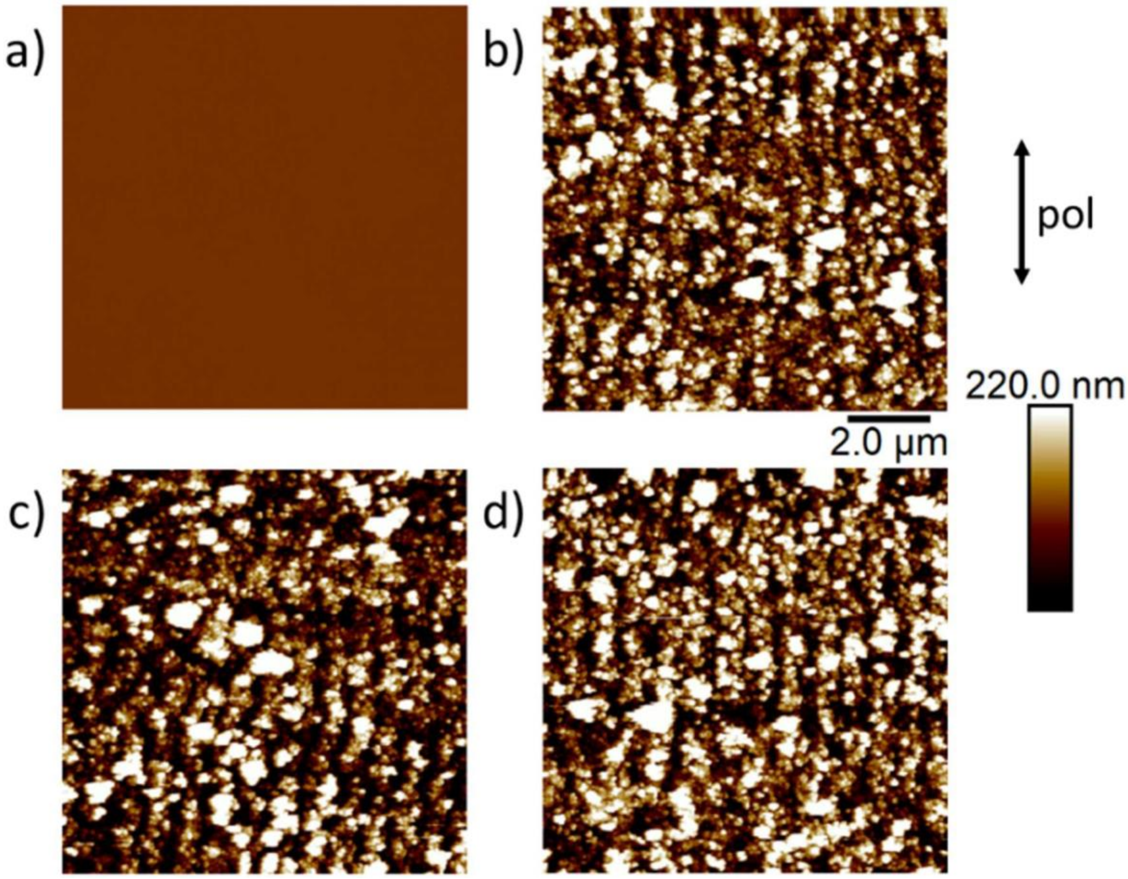

Figure 3.1. *10 x 10 µm^2 AFM image of a 79 nm thin film of PET deposited on a silicon substrate a) before irradiation and after being irradiated with b) 20000 pulses, c) 50000 pulses, d) 100000 pulses at a fluence of 21 mJ/cm^2.*

As for the relation of these features with the number of pulses, we show them in Figure 3.2. Considering the deviation in our measurements, we can state that both the period and depth of the structures remained almost constant in this range.

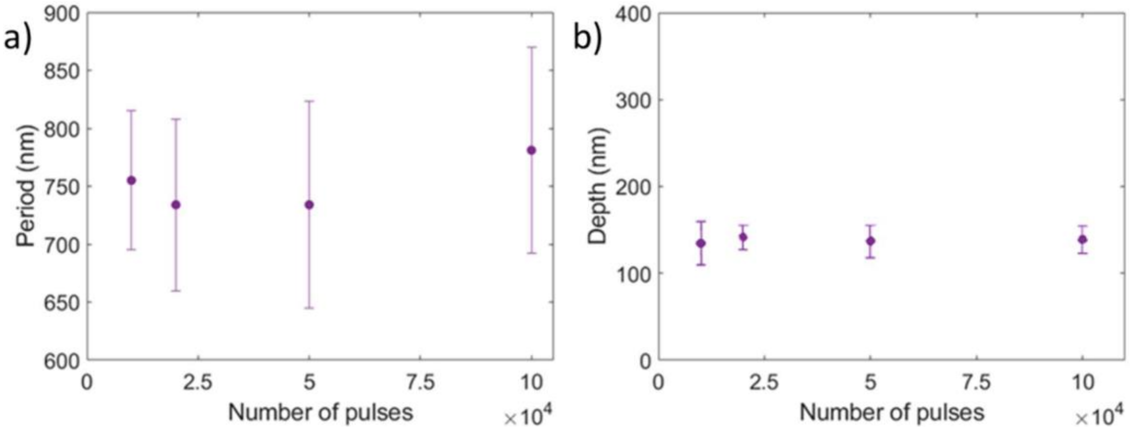

***Figure 3.2**. Dependence of a) the period and b) the depth of the structures with the number of pulses for 21 mJ/cm ^{2} in a 79 nm thin film of PET on a silicon substrate.*

Concerning the sample with the 120±20 nm thick film, we irradiated it with 1000 to 100000 pulses at fluences from 12 to 46 mJ/cm^2. LIPSS appeared parallel to the polarization of the laser on the spots that had been irradiated with 2000 to 100000 pulses at fluences from 18 to 26 mJ/cm^2. In Figure 3.3, we show an example of the evolution of the structures with increasing number of pulses. It was similar to the one described for the sample with the 79 nm thick film.

LIPSS period was around 700 nm and their depth around 200 nm. As for the relation of these characteristics with the parameters of irradiation, we show them in Figure 3.4. They both increased with the number of pulses until they reached a plateau. Regarding their relationship with fluence, the fluence range at which LIPSS appeared for a given number of pulses was very narrow. This means that we found LIPSS for one or two of the chosen irradiation fluences for each number of pulses, with lower fluences needing a higher number of pulses for LIPSS to appear in comparison to irradiation at higher fluences, as we can see in Figure 3.4. This is why stating a definite behavior of the period and depth with fluence is complicated, both the period and depth of the structures appeared to increase with fluence. As we mentioned in Section 1.3, this behavior is well known and has been reported for many materials [4–6].

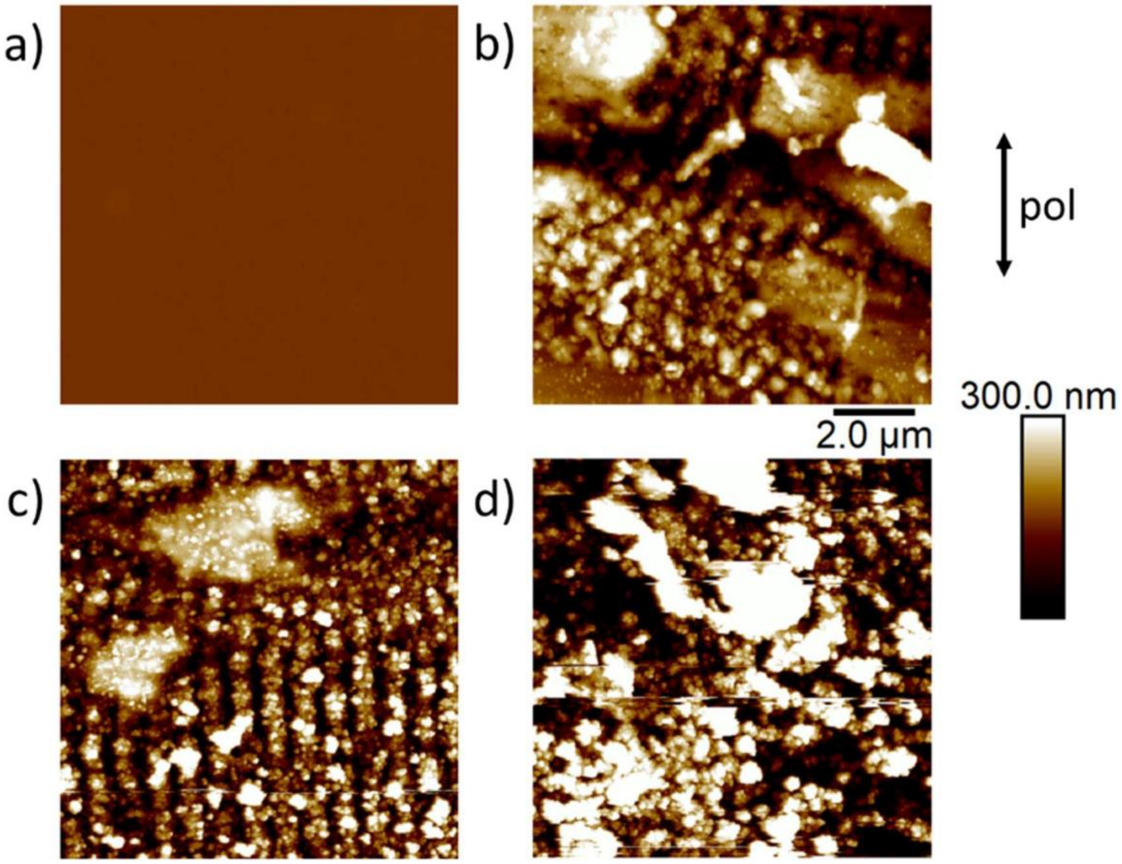

Figure 3.3. *10 x 10 µm² AFM images of a 120 nm thin film of PET deposited on a silicon substrate a) before irradiation and after being irradiated at a fluence of 26 mJ/cm² with b) 2000 pulses, c) 5000 pulses and d) 10000 pulses. The double-headed arrow shows the polarization of the laser.*

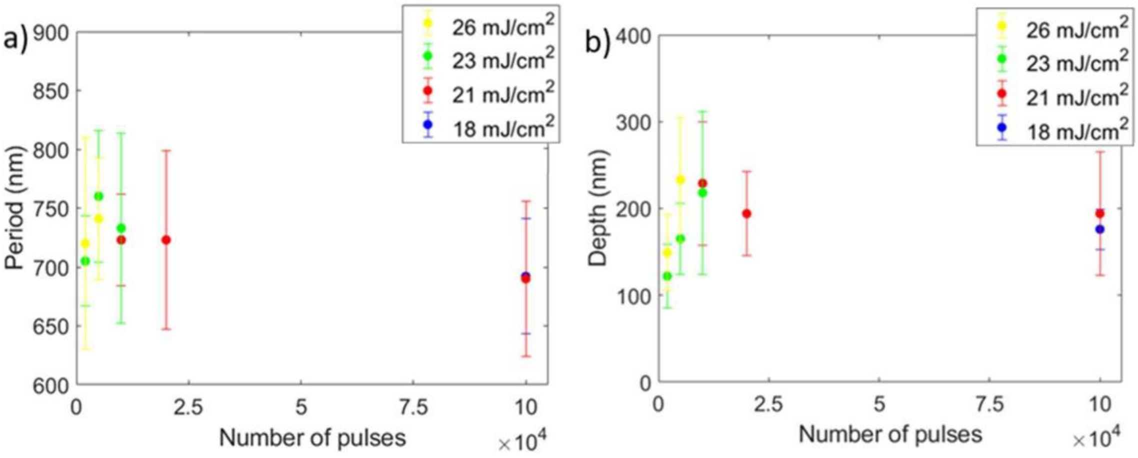

Figure 3.4*. Dependence of a) the period and b) the depth of the structures with the number of pulses for different fluences in a 120 nm thin film of PET on a silicon substrate.*

Concerning the sample with the 16.0±0.5 µm thick film, we irradiated it with 1000 to 100000 pulses at fluences from 3.4 to 12 mJ/cm^2. We reduced the fluence in this case because at the fluence range used for the other films the sample was completely ablated. We did not observe LIPSS formation for any irradiation condition in this range. However, we observed visible changes in the sample, and its roughness decreased slightly –from R_q = 250 ± 20 nm | σ = 1200 ± 200 nm before irradiation, to R_q = 160 ± 40 nm | σ = 940 ± 110 nm after having been irradiated with 10000 pulses at a fluence of 5.8 mJ/cm^2. In Figure 3.5, we show the differences in topography before and after irradiation.

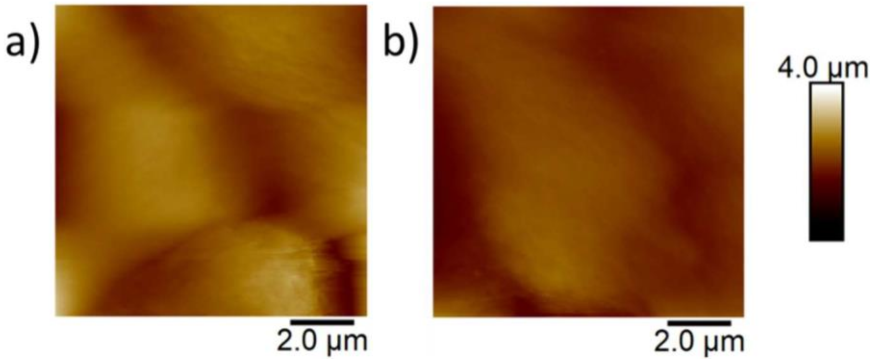

Figure 3.5. *10 x 10 µm^2 AFM pictures of a 16 µm film of PET on a silicon substrate a) before and b) after irradiation with 10000 pulses at a fluence of 5.8 mJ/cm^2.*

In summary, for PET thin films deposited on silicon substrates, LIPSS appeared parallel to the polarization of the laser with a period close to its wavelength, in the samples with film thicknesses from 79 to 120 nm but not in the one with a 16 µm thick film. In the samples where LIPSS appeared, the thickness of the film provided differences on their features: the period of the structures was larger in the 79 nm film than in the 120 nm film and the structures were deeper in the 120 nm film than in the 79 nm film. Moreover, LIPSS appeared in the 79 nm film for just one fluence, while in the 120 nm their formation range was broader.

3.2. Thin films of PET on glass substrates

We studied the formation of LIPSS on PET thin films of different thicknesses deposited on glass substrates. As described in Section 2.2, the samples had thin films of thicknesses from 115 nm to 16 µm.

We irradiated the sample with the 115±14 nm thick film with 1000 to 100000 pulses with fluences from 25 to 99 mJ/cm^2. In this case, LIPSS appeared parallel to the polarization of the laser at the spots that had been irradiated with 2000 to 100000 pulses with fluences from 44 to 63 mJ/cm^2. In Figure 3.6, we show an example of the evolution of the topography with the number of pulses. This evolution is similar to the one we showed for samples with silicon substrates.

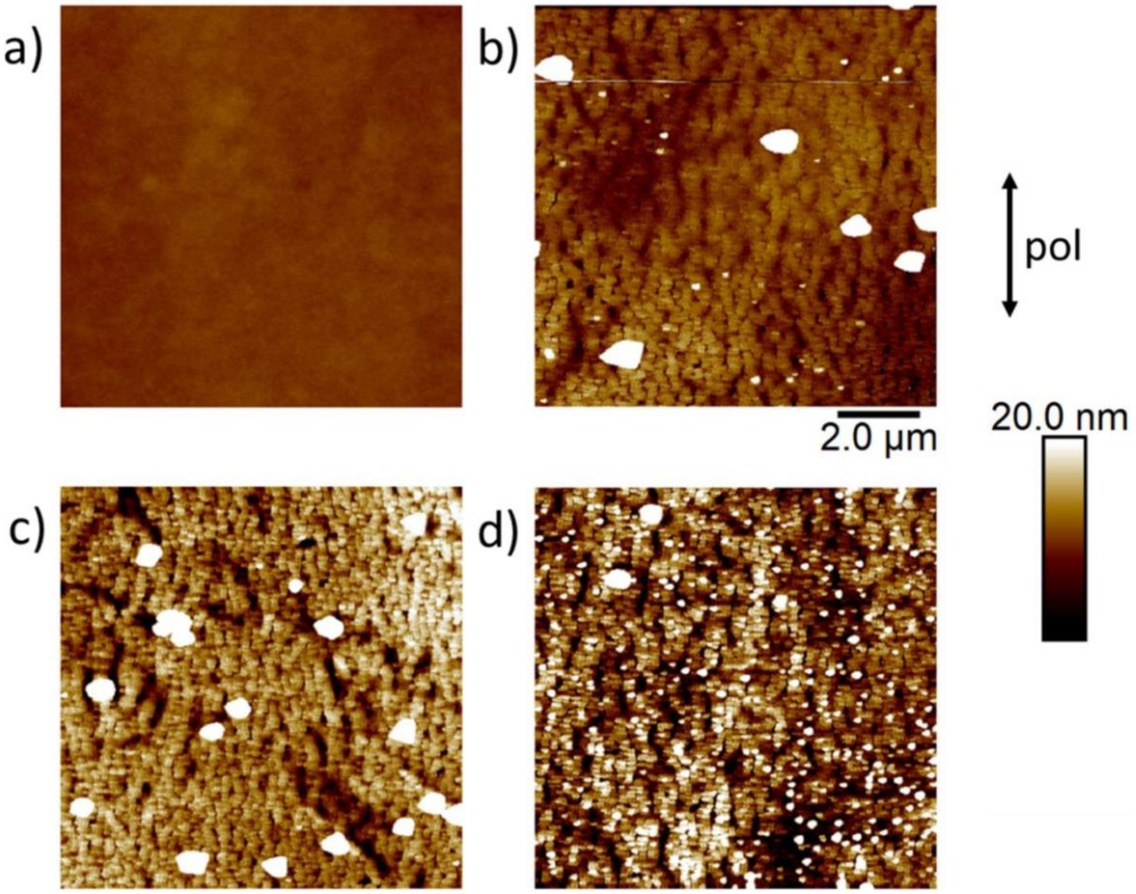

Figure 3.6. *10 x 10 µm^2 AFM image of a 115 nm thin film of PET deposited on a glass substrate a) before irradiation and after being irradiated with b) 2000 pulses, c) 5000 pulses, d)100000 pulses, at a fluence of 56 mJ/cm^2. The double-headed arrow shows the direction of the polarization of the laser.*

The period of the structures was ∼350 nm, around half the expected one, and their depth around 20 nm. We show the relation of these characteristics with the fluence and number of pulses in Figure 3.7. Their period remained almost constant with the number of pulses and their depth grew until it reached a plateau. As for their relationship with fluence, their depth tended to increase with it, but there was no clear-cut relation, and their period presented a more complicated behavior.

Besides the structures discussed until now, HSFL perpendicular to the polarization appeared at the spots that had been irradiated with 1000 pulses at fluences ranging from 56 to 73 mJ/cm^2 with an even smaller period of 150±40 nm and a depth of 18±8 nm. In Figure 3.8 we show an example of these structures.

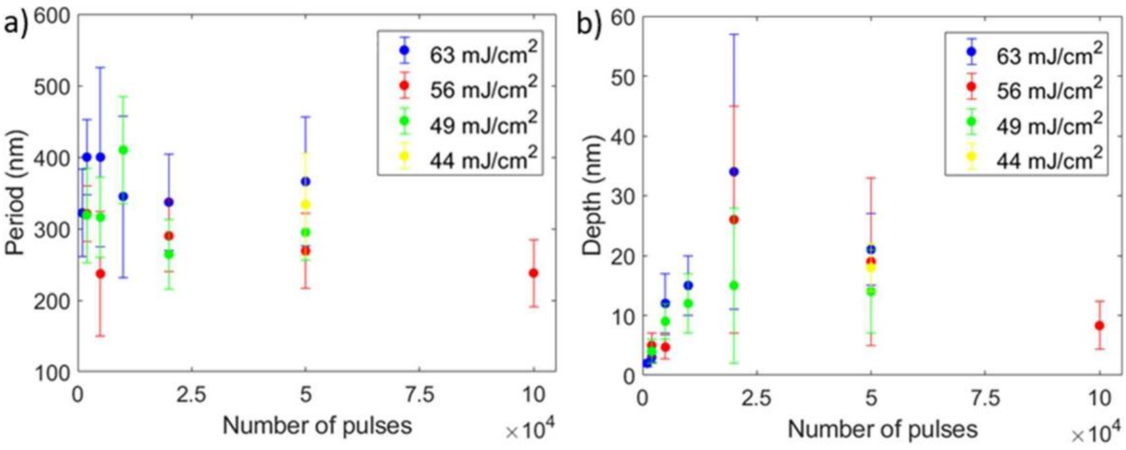

Figure 3.7. *Dependence of a) the period and b) the depth of the structures with the number of pulses for different fluences in the 115 nm thick film of PET on a glass substrate.*

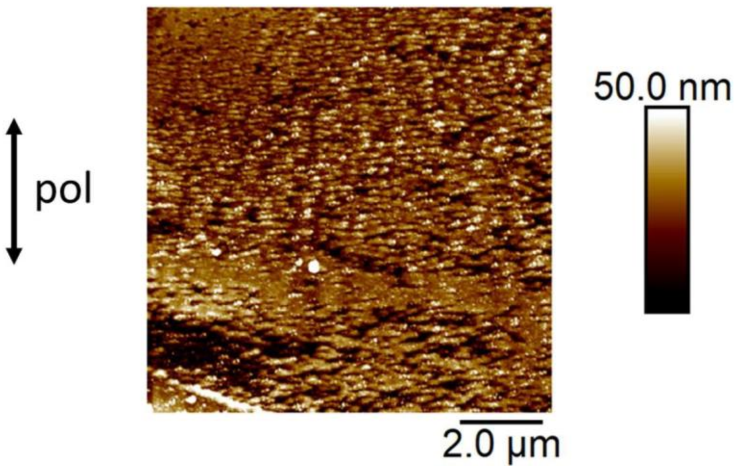

Figure 3.8. *10 x 10 µm^2 AFM image of a 115 nm thin film of PET deposited on a glass substrate after being irradiated with 1000 pulses at a fluence of 56 mJ/cm^2. The double-headed arrow shows the direction of the polarization of the laser.*

Regarding the sample with the 205±25 nm thick film, we irradiated it with 1000 to 100000 pulses with fluences from 23 to 84 mJ/cm^2. LIPSS appeared parallel to the polarization of the laser at the spots that had been irradiated with 1000 to 100000 pulses at fluences ranging from 44 to 63 mJ/cm^2. In Figure 3.9 we show an example of the evolution of the structures with increasing number of pulses. This evolution was similar to the one reported for the samples with silicon substrates.

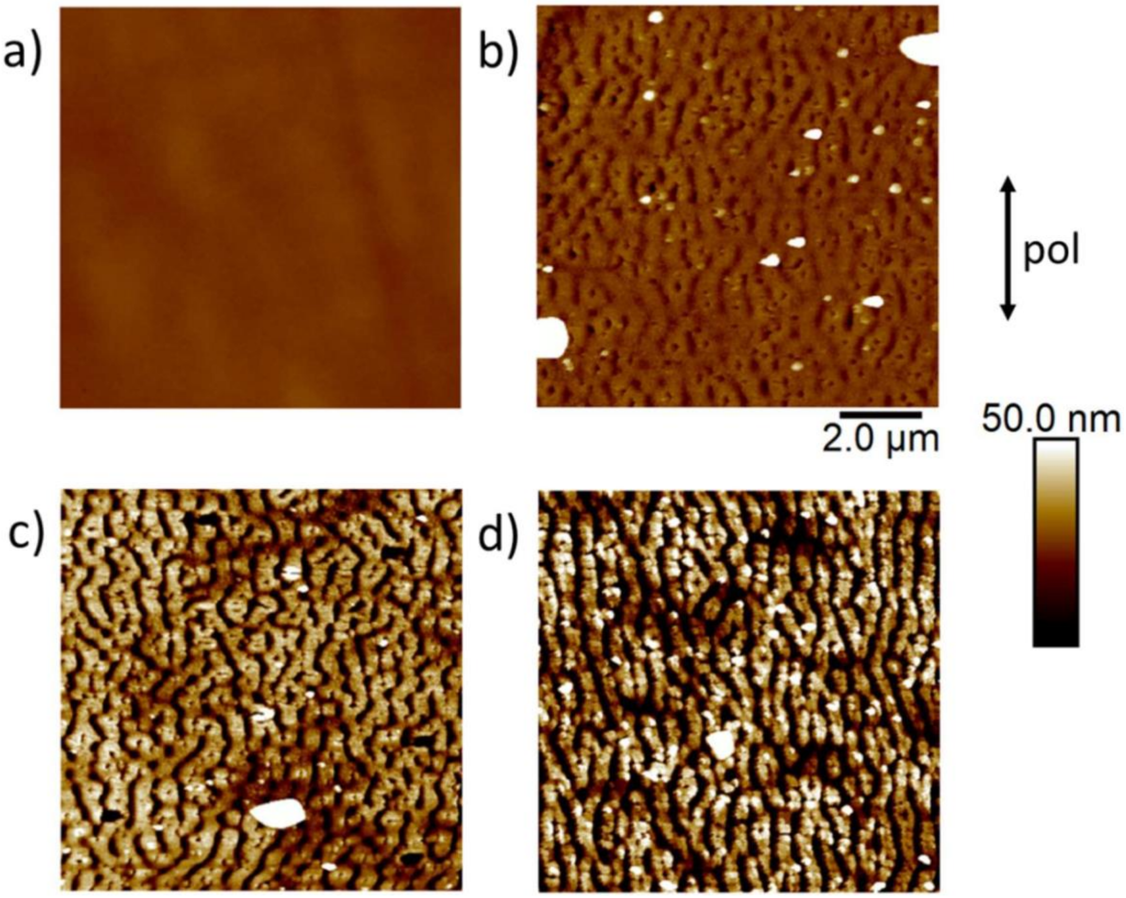

Figure 3.9. *10 x 10 µm^2 AFM image of a 205 nm thin film of PET deposited on a glass substrate a) before irradiation and after being irradiated with b) 2000 pulses, c) 10000 pulses and d) 100000 pulses, at a fluence of 46 mJ/cm^2.*

On average, the structures were wavier than the ones found in other samples. Their period was around ~600 nm and their depth around ~75 nm. As for the relation of these characteristics with the irradiation parameters, we show it in Figure 3.10. The period of the structures remained constant with the number of pulses and their depth grew until it reached a plateau. Regarding their relationship with fluence, the range at which LIPSS appear for a given number of pulses was very narrow. As a result, we found LIPSS for one or two fluences for each number of pulses. Lower fluences needed a higher number of pulses and higher fluences a smaller number of pulses for LIPSS to appear, as shown in Figure 3.10. It is for this reason that stating a definite behavior of the period and depth with fluence is complicated, but it seemed like it had the same influence in these characteristics as the number of pulses.

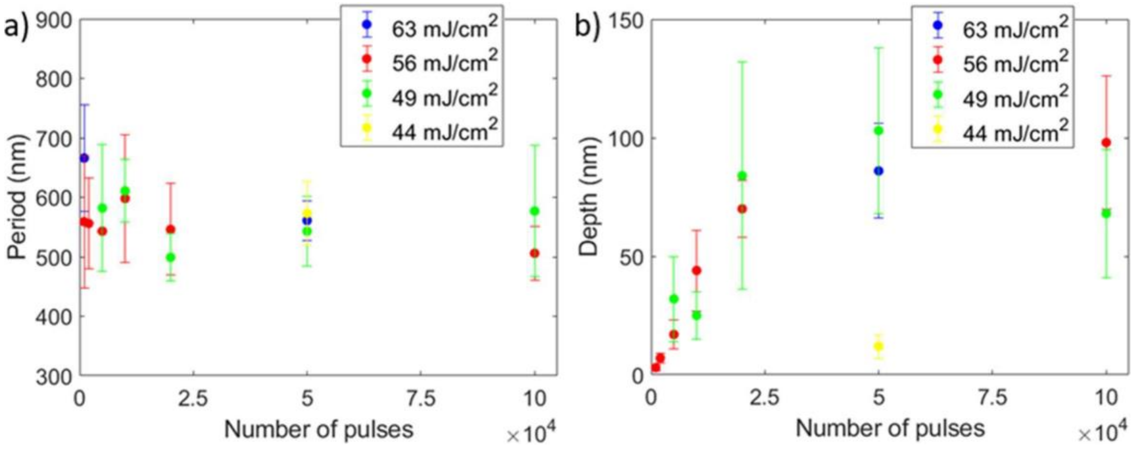

Figure 3.10. *Dependence of a) the period and b) the depth of the structures with the number of pulses for different fluences in the 205 nm thick film of PET on a glass substrate.*

We irradiated the sample with the 16.0±0.5 µm film with 1000 to 100000 pulses and fluences from 3.4 to 12 mJ/cm^2. As we observed for samples with thin films of the same thickness deposited on silicon substrates, the material was ablated at fluences close to the ranges used for thinner films. Therefore, we had to use much lower fluences than in the samples with thinner films. We did not observe LIPSS formation in any of these irradiation conditions. However, the irradiation did cause visible changes in the sample, although there were not significant changes in its roughness –from R_q = 101 ± 3 nm | σ = 1280 ± 120 nm before irradiation to R_q = 97 ± 2 nm | σ = 1250 ± 14 nm after being irradiated with 5000 pulses at a fluence of 8.9 mJ/cm^2. In Figure 3.11 we show the differences in topography before and after irradiation.

In conclusion, LIPSS appeared parallel to the polarization of the laser for the 115 nm thick film and the 205 nm thick film. However, they did not appear in the thicker films. The thickness of the film caused important changes in LIPSS characteristics, although their formation range did not significantly change. In the 115 nm thick film, LIPSS had a period around half the expected one, while in the 205 nm thick one, their period was close to λ and the structures were deeper. Moreover, in the 115 nm thick film, HSFL appeared perpendicular to the polarization of the laser with a period smaller than $\lambda/4$.

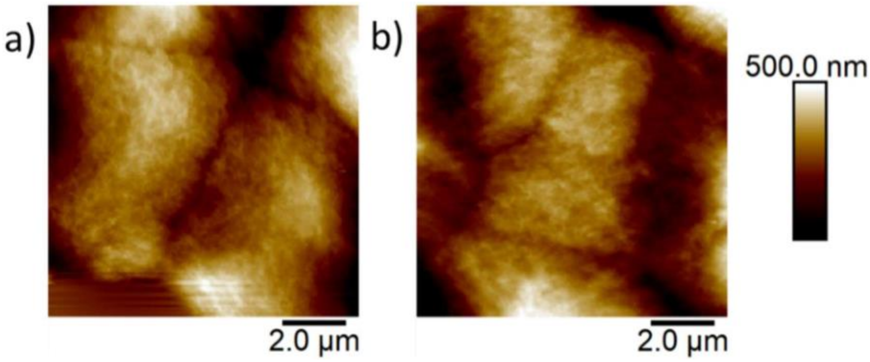

Figure 3.11. *10 x 10 µm² AFM pictures of a 16 µm film of PET on a glass substrate a) before and b) after irradiation with 50000 pulses at a fluence of 8.9 mJ/cm².*

3.3. Thin films of PET on PET substrates

We studied the formation of LIPSS on PET thin films of different thickness deposited on PET substrates. As described in Section 2.2, we prepared two samples: one with a 243±22 nm thick film and another with a 318±36 nm thick one. We irradiated both samples with 1000 to 100000 pulses with fluences from 3.0 to 8.1 mJ/cm². We did not observe LIPSS formation in this range in any of the two samples. However, we noticed a change in the roughness of the 243 nm thick sample from $R_q = 13 \pm 2$ nm | $\sigma = 550 \pm 60$ nm before irradiation, to $R_q = 64 \pm 17$ nm | $\sigma = 1080 \pm 110$ nm after being irradiated with 5000 pulses at a fluence of 4.7 mJ/cm²; and of the 318 nm thick sample from $R_q = 5 \pm 1$ nm | $\sigma = 300 \pm 90$ nm before irradiation, to $R_q = 33 \pm 16$ nm | $\sigma = 1130 \pm 150$ nm after being irradiated in the same conditions. In Figures 3.12 and 3.13, we show the differences in topography before and after irradiation. We took only 5 x 5 µm² AFM images because the high roughness of the samples made measuring larger areas challenging.

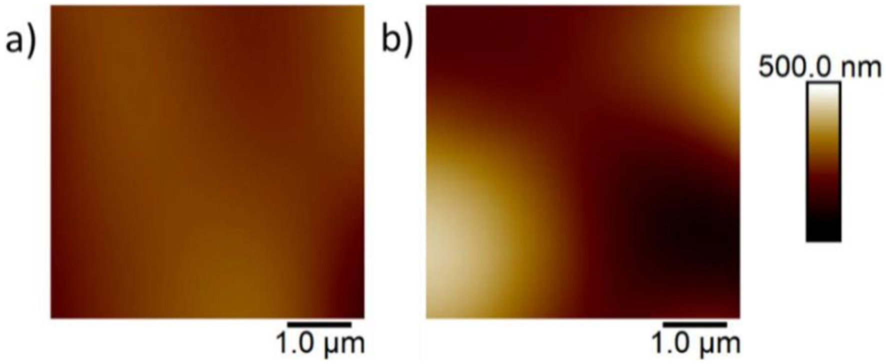

Figure 3.12. *5 x 5 μm² AFM pictures of a 243 nm film of PET on a PET substrate a) before and b) after irradiation with 5000 pulses at a fluence of 4.7 mJ/cm².*

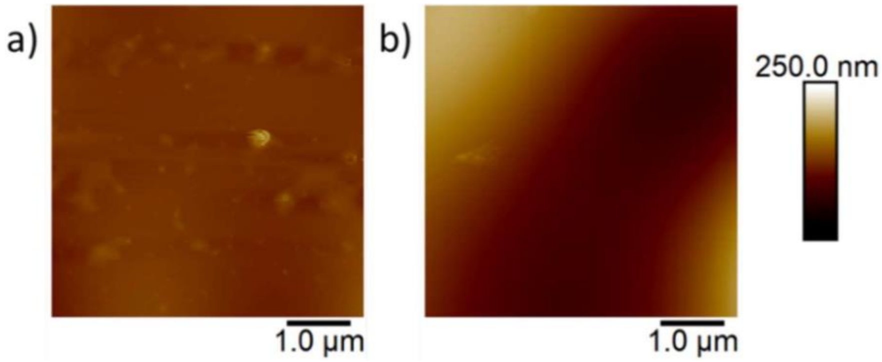

Figure 3.13. *5 x 5 μm² AFM pictures of a 318 nm film of PET on a PET substrate a) before and b) after irradiation with 5000 pulses at a fluence of 4.7 mJ/cm².*

3.4. Thin films of PET on steel substrates

We studied the formation of LIPSS on PET thin films of different thickness deposited on steel substrates. As described in Section 2.2, we irradiated two samples, one with a film 210±28 nm thick and another with a 298±58 nm thick one. We irradiated both with 1000 to 100000 pulses and fluences from 5.6 to 11.9 mJ/cm². We did not find LIPSS formation in this range in either of the two samples. However, we observed a change in the roughness of the 210 nm thick sample from R_q = 24 ± 7 nm | σ = 340 ± 20 nm before irradiation, to R_q = 96 ± 23 nm | σ = 570 ± 110 nm after being irradiated with 50000 pulses at a fluence of 6.4 mJ/cm²; and in the 298 nm thick sample from R_q = 46 ± 16 nm | σ = 524 ± 142 nm before irradiation, to R_q = 250 ± 30 nm | σ = 1450 ± 140 nm after being irradiated with 10000 pulses at a fluence of 6.4 mJ/cm². In Figures 3.14 and 3.15, we show the differences in topography before and after irradiation. As we did in the samples with PET substrates, we took only 5 x 5 µm^2 AFM images because of the high roughness of the samples.

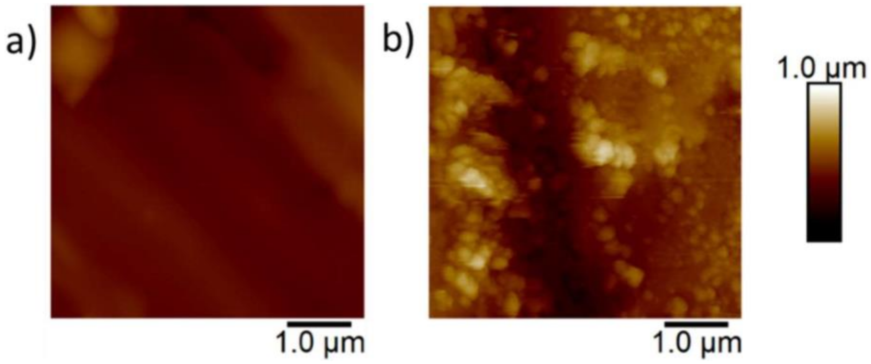

Figure 3.14. *5 x 5 µm^2 AFM pictures of a 210 nm film of PET on a steel substrate a) before and b) after irradiation with 50000 pulses at a fluence of 6.4 mJ/cm^2.*

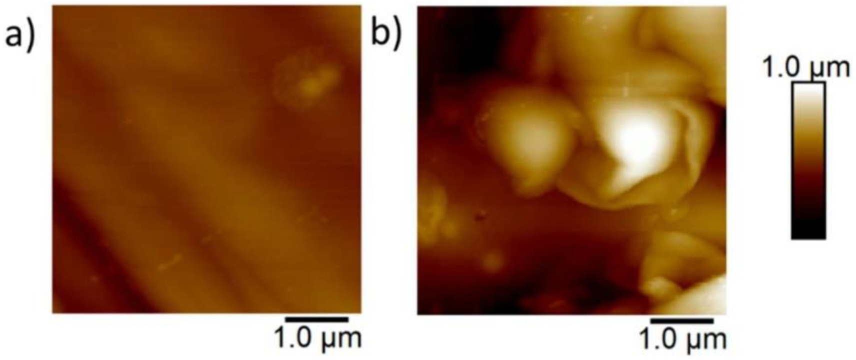

Figure 3.15. *5 x 5 µm^2 AFM pictures of a 298 nm film of PET on a steel substrate a) before and b) after irradiation with 10000 pulses at a fluence of 6.4 mJ/cm^2.*

3.5. Thin films of PET on gold substrates

We studied the formation of LIPSS on PET thin films of different thickness deposited on gold substrates. As described in Section 2.2, the samples were thin films of thicknesses from 90 nm to 16 µm. We irradiated the samples with 1000 to 100000 pulses at fluences from 2.3 to 17.5 mJ/cm^2. We found LIPSS perpendicular to the laser polarization in the samples with film thicknesses from 90 to 150 nm. As mentioned in Section 1.3, LIPSS in bulk polymers appear parallel to the polarization of the laser. The fact that, unlike the samples with other substrates reported above, LIPSS appeared here perpendicular to the laser polarization points to an influence of the substrate in the formation mechanism of LIPSS that we will discuss in Section 3.6. Concerning the effects of laser irradiation on the topography of the different samples as a function of fluence, it was similar for the samples 90 nm, 102 nm and 150 nm thick. As shown in Figure 3.16, it was the same as the one we showed in samples with silicon or glass substrates.

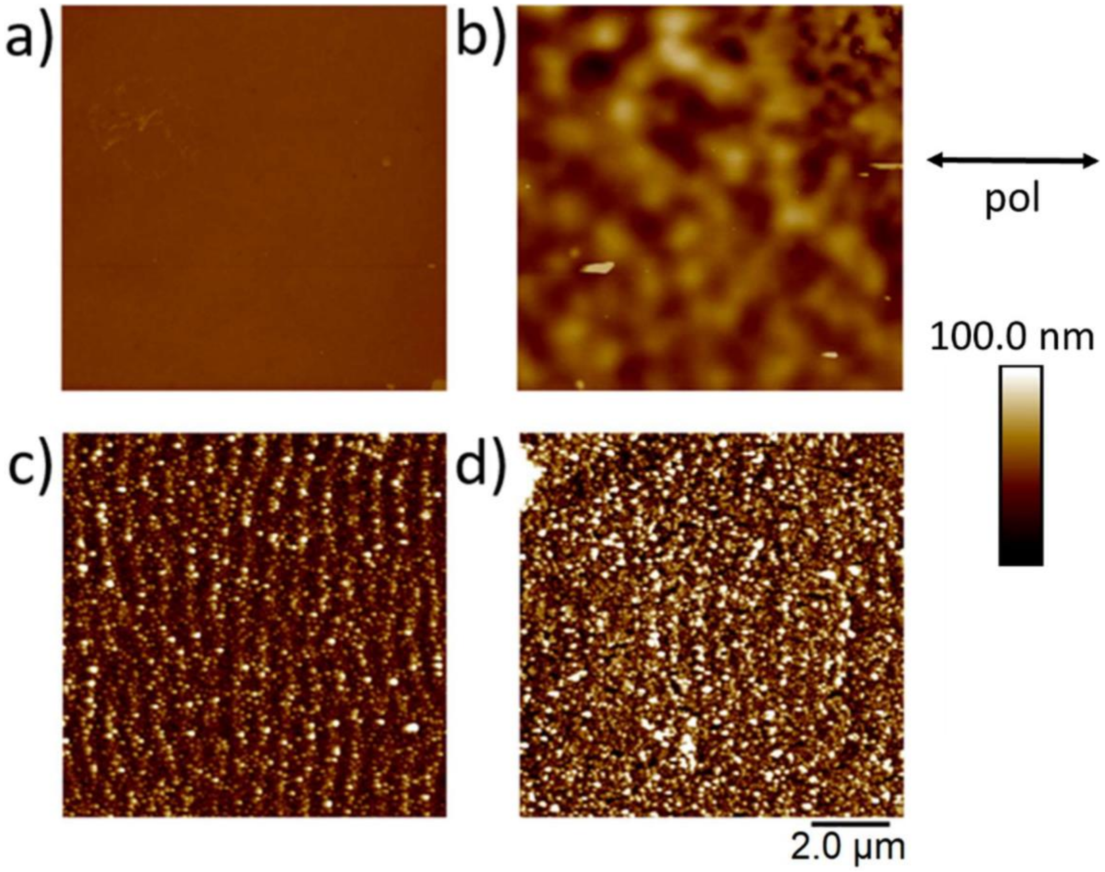

Figure 3.16. *10 x 10 µm^2 topography AFM images of the sample 150 nm thick on low R_q gold a) before being irradiated and after irradiation with 50000 pulses at a fluence of b) 4.4 mJ/cm^2, c) 5.8 mJ/cm^2 and d) 8.9 mJ/cm^2. The black arrow shows the direction of the polarization of the laser.*

The formation range and LIPSS depth and period in each sample are given in Table 3.1 and we show their behavior with fluence in Figure 3.17. The period of the structures increased with fluence, in some cases reaching a plateau. As for the depth of the structures in these samples, it seemed to grow with fluence. However, in some cases, the deviation in the measurements made it difficult to ascertain if the depth was increasing or remaining constant. Regarding the influence of the number of pulses, LIPSS appeared for a number of pulses above 50000. With our irradiation conditions, that meant that we had LIPSS for 50000 and 100000 pulses for each fluence. The depth of the structures was on average slightly smaller for 50000 pulses than for 100000 pulses and their period was almost the same.

Table 3.1. *Properties of the samples –substrate roughness and thin film thickness–, fluence and pulse number range at which LIPSS appeared, and their characteristics.*

Substrate $R_q\|\sigma$ (nm)	Thin film thickness (nm)	Fluence (mJ/cm^2)	Pulse Number	Period (nm)	Depth (nm)
2.4 | 30	90	2.7-3.6	50000-100000	650-740	20-50
2.4 | 30	102	4.0-6.3	50000-100000	530-630	20-45
2.4 | 30	150	4.4-8.9	50000-100000	600-680	40-65
2.4 | 30	1300	-	-	-	-
2.4 | 30	16000	-	-	-	-

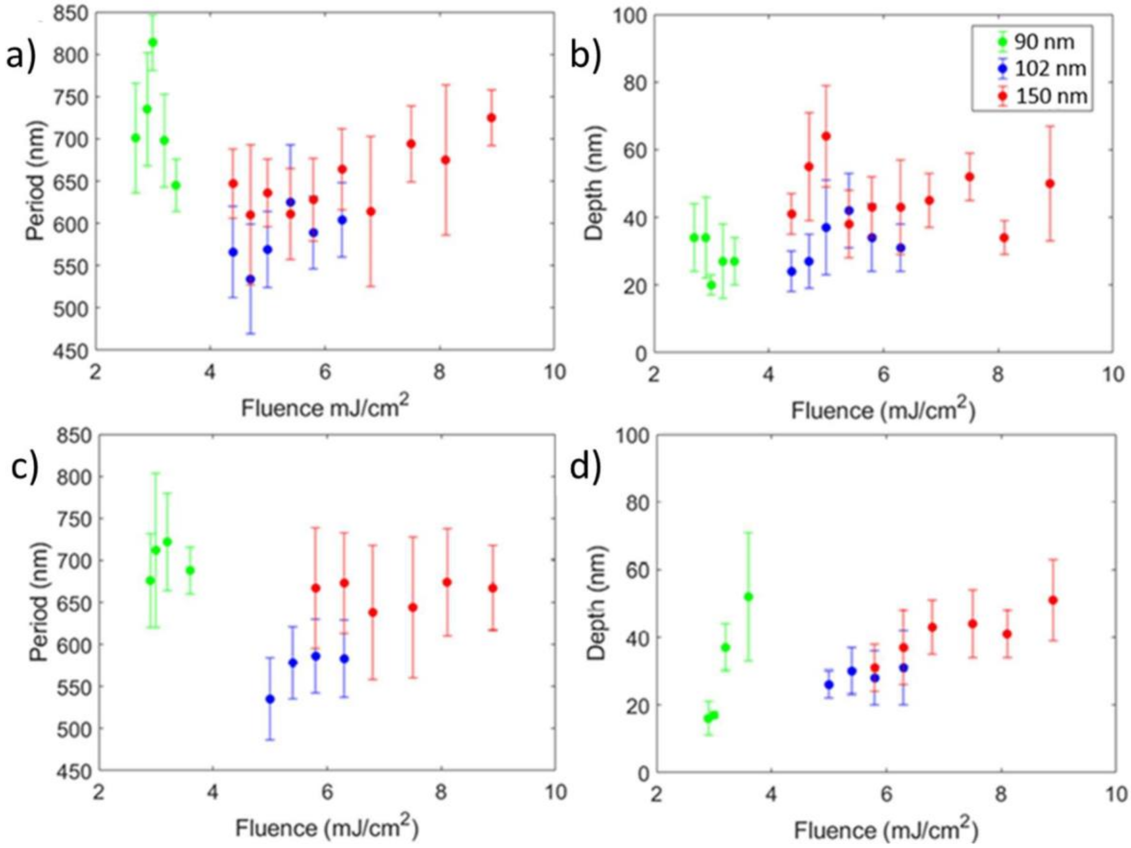

Figure 3.17. *Dependence of a) the period and b) the depth of LIPSS with laser fluence for 100000 pulses and c) the period and d) the depth of LIPSS for 50000 pulses for the thin films from 90 to 150 nm thickness deposited on the low R_{q} gold substrate.*

For the films 1.3 and 16 microns thick, we explored fluences from 2.3 to 9.9 mJ/cm^2 and pulses from 1000 to 100000. LIPSS were not found in this range. However, the laser did induce visible changes in these samples.

In the 1.3 µm thick film, there was a small roughness growth from R_q = 1.05 nm | σ = 650 nm before irradiation to R_q = 1.5 nm | σ = 1050 nm after irradiation.

As for the 16 µm thick film, its roughness diminished from R_q = 80 nm | σ = 880 nm before irradiation to R_q = 54 nm | σ = 571 nm after irradiation. We will discuss why LIPSS are not formed for films above a certain thickness in Section 3.6.

The AFM topography images before and after irradiation for samples where LIPSS formation was not achieved are shown in Figure 3.18.

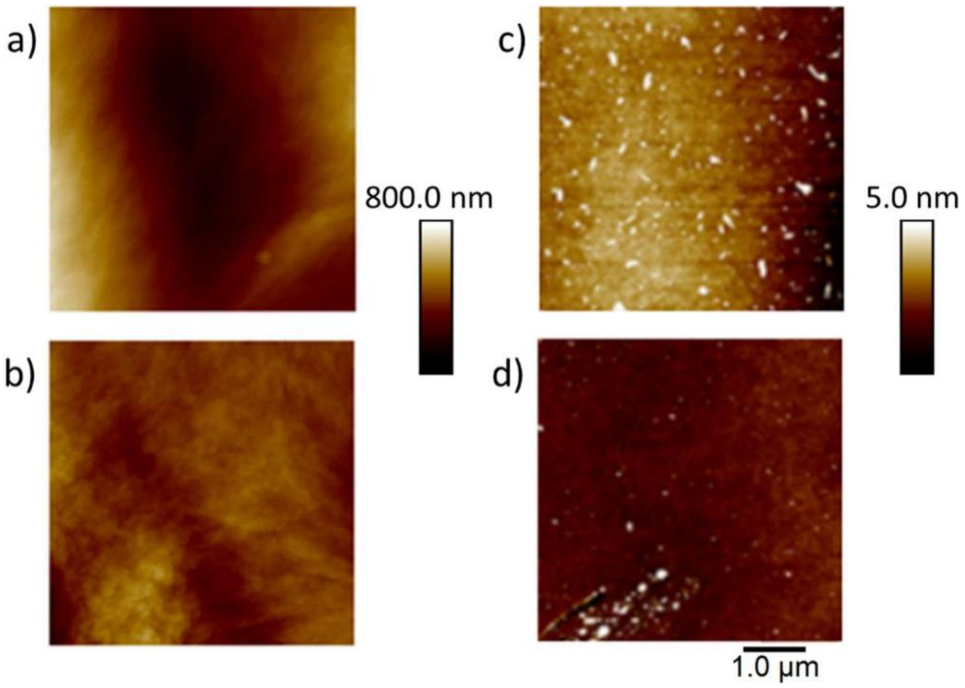

Figure 3.18. *Comparison of induced morphological changes at the surfaces before and after irradiation. The 5 x 5 µm^2 topography AFM images correspond to: 16 µm thick film on the low roughness gold substrate a) before irradiation and b) after irradiation with 50000 pulses at a fluence of 3.0 mJ/cm^2; 1.3 µm thick film on the low roughness gold substrate c) before irradiation and d) after irradiation with 100000 at a fluence of 2.3 mJ/cm^2. LIPSS formation was never observed for these samples regardless the laser fluence and number of pulses.*

3.6. Discussion of the effect of the nature of the substrate and thickness of the thin film on LIPSS formation

In this section we discuss the experimental differences on the formation of LIPSS on PET films, as a function of the substrate where the film was deposited. In order to help with this discussion, we condense in Table 3.3 the data of all the samples where LIPSS formation was achieved and their characteristics. Besides, we show in Table 3.4 the relevant properties of the different substrates where LIPSS appeared.

Table 3.3. *Features of the LIPSS generated in all the different samples and their formation range.*

Substrate	**Thin film thickness (nm)**	**Fluence range (mJ/cm^2)**	**Pulses range**	**Period (nm)**	**Depth (nm)**
Glass (HSFL)	115	56-73	1000	110-190	10-26
Glass	115	44-63	2000-100000	250-400	2-30
Glass	205	44-63	1000-100000	500-650	10-100
Silicon	79	21	10000-100000	730-780	130-160
Silicon	120	18-26	2000-100000	700-750	100-250
Gold	90	2.7-3.6	50000-100000	650-740	20-50
Gold	102	4.0-6.3	50000-100000	530-630	20-45
Gold	150	4.4-8.9	50000-100000	600-680	40-65

Table 3.4. *Optical properties –refractive index at 795 nm (n_{795}) and absorption coefficient at 795 nm α_{795}– and thermal diffusivity (α) of the substrates in which LIPSS where found.*

Substrate	**n_{795}**	**α_{795}(cm^{-1})**	**α (m^{2}s^{-1})**
Glass	1.5173 [7]	0.38110 [7]	$5.15\cdot10^{-7}$ [8]
Silicon	3.6981 [9]	$1.0802\cdot10^{3}$ [9]	$9.97\cdot10^{-5}$ [8]
Gold	0.15198 [10]	$7.6917\cdot10^{5}$ [10]	$1.27\cdot10^{-4}$ [11]

LIPSS appeared parallel to the polarization of the laser in the samples with glass or silicon substrates and perpendicular in the samples with gold substrates. Moreover, we observed LIPSS formation for the thinner samples (tens to hundreds of nm) with glass, silicon or gold substrates but not for the thicker ones (microns), nor for the ones with steel or PET substrates. Besides, LIPSS in different samples appeared for different fluences and number of pulses and with different periods and depths. Additionally, we only observed HSFL formation in the thinnest sample with a glass substrate. Several of these results made us confident that the substrate was involved in the formation mechanism of LIPSS. Therefore, we had to come up with possible formation mechanisms, since the more popular explanation for LIPSS formation –the interference between a surface scattered wave (SSW) and the incident irradiation [12–14], detailed in Section 1.3– does not take the substrate into account and it cannot explain why LIPSS formation does not take place above a certain thin film thickness.

Our first hypothesis assumed the interference of the incident irradiation with another SSW excited on the interface substrate-film (SF-SSW) which would compete with the SSW excited on the air-film interface (AF-SSW). For thin enough films, the penetration distance of this SF-SSW could be enough to affect the surface of the thin film and trigger LIPSS formation. However, we need to explain why this SF-SSW can trigger LIPSS formation when the AF-SSW one does not. Its excitation must be more efficient for this theory to make sense. In the case of silicon and gold substrates, we could say that the scattering in the thin film-substrate interface must be much higher than in the air-thin film interface since, at this wavelength, the materials are very different as far as their optical properties are concerned. This would make the SF-SSW more intense than the AF-SSW, so that the resulting periodic field is able to heat the polymer above T_g –the required temperature at which polymeric chains can flow and form the structures [2,3], as mentioned in Section 1.3.

However, for samples deposited on glass substrates, since glass is as similar to PET as air is in terms of optical properties –it is transparent and with a close refractive index to PET (see Table 3.4)– at the wavelength we used, the SF-SSW and AF-SSW will have similar intensities. Therefore, for our theory to work should postulate that even if the SSWs are not intense enough to trigger LIPSS formation by themselves, for thin enough films, the two SSWs would interfere resulting in an intensity that can trigger LIPSS formation.

As for the samples on substrates where LIPSS did not appear, we can also explain why if we think about the excitation and propagation of the SF-SSW. In the samples on steel substrates, as a result of their high R_q, there would be higher scattering than in the samples with other substrates, so the intensity of the SF-SSW would be higher. However, this high R_q would also interact with the SF-SSW causing its periodicity to be lost. In our experiments, we observed an increase in the R_q of the thin film after irradiation but no LIPSS formation, which is the result that one would expect. We will discuss the effect of the roughness of the substrate in more depth in the next chapter. In the case of the samples on PET substrates, the scattering in the substrate-thin film interface would be even smaller than in the air-thin film interface, since the substrate and the thin film are almost identical, and the intensity of the SSWs would not be enough to trigger LIPSS formation.

In the case of the samples on a gold substrate, LIPSS appear perpendicular to the polarization of the laser. This and the metallic nature of gold lead us to think that, in this case, the SF-should be a Surface Plasmon Polariton (SPP). We will discuss this theory in more detail in the next chapter, reinforcing it with numerical simulations.

Concerning the difference in the energy needed for LIPSS formation in samples on different substrates, taking this mechanism into account we can also explain why the samples on gold substrates needed the lowest fluences. The field enhancement effect which is well known to happen in metallic surfaces [15], could make the local fluence responsible for exciting the SF-SSW much higher than the irradiation fluence. As for the much higher fluences we needed to trigger LIPSS formation in samples on glass substrates, the reason could be the different formation mechanism based on the interference of two lower intensity SSWs and the transparency of glass at this wavelength.

We can also explain why LIPSS formation needed more energy in the samples with thicker films. Since the SF-SSW is excited in the substrate-thin film interface, the thicker the sample the more difficult it would be for the SF-SSW to affect the field at the surface and more energy would be needed. In the limit case where the thin film is too thick, we would overcome the ablation threshold before the SF-SSW can significantly change the field at the surface, which would explain why we did not find LIPSS in the thicker films. The other mechanism that could affect the energy needed for LIPSS formation for different thin film thicknesses would be that, as reported by Cui et al. [8], the substrate would be less effective as a heatsink the thicker the film. This would mean that more energy would be needed to reach $\mathrm{T_g}$ the thinner the film. In our experiments, the samples on silicon substrates followed this tendency but in the samples on gold and glass substrates we noticed the opposite one. These tendencies allow us to identify which of the two mechanisms prevailed in each case.

Regarding the different period of the LIPSS on samples on different substrates, this theory can also explain such differences. In Section 1.3 we showed the formula for the period of LIPSS in eq. 1.3. This equation related the period of the LIPSS with n_{eff}. n_{eff} was defined as the effective refractive index of a region close to the surface of the film, called selvedge [16]. However, that was for the case where the AF-SSW is the one that triggers LIPSS formation and following our theory the SF-SSW would be the main responsible of LIPSS formation. Correspondingly, the equation for the period of LIPSS would remain the same, but with n_{eff} being now the effective refractive index close to the substrate-thin film interface. This quantity would be affected by the material of the substrate since it would contribute with a different refractive index. Moreover, the thickness of the thin film can also have an effect in n_{eff} if it is thin enough. That is because the selvedge region would be made out of the substrate, the thin film, and air. Therefore, changing the thickness of the thin film would change n_{eff} between the limit case where the thin film is thicker than the selvedge region so there is no air in it, and the limit case where the thickness of the thin film is 0 so the selvedge region is only made out of the substrate and air.

Unfortunately, this theory does not explain the period of LIPSS in the 115 nm thick film deposited on glass. In this case, we observed two kinds of structures, one parallel to the polarization of the laser with a period that is close to half the expected one; and another perpendicular to the polarization with a period smaller than $\lambda/4$ (HSFL). As mentioned in Section 1.3, HSFL cannot be explained by the common theory though, being a source of discussion in the scientific community even when they appear in simpler bulk samples. Several explanations have been proposed to understand them like a model based on self-organization from highly electrostatic instabilities originated by the laser [17], another one based on thin-films hydrodynamics [18] or one based on the analysis of an electronic excitation when short-lived plasma is created [19,20]. From our experiments we do not reach a conclusion as to which of these models, if any, is the correct one.

As for the depth of the structures in different samples, we observed how it increased with the thickness of the sample, and it was higher for samples on silicon substrates than those on gold substrates. These aspects can be explained turning to the aforementioned effect of the substrate as a heatsink. In thin films, the thicker the film, the deeper the zone that can heat up to T_g as the influence of the substrate would be lessened. As for the different substrates, silicon has a smaller thermal diffusivity than gold (see Table 3.4), so it was a worse heatsink, and allowed the thin film to heat up to T_g at greater depths than gold. Following this explanation, as glass is the substrate with the lowest thermal diffusivity (see Table 3.4), one would expect it to be the one with the deeper LIPSS. However, in our experiments the samples on glass substrates have LIPSS with depths between those of the samples with gold substrates and those of the samples with silicon substrates. This contradiction can be solved if we notice the difference in optical properties between silicon, gold and glass. As reported by Cui et al. in [8], there is almost no reflected or absorbed intensity as a result of the transparency of glass, making the temperature increment lower, which can make up for its lower heat dissipation.

3.7. Conclusions

We generated LIPSS with 64 fs laser pulses with a wavelength of 795 nm in PET thin films on dielectric, semiconductor, and metallic substrates.

In our irradiation conditions, LIPSS appeared in samples on gold, silicon and glass substrates but not in those on PET or steel substrates. As for the thickness of the thin film, LIPSS appeared for thicknesses from 79 nm to 205 nm but not for thicknesses larger than 1300 nm. The material of the substrate and the thickness of the thin film are important parameters in LIPSS formation. Not only do they determine whether LIPSS can be generated but set the LIPSS formation range and characteristics.

We proposed that the interference of the incident irradiation with a SSW excited in the thin film-substrate interface contributes to the mechanism that triggers LIPSS formation in our samples. In the case of LIPSS in the samples with gold substrates this SSW could be a SPP. We will explore this in Chapter 4 with the help of numerical simulations.

We found structures parallel to the polarization with a period of ∼350 nm in one of our samples as well as HSFL perpendicular to the polarization with a period of ∼150 nm for only this sample –115 nm thin film on a glass substrate. More work is needed to understand the characteristics of LIPSS in this sample.

3.8. References

[1] J. Prada-Rodrigo, R.I. Rodríguez-Beltrán, S. Paszkiewicz, A. Szymczyk, T.A. Ezquerra, P. Moreno, E. Rebollar, Laser-induced periodic surface structuring of poly(trimethylene terephthalate) films containing tungsten disulfide nanotubes, Polymers 12 (2020) 1090. https://doi.org/10.3390/POLYM12051090.

[2] E. Rebollar, J.R. Vázquez De Aldana, I. Martín-Fabiani, M. Hernández, D.R. Rueda, T.A. Ezquerra, C. Domingo, P. Moreno, M. Castillejo, Assessment of femtosecond laser induced periodic surface structures on polymer films, Physical Chemistry Chemical Physics 15 (2013) 11287–11298. https://doi.org/10.1039/c3cp51523k.

[3] E. Rebollar, M. Castillejo, T.A. Ezquerra, Laser induced periodic surface structures on polymer films: From fundamentals to applications, European Polymer Journal 73 (2015) 162–174. https://doi.org/10.1016/j.eurpolymj.2015.10.012.

[4] M. Csete, Z. Bor, Laser-induced periodic surface structure formation on polyethylene-terephthalate, Applied Surface Science 133 (1998) 5–16. https://doi.org/10.1016/S0169-4332(98)00192-5.

[5] M. Hashida, Y. Ikuta, Y. Miyasaka, S. Tokita, S. Sakabe, Simple formula for the interspaces of periodic grating structures self-organized on metal surfaces by femtosecond laser ablation, Applied Physics Letters 102 (2013) 174106. https://doi.org/10.1063/1.4803940.

[6] J. Bonse, A. Rosenfeld, J. Krüger, On the role of surface plasmon polaritons in the formation of laser-induced periodic surface structures upon irradiation of silicon by femtosecond-laser pulses, Journal of Applied Physics 106 (2009) 104910. https://doi.org/10.1063/1.3261734.

[7] M. Rubin, Optical properties of soda lime silica glasses, Solar Energy Materials 12 (1985) 275–288. https://doi.org/10.1016/0165-1633(85)90052-8.

[8] J. Cui, A. Nogales, T.A. Ezquerra, E. Rebollar, Influence of substrate and film thickness on polymer LIPSS formation, Applied Surface Science 394 (2017) 125–131. https://doi.org/10.1016/j.apsusc.2016.10.045.

[9] D.E. Aspnes, A.A. Studna, Dielectric functions and optical parameters of Si, Ge, GaP, GaAs, GaSb, InP, InAs, and InSb from 1.5 to 6.0 eV, Physical Review B 27 (1983) 985–1009. https://doi.org/10.1103/PHYSREVB.27.985.

[10] P.B. Johnson, R.W. Christy, Optical constants of the noble metals, Physical Review B 6 (1972) 4370–4379. https://doi.org/10.1103/PHYSREVB.6.4370.

[11] Thermal Diffusivity Table, (n.d.). https://www.engineersedge.com/heat_transfer/thermal_diffusivity_table_13953.htm (accessed April 10, 2023).

[12] J.E. Sipe, J.F. Young, J.S. Preston, H.M. van Driel, Laser-induced periodic surface structure. I. Theory, Physical Review B 27 (1983) 1141–1154. https://doi.org/10.1103/PhysRevB.27.1141.

[13] J.F. Young, J.S. Preston, H.M. van Driel, J.E. Sipe, Laser induced periodic surface structure. II. Experiments on Ge, Si, Al and brass, Physical Review B 27 (1983) 1155–1172. https://doi.org/10.1103/PhysRevB.27.1155.

[14] J.F. Young, J.E. Sipe, H.M. van Driel, Laser-induced periodic surface structure. III. Fluence regimes, the role of feedback, and details of the induced topography in germanium, Physical Review B 30 (1984) 2001–2015. https://doi.org/10.1103/PhysRevB.30.2001.

[15] K. Arya, Z.B. Su, J.L. Birman, Localization of the Surface Plasmon Polariton Caused by Random Roughness and its Role in Surface-Enhanced Optical Phenomena, Physical Review Letters 54 (1985). https://doi.org/10.1103/PhysRevLett.54.1559.

[16] J.E. Sipe, Bulk-selvedge coupling theory for the optical properties of surfaces, Physical Review B 22 (1980) 1589–1599. https://doi.org/10.1103/PhysRevB.22.1589.

[17] O. Varlamova, J. Reif, S. Varlamov, M. Bestehorn, Self-organized Surface Patterns Originating from Laser-Induced Instability, in: S. Sakabe, C. Lienau, R. Grunwald (Eds.), Progress in Nonlinear Nano-Optics. Nano-Optics and Nanophotonics., Springer, Cham, 2015: pp. 3–29. https://doi.org/10.1007/978-3-319-12217-5_1.

[18] G.D. Tsibidis, C. Fotakis, E. Stratakis, From ripples to spikes: A hydrodynamical mechanism to interpret femtosecond laser-induced self-assembled structures, Physical Review B 92 (2015) 041405. https://doi.org/10.1103/PhysRevB.92.041405.

[19] R. Buividas, M. Mikutis, S. Juodkazis, Surface and bulk structuring of materials by ripples with long and short laser pulses: Recent advances, Progress in Quantum Electronics 38 (2014) 119–156. https://doi.org/10.1016/J.PQUANTELEC.2014.03.002.

[20] L. Wang, B. Bin Xu, X.W. Cao, Q.K. Li, W.J. Tian, Q.D. Chen, S. Juodkazis, H.B. Sun, Competition between subwavelength and deep-subwavelength structures ablated by ultrashort laser pulses, Optica 4 (2017) 637–642. https://doi.org/10.1364/OPTICA.4.000637.

Chapter 4

Theoretical-practical study of LIPSS formation in thin films of PET on gold substrates with fs Gaussian pulses

In Section 1.3, we discussed the additional considerations one must take into account when trying to understand LIPSS formation in thin films. We already observed the influence of depositing the thin films of PET on substrates made of different materials in Chapter 3. Specifically, in Section 3.5 we noticed a change in behavior for different thickness of the thin film deposited on a gold substrate. This, together with the orientation of LIPSS —perpendicular to the polarization of the laser— and gold being one of the materials usually studied in SPP formation [1–3], leads us to the hypothesis that the formation mechanism could be related to the SPP excited in the boundary between substrate and thin film. The bibliography cited in Section 1.3 supports this hypothesis since it shows the importance of the thickness of the film and the roughness of the interface in the formation and properties of SPP [4–7] and how it translates to LIPSS formation [8]. Nürnberger *et al.* also reported that SPP is one of two competing methods that cause the inhomogeneous electric field that ends up triggering LIPSS formation [9]. Interestingly, as mentioned above, we did not find LIPSS for the thicker films, which suggests that the other trigger mechanism discussed in that reference, *i.e.*, the excitation of a surface scattered wave in the surface of the thin film, did not intervene in our case.

In this chapter, we check the validity of this hypothesis, and we study the influence of roughness in LIPSS formation. To do so, we study the features of the SPPs that are excited by roughness in the thin film-substrate interface performing numerical simulations by the method described in Section 2.6 and comparing the results with the experimental results in Section 3.5. Besides, we try to generate LIPSS in polymer films deposited om a gold substrate with much larger roughness than the one studied in Section 3.5. In this way, we tried to ascertain the effect of roughness on the formation mechanism of LIPSS in our case, and whether it is similar to the effect of roughness on SPPs mentioned in Section 1.3. When a SPP is formed, the relevant properties for the formation of LIPSS are: (i) period, which will be the expected period of the

LIPSS as well, since it is the only spatial modulation of the electric field along the surface; (ii) penetration length, which gives a measure of how SPP can affect the distribution of the electric field on the film surface as compared to film thickness; and (iii) intensity, more precisely, the ratio to the intensity of the incident field which allows us to understand the importance of its contribution to the total field and whether it is enough to unleash the process of LIPSS formation. The results discussed in this chapter were published in [10].

4.1. Influence of the thickness of the thin films

Figure 4.1 shows the comparison between the theory described in Section 1.3 and our numerical simulations.

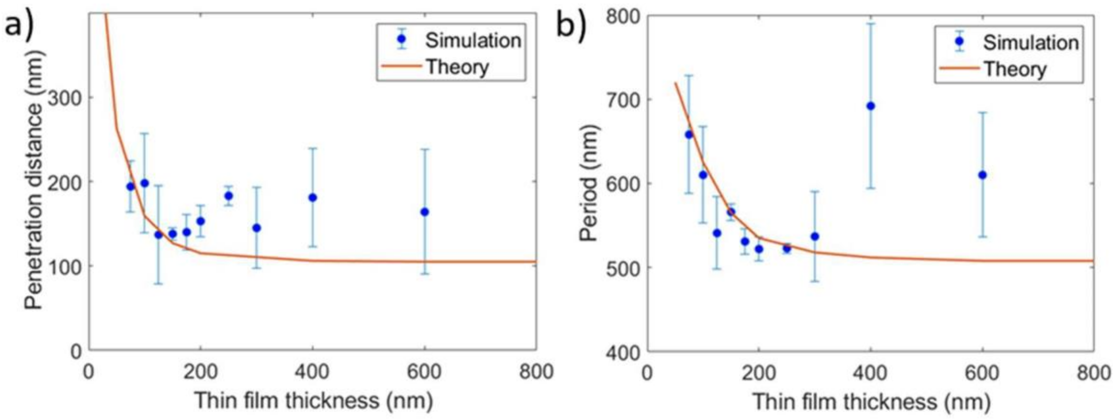

Figure 4.1. *Dependence of the a) penetration distance and b) period of the SPP with the thin film thickness for gold substrate roughness parameters* $R_{\mathrm{q}} = 2.8 \pm 0.1$ *nm and* $\sigma = 30$ *nm. Measurements taken from the simulations (blue) and theoretical results (red) are compared. The roughness parameters were chosen to be as close as possible to our gold substrate samples fabricated by sputtering.*

The results of the simulations for the SPP period and penetration length followed the theory for thicknesses up to approximately 360 nm. That is, both the SPP period and the penetration length became smaller the thicker the thin film. Above that value, the simulations did not match the results of the theoretical model. This abrupt discrepancy was due to the coexistence inside the thin film of SPPs with higher-order TM modes of light propagation that cannot be excited in thinner films [11]. Moreover, a film thickness larger than the penetration length prevents LIPSS formation as long as the SPP intensity on the surface would be unable to significantly modulate the electric field. We discarded the effect of high order modes since they could only be excited for films thicker than 360 nm while their penetration length was around 200 nm at most, so they could never reach the surface and change the electric field, and thus we considered they did not alter the formation of LIPSS.

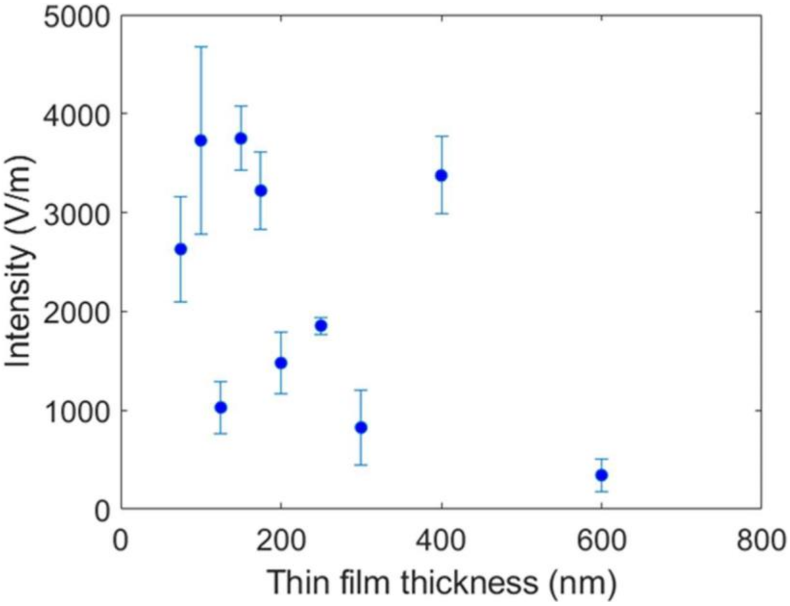

Figure 4.2*. Relation of the amplitude of the simulated SPP with the thin film thickness for gold substrate roughness parameters* $R_\mathrm{q} = 2.8 \pm 0.1$ *nm and* $\sigma = 30$ *nm. The roughness parameters were chosen to be as close as possible to our gold substrate samples fabricated by sputtering. The amplitude of the incident field was 2.1 ×* 10^4 *V/m.*

4.2. Influence of the roughness (R_q and σ) of the substrate

4.2.1. Experimental

In Chapter 3, we tried to generate LIPSS in samples with two metallic substrates. We were successful in the case of gold substrates but not in the steel ones. One possible explanation is that the roughness of the steel substrate was too high to allow for LIPSS formation to take place. Here we try to generate LIPSS in a sample with the high R_q gold substrate described in Section 2.2. If we are unable to generate LIPSS then that backs up the previous explanation.

We explored fluences from 4.4 to 17.8 mJ/cm^2 and pulses from 1000 to 100000 (from the appearance of surface modifications to the first signs of polymer ablation) finding that LIPSS did not form. Laser irradiation did induce changes in roughness though, it increased from R_q = 16 nm | σ = 820 nm to R_q = 54 nm | σ = 531 nm after irradiation with 10000 pulses at a fluence of 10.9 mJ/cm^2. We show the AFM measurements of these cases in Figure 4.3.

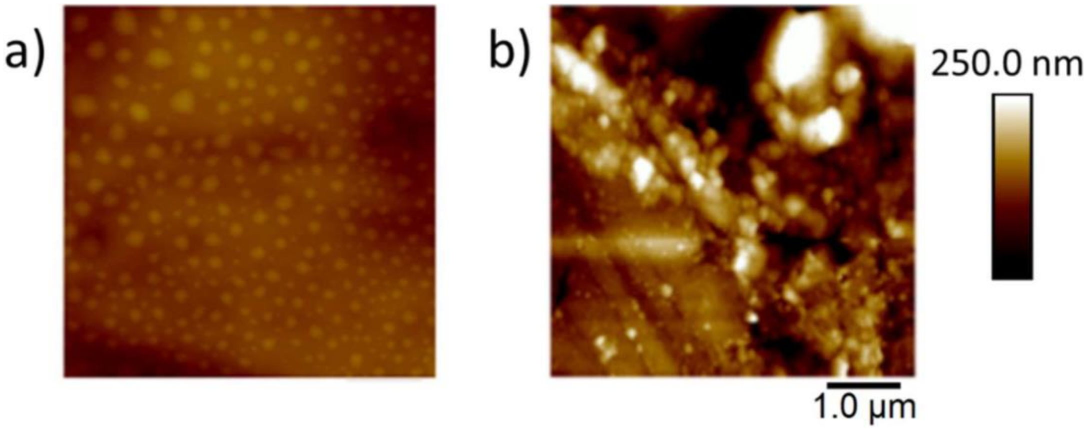

Figure 4.3. *AFM 5 x 5 µm^2 images of the sample with a 165 nm thick film on a high R_q substrate a) before and b) after irradiation with an energy which induced morphological changes.*

This dependence of LIPSS formation with the roughness of the substrate supports the hypothesis that the formation mechanism could be related to the SPP excited in the boundary between substrate and thin film. In the next subsection we will explore if our numerical simulations of the SPP can reproduce this result. We will also calculate intermediate cases to evaluate the influence of R_q and σ in the SPP field.

4.2.2. Simulations

In our simulations, the amplitude of the SPP increases with R_q, reaching a plateau above R_q = 20 nm (Figure 4.4). This increase in amplitude can be attributed to a higher excitation efficiency. Moreover, for R_q above 20 nm, the error became too large to determine a period. This means the SPP lost its periodicity. To sum up, the larger the R_q, the higher the coupling between the incident beam and the SPP, resulting in higher amplitude. However, for R_q values higher than a certain threshold, periodicity was destroyed. Although there was a formation of hot spots on the surface, due to excessive scattering induced by oversized roughness, they cannot propagate to generate a periodic field (SPP) [12]. The final effect was a local field enhancement dependent on the specific roughness profile of the substrate but without periodicity (Figure 4.5). This explains why we did not observe LIPSS formation for the sample with the higher R_q substrate, but we did observe an increase in its roughness after irradiation.

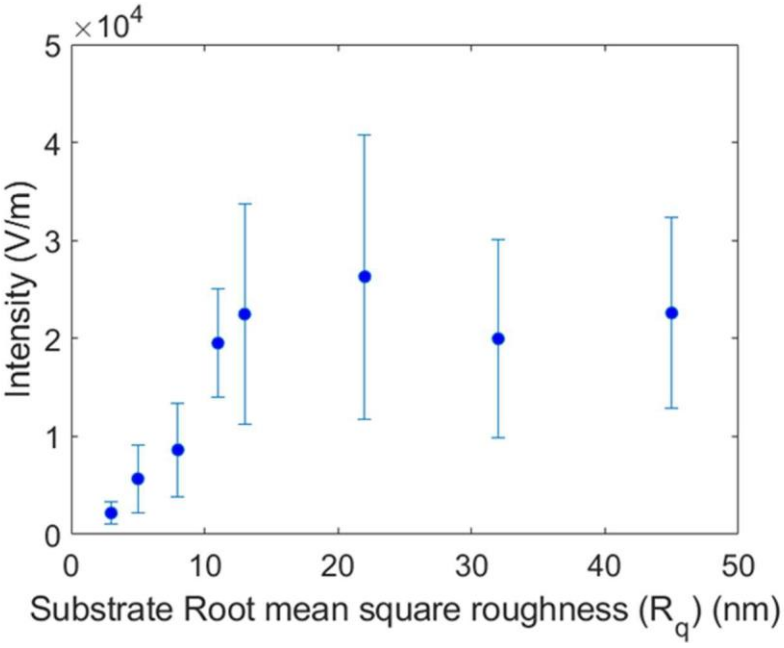

Figure 4.4. *Relation of the simulated amplitude of the generated SPP with the* R_q *of the substrate for a thin film thickness of 100 nm and* $\sigma = 30$ *nm. The amplitude of the incident field was 2.1 x* 10^4 *V/m.*

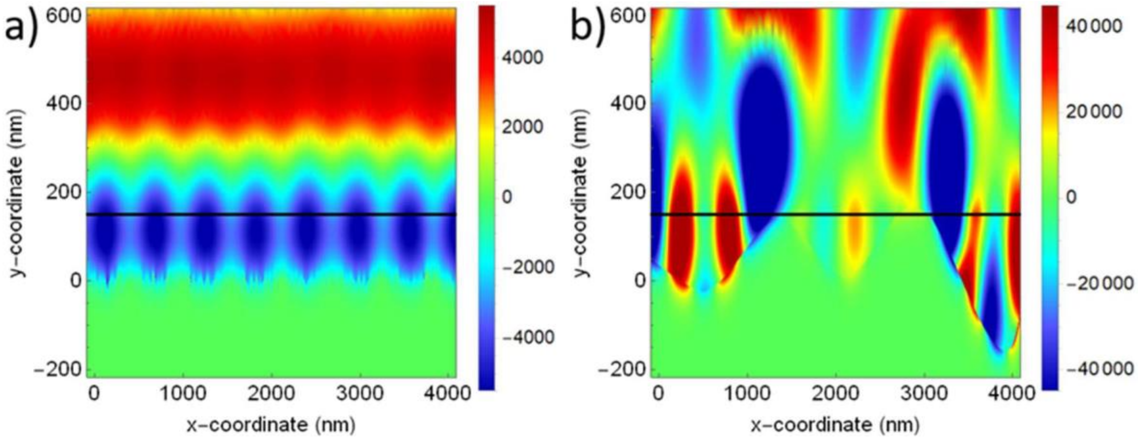

Figure 4.5. X *component of the electric field (V/m) for 150 nm thick thin films with roughness parameters a)* $R_\mathrm{q} = 2.8$ *nm,* $\sigma = 30$ *nm and b)* $R_\mathrm{q} = 70$ *nm,* $\sigma = 1600$ *nm. The parameters were chosen to mimic the experimental conditions of a thin film on a) the low* R_q *substrate and b) the high* R_q *substrate. The black line at* $y = 200$ *nm indicates the surface of the polymer. The mean line of the substrate-thin film boundary is located at* $y = 0$.

Another effect of roughness not considered by the theoretical models mentioned in Section 1.3 —which are valid for small roughness— is that if the average roughness is comparable to the film thickness and the penetration length of the SPP, at a point of the surface the real situation is that thickness might be much smaller or larger than the average thickness of the film. This implies that, for each point, the penetration length will be enough to reach the surface or not, depending on the local surface profile. Thus, even if we had a perfectly periodical SPP on the substrate-thin film interface, the electric field on the surface of the thin film, and therefore LIPSS formation, would strongly depend on the particular roughness profile and LIPSS would not appear anyhow.

According to eq. 1.17, the dependence of the wavevector with R_q is $\Delta K_\mathrm{SPP} = \gamma R_\mathrm{q}^2$, where γ is a quantity independent of R_q. In Figure 4.6, we have fitted γ by the minimum squares method for the period and penetration length, using their dependence with K_SPP in eq. 1.10, getting almost the same value, which indicates a good agreement between theory and simulations. For small changes in R_q, the period of the SPP diminishes with R_q as the theory predicts, although, above $R_\mathrm{q} = 20$ nm, the definition of a period becomes questionable as far as SPP scattering can break its periodicity.

As for the penetration distance, although the theory states that it should diminish with R_q, and the fitted curve suggests it behaves in this way, the statistical error is so high that stating a definite behavior is risky (Figure 4.6).

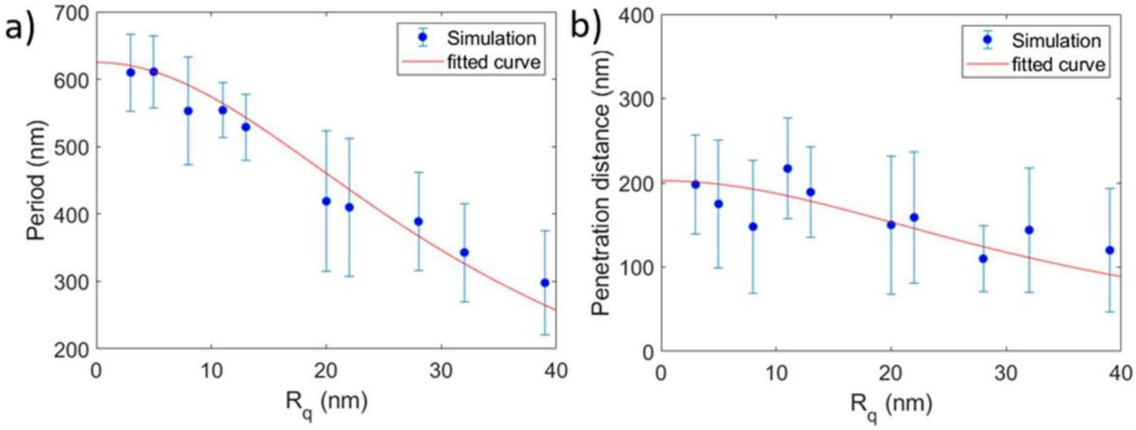

Figure 4.6. *Relation of the SPP a) period and b) penetration distance with the* R_q *of the substrate for a thin film thickness of 100 nm and* $\sigma = 30$ *nm. We show in blue the measurements taken from the simulations and in orange the minimum squares fitted curve to the theory.*

Regarding the effect of the correlation length, as it can be seen in Figure 4.7, it can result in the generation of hotspots smaller than the SPP wavelength if it is much smaller than the SPP period. These hotspots may be caused by the generation of localized plasmons in the nanobumps and nanoholes of the surface. If this is the case, the thin film is not thick enough to rearrange those hotspots and can induce the destruction of the SPP periodicity or, in less severe cases, the creation of a substructure in the SPP wave, which will depend on the specific substrate roughness.

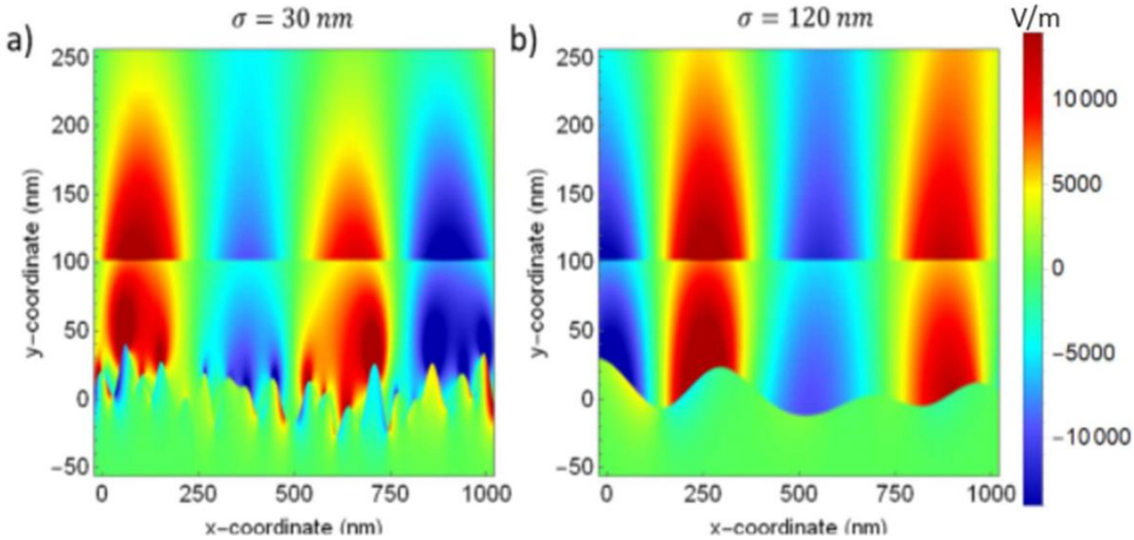

Figure 4.7. *Simulated Y component of the electric field (V/m) for a thin film 100 nm thick and substrate roughness* $R_{\mathrm{q}} = 13$ *nm with a)* $\sigma = 30$ *nm and b)* $\sigma = 120$ *nm. The surface of the thin film is at* $y = 100$ *nm and the average height of the substrate-thin film boundary is at* $y = 0$.

4.3. Conclusions

We have performed numerical simulations of the influence of the substrate roughness and film thickness on the formation of LIPSS in PET films deposited on gold with a near-infrared ultrashort pulsed laser and compared them with experimental results.

When LIPSS did not appear experimentally, the simulations allowed to understand why: (i) for the gold substrate with high R_{q}, we measure such a large dispersion in the simulated period of SPP that we should not be talking about periodic structures; and (ii) for the thickest films, the penetration distance of the SPP is much smaller than the film thickness, so the coupling with the electric field at the film surface is negligible. We observe the same tendencies in the experimental period of LIPSS and the period of the SPP measured in the simulations.

Our simulations are not only coherent with the theoretical models in their application range (small roughness and film thickness), but also allow us to understand qualitatively the behavior of SPP out of that range. They are able to reproduce the general tendency of the experimental results and predict the range of substrate roughness and thin film thickness at which LIPSS form.

Besides, both the experiments and simulations agree with the hypothesis that for LIPSS in thin films of a non-absorbing polymer deposited on a metal, the inhomogeneous electric field that triggers the mechanism of LIPSS formation is the SPP generated in the thin film-substrate interface.

4.4. References

[1] C. Chen, Z. Liu, C. Cai, Z.M. Qi, Facile fabrication of nanoporous gold films for surface plasmon resonance (SPR) sensing and SPR-based SERS, Journal of Material Chemistry C 9 (2021) 6815–6822. https://doi.org/10.1039/D1TC01046H.

[2] Y. Wu, X. Wang, X. Wen, J. Zhu, X. Bai, T. Jia, H. Yang, L. Zhang, Y. Qi, Surface-enhanced Raman scattering based on hybrid surface plasmon excited by Au nanodisk and Au film coupling structure, Physics Letters A 384 (2020) 126544. https://doi.org/10.1016/J.PHYSLETA.2020.126544.

[3] Z. Fan, Surface plasmon resonance refractive index sensor based on photonic crystal fiber covering nano-ring gold film, Optical Fiber Technology 50 (2019) 194–199. https://doi.org/10.1016/J.YOFTE.2019.03.018.

[4] E. Fontana, R.H. Pantell, Characterization of multilayer rough surfaces by use of surface-plasmon spectroscopy, Physical Review B 37 (1988) 3164–3182. https://doi.org/10.1103/PhysRevB.37.3164.

[5] F. Toigo, A. Marvin, V. Celli, N.R. Hill, Optical properties of rough surfaces: General theory and the small roughness limit, Physical Review B 15 (1977) 5618–5626. https://doi.org/10.1103/PhysRevB.15.5618.

[6] S. Schröder, A. Duparré, L. Coriand, A. Tünnermann, D.H. Penalver, J.E. Harvey, Modeling of light scattering in different regimes of surface roughness, Optics Express 19 (2011) 9820. https://doi.org/10.1364/OE.19.009820.

[7] K. Arya, Z.B. Su, J.L. Birman, Localization of the Surface Plasmon Polariton Caused by Random Roughness and its Role in Surface-Enhanced Optical Phenomena, Physical Review Letters 54 (1985). https://doi.org/10.1103/PhysRevLett.54.1559.

[8] Y. Fuentes-Edfuf, J.A. Sánchez-Gil, C. Florian, V. Giannini, J. Solis, J. Siegel, Surface Plasmon Polaritons on Rough Metal Surfaces: Role in the Formation of Laser-Induced Periodic Surface Structures, ACS Omega 4 (2019) 6939–6946. https://doi.org/10.1021/acsomega.9b00546.

[9] P. Nürnberger, H.M. Reinhardt, H.C. Kim, E. Pfeifer, M. Kroll, S. Müller, F. Yang, N.A. Hampp, Orthogonally superimposed laser-induced periodic surface structures (LIPSS) upon nanosecond laser pulse irradiation of SiO 2 /Si layered systems, Applied Surface Science 425 (2017) 682–688. https://doi.org/10.1016/j.apsusc.2017.06.316.

[10] J. Prada-Rodrigo, R.I. Rodríguez-Beltrán, T.A. Ezquerra, P. Moreno, E. Rebollar, Influence of film thickness and substrate roughness on the formation of laser induced periodic surface structures

in poly(ethylene terephthalate) films deposited over gold substrates, Optics & Laser Technology 159 (2023) 109007. https://doi.org/10.1016/J.OPTLASTEC.2022.109007.

[11] Z. Schlesinger, A.J. Sievers, ir surface-plasmon attenuation coefficients for Ge-coated Ag and Au metals, Physical Review B 26 (1982) 6444–6454. https://doi.org/10.1103/PhysRevB.26.6444.

[12] A. v. Zayats, I.I. Smolyaninov, A.A. Maradudin, Nano-optics of surface plasmon polaritons, Physics Reports 408 (2005) 131–314. https://doi.org/10.1016/J.PHYSREP.2004.11.001.

Chapter 5

LIPSS in the nanocomposite PTT-WS$_2$ with fs Gaussian pulses

Chapters 3 and 4 were focused on the formation mechanism of LIPSS. From this chapter onwards, we change our focus to LIPSS capabilities to change the properties of the samples. In Section 1.1, we explained the interest of nanocomposites as a way of improving the properties of polymers using nanomaterials as additives in a very small percentage of the material composition. Besides, in Section 1.2, we discussed the advantages of nanostructuring polymers and, in Section 1.3, we presented LIPSS as a suitable technique to obtain surface nanostructured materials.

In this chapter, we study the formation of LIPSS in PTT-WS$_2$, a nanocomposite described in Section 2.1, and we compare the results with LIPSS formed on the surface of PTT. We systematically irradiate samples of both materials with linearly polarized Gaussian fs UV pulses, using the set-up described in Section 2.3, and study the change in the topography of the samples as a function of the laser fluence and the number of pulses used. We also characterize the wettability and surface energy, as well as micromechanical properties of both materials, before and after irradiation, by the methods described in Section 2.4.

The results of this study were published in [1].

5.1. Topography

We have successfully produced LIPSS in a narrow fluence range, from 15.9 to 31.3 mJ/cm^2 for PTT, and from 19.1 to 33.9 mJ/cm^2 for PTT-WS$_2$. In both materials, LIPSS formed parallel to the laser polarization with a period close to the wavelength of the laser. The fluence range where LIPSS appeared was below the ablation range in both materials. To prove it, we measured the topography image of the limit between a non-irradiated and an irradiated area (Figure 5.1) with

AFM. In this image, we notice how the peaks and valleys of the structures lie, respectively, above and below the original surface.

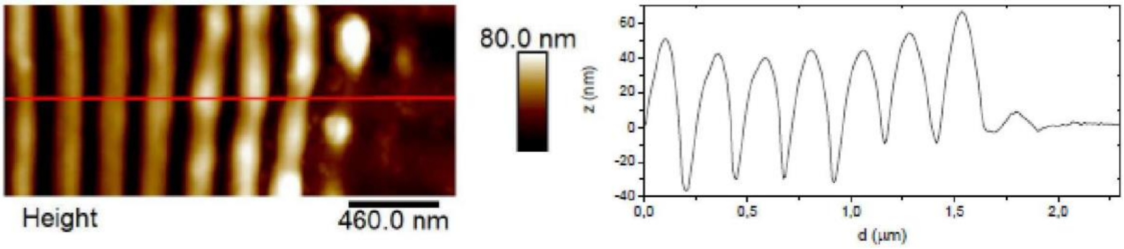

Figure 5.1. *AFM image and corresponding profile at the boundary of an irradiated area of PTT with 10000 pulses at 16.9 mJ/cm^2.*

Figures 5.2 and 5.3 display subsets of AFM measurements which are representative of the evolution of the topography of the samples as we increased the fluence and the number of pulses respectively. The initial samples had low roughness —PTT R_q = 3 nm, PTT-WS$_2$ R_q = 4 nm— and, when we irradiated them with barely enough energy to trigger LIPSS formation, LIPSS of small length and depth started appearing parallel to the laser polarization with a period close to the wavelength of the laser, which became longer and deeper as we increased the energy deposited until we reached a certain threshold where LIPSS started losing periodicity and became disordered structures.

From the difference in the ranges of fluences and number of pulses which led to LIPSS formation, we concluded that the presence of the nanoadditive increased the energy density needed to trigger LIPSS formation. Since we knew that T_g is the same for both samples, as shown in Section 2.1, this could be caused by the higher thermal dissipation of PTT-WS$_2$ —from $9.6 \cdot 10^{-7}$ m^{2}s^{-1} in PTT to $10.6 \cdot 10^{-7}$ m^{2}s^{-1} in PTT-WS$_2$— or its higher crystallization percentage —from 30.1% in PTT to 32.1% in PTT-WS$_2$. The thermal dissipation affects the LIPSS formation threshold, because the higher it is, the less efficient the laser heating, and, therefore, the more fluence and pulses are necessary to heat the sample. Regarding crystallization percentage, as explained in Section 1.1, crystallized polymers need to reach a temperature (T_m), which is much higher than the one amorphous polymers need (T_g) to be able to flow and form LIPSS, so an increase in crystallinity implies an increase in the temperature needed for LIPSS formation, and thus, more fluence and pulses are needed to reach it.

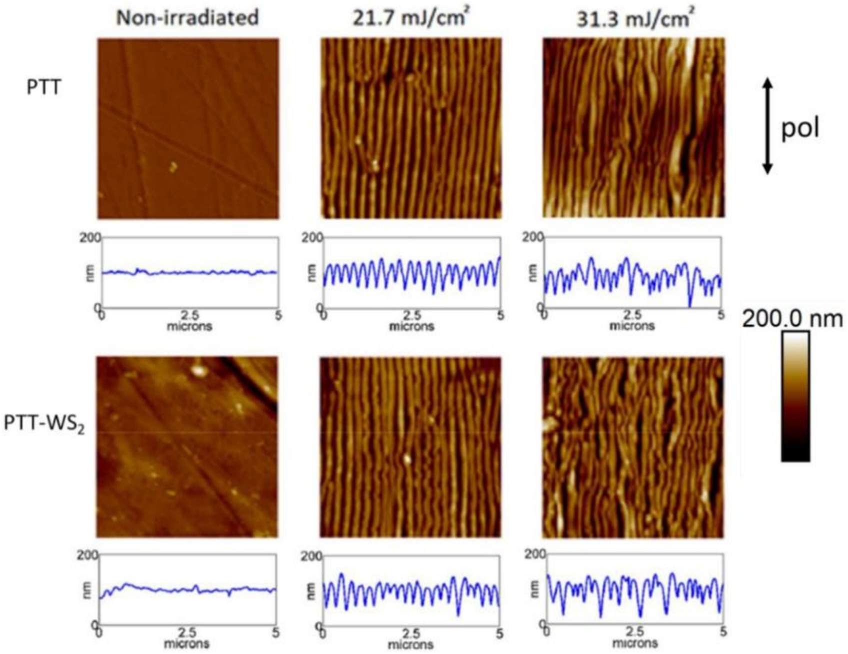

Figure 5.2. *AFM images (5 × 5 µm^2) and height profiles over five-micron horizontal lines of PTT (upper row) and PTT-WS$_2$ (lower row) samples after irradiation with 10000 pulses and increasing fluences. The laser polarization direction is represented by the double-sided black arrow.*

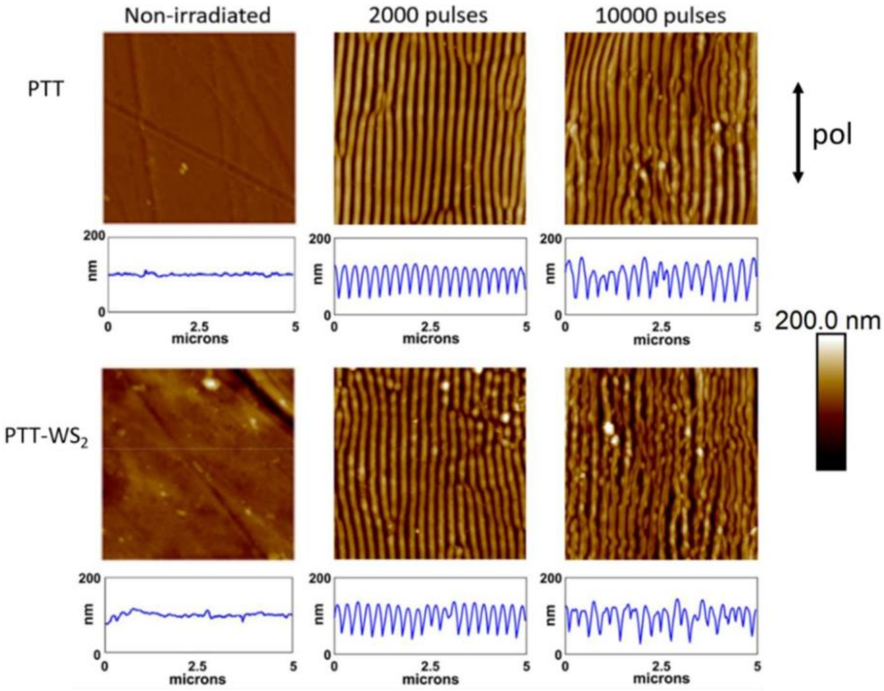

Figure 5.3. *AFM images (5 × 5 µm^2) and height profiles over five-micron horizontal lines of PTT (upper row) and PTT-WS$_2$ (lower row) samples after irradiation with increasing number of pulses at a fluence of 26.9 mJ/cm^2. The laser polarization direction is represented by the double-sided black arrow.*

For the determination of the period and depth of the structures, we acquired three 5 × 5 μm^2 AFM images in different regions of the spots. We made horizontal cuts to measure the period and height of the structures. We performed fourteen measurements per image and gave the result as their average and the indetermination as their statistical deviation. Employing this method, we got the dependence of the period and depth of LIPSS on the number of pulses and fluence. We display a representative sample of these measurements in Figures 5.4 and 5.5.

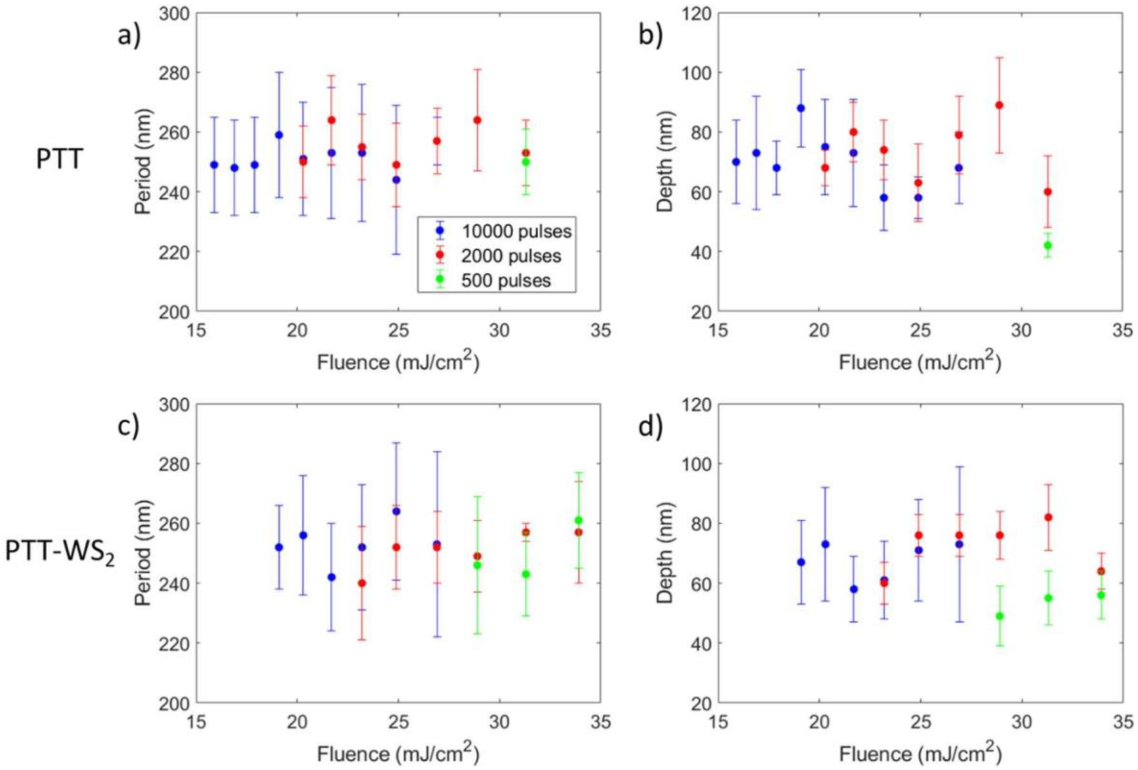

Figure 5.4. *Dependence of LIPSS period in a) PTT and c) PTT-WS$_2$ and depth in b) PTT and d) PTT-WS$_2$ on the irradiation fluence for different number of pulses, as labelled.*

For PTT, LIPSS formed in a fluence range from 15.9 to 31.3 mJ/cm^2, and from 19.1 to 33.9 mJ/cm^2 for PTT-WS$_2$. For both materials, the period of the structures remained almost constant with fluence and number of pulses, close to the wavelength of the laser. Regarding the depth of the structures, there was no clear dependence with the fluence, but it grew with the number of pulses until it reached a plateau for most of the fluences studied.

This dependence of the characteristics of the structures with the fluence and number of pulses has already been reported for other polymeric materials [2] and has been explained according to the mechanisms of LIPSS formation in polymers. As previously discussed, the polymer temperature must increase above its T_g so segmental chain dynamics are allowed. When increasing the fluence of the laser pulses, the maximum depth of the sample that is heated above T_g increases, and so, the depth of the structures grows. If we keep increasing the fluence, it will get to a point where the whole surface of the polymer can flow and LIPSS stop forming. LIPSS dependence with the number of pulses is similar to their behavior with the fluence. This is a consequence of the well-known importance of the feedback and incubation mechanisms present in the formation of LIPSS [3].

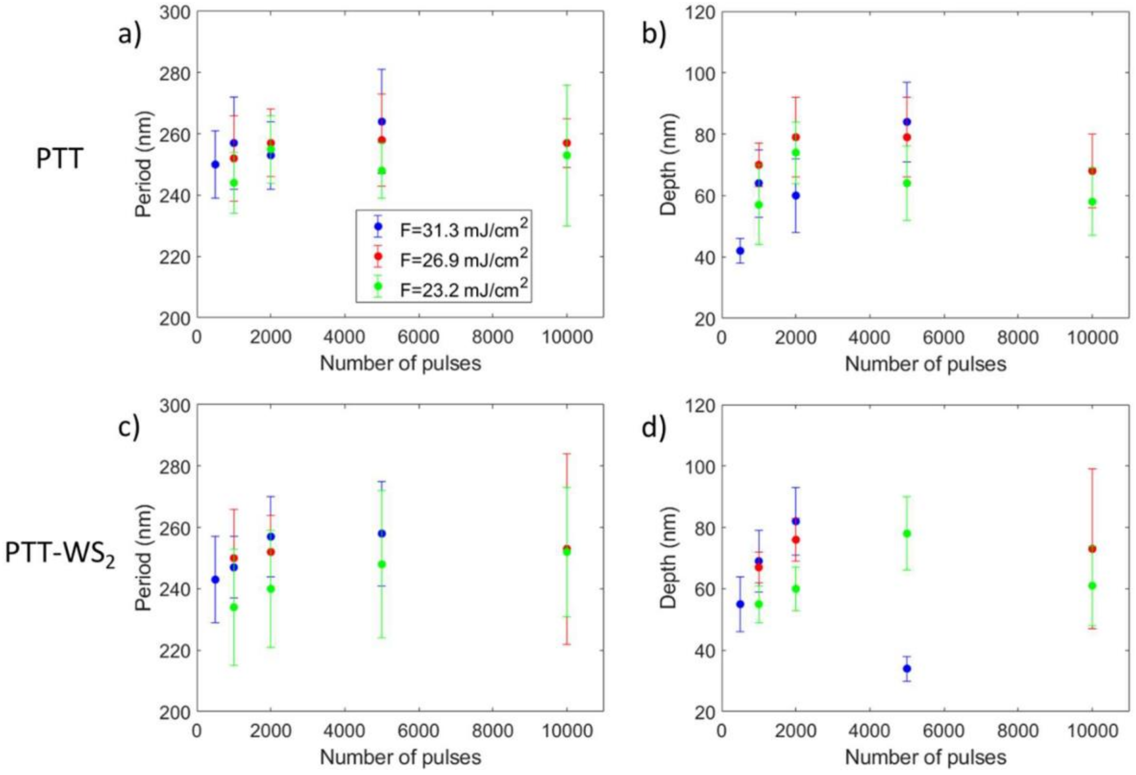

Figure 5.5. *Dependence of LIPSS period in a) PTT and c) PTT-WS$_2$ and depth in b) PTT and d) PTT-WS$_2$ on the number of pulses for different irradiation fluences, as labelled.*

5.2. Wettability and surface energy

Figure 5.6 shows the measurement of contact angle for both raw and nanostructured PTT and PTT-WS$_2$ and the three test liquids (deionized water, glycerol and paraffin oil). We chose one of the samples, with the irradiation conditions that resulted in more regular LIPSS —5000 pulses at a fluence of 20.3 mJ/cm^2—, as the nanostructured sample. We took five measurements for each sample-liquid pair and show the average results and their statistical deviation in Table 5.1.

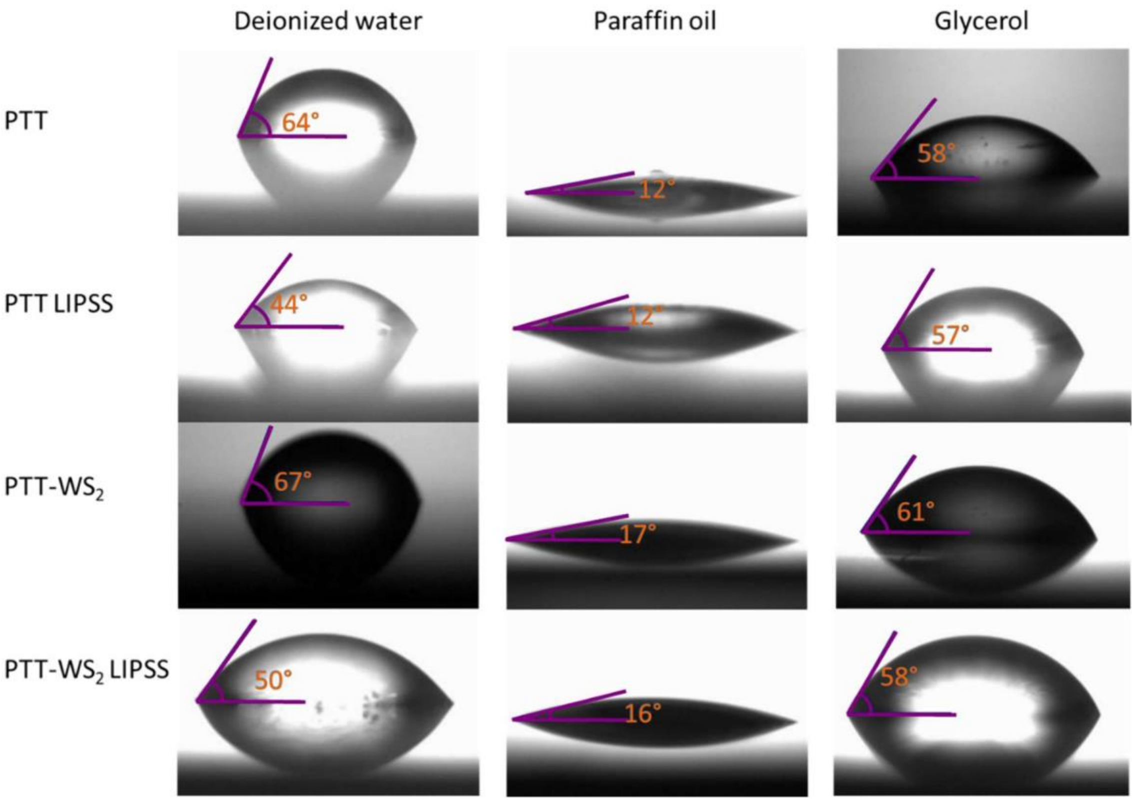

Figure 5.6. *Measurement of the contact angles of the three sample liquids in our raw samples and after being irradiated with 5000 pulses at a fluence of 20.3 mJ/cm^2.*

Table 5.1. *Average contact angles measured by means of the sessile drop technique with deionized water, glycerol and paraffin oil for non-irradiated samples and samples irradiated with 5000 pulses and a fluence of 20.3 mJ/cm^2.*

Sample	Deionized water	Glycerol	Paraffin Oil
PTT	64±1	58±5	12±1
PTT LIPSS	44±4	57±3	12±4
PTT-WS$_2$	67±3	61±5	17±5
PTT-WS$_2$ LIPSS	50±4	58±3	16±2

Both PTT and PTT-WS$_2$ were found to be hydrophilic before and after LIPSS formation on their surfaces. There were no significant differences between both materials, which could be expected given the percentage of additive was very small. For irradiated samples, the water CA decreased, which indicates that the materials became more hydrophilic after irradiation. This could be explained assuming a homogeneous wetting model for water, Wenzel's model [4]. This model assumes that resulting from viscosity and chemical interactions, the contact between water and the surface of the sample is not altered by the presence of air. It explains the variation of the contact angle as a function of a parameter called r. The r parameter is given by the relation between the total surface of solid in the solid-liquid interface, and the projection of the total surface of solid in the interface:

$$r = \frac{\text{o al Su faee}}{\text{p ojee ed Su faee}} \tag{5.1}$$

$$cos\theta^* = r\ cos\theta \tag{5.2}$$

Therefore, since r increases after LIPSS formation, if the original sample is hydrophilic, it will become more hydrophilic, and if it is hydrophobic, it will become more hydrophobic. However, for glycerol and paraffin oil, there are no significant changes in CA values after irradiation.

As explained in Section 2.5, we calculated the surface energies following OWRK's model and Van Oss, Chaudhury and Good's model. They are presented in Tables 5.2 and 5.3 respectively.

Table 5.2. *Values of the polar (γ^p), dispersive (γ^d) and total (γ^{TOT}) contributions to the surface energy for non-irradiated samples and samples irradiated with 5000 pulses and a fluence of 20.3 mJ/cm^2. Calculated according to the OWRK's model (mJ/m^2).*

Sample	γ^p	γ^d	γ^{TOT}
PTT	14±1	27±1	41±1
PTT LIPSS	27±3	23±3	50±4
PTT-WS$_2$	13±1	26±1	39±1
PTT-WS$_2$ LIPSS	23±2	24±2	47±3

Table 5.3. *Values of the polar positive (γ^+), polar negative (γ^-), dispersive (γ^d) and total (γ^{TOT}) surface energy for non-irradiated samples and samples irradiated with 5000 pulses and a fluence of 20.3 mJ/cm^2 according to the van Oss, Chaudhury and Good's model (mJ/m^2).*

Sample	γ^+	γ^-	γ^p	γ^d	γ^{TOT}
PTT	1.59±0.07	17±1	10.5±0.5	28.2±0.2	38.7±0.5
PTT LIPSS	0.40±0.04	47±2	8.7±0.5	28.2±0.4	36.7±0.7
PTT-WS$_2$	1.32±0.08	17±3	9±1	27.6±0.7	37±1
PTT-WS$_2$ LIPSS	0.57±0.05	39±5	9.4±0.7	27.9±0.3	37.3±0.8

The values obtained for the surface energy components differed depending on the method used for their calculation, mainly γ^{p}. In OWRK's model, for both materials, γ^{p} increased when the sample was irradiated while γ^{d} slightly decreased, which adds up to a small increment of γ^{TOT}. Meanwhile, in Van Oss, Chaudhury and Good's model, for all the samples, γ^{+} was much smaller than γ^{-}. This difference was even more prominent for irradiated samples, given the increase in γ^{-} and the decrease in γ^{+} after irradiation. Since γ^{d} remained constant, γ^{TOT} changed directly in relation to the changes in the polar components. There were no significant changes in the total surface energy of both samples. The discrepancies can be attributed to the unreliability of OWRK's model to calculate γ^{p} when hydrogen bridges come into play (see Fowkes [5] and Panzer [6]) as it was the case when water was our test liquid in the contact angle measurements.

In summary, the total surface energy did not change significantly from non-irradiated to irradiated samples. However, there was an important increase in the negative polar component of the irradiated samples. This cannot be exclusively explained on the basis of a topography change, though. It suggests the formation of polar hydrophilic species caused by a reaction with the oxygen in the air, catalyzed by the ionization and high temperature on the surface of the sample while the irradiation took place.

Micro-Raman spectroscopy analysis of the irradiated films is displayed in Figure 5.7.

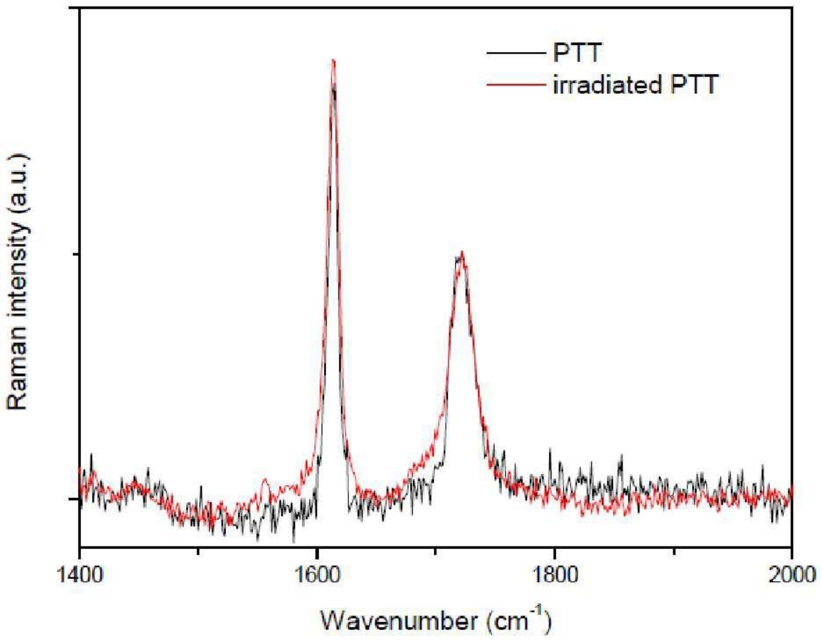

Figure 5.7. *Micro-Raman spectra of PTT before and after irradiation with 5000 pulses at a fluence of 20.3 mJ/cm*^{2}.

This analysis revealed a slight broadening of the band corresponding to the stretching vibration of the C=O bond (band at around 1722 cm^{-1}), which is an indication of new carboxylic acid group formation. Similar results have been reported previously for the case of PET [7,8].

5.3. Micromechanical properties

As discussed in Section 2.4, to obtain the elastic modulus of the samples we need to know their Poisson ratio (eq. 2.4). In these cases, ν_{Sample} was fixed to a constant value of 0.3, since we did not find any reason to think that the nanocomposite would have a different Poisson ratio than PTT, as the nanotubes were randomly oriented.

Figures 5.8 and 5.9 show the mechanical properties of PTT and PTT-WS$_2$ before and after irradiation.

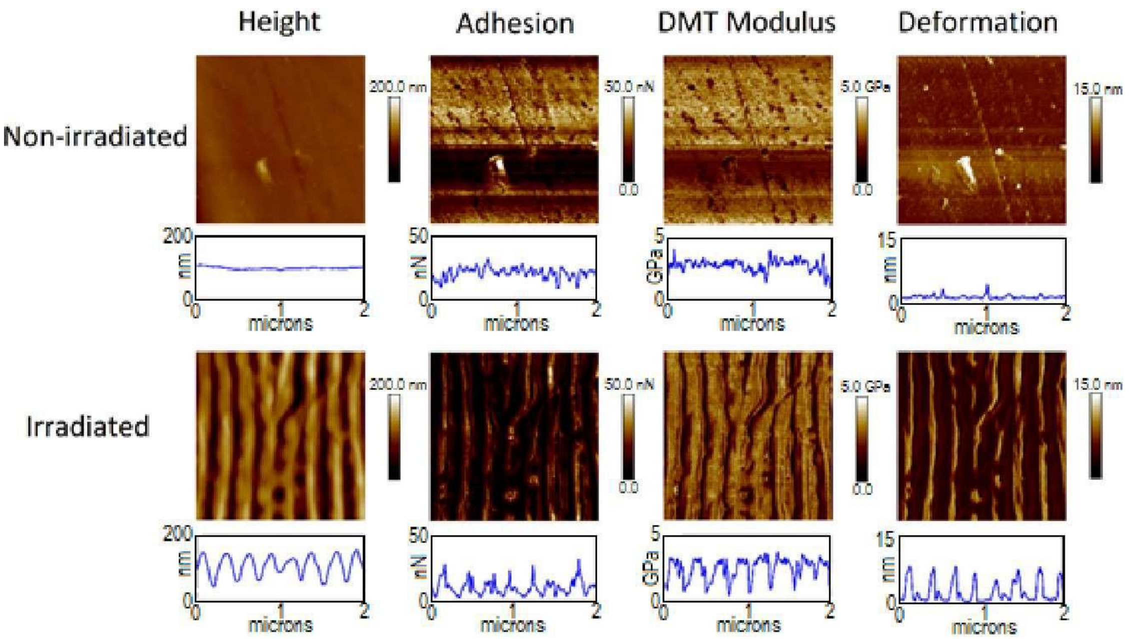

Figure 5.8. *PF-QNM measurements of PTT surfaces before and after irradiation with 5000 pulses at a fluence of 20.3 mJ/cm^2. (2 × 2 μm^2 images and their corresponding profiles over a 2 μm horizontal line).*

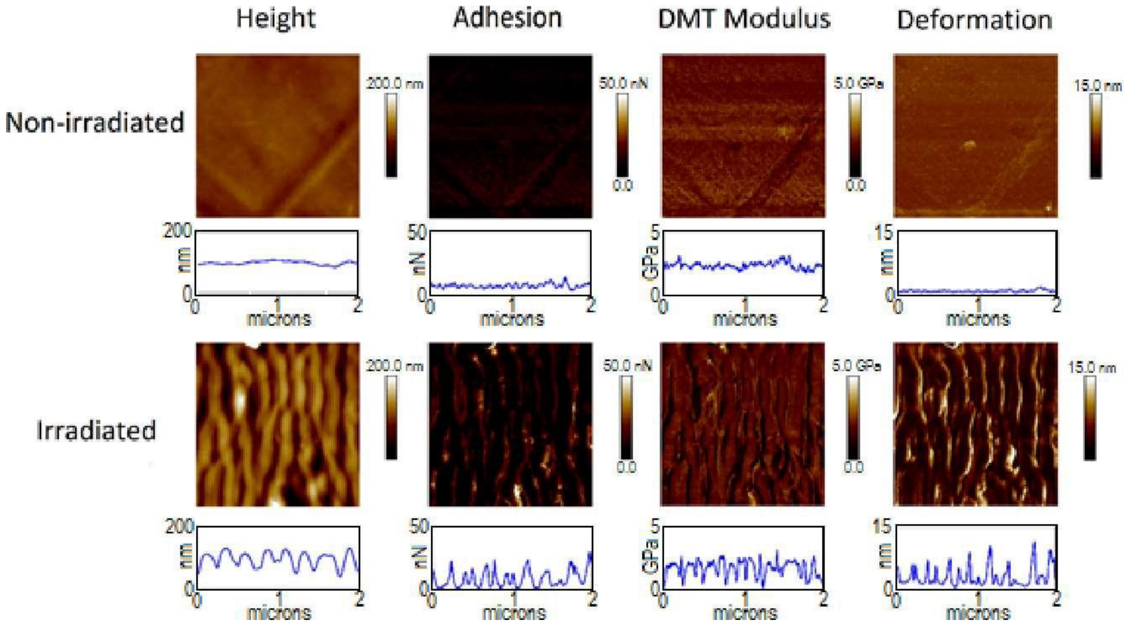

Figure 5.9. *PF-QNM measurements of PTT-WS$_2$ surfaces before and after irradiation with 5000 pulses at a fluence of 20.3 mJ/cm^2. (2 × 2 μm^2 images and their corresponding profiles over a 2 μm horizontal line).*

The non-irradiated samples presented a very small roughness, as measured with AFM, and their adhesion forces, Young's Modulus (where eq. 2.3 has already been applied to the values in the images) and deformation (shown in Table 5.4) were homogenous in the whole image. The irradiated samples exhibited values of the mechanical properties that, nonetheless, were topographically dependent, showing nonhomogeneous values across the nanostructured surface. This effect is not due to the actual properties of the sample, but it is an effect derived from the way we were measuring them. When we adjusted the radius of the tip, as it was explained in Section 2.4, it was not considered that the sample surface might be curved, so the measurements gave only real values for plane surfaces. Therefore, reliable values of the mechanical properties must be taken from the tops of the hills and the bottom of the valleys of the LIPSS, as in these zones the contact between the tip and the material could be considered equivalent to the normal contact of the tip with a planar surface, in contrast with the contact with the walls of the nanostructures. Following this criterion, we obtained the results in Table 5.4.

The measurements for the non-irradiated samples agreed with previous characterizations [9]. For the irradiated samples, we found that there were no significant changes in the values of the elastic modulus, but the adhesion force decreased by a factor of approximately four. The decrease of adhesion force after surface nanostructuring has already been reported in other polymers such as poly(methyl methacrylate) (PMMA) and polyurethane acrylate (MINS) after soft lithography [10], and PET after plasma etching [11]. However, that decrease was attributed to a smaller contact surface between the sample and the measuring device, as a result of the new surface morphology. Since in our experiment, the spatial resolution of our measuring technique —PF-QNM— was smaller than the size of the LIPSS, this decrease in adhesion cannot be explained on the same basis. Together with the magnitude of the contact surface between tip and sample, according to Dupré's equation [12], the adhesion force between two surfaces is given by their respective surface and interaction energies. As long as the tip is always the same standardized one, a change in adhesion implies modifications either on the total surface energy of the sample or on its interaction with the tip. From the contact angle measurements, we knew that although there is no appreciable change in the total surface energy, there is an important decrease in the polar positive component as well as an important increase in the polar negative component. Although a combination of several intermolecular interactions and phenomena influencing adhesion should be considered —factors such as van der Waals or dipole-induced forces, electrostatic forces, H-bonding and capillary forces— electrostatic and H-bonding interactions represent a major part of the molecular forces acting between both contact surfaces. Considering that the negative polar component of the surface increased after irradiation and that silicon surface might be easily negatively charged, electrostatic repulsion may play the most relevant role in this case.

Table 5.4. *Measurements of the deformation, adhesion forces, and Young's Modulus (E) obtained with PF-QNM for non-irradiated samples and samples irradiated with 5000 pulses and a fluence of 20.3 mJ/cm^2.*

Sample	E (GPa)	Adhesion (nN)	Deformation (nm)
Non-irradiated PTT	3.0±0.5	24.0±8.0	2.1±0.8
Irradiated PTT	3.3±0.2	6.8±1.3	0.5±0.2
Non-irradiated PTT-WS$_2$	2.4±0.2	9.0±2.0	1.3±0.3
Irradiated PTT-WS$_2$	2.3±0.2	2.2±0.7	2.1±0.4

Additionally, if we consider that the surface becomes more hydrophilic, low values of adhesion have been obtained before for –OH coated surfaces [13] and this was explained considering that high polarity of this tail group confers a high reactivity especially with contamination in air, and similar for –COOH groups. Furthermore, similar results to ours have been previously observed by repetitive UV laser irradiation of PMMA at fluences below ablation threshold and are related to the UV photomodification of the polymer [14].

5.4. Conclusions

We have induced LIPSS with UV femtosecond laser pulses in both PTT and PTT-WS_2 surfaces. In all cases, the nanostructures were parallel to the polarization of the incident laser. The period of the structures was around 260 nm, close to the laser wavelength (265 nm).

LIPSS emerged for fluences below the ablation threshold of the materials, from 15.9 to 31.3 mJ/cm^2 for PTT, and from 19.1 to 33.9 mJ/cm^2 for PTT-WS_2, conditioned by the number of pulses (500–10000). From this data, we can conclude that the presence of the nanoadditive leads to an increase of the energy density needed to trigger LIPSS formation. We explained this as the effect of the higher crystallization percentage and thermal dissipation of PTT-WS_2.

The behavior of LIPSS period and depth with the fluence and number of pulses was similar to that reported for other polymers and was explained turning to the formation mechanism of LIPSS in polymers and the importance of feedback and incubation in the generation of LIPSS.

We have studied the wettability and surface energy of the samples, finding that the former increased with the formation of LIPSS, whereas the total surface energy remained constant. However, its negative polar component increased heavily. This suggests the formation of polar hydrophilic species, caused by a reaction with the oxygen in the air, catalyzed by the ionization and high temperature of the surface of the sample while the irradiation took place. This theory was corroborated by micro-Raman spectroscopy that showed the formation of new carboxylic acid groups.

We characterized the topography and mechanical properties of the sample, finding that the formation of LIPSS did not change the Young's modulus remarkably, but it induced a decrease of the adhesion force in both materials by a factor of four. We attributed this effect to the change of surface chemistry, as it was also indicated by the contact angle measurements.

In conclusion, LIPSS appeared at slightly higher energies for the nanocomposite than for raw PTT but produced almost equal effects in both PTT and PTT-WS_2. Therefore, LIPSS surface nanostructuring can be used in this nanocomposite without any demerit. Hence, we can use LIPSS to easily change the surface properties of the nanocomposite, specifically the mechanical ones. Moreover, given the high control over the nanostructured area, we could create small zones with different nanostructures and thus, different surface properties.

5.5. References

[1] J. Prada-Rodrigo, R.I. Rodríguez-Beltrán, S. Paszkiewicz, A. Szymczyk, T.A. Ezquerra, P. Moreno, E. Rebollar, Laser-induced periodic surface structuring of poly(trimethylene terephthalate) films containing tungsten disulfide nanotubes, Polymers 12 (2020) 1090. https://doi.org/10.3390/POLYM12051090.

[2] E. Rebollar, S. Pérez, J.J. Hernández, I. Martín-Fabiani, D.R. Rueda, T.A. Ezquerra, M. Castillejo, Assessment and formation mechanism of laser-induced periodic surface structures on polymer spin-coated films in real and reciprocal space, Langmuir 27 (2011) 5596–5606. https://doi.org/10.1021/la200451c.

[3] J.F. Young, J.E. Sipe, H.M. Van Driel, Laser-induced periodic surface structure. III. Fluence regimes, the role of feedback, and details of the induced topography in germanium, Physical Review B 30 (1984) 2001–2015. https://doi.org/10.1103/PhysRevB.30.2001.

[4] R.N. Wenzel, Resistance of solid surfaces to wetting by water, Industrial and Engineering Chemistry. 28 (1936) 988–994. https://doi.org/10.1021/ie50320a024.

[5] F.M. Fowkes, Role of acid-base interfacial bonding in adhesion, Journal of Adhesion Science and Technology 1 (1987) 7–27. https://doi.org/10.1163/156856187X00049.

[6] J. Panzer, Components of solid surface free energy from wetting measurements, Journal of Colloid and Interface Science 44 (1973) 142–161. https://doi.org/10.1016/0021-9797(73)90201-4.

[7] E. Rebollar, S. Pérez, M. Hernández, C. Domingo, M. Martín, T.A. Ezquerra, J.P. García-Ruiz, M. Castillejo, Physicochemical modifications accompanying UV laser induced surface structures on poly(ethylene terephthalate) and their effect on adhesion of mesenchymal cells, Physical Chemistry Chemical Physics 16 (2014) 17551–17559. https://doi.org/10.1039/c4cp02434f.

[8] D. Knittel, E. Schollmeyer, Surface structuring of synthetic fibres by UV laser irradiation. Part III. Surface functionality changes resulting from excimer-laser irradiation, Polymer International 45 (1998) 103–109. https://doi.org/10.1002/(SICI)1097-0126(199801)45:1<103::AID-PI917>3.0.CO;2-2.

[9] S. Paszkiewicz, A. Szymczyk, I. Janowska, R. Jedrzejewski, A. Linares, T.A. Ezquerra, H.D. Wagner, R. Tenne, Z. Rosłaniec, Comparative study on the properties of poly(trimethylene terephthalate) -based nanocomposites containing multi-walled carbon (MWCNT) and tungsten disulfide (INT-WS2) nanotubes, Polymers for Advanced Technologies 28 (2017) 645–657. https://doi.org/10.1002/pat.3964.

[10] Z. Burton, B. Bhushan, Hydrophobicity, Adhesion, and Friction Properties of Nanopatterned Polymers and Scale Dependence for Micro- and Nanoelectromechanical Systems, Nano Letters 5 (2005) 1607–1613. https://doi.org/10.1021/nl050861b.

[11] E. Wohlfart, J.P. Fernández-Blázquez, E. Knoche, A. Bello, E. Pérez, E. Arzt, A. del Campo, Nanofibrillar Patterns by Plasma Etching: The Influence of Polymer Crystallinity and Orientation in Surface Morphology, Macromolecules 43 (2010) 9908–9917. https://doi.org/10.1021/ma101889s.

[12] A. Dupree, Theorie Mechanique de la Chaleur, Gauthier-Villars, Paris, 1869.

[13] S. Oras, S. Vlassov, M. Berholts, R. Lõhmus, K. Mougin, Tuning adhesion forces between functionalized gold colloidal nanoparticles and silicon AFM tips: role of ligands and capillary forces, Beilstein Journal of Nanotechnology 9 (2018) 660–670. https://doi.org/10.3762/bjnano.9.61.

[14] B. Hopp, T. Smausz, J. Kokavecz, N. Kresz, Z. Bor, S. Hild, O. Marti, Investigation of incubation in ArF excimer laser irradiated poly(methyl-methacrylate) using pulsed force mode atomic force microscopy, Journal of Applied Physics 96 (2004) 5548–5551. https://doi.org/10.1063/1.1803632.

Chapter 6

LIPSS generated by complex beams in PET and semiconductive organic materials

In the previous chapter, we switched from the more theoretical study of LIPSS done in Chapters 3 and 4 to a study that focused on the capability of LIPSS to change the properties of the samples. In this Chapter, we keep investigating this aspect of LIPSS. We do so by using vector beams and optical vortex beams to generate LIPSS with complex structures in PET. We also apply this method to a semiconductive polymer (P3HT) and an organic semiconductor ($PC_{71}BM$) that, as we mentioned in Section 2.1, are often used together in organic solar cells. We characterize the changes that LIPSS formation induces in their topography, conductivity, wettability and surface chemistry with the techniques described in Section 2.4 –AFM and confocal microscopy, C-AFM, sessile drop and micro-Raman spectroscopy, respectively.

6.1. LIPSS generated with femtosecond vector beams in PET

We used femtosecond vector beams at a wavelength of 515 nm —as explained in Section 2.3— to generate LIPSS in PET thin films of different thicknesses deposited on silicon, glass and low R_q gold substrates —described in Section 2.2. The repetition rate of the laser may be varied from 10 Hz to 3 kHz. Therefore, we adjusted the repetition rate to the number of pulses needed bearing in mind that the minimum aperture time of the mechanical shutter was 100 ms. Since the behavior of the samples was very similar for all the vector beam polarizations, we show only one of them.

6.1.1. PET on silicon substrates

We irradiated three samples at a repetition rate of 10 Hz, one with a 79±3 nm thick PET thin film, one with a 120±20 nm thick film and another one with a 441±14 nm thick film.

We irradiated the sample with the 79 nm film with 2 to 2000 pulses at fluences from 83 to 198 mJ/cm^2. In Figure 6.1, we show the evolution of the topography with the number of pulses in a region of a spot irradiated with a radial vector beam. LIPSS appeared parallel to the polarization of the laser after irradiation with 5 to 500 pulses at fluences from 102 to 198 mJ/cm^2. Since LIPSS are parallel to polarization, we observed vertical structures in this area. The raw sample had low roughness and after irradiation with a low number of pulses LIPSS started appearing. They increased in depth with the number of pulses but for a high enough number of pulses the periodicity was lost. This is an expected result which we have mentioned in previous chapters.

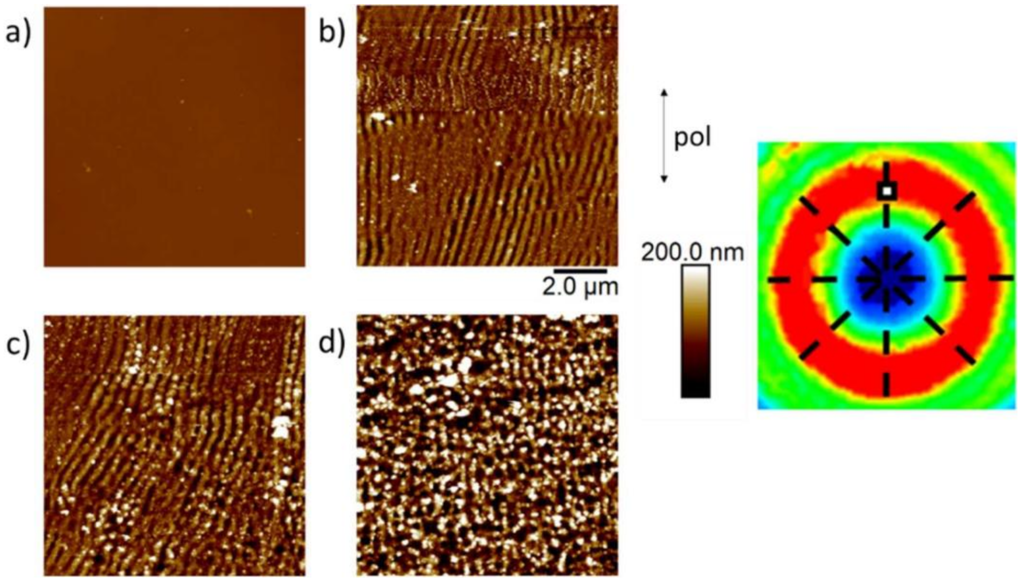

Figure 6.1. *10 x 10 µm^2 AFM image of a spot irradiated with a radial vector beam built from femtosecond laser pulses at 10 Hz and a fluence of 158 mJ/cm^2 in a 79 nm thick film of PET on the silicon substrate a) before irradiation, b) with 5 pulses, c) with 7 pulses, d) with 10 pulses. The scheme in the right side represents the kind of beam with the black lines showing the direction of the polarization and the white square the location where the measurements were carried out.*

In Figure 6.2, we show the dependence on the number of pulses of the features of the structures for three different fluences. In all cases, the period of the structures remained almost constant (~400 nm). As for their depth, it grew with the number of pulses for the two higher fluences (~100-200 nm), and it was much smaller (~3 nm) and almost constant with the number of pulses for the lowest fluence.

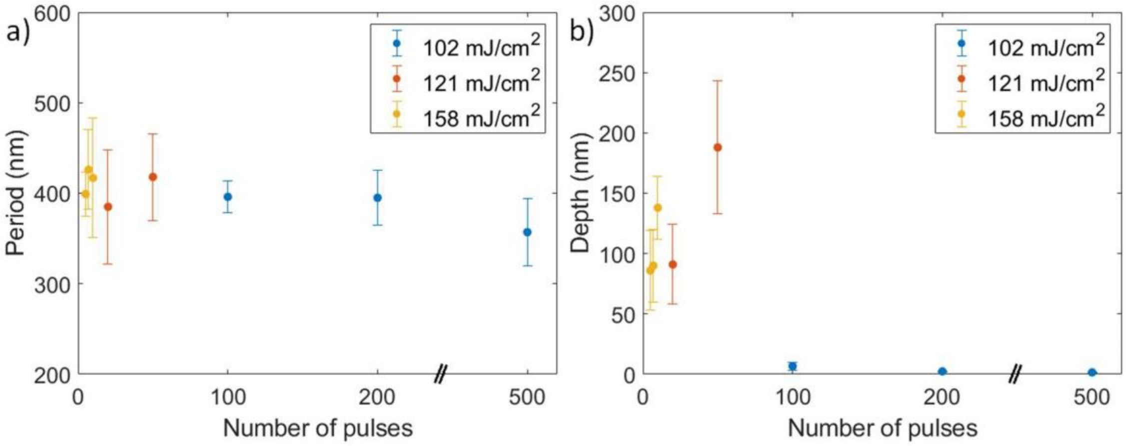

Figure 6.2. *Dependence with the number of pulses of the a) period and b) depth of LIPSS in a 79 nm thick PET film on a silicon substrate and fluences of 102 mJ/cm^2, 121 mJ/cm^2 and 158 mJ/cm^2.*

As for the sample with the 120 nm thick film, we irradiated it with the same number of pulses and fluences as the previous sample, but LIPSS appeared in a smaller formation range: from 5 to 10 pulses and fluences from 132 to 148 mJ/cm^2. The structures were parallel to the polarization of the laser, and they had a period of 450±40 nm and a depth of 140±40 nm. In Figure 6.3, we show the evolution of the topography with the number of pulses, which exhibited the same behavior as the previous sample.

Finally, we show in Figure 6.4 the evolution of the sample with the 441 nm thick thin film after irradiation with an increasing number of pulses. We irradiated the sample with the same number of pulses and fluences as the previous two, but we could only find LIPSS of short length after irradiating the sample at a fluence of 182 mJ/cm^2 with 5 pulses (Figure 6.4 b). They had a period of 480±50 nm and a depth of 80±20 nm. The fact that they appear only for one set of irradiation parameters and their small length makes us wonder whether LIPSS formation had been aided —in this particular case— by a surface defect like a scratch, as it has been known to happen in other samples described in the literature [4]. We would need to repeat these experiments in the future and collect more data to know what the reason of this weird behavior was.

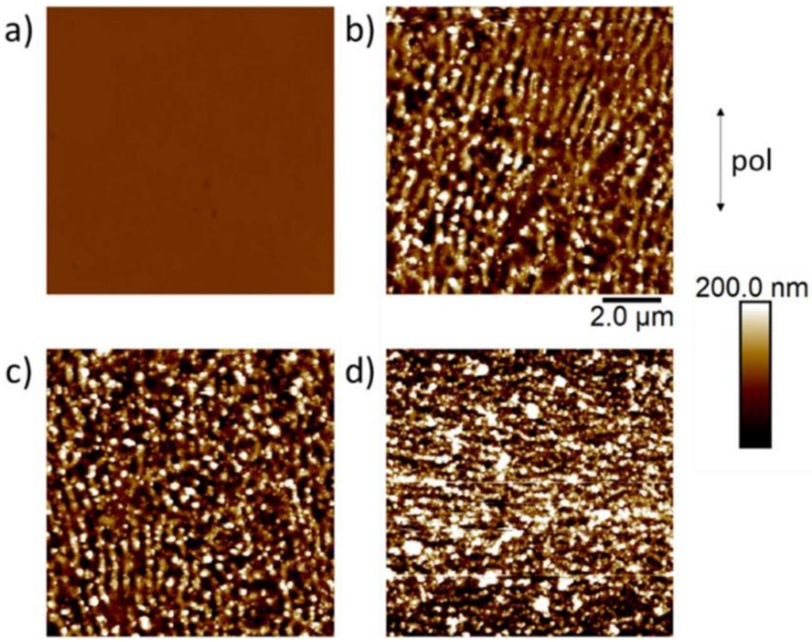

Figure 6.3. *10 x 10 µm^2 AFM image of a spot irradiated with a radial vector beam –the same region as of Figure 6.1– built from femtosecond laser pulses at 10 Hz and a fluence of 132 mJ/cm^2 in a 120 nm thick film of PET on a silicon substrate a) before irradiation, b) 7 pulses, c) 10 pulses, d) 20 pulses.*

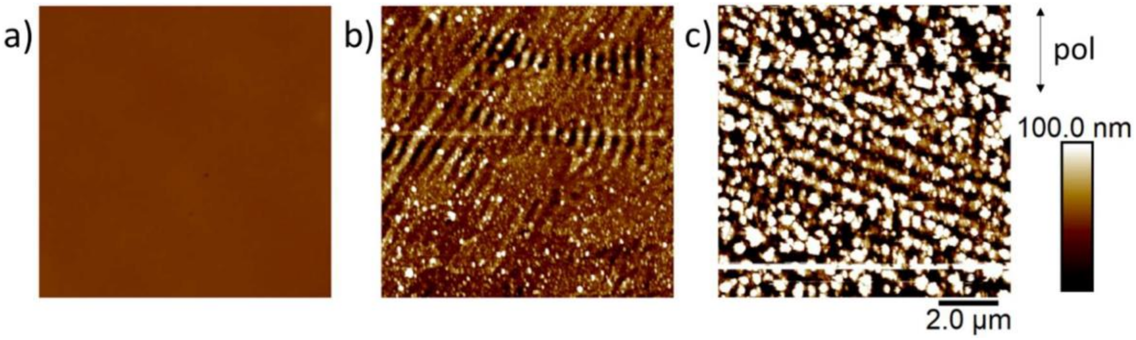

Figure 6.4. *10 x 10 µm^2 AFM image of a spot irradiated with a radial vector beam –the same area described in Figure 6.1– from a femtosecond laser at 10 Hz in a 441 nm thick film of PET on the silicon substrate at a fluence of 182 mJ/cm^2 a) before irradiation, b) with 5 pulses, c) with 10 pulses.*

In conclusion, LIPSS appeared parallel to the polarization of the laser in the three samples. Their formation range was the widest for the thinnest film and became narrower the thicker the film. Regarding their characteristics, the period of the structures grew from ∼400 nm in the thinner film to ∼480 nm in the thickest one. As for their depth, it diminished from ∼200 nm in the thinner film to ~80 nm in the thickest one. If we compare the formation range to the one obtained in Chapter 3 for the same kind of samples but irradiated with Gaussian pulses with a wavelength of 795 nm and a repetition rate of 5 kHz, we easily realize that LIPSS appeared here for a much lower number of pulses. Moreover, in Chapter 3, both the fluence and number of pulses formation range widened with the thickness of the film, unlike what we observed here. Regarding the period and depth of the LIPSS, they also behaved the opposite way with the thin film thickness than the ones studied in Chapter 3. We are unsure whether the differences were caused by the change in wavelength and repetition rate of the laser or by the use of structured beams.

6.1.2. PET on gold substrates

We irradiated two samples, one with a 150±5 nm thick PET thin film and another with a 1300±10 nm thick one.

We irradiated the 150 nm thick sample with 2 to 100 pulses at fluences from 22 to 53 mJ/cm^2 at a repetition rate of 10 Hz, and with 300 to 150000 pulses at fluences from 5.9 to 38 mJ/cm^2 at a repetition rate of 3 kHz. We found structures perpendicular to the polarization of the laser at spots that had been irradiated with 50 to 100 pulses at a fluence of 53 mJ/cm^2 and a repetition rate of 10 Hz, but they were too disordered to be called LIPSS. Regarding the irradiations at 3 kHz, they increased the roughness of the sample but did not induce any structures.

In Figure 6.5, we show the typical evolution of the 150 nm thick sample after irradiation with increasing number of pulses. The evolution of this disordered structures after being irradiated with increasing number of pulses was very similar to the one of LIPSS in the samples on silicon substrates. The only difference is that the film was slightly ablated for the higher number of pulses in this case. The period of the structures was 280±50 nm and their depth 70±20 nm.

As for the sample with the 1300 nm film, we irradiated it with 300 to 150000 pulses at fluences from 4.5 to 35 mJ/cm^2 and a repetition rate of 3 KHz. We did not find LIPSS in this range, but we did notice that the irradiation produced changes on the topography of the sample, as shown in Figure 6.6.

To sum up, LIPSS appeared perpendicular to the polarization of the laser for the 150 nm thick sample deposited on low R_q gold substrate. However, we did not find periodic structures in the 1300 nm thick sample on low $R_\mathrm{q}$gold substrate. Both the orientation of the LIPSS and their appearance only for thin enough films are coherent to our previous experiments with Gaussian beams in the same kind of samples, discussed in Chapter 3.

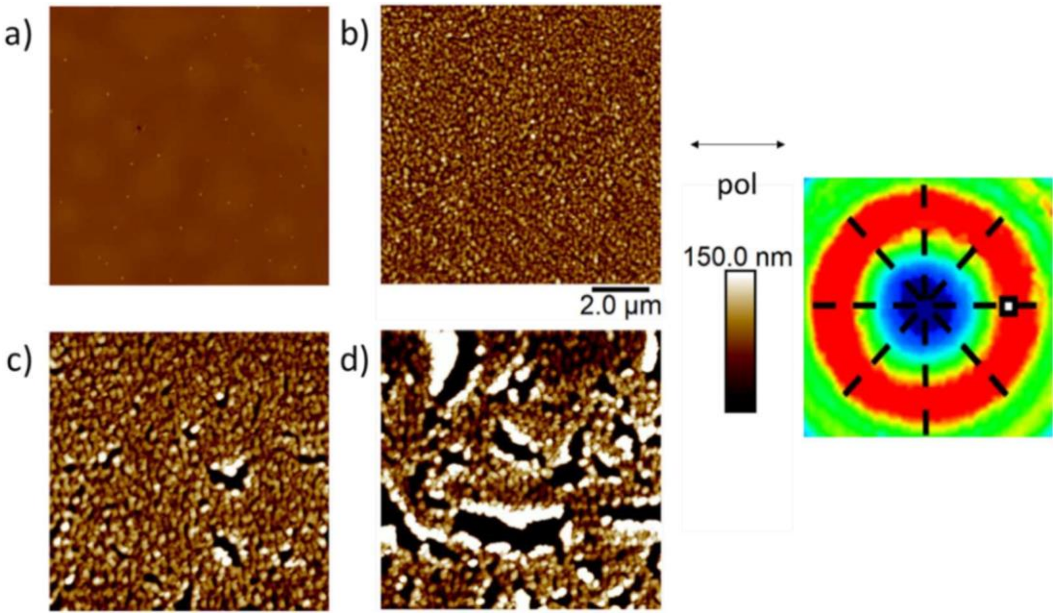

Figure 6.5. *10 x 10 µm^2 AFM image of a spot irradiated with a radial vector beam built from femtosecond pulses at 10 Hz and a fluence of 53 mJ/cm^2 in a 150 nm thick film of PET on the low roughness gold substrate a) before irradiation, b) 10 pulses, c) 50 pulses, d) 100 pulses. The scheme in the right side represents the kind of beam, with the black lines showing the direction of the polarization and the white square the location where the measurement was carried out.*

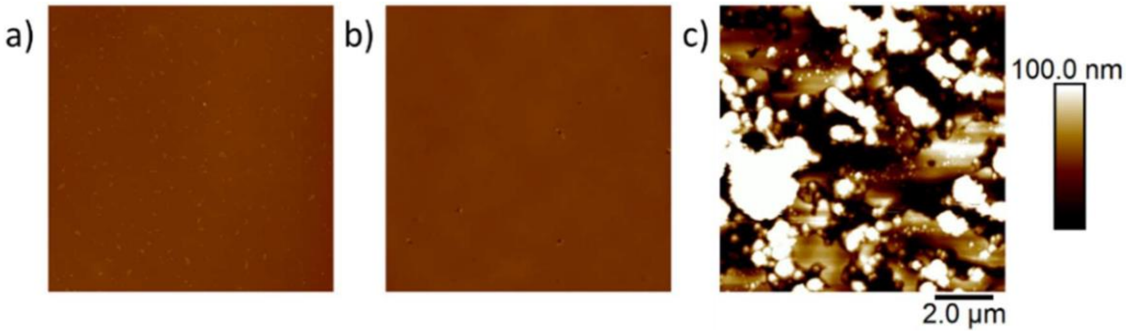

Figure 6.6. *10 x 10 µm^2 AFM images showing the change in the topography of the 1300 nm thick sample. We show the sample a) before irradiation, and the spot after being irradiated with a radial vector beam —the same region as in Figure 6.5— at a repetition rate of 3 kHz with 150000 pulses at a fluence of b) 4.5 mJ/cm^2 and c) 21 mJ/cm^2.*

6.1.3. PET on glass substrates

We irradiated two samples with 300 to 150000 pulses at fluences from 53 to 116 mJ/cm^2 and at a repetition rate of 3 kHz. One with a 115±14 nm thick film and another one with a 205±25 nm thick film.

We found LIPSS in the 115 nm thick sample at the spots that had been irradiated with 30000 to 60000 pulses at a fluence of 85 mJ/cm^2. Their period was around 330±30 nm and their depth around 85±6 nm. We show the evolution of the topography of the sample with the number of pulses in Figure 6.7.

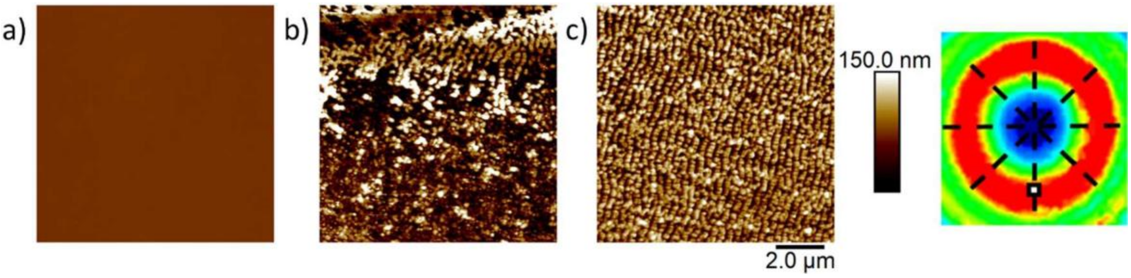

Figure 6.7. *10 x 10 µm^2 AFM images showing the evolution of the 115 nm thick sample with the number of pulses. We show the sample a) before irradiation, and a spot after being irradiated with a radial vector beam at a repetition rate of 3 kHz and a fluence of 85 mJ/cm^2 b) 30000 pulses and c) 60000 pulses. The scheme in the right side represents the kind of beam with the black lines showing the direction of the polarization and the white square the region where the measurements were carried out.*

Regarding the 205 nm thick sample, we observed short structures parallel to the polarization of the laser at the spots that had been irradiated with 30000 to 60000 pulses at a fluence of 85 mJ/cm^2. We also found short structures perpendicular to the polarization of the laser at the spot irradiated with 6000 pulses at a fluence of 85 mJ/cm^2. Given the short length of the structures, it was difficult to measure their period and depth, but the structures that appeared after irradiation with 30000 to 60000 pulses have a period around 300 nm and a depth around 20 nm, while the other structures have a period around 100 nm and a depth around 20 nm. We show the evolution of the topography of the sample in Figure 6.8, where we can also see both kinds of structures.

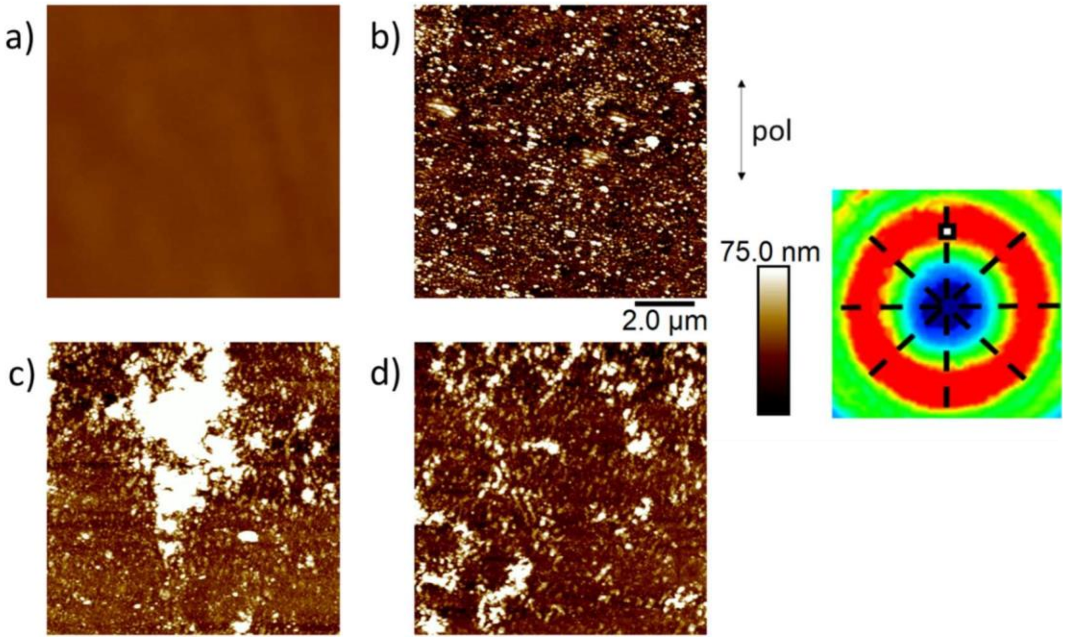

Figure 6.8. *10 x 10 µm² AFM images showing the evolution of the 205 nm thick sample with the number of pulses. We show the sample a) before irradiation, and a spot after being irradiated with a radial vector beam with a fluence of 85 mJ/cm² and b) 6000 pulses, c) 30000 pulses d) 60000 pulses at a repetition rate of 3 kHz. The scheme in the right side represents the kind of beam with the black lines showing the direction of the polarization and the white square the region where the measurements were carried out.*

In conclusion, we found LIPSS parallel to the polarization in the 115 nm thick sample in a narrow fluence and number of pulses range with a period ∼330 nm. Furthermore, in the 205 nm thick sample we found short structures difficult to identify. However, we think that the structures obtained for 6000 pulses at 85 mJ/cm² are HSFL, since they appear perpendicular to the polarization of the laser with a very small period (∼100 nm), and the structures obtained from 30000 to 60000 pulses at 85 mJ/cm² are LSFL, since they appear parallel to the polarization of the laser and with a period ∼300 nm ≥ λ/2.

6.2. LIPSS generated by complex beams in P3HT

6.2.1. LIPSS generated with femtosecond vector beams

We irradiated P3HT with the same femtosecond vector beams employed for PET in the previous section, but with a repetition rate of 1 kHz. LIPSS in P3HT appeared parallel to the polarization of the laser. In Figure 6.9, we show the direction of LIPSS in five areas of the spot, showing how for radial polarization we have wheel-spokes structures. In this case we did not perform systematic irradiations to find LIPSS formation range. However, LIPSS appeared after irradiating the sample at a fluence of 33 mJ/cm^2 with 500-5000 pulses. The dependence of the period and depth of the structures with the number of pulses is shown in Figure 6.10. Both their depth and their period remained almost constant around 20 nm and 420 nm, respectively.

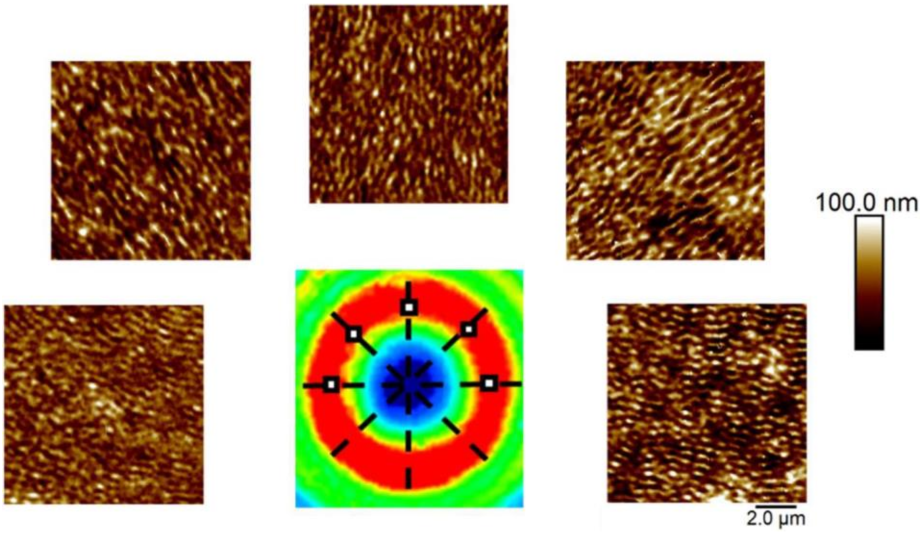

Figure 6.9. *Orientation of the structures in P3HT at different areas of the spot irradiated with radial vector beams with 2000 pulses at 33 mJ/cm^2 from a femtosecond laser at 1 kHz.*

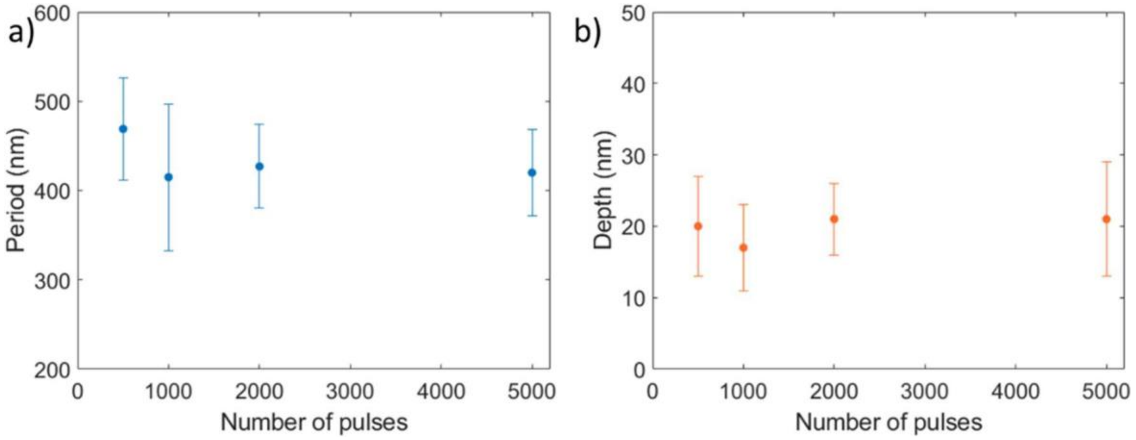

Figure 6.10. *Dependence of the a) period and b) depth of the structures in P3HT with the number of pulses at a fluence of 33 mJ/cm^2.*

6.2.2. LIPSS generated with nanosecond complex beams

6.2.2.1. Topography

On the basis of our previous work with Gaussian pulses with similar irradiation conditions [5], we irradiated P3HT with fluences from 11 to 42 mJ/cm^2 and 1200 to 8400 pulses, as long as this was the range of parameters for which LIPSS appeared. Given the size of our spots, to measure the period, depth and orientation of the structures we decided to take five 10 x 10 µm^2 AFM images distributed across the spot and one 100 x 100 µm^2 confocal microscope image.

The structures formed by vector beams were parallel to the electric field polarization at each point of the beam, creating wheel-spokes-like structures for radial vector beams, concentrical structures for azimuthal vector beams and whirlwind-like structures for spiral vector beams. In Figure 6.11, we show three images of the left side of a spot irradiated with a radial vector beam taken with different techniques. Since the structures are parallel to the polarization of the beam, they appear horizontal.

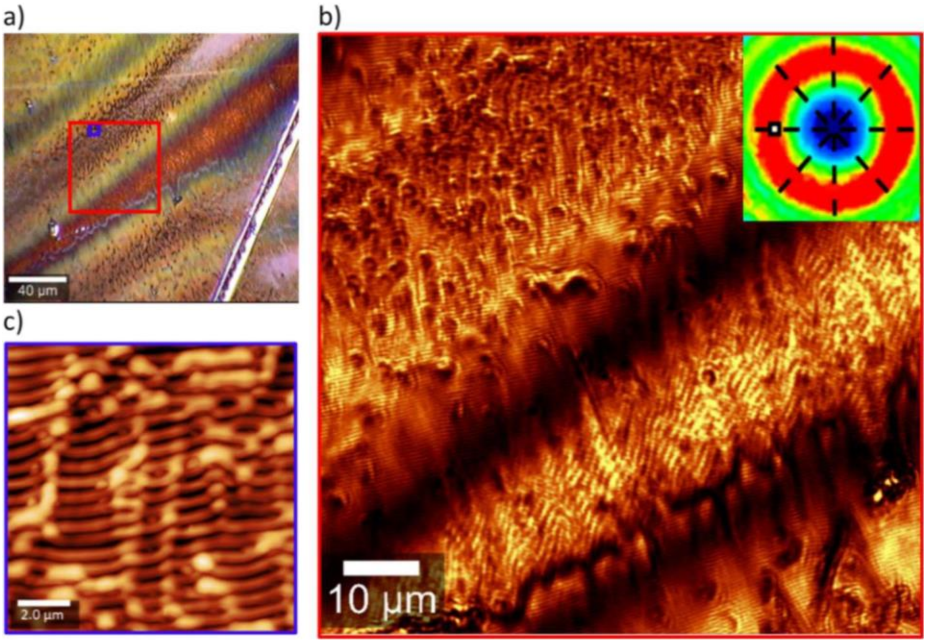

Figure 6.11. *Images of the left side of a spot in P3HT for radial vector beams from a nanosecond laser at 6000 pulses and 23 mJ/cm^2 taken by a) an optical microscope x20, b) a confocal microscope and c) AFM. The blue rectangle in a) shows the AFM measurement area and the red one the confocal measurement area. The red, green, and blue inset image in b) represents the kind of beam. The black lines show the direction of the polarization and the white square the area of the measurement.*

In Figures 6.12 and 6.13, we present AFM images of different areas of the spot to show the orientation of the ripples for the optimal conditions of fluence and number of pulses. We took the radial and azimuthal vector beams as an example.

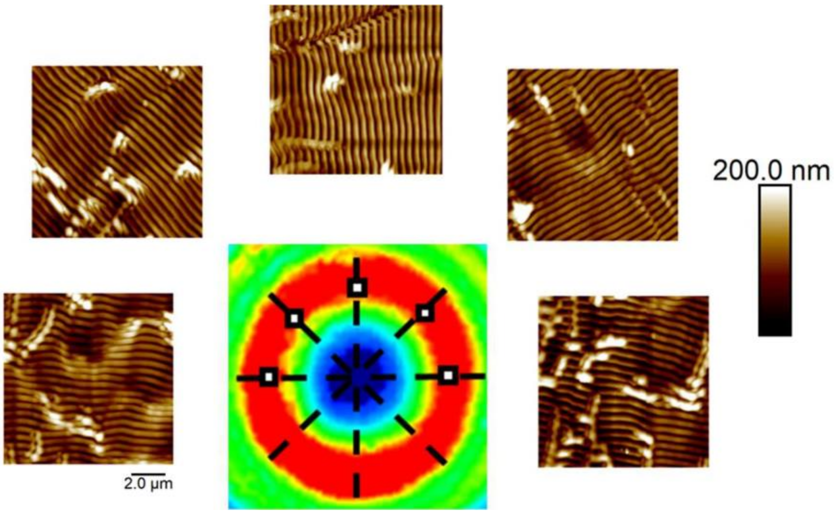

Figure 6.12. *Orientation of the structures in P3HT at different areas of the spot for radial vector beams from a nanosecond laser for 6000 pulses at 23 mJ/cm^2.*

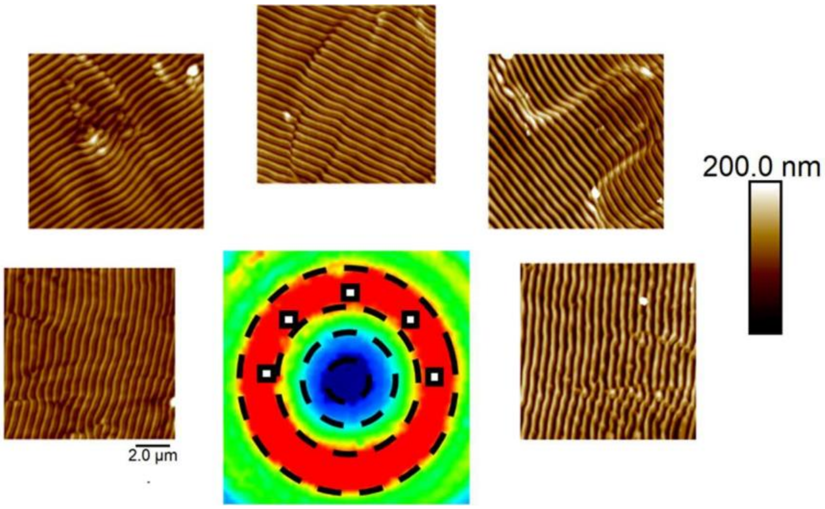

Figure 6.13. *Orientation of the structures in P3HT at different areas of the spot for azimuthal vector beams from a nanosecond laser for 6000 pulses at 23 mJ/cm^2.*

Regarding the influence of fluence and number of pulses in the period and depth of the structures, we found that it was independent of the polarization of the vector beam, and similar to the one found for Gaussian beams. Figures 6.14 and 6.15 show the evolution of a sample of

P3HT after being irradiated with increasing fluences and number of pulses, respectively. The evolution was similar in both cases, for low number of pulses and fluences we could only detect shallow structures, and, when we increased the energy deposited, these structures correspondingly deepen until they begin to lose periodicity.

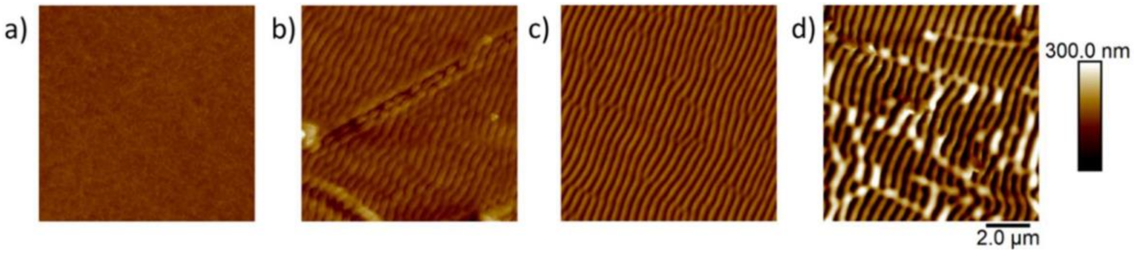

Figure 6.14. *10 x 10 µm^2 AFM image of the right part of the spot irradiated with an azimuthal vector beam –see the scheme in Figure 6.13– from a nanosecond laser in P3HT with 6000 pulses at a fluence of a) before irradiation, b) 11 mJ/cm^2, c) 17 mJ/cm^2, d) 36 mJ/cm^2.*

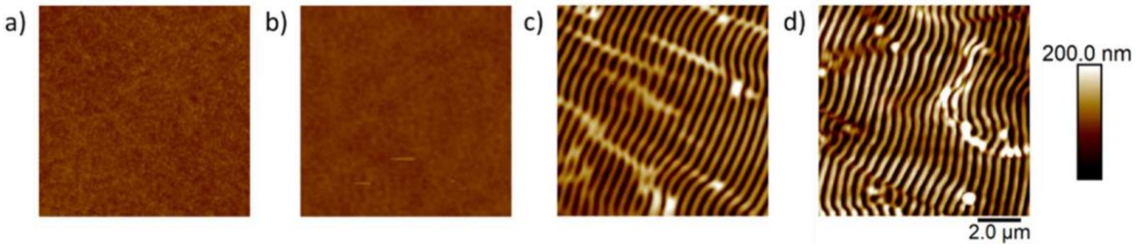

Figure 6.15. *10 x 10 µm^2 AFM image of the right part of the spot irradiated with an azimuthal vector beam –see the scheme in Figure 6.13– from a nanosecond laser in P3HT with a) before irradiation, b) 1200 pulses, c) 3600 pulses, d) 8400 pulses at a fluence of 23 mJ/cm^2.*

LIPSS appeared for almost all the irradiation conditions. For the lowest number of pulses, *i.e.* 1200, a fluence above 30 mJ/cm^2 was needed for LIPSS formation. For a number of pulses above 6000, the structures lost their periodicity above a fluence of 42 mJ/cm^2. This interplay between number of pulses and fluence is a consequence of the well-known accumulation effects involved in LIPSS formation [6]. Their period grew from around 400 nm for the lowest fluences up to a value of approximately 475 nm at 30 mJ/cm^2 remaining almost constant for higher fluences. Their depth increased until it reached a plateau that depends on the number of pulses at around 30 mJ/cm^2, as seen in Figure 6.16. The structures were much deeper but had a similar period to the ones generated with femtosecond pulses for the same fluence and number of pulses.

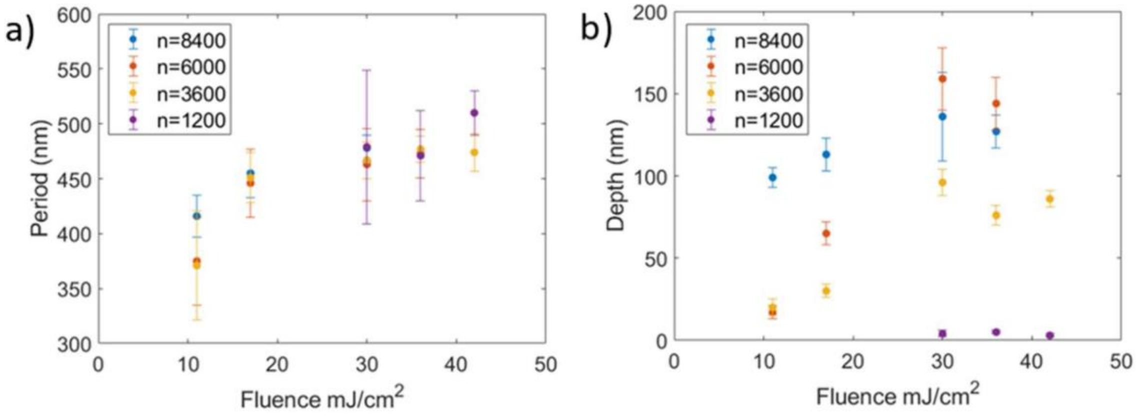

Figure 6.16. *Dependence of the a) period and b) depth of the structures in P3HT with the fluence for different number of pulses for azimuthal vector beams.*

We also studied LIPSS generation using optical vortex beams. The structures generated by vortex beams can be seen in Figure 6.17. They are honeycomb-like structures with a periodicity close to that of the structures generated with vector beams but a smaller depth. For 42 mJ/cm^2 and 6000 pulses, the structures have a period of 462±66 nm and a depth of 35±5 nm. In principle, the phase of the irradiation should not affect the structures, and its shape should be due to the circular polarization of the laser beam. However, in other materials the nanostructures that result from circularly polarized irradiation are uniformly distributed nanodots [3]. This is close to the negative of what we see in Figure 6.17. Although we could not find experimental structures like ours in the bibliography, Varlamova *et al.* [7] simulated structures close to ours, when trying to explain their experimental nanodots.

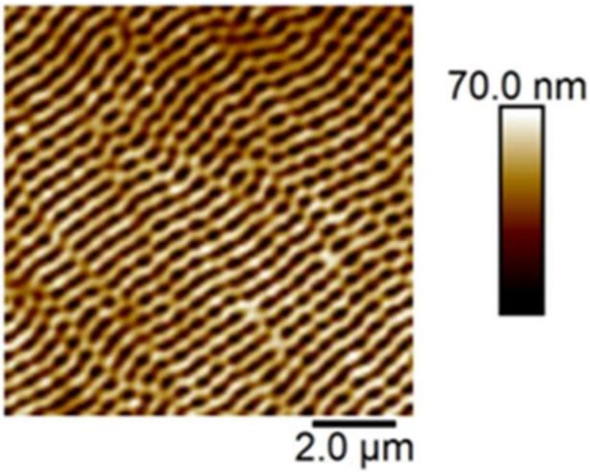

Figure 6.17. *Structures in P3HT irradiated with vortex beams with 6000 pulses at 42 mJ/cm^2.*

6.2.2.2. Conductivity

As for the effect on the conductivity, it can be seen in Figure 6.18. The conductivity in the hills was lower than the one in the valleys due to the amorphization of the P3HT up there. The explanation for this behavior was reported in more detail in [5]. As explained in Section 1.1, P3HT conductivity is linked to its regioregularity and crystallinity. This amorphization of P3HT in the hills drastically lowers these properties, producing abrupt decrease in conductivity.

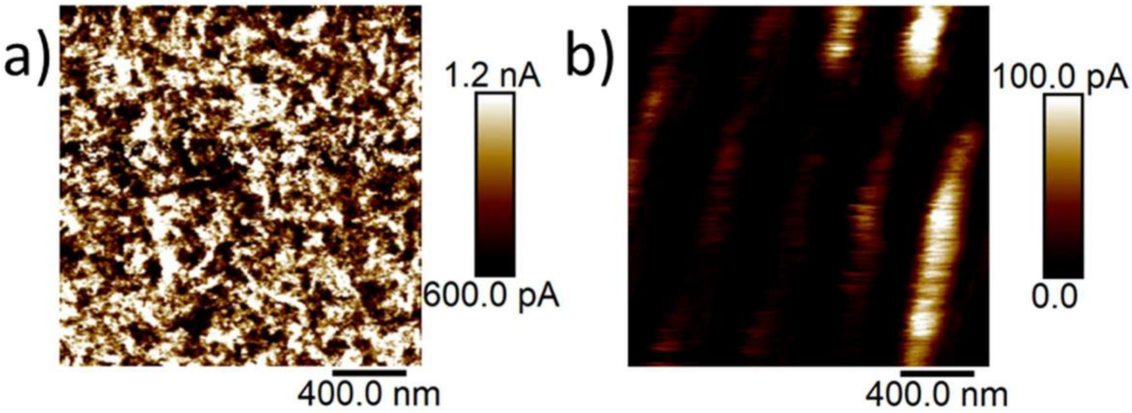

Figure 6.18. *2 x 2 μm² C-AFM images of P3HT a) before and b) after irradiation with 3600 pulses at a fluence of 23 mJ/cm² with a vector beam with azimuthal polarization.*

6.2.2.3. Wettability

To analyze the change in wettability, we prepared samples with nanostructures on an area wide enough to contain a drop of water (6.4 x 5.5 mm²). We irradiated the sample surface following a pattern of slightly overlapping scans (the pitch was 0.9 mm whereas the spot diameter was 1 mm). We measured the contact angle of three drops of deionized water for each polarization case and a raw sample. We performed the measurements five months after the irradiation.

The raw samples had a contact angle of 102±3°, which means they were slightly hydrophobic. After irradiation with 3600 pulses at a fluence 34 mJ/cm² the contact angle diminished to around 85±6°, so we can say the samples became slightly hydrophilic. This result was maintained irrespectively of the beam polarization. The contact angle before irradiation is consistent to the one reported previously by members of our group (96±2°) [5]. However, in that work, it was shown that for Gaussian beams, with the same wavelength as the ones we used here, there was a slight increase instead of a decrease in the contact angle after processing. This small change might be caused by the difference in the repetition rate, which was half the one we employed in this work.

The change in wettability that appears after laser nanostructuring can have either a morphological or a chemical explanation. The morphological contribution can only increase the character of the raw sample (Wenzel's model [8]) or make a sample more hydrophobic (Cassie-Baxter model [9]), so it is unable to explain our case. Therefore, this change must have a chemical explanation: the formation of hydrophilic species. They would form due to a reaction with the atmospheric gases catalyzed by the high temperatures and ionization during laser irradiation.

Given the success achieved in P3HT, we decided to extend the study to an organic semiconductor which is also absorbent at this wavelength and, as discussed in Section 2.1, is frequently used with P3HT in solar cells applications: $PC_{71}BM$ [10].

6.3. LIPSS generated with nanosecond complex beams in $PC_{71}BM$

On the basis of our previous work with Gaussian pulses with similar irradiation conditions [11], we irradiated $PC_{71}BM$ with fluences from 17 to 19 mJ/cm^2 and 1200 to 8400 pulses, as far as those were the conditions where LIPSS were found. The structures formed by vector beams were parallel to the electric field polarization at each point of the beam, creating wheel-spokes-like structures for radial vector beams, concentrical structures for azimuthal vector beams and whirlwind-like structures for spiral vector beams. In Figure 6.19, we show three images, with different magnifications, taken with different techniques, showing the bottom side of a spot that had been irradiated with radial vector beams. Since the LIPSS appeared parallel to the polarization, which is vertical in this area, we observed vertical structures. Besides, in Figures 6.20 and 6.21, we show AFM images of different areas of the spot of a radial (Figure 6.20) and an azimuthal (Figure 6.21) vector beam to show the orientation of the ripples for optimal conditions of fluence and number of pulses.

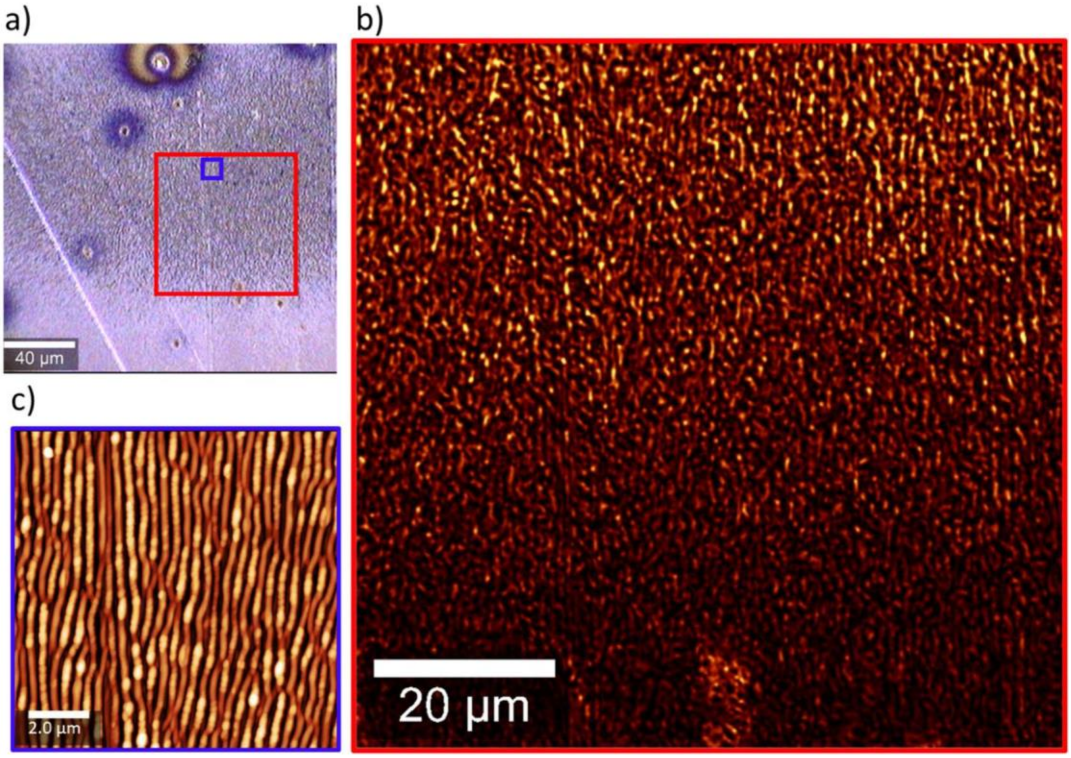

Figure 6.19. *Images of a spot in PC$_{71}$BM for radial vector beams –the same region as in Figure 6.7– from a nanosecond laser at 6000 pulses and 17 mJ/cm^2 taken by a) an optical microscope x20, b) a confocal microscope and c) AFM. The blue rectangle in a) shows the AFM measurement area and the red one the confocal measurement area.*

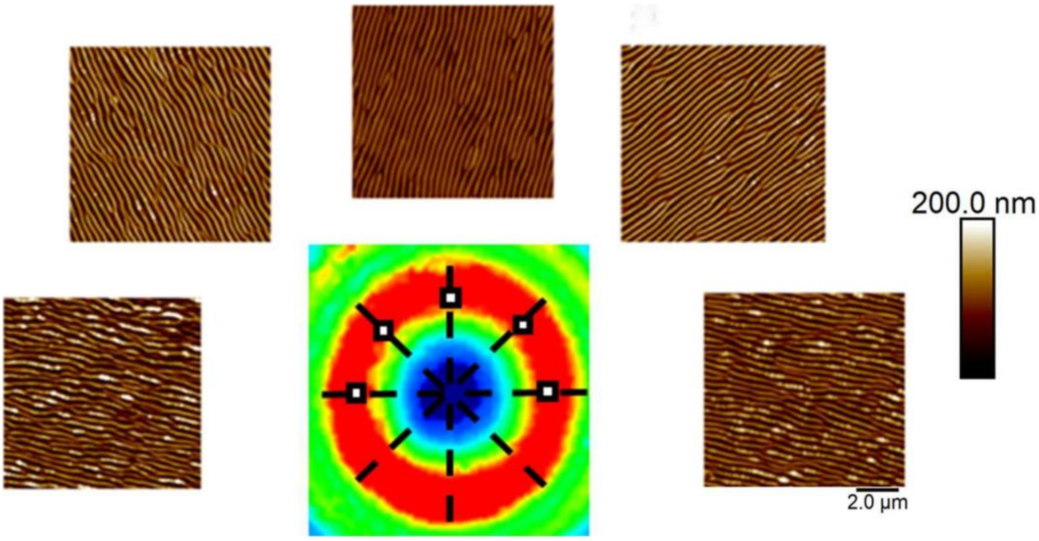

Figure 6.20. *Orientation of the structures in PC$_{71}$BM at different areas of the spot irradiated with radial vector beams from a nanosecond laser with 6000 pulses at 17 mJ/cm^2.*

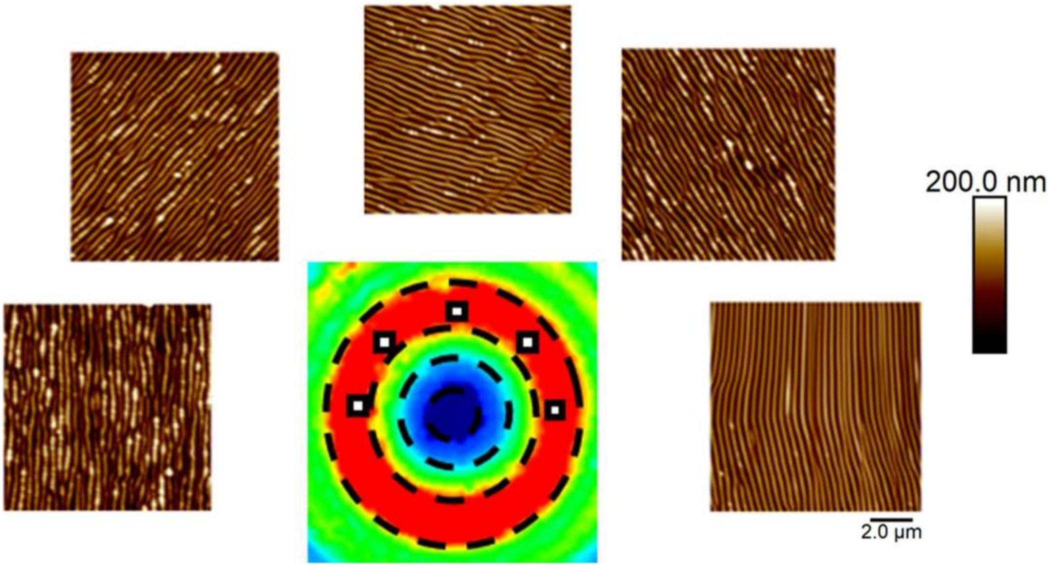

Figure 6.21. *Orientation of the structures in* $PC_{71}BM$ *at different areas of the spot irradiated with azimuthal vector beams from a nanosecond laser with 6000 pulses at 17 mJ/cm*^{2}*.*

In $PC_{71}BM$ LIPSS appeared from 1200 to 8400 pulses with a fluence from 17 to 19 mJ/cm^2. Their period is around 340 nm, and their depth grows from 30 to 100 nm when increasing fluence and number of pulses as seen in Figure 6.22.

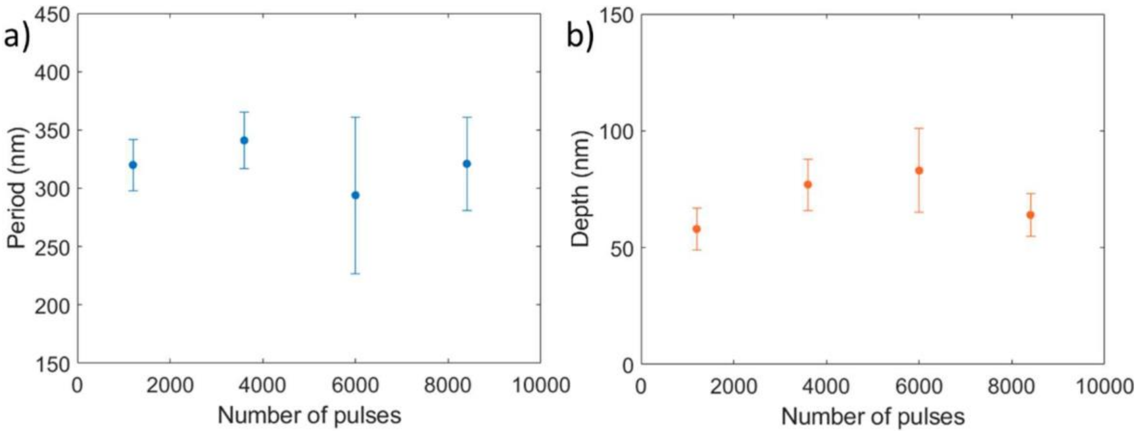

Figure 6.22. *Dependence of the a) period and b) depth of the structures in* $PC_{71}BM$ *with the number of pulses at a fluence of 17 mJ/cm*^{2} *with azimuthal vector beams.*

The structures generated by vortex beams are similar to the ones found in P3HT, as can be seen in Figure 6.23. They are honeycomb-like structures with the same periodicity and depth as the structures generated with vector beams.

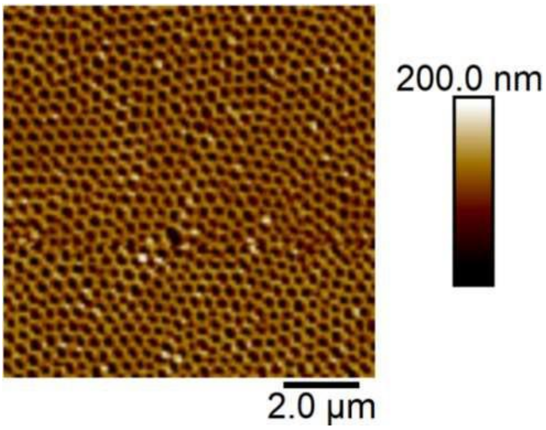

Figure 6.23. *Structures in* $PC_{71}BM$ *for vortex beams for 8400 pulses at 17 mJ/cm*^{2}.

6.4. Conclusions

We were able to generate LIPSS with complex shapes using vector beams and optical vortex beams in PET, P3HT and $PC_{71}BM$.

In the PET samples on Si substrates, LIPSS appeared, parallel to the polarization of the laser, for thin films from 79 to 441 nm thick. Their period increased with the thickness of the film from 400 to 480 nm. As for their depth, it decreased with the thickness from 200 to 80 nm. In general, the behavior of the structures is quite different to the one discussed in Chapter 3 for the same kind of samples but a different femtosecond laser. We are not sure whether the differences were caused by the change in wavelength and repetition rate of the laser or by the use of vector beams.

In the ones with gold substrates, structures appeared perpendicular to the polarization of the laser for the 150 nm thick sample, not ordered enough to be called LIPSS. However, we did not find any structures in the 1300 nm thick sample. Both the orientation of the structures and their appearance only for thin enough films are coherent to our previous experiments with Gaussian beams in the same kind of samples, discussed in Chapter 3. However, they appear here much more disorderly.

In the ones on glass substrates, we found LIPSS parallel to the polarization in the 115 nm thick sample in a narrow fluence and number of pulses range with a period ∼330 nm. Furthermore, in the 205 nm thick sample we found two kinds of short structures: HSFL perpendicular to the polarization of the laser with a period of ∼100 nm at the spots irradiated with 6000 pulses at 85 mJ/cm^2, and LSFL with a period ~300 nm at the spots irradiated with 30000 to 60000 pulses at 85 mJ/cm^2.

We generated LIPSS in P3HT both with femtosecond and nanosecond vector beams. LIPSS appeared parallel to the polarization of the laser in both cases with a period close to its wavelength. However, the structures were much deeper for nanosecond pulses (~100 nm) than for femtosecond pulses (~20 nm).

Regarding the LIPSS generated with nanosecond pulses in P3HT and PC$_{71}$BM, their formation range and characteristics were similar to the ones generated with Gaussian beams. LIPSS affected the conductivity of P3HT and PC$_{71}$BM, creating a sort of wires with the original conductivity of the samples in the valleys of the structures.

The wettability of P3HT changed from slightly hydrophobic to slightly hydrophilic after LIPSS formation. We explain this change as the influence of the hydrophilic species that appear due to a reaction with the atmospheric gases catalyzed by the high temperatures and ionization during laser irradiation.

Finally, the irradiation with optical vortex beams resulted in the creation of periodic honeycomb-like structures in both P3HT and PC$_{71}$BM. The different phase of the irradiation of optical vortex beams should not affect the structures, and its shape should be due to the circular polarization of the laser beam. However, in other materials the nanostructures that result from circularly polarized irradiation are uniformly distributed nanodots.

6.5. References

[1] J. Prada-Rodrigo, R.I. Rodríguez-Beltrán, S. Paszkiewicz, A. Szymczyk, T.A. Ezquerra, P. Moreno, E. Rebollar, Laser-induced periodic surface structuring of poly(trimethylene terephthalate) films containing tungsten disulfide nanotubes, Polymers 12 (2020) 1090. https://doi.org/10.3390/POLYM12051090.

[2] E. Rebollar, J.R. Vázquez De Aldana, I. Martín-Fabiani, M. Hernández, D.R. Rueda, T.A. Ezquerra, C. Domingo, P. Moreno, M. Castillejo, Assessment of femtosecond laser induced periodic surface structures on polymer films, Physical Chemistry Chemical Physics 15 (2013) 11287–11298. https://doi.org/10.1039/c3cp51523k.

[3] E. Rebollar, M. Castillejo, T.A. Ezquerra, Laser induced periodic surface structures on polymer films: From fundamentals to applications, European Polymer Journal 73 (2015) 162–174. https://doi.org/10.1016/j.eurpolymj.2015.10.012.

[4] M.J. Soileau, Ripple Structures Associated with Ordered Surface Defects in Dielectrics, IEEE Journal of Quantum Electronics 20 (1984) 464–467. https://doi.org/10.1109/JQE.1984.1072422.

[5] E. Gutiérrez-Fernández, T.A. Ezquerra, A. Nogales, E. Rebollar, Straightforward patterning of functional polymers by sequential nanosecond pulsed laser irradiation, Nanomaterials 11 (2021) 1123. https://doi.org/10.3390/NANO11051123/S1.

[6] J.F. Young, J.E. Sipe, H.M. van Driel, Laser-induced periodic surface structure. III. Fluence regimes, the role of feedback, and details of the induced topography in germanium, Physical Review B 30 (1984) 2001–2015. https://doi.org/10.1103/PhysRevB.30.2001.

[7] O. Varlamova, J. Reif, S. Varlamov, M. Bestehorn, Self-organized Surface Patterns Originating from Laser-Induced Instability, in: S. Sakabe, C. Lienau, R. Grunwald (Eds.), Progress in Nonlinear Nano-Optics. Nano-Optics and Nanophotonics., Springer, Cham, 2015: pp. 3–29. https://doi.org/10.1007/978-3-319-12217-5_1.

[8] R.N. Wenzel, Resistance of solid surfaces to wetting by water, Industrial and Engineering Chemistry. 28 (1936) 988–994. https://doi.org/10.1021/ie50320a024.

[9] A.B.D. Cassie, S. Baxter, Wettability of porous surfaces, Transactions of the Faraday Society 40 (1944) 546–551. https://doi.org/10.1039/TF9444000546.

[10] O. Inganäs, Organic Photovoltaics over Three Decades, Advanced Materials 30 (2018) 1800388. https://doi.org/10.1002/ADMA.201800388.

[11] E. Gutiérrez-Fernández, Á. Rodríguez-Rodríguez, M.C. García-Gutiérrez, A. Nogales, T.A. Ezquerra, E. Rebollar, Functional nanostructured surfaces induced by laser on fullerene thin films, Applied Surface Science 476 (2019) 668–675. https://doi.org/10.1016/j.apsusc.2019.01.141.

Chapter 7

Conclusions

In summary, in this work we have firstly carried out a series of experiments with the objective of finding how different parameters affect LIPSS formation in thin films of polymers. Secondly, we have also studied the effect of LIPSS formation in the modification of the properties of the samples by characterizing the change in the micromechanical properties, topography, wettability, surface energy, surface chemistry and conductivity of the samples after irradiation.

1) Study on how the thickness of the thin film and the roughness and material of the substrate affect LIPSS generation in thin polymeric films with low optical linear absorption

We irradiated thin films of PET of different thickness deposited on different substrates, with a 795 nm wavelength femtosecond laser.

As seen in Table 7.1, LIPSS were generated for thin films but not for micrometric films. LIPSS were also generated on samples with silicon, gold, and glass substrates; but not on samples with steel, PET or high R_q gold substrates. As for their direction, LIPSS appeared perpendicular to the polarization of the laser in the samples with gold substrates and parallel to it in the other samples. Moreover, in the samples where LIPSS were generated, the thickness of the thin film and the material of the substrate affected the period and depth of the structures.

In the case of samples on gold substrates, LIPSS appeared perpendicular to the expected direction. Because of this, we decided to study it further with the help of numerical simulations of the electric field. Through them, we explored in more detail the effect of the thin film thickness and substrate roughness in LIPSS formation. Moreover, we compared it with the theoretical effect of these parameters on Surface Plasmon Polaritons (SPP) and our experimental results. We found good agreement between our simulations and the theory in its application range. Moreover, using our simulations we could qualitatively understand what happened outside of this range. Besides, these simulations qualitatively reproduced our experimental results.

Table 7.1. *LIPSS type, direction relative to the laser polarization, and formation range for each sample. "N.A" means that LIPSS did not appear in that sample.*

Substrate	Thickness (nm)	LIPSS direction	LIPSS Type	Fluence (mJ/cm^2)	Number of pulses
Low R_q Gold	90	⊥	LSFL	2.7-3.6	50k-100k
Low R_q Gold	102	⊥	LSFL	4.0-6.3	50k-100k
Low R_q Gold	150	⊥	LSFL	4.4-8.9	50k-100k
Low R_q Gold	1300	N.A.	N.A.	N.A.	N.A.
Low R_q Gold	16000	N.A.	N.A.	N.A.	N.A.
Silicon	79	ǁ	LSFL	21	10k-100k
Silicon	120	ǁ	LSFL	18-26	2k-100k
Silicon	16000	N.A.	N.A.	N.A.	N.A.
Glass	115	ǁ & ⊥	LSFL & HSFL	44-73	1k-100k
Glass	205	ǁ	LSFL	44-63	1k-100k
Glass	16000	N.A.	N.A.	N.A.	N.A.
PET	243	N.A.	N.A.	N.A.	N.A.
PET	318	N.A.	N.A.	N.A.	N.A.
Steel	210	N.A.	N.A.	N.A.	N.A.
Steel	298	N.A.	N.A.	N.A.	N.A.
High R_q Gold	165	N.A.	N.A.	N.A.	N.A.

From these results we extract the following conclusions:

- **The material and roughness of the substrate and the thickness of the thin film are key parameters in LIPSS formation:** For femtosecond pulses in thin films of a polymer with low optical linear absorption, not only do they change LIPSS formation range and characteristics, but they can also be the factor that determines if LIPSS can be generated. In the case of the thickness of the thin film, we can apply this conclusion to bulk polymers if we think of them as a film with very high thickness. It is possible for LIPSS to not appear in a polymer in bulk and to appear for thin enough thin films.
- **The formation mechanism for LIPSS in these samples is affected by the excitation of a Surface Scattered Wave (SSW) in the substrate-thin film interface:** For femtosecond pulses in thin films of a polymer with low optical linear absorption, this SSW is more

intense than the usual SSW excited in the surface of the sample and it is the reason behind the importance of the material and roughness of the substrate, and the thickness of the thin film. Considering its influence, we can explain all our experimental results except the ones related to thinnest sample on a glass substrate. In this sample, both LSFL and HSFL appeared with periods that we were unable to explain completely.

- **In the case of samples on gold substrates this SSW is a SPP:** The numerical simulations of the electric field showed the formation of an SPP in the substrate-thin film interface. Moreover, they reproduced our experimental results, which made us confident that in the samples with gold substrates the aforementioned SSW is a SPP.
- **In the case of samples on gold substrates LIPSS period diminishes with the substrate $\boldsymbol{R_q}$ and the thickness of the thin film:** Using numerical simulations, we explored in more detail the effect of the thin film thickness and substrate roughness and compared it with the theory on how these parameters affect SPPs and our experiments. We found good agreement between our simulations and the theory in its application range.

As for future research paths, we propose the following:

- **Investigating the substrate roughness and film thickness regime that allows LIPSS formation:** For logistical reasons, in this thesis we only irradiated samples on substrates with either very low or very high roughness. As for film thicknesses, in our thesis we did not irradiate samples between 205 nm and 1300 nm. Although we studied intermediate cases with our numerical simulations, it would be interesting to try to study them experimentally and check if we reproduce the results of the simulations.
- **Investigating the optical linear absorption range at which the SSW excited in the substrate-thin film interface influences LIPSS formation:** The irradiation of the same kind of samples with femtosecond Gaussian beams, but with different wavelengths would allow us to explore different optical linear absorption ranges and define the range in which we need to take this SSW into account. The study could be made for samples on low R_q gold substrates, since the difference in orientation would be the easiest property to monitor.
- **Investigating the structures that appeared in the thinnest sample on a glass substrate:** The irradiation of samples with thicknesses between 100 and 200 nm could help us understand the different structures observed as a function of thickness. Another option would be to try to extend the numerical simulations done for samples

on gold substrates to these samples and study the differences in the electric field between samples of different thicknesses.

2) Study of the effect of LIPSS formation on the modification of the properties of materials

We have studied LIPSS generation in self-standing films of a nanocomposite made from a PTT matrix dopped with WS_2 nanotubes. Moreover, we have tried to use complex beams to generate complex structures in one step, applying this method to thin films of PET deposited on different substrates, as well as thin films of P3HT and $PC_{71}BM$, two organic semiconductors with applications in organic solar cells, deposited on dopped silicon.

Regarding the PTT-WS_2 samples, we irradiated them with femtosecond Gaussian beams at 265 nm generating LIPSS. We also studied LIPSS generation in plain PTT samples to investigate the effect of the nanoadditive. In both samples the structures appeared parallel to the polarization of the laser with a period close to its wavelength. The presence of the nanoadditive led to an increase of the energy density needed to trigger LIPSS formation. We explained this as the effect of the higher crystallization percentage and thermal dissipation of PTT-WS_2. Besides, we characterized the wettability and surface energy of the samples. In both of them, the wettability increased with the formation of LIPSS, and the total surface energy remained constant. However, its negative polar component increased heavily. This was due to the formation of polar hydrophilic species, caused by a reaction with the oxygen in the air, catalyzed by the ionization and high temperature of the surface of the sample while the irradiation took place. Finally, we used PF-QNM to characterize the change in the surface nanomechanical properties after irradiation. In both samples, the formation of LIPSS did not change the Young's modulus remarkably, but it induced a decrease of the adhesion force by a factor of four. We attributed this effect to the change of surface chemistry.

From these results we extract the following conclusions:

- **LIPSS can be used to change the topography of these samples, giving them added functionality, without damaging them:** This technique is non-ablative and the Young's modulus of the sample remained unchanged.
- **LIPSS allow the creation of small zones with different nanostructures**: Given the high control over the irradiated area, we could change the irradiation parameters at different areas of a sample, creating small zones with nanostructures with different periods, depths and orientations.

- **LIPSS surface nanostructuring can be used in this nanocomposite without any demerit:** Besides needing a small increase in the intensity of irradiation, LIPSS appeared with the same characteristics in PTT and PTT-WS_2, and the changes they provoked in the surface properties of the samples were very similar.

We also propose the following research line:

- **Investigating the influence of the percentage of nanoadditive and its orientation in LIPSS formation:** In our experiments, the percentage of nanoadditive was 0.5% in weight and it was evenly distributed in the PTT matrix with the nanotubes taking random orientations. It would be interesting to check if the mild impact (described above) that the nanoadditive made on LIPSS generation would increase if we augmented this percentage or if the nanotubes were predominantly oriented in one direction.

Concerning the irradiations with complex beams, we irradiated thin films of PET on different substrates with femtosecond vector beams at a wavelength of 515 nm. LIPSS appeared parallel to the polarization of the beams in samples with silicon or glass substrates. However, in samples on gold substrates, structures oriented perpendicular to the polarization appeared, but too disordered to be called LIPSS.

From our results we extracted the following conclusions.

- **We achieved the formation of LIPSS in PET with complex shapes using a single-step process:** We generated structures in the shape of wheel-spokes, concentric circles, and spirals in one-step using femtosecond vector beams.
- **There are differences between LIPSS induced by Gaussian beams and those induced with vector beams:** LIPSS appeared in a different fluence and pulses ranges and changed differently with the thickness of the thin films. However, we are unsure whether the differences are due to the difference in wavelength (795 nm in one case to 513 nm in the other) and repetition rate (5 kHz vs 10 Hz-3 kHz) or due to the use of vector beams instead of Gaussian beams.

As for future research paths, we propose the following:

- **Investigating the differences between LIPSS induced by Gaussian beams and those induced with vector beams:** To isolate the effect of the kind of beam from that of the irradiation wavelength and repetition rate, we could repeat the experiment with Gaussian and vector beams with the same wavelengths and repetition rates.

Regarding P3HT, we used femtosecond vector beams at a wavelength of 515 nm finding LIPSS parallel to the polarization of the laser with a period close to the irradiation wavelength. We also used nanosecond vector and optical vortex beams at 532 nm. Using nanosecond vector beams we found LIPSS parallel to polarization with a period close to irradiation wavelength much deeper and better defined that the ones generated with femtosecond pulses. Moreover, we measured a steep decline of conductivity on the upper part of the structures compared to the change in their lower part. We affirmed that this change was caused by a loss of crystallinity. Besides, we characterized the change in wettability finding the same response for the different polarizations of the beam. For all of them, the sample became more hydrophilic after irradiation. We think this effect is due to chemical changes caused by oxidation by laser irradiation. Additionally, after irradiation with optical vortex beams, we observed honeycomb-like LIPSS with similar periods and depths to the ones generated with vector beams.

Finally, we irradiated $PC_{71}BM$ films with nanosecond vector and optical vortex beams at 532 nm producing LIPSS parallel to the polarization of the laser of a smaller period than those found in P3HT and in a much narrower fluence range. Their characteristics evolved with the irradiation parameters like the structures found in P3HT.

From these results we extract the following conclusions:

- **We achieved the formation of LIPSS in P3HT and $PC_{71}BM$ with complex shapes using a single-step process:** The use of vector beams allowed the creation of LIPSS in a radial, concentrical or spiral pattern –following the polarization of the beam.
- **These structures could be applied to the creation of nanowires with these complex shapes:** The steep decline of the conductivity on the upper part of the structures could be used to create nanowires with these different geometries.
- **We achieved the generation of LIPSS with a honeycomb-like shape in one step:** The use of optical vortex beams allowed the creation of LIPSS with a honeycomb-like shape. The different phase of the irradiation of optical vortex beams should not affect the structures, and its shape should be due to the circular polarization of the laser beam. However, in other materials the nanostructures that result from circularly polarized irradiation are uniformly distributed nanodots.

As for future research paths, we propose the following:

- **Investigating the origin of the LIPSS with a honeycomb-like shape:** In other to know whether this shape is caused by the circular polarization of the beam or the different phase of optical vortex beams, one possibility is to irradiate P3HT and $PC_{71}BM$ with nanosecond Gaussian beams with different ellipticities and check if we can recreate this honeycomb-like structures.

3) Methodological conclusions

Besides these scientific conclusions, from a methodological standpoint, while I was working on this thesis I have applied and acquired expertise on the following techniques:

- **Surface processing of polymers**: I learned how to process polymers both as thin films and in bulk, with femto- and nanosecond Gaussian, vector and optical vortex beams at wavelengths that went from the near infrared to the ultraviolet.
- **Characterization**: I learned different techniques to characterize several surface properties of polymers both before and after irradiation. Specifically, the PhD student can use the following techniques independently: AFM to characterize the topography of the samples, and the sessile drop technique to characterize their wettability.
- **Calculation of their surface energy:** I learned two different methods to calculate different contributions to the surface energy from contact angle measurements performed using the sessile drop technique. He also learned how to critically compare the results given by the two methods.
- **Numerical simulations of the electric field:** I learned how to use the Wave Optics Module of COMSOL Multyphisics ™, a program based on Finite Elements Methods to simulate the electric field in a thin film of polymer deposited on a gold substrate. I worked independently to understand what approximations and parameters he should use to get the desired results.

To conclude, in this work we have studied how different parameters affect LIPSS formation in thin films of polymers and the capabilities of LIPSS formation to modify the properties of the samples. As the main contribution of this thesis, **we have identified the key role of the material and roughness of the substrate and the thickness of the thin film on the formation of LIPSS in thin films of polymers with low optical linear absorption deposited on different substrates, finding an explanation for this importance in the generation of a SSW in the substrate-thin film interface and studying it in detail with numerical simulations.** In this sense, we believe that we have contributed to the better understanding of LIPSS formation in thin films of polymers using femtosecond pulses.

Capítulo 7

Conclusiones

En resumen, en este trabajo primero estudiamos experimentalmente cómo diferentes parámetros afectan a la formación de LIPSS en películas delgadas de polímeros. Además, estudiamos el efecto de la formación de LIPSS en la modificación de las propiedades de las muestras caracterizando el cambio en las propiedades micromecánicas, topografía, mojabilidad, energía superficial, química superficial y conductividad de las muestras tras la irradiación.

1) Efecto del espesor de la película delgada y la rugosidad y el material del substrato en la formación de LIPSS en películas poliméricas delgadas con baja absorción lineal óptica

Irradiamos películas delgadas de PET de diferente espesor depositadas sobre diferentes substratos, con un láser de femtosegundo con una longitud de onda de 795 nm.

Como se ve en la Tabla 7.1, las LIPSS se generaron para películas delgadas, pero no para películas micrométricas. Las LIPSS también se generaron en muestras con substratos de silicio, oro y vidrio, pero no en muestras con substratos de acero, PET u oro de alta R_q. En cuanto a su dirección, las LIPSS aparecieron perpendiculares a la polarización del láser en las muestras con substratos de oro y paralelas a ella en las demás muestras. Además, en las muestras donde se generaron LIPSS, el espesor de la película delgada y el material del substrato afectaron al período y la profundidad de las estructuras.

El caso de las muestras sobre substratos de oro, para el que las LIPSS aparecieron en la dirección perpendicular a la que esperábamos, se estudió en más detalle con la ayuda de simulaciones numéricas del campo eléctrico. Mediante éstas, exploramos con más detalle el efecto del espesor de la película delgada y la rugosidad del substrato a la formación de LIPSS. Además, lo comparamos con el efecto teórico que tienen estos parámetros en los Plasmones Polaritones Superficiales (SPPs) y con nuestros resultados experimentales. Los resultados de nuestras simulaciones reprodujeron la teoría en su rango de aplicación. Además, usando nuestras simulaciones pudimos entender cualitativamente lo que sucede fuera de este rango. Las simulaciones también reprodujeron cualitativamente nuestros resultados experimentales.

Table 7.1. *Tipo de LIPSS, dirección respecto a la polarización del láser y rango de formación en cada muestra. "N.A" indica que las LIPSS no aparecieron en esa muestra.*

Substrato	**Espesor (nm)**	**Dirección de las LIPSS**	**Tipo de LIPSS**	**Fluencia (mJ/cm^2)**	**Número de pulsos**
Oro de baja R_q	90	$\perp$	LSFL	2.7-3.6	50k-100k
Oro de baja R_q	102	$\perp$	LSFL	4.0-6.3	50k-100k
Oro de baja R_q	150	$\perp$	LSFL	4.4-8.9	50k-100k
Oro de baja R_q	1300	N.A.	N.A.	N.A.	N.A.
Oro de baja R_q	16000	N.A.	N.A.	N.A.	N.A.
Silicio	79	$\parallel$	LSFL	21	10k-100k
Silicio	120	$\parallel$	LSFL	18-26	2k-100k
Silicio	16000	N.A.	N.A.	N.A.	N.A.
Vidrio	115	$\parallel$ y $\perp$	LSFL y HSFL	44-73	1k-100k
Vidrio	205	$\parallel$	LSFL	44-63	1k-100k
Vidrio	16000	N.A.	N.A.	N.A.	N.A.
PET	243	N.A.	N.A.	N.A.	N.A.
PET	318	N.A.	N.A.	N.A.	N.A.
Acero	210	N.A.	N.A.	N.A.	N.A.
Acero	298	N.A.	N.A.	N.A.	N.A.
Oro de alta R_q	165	N.A.	N.A.	N.A.	N.A.

De estos resultados extraemos las siguientes conclusiones:

- **El material y la rugosidad del substrato y el espesor de la película delgada son parámetros clave en la formación de LIPSS:** Para pulsos de femtosegundos en películas delgadas de un polímero con baja absorción lineal óptica, no solo cambian el rango de formación de las LIPSS y sus características, sino que también pueden ser el factor que determine si se pueden generar LIPSS o no. En el caso del espesor de la película delgada, podemos aplicar esta conclusión a polímeros en *bulk* si los describimos como películas con un espesor muy alto. Es posible que las LIPSS no aparezcan en un polímero en *bulk* pero sí en películas delgadas del mismo polímero.

- **El mecanismo de formación de LIPSS en estas muestras se ve afectado por la excitación de una onda superficial generada por dispersión (SSW) en la interfaz substrato-película delgada:** Para pulsos de femtosegundos en películas delgadas de un polímero con baja absorción lineal óptica, esta SSW es más intensa que la SSW habitual excitada en la superficie de la muestra y es la razón detrás de la importancia del material y la rugosidad del substrato y el espesor de la película delgada en la formación de LIPSS. Teniendo en cuenta su influencia, podemos explicar todos nuestros resultados experimentales excepto los relacionados con la muestra más delgada sobre un substrato de vidrio. En esta muestra, tanto LSFL y HSFL aparecieron con períodos que no pudimos explicar por completo.
- **En el caso de muestras sobre substratos de oro, esta SSW es un SPP:** Las simulaciones numéricas del campo eléctrico mostraron la formación de SPP en la interfaz substrato-película delgada. Además, estas simulaciones reprodujeron cualitativamente nuestros resultados experimentales, lo que nos aseguró que en las muestras con sustratos de oro la SSW mencionada anteriormente es un SPP.
- **En el caso de muestras sobre sustratos de oro, el período de las LIPSS disminuye con el R_q del substrato y el espesor de la película delgada:** Usando simulaciones numéricas, exploramos con más detalle el efecto del espesor de la película delgada y la rugosidad del substrato y lo comparamos con la teoría sobre cómo estos parámetros afectan a los SPP, y con nuestros experimentos. Encontramos un buen acuerdo entre nuestras simulaciones y la teoría en su rango de aplicación.

En cuanto a las futuras líneas de investigación, proponemos lo siguiente:

- **Investigar el régimen de rugosidad del substrato y de espesor de la película que permite la formación de LIPSS:** Por cuestiones logísticas, en esta tesis sólo irradiamos muestras sobre substratos con rugosidad o muy baja o muy alta. En cuanto a espesor de la película, no irradiamos espesores entre 205 nm y 1300 nm. Aunque estudiamos casos intermedios con nuestras simulaciones numéricas, sería interesante intentar estudiarlas experimentalmente y ver si reproducimos los resultados de las simulaciones.
- **Investigar el rango de absorción lineal óptica en el que el SSW excitado en la interfaz substrato-película delgada influye en la formación de LIPSS:** La irradiación del mismo tipo de muestras con haces Gaussianos de femtosegundos, pero con diferentes longitudes de onda, nos permitiría explorar diferentes rangos de absorción lineal óptica y definir el rango en el que debemos tener en cuenta esta SSW. El estudio podría hacerse

para muestras sobre substratos de oro, ya que la diferencia de orientación sería la propiedad más fácil de monitorizar.

- **Investigar las estructuras que aparecieron en la muestra más delgada sobre un substrato de vidrio:** La irradiación de muestras con distintos espesores entre 100 y 200 nm podría ayudarnos a comprender el efecto del espesor de la película en la formación de distintas estructuras. Otra opción sería tratar de extender las simulaciones numéricas realizadas para muestras sobre substratos de oro a estas muestras y estudiar las diferencias en el campo eléctrico entre muestras con distintos espesores.

2) Estudio del efecto de la formación de LIPSS en la modificación de las propiedades de los materiales

Hemos estudiado la generación de LIPSS en películas autosoportadas de un nanocompuesto formado de una matriz de PTT dopada con nanotubos de WS_2. Además, hemos tratado de utilizar haces complejos para generar estructuras complejas en un solo paso, aplicando este método a películas delgadas de PET depositadas sobre diferentes substratos, así como a películas delgadas de P3HT y $PC_{71}BM$, dos semiconductores orgánicos con aplicaciones en células solares orgánicas, depositadas sobre Silicio dopado.

En cuanto a las muestras de PTT-WS_2, las irradiamos con haces Gaussianos de femtosegundos a 265 nm generando LIPSS. También estudiamos la generación de LIPSS en muestras de PTT para investigar el efecto del nanoaditivo. En ambas muestras las estructuras aparecieron paralelas a la polarización del láser con un período cercano a su longitud de onda. La presencia del nanoaditivo condujo a un aumento de la densidad de energía necesaria para desencadenar la formación de LIPSS. Explicamos esto como el efecto del mayor porcentaje de cristalización y disipación térmica del PTT-WS_2. Además, caracterizamos la mojabilidad y la energía superficial de las muestras. En ambas muestras, la mojabilidad aumentó con la formación de LIPSS, y la energía superficial total se mantuvo constante. Sin embargo, su componente polar negativa aumentó considerablemente. Esto se debió a la formación de especies hidrófilas polares, causadas por una reacción con el oxígeno en el aire, catalizada por la ionización y la alta temperatura de la superficie de la muestra mientras se producía la irradiación. Finalmente, utilizamos PF-QNM para caracterizar el cambio en las propiedades nanomecánicas de la superficie después de la irradiación. En ambas muestras, la formación de LIPSS no cambió notablemente el módulo de Young, pero indujo una disminución de la fuerza de adhesión en un factor de cuatro. Atribuimos este efecto al cambio de la química superficial. De estos resultados extraemos las siguientes conclusiones:

- **Las LIPSS se pueden utilizar para cambiar la topografía de estas muestras, dándoles una funcionalidad adicional, sin dañarlas:** Esta técnica no es ablativa y el módulo de Young de la muestra se mantuvo sin cambios tras la irradiación.
- **Los LIPSS permiten la creación de pequeñas zonas con nanoestructuras diferentes**: Gracias al alto control sobre el área irradiada, podríamos cambiar los parámetros de irradiación en diferentes áreas de una muestra, creando pequeñas zonas con nanoestructuras con diferentes periodos, profundidades y orientaciones.
- **El nanoestructurado superficial con LIPSS se puede utilizar en este nanocompuesto sin ningún demérito:** Exceptuando que se necesita un pequeño aumento en la intensidad de la irradiación, las LIPSS aparecieron con las mismas características en PTT y PTT-WS_2, y los cambios que provocaron en las propiedades superficiales de las muestras fueron muy similares.

También proponemos la siguiente línea de investigación:

- **Investigar la influencia del porcentaje de nanoaditivo y su orientación en la formación de LIPSS:** En nuestros experimentos, el porcentaje de nanoaditivo fue del 0,5% en peso y se distribuyó uniformemente en la matriz PTT con los nanotubos tomando orientaciones aleatorias. Sería interesante comprobar si el leve impacto (descrito anteriormente) que el nanoaditivo tuvo en la generación de LIPSS aumentaría si incrementamos este porcentaje o si los nanotubos estuvieran predominantemente orientados en una dirección.

En cuanto a las irradiaciones con haces complejos, irradiamos películas delgadas de PET sobre diferentes substratos con haces vectoriales de femtosegundos a una longitud de onda de 515 nm. Las LIPSS aparecieron paralelas a la polarización de los haces en muestras sobre substratos de silicio o vidrio. Sin embargo, en muestras sobre substratos de oro, aparecieron estructuras orientadas perpendiculares a la polarización, pero demasiado desordenadas para ser llamadas LIPSS.

De estos resultados se extrajeron las siguientes conclusiones.

- **Conseguimos generar LIPSS en PET con formas complejas utilizando un proceso de un solo paso:** Generamos estructuras en forma de radios de bicicleta, círculos concéntricos y espirales en un solo paso utilizando haces vectoriales de femtosegundos.

- **Hay diferencias en las LIPSS inducidas por haces Gaussianos y aquellas inducidas con haces vectoriales:** Las LIPSS aparecieron en un rango de fluencia y pulsos diferente y cambian de manera diferente con el espesor de las películas delgadas. Sin embargo, no estamos seguros de si las diferencias se deben a la diferencia en la longitud de onda (795 nm en un caso, 513 nm en el otro) y la tasa de repetición (5 kHz frente a 10 Hz-3 kHz) o son debidas al uso de haces vectoriales en lugar de haces Gaussianos.

En cuanto a las futuras líneas de investigación, proponemos la siguiente:

- **Investigar las diferencias entre las LIPSS inducidas por haces Gaussianos y las inducidas con haces vectoriales:** Para aislar el efecto del tipo de haz del de la longitud de onda de irradiación y la tasa de repetición, podríamos repetir el experimento con haces Gaussianos y vectoriales con las mismas longitudes de onda y tasas de repetición.

Con respecto al P3HT, utilizamos haces vectoriales de femtosegundos a una longitud de onda de 515 nm. Encontramos LIPSS paralelas a la polarización del haz. También utilizamos haces vectoriales y de vórtice óptico de nanosegundos a 532 nm. Utilizando haces vectoriales de nanosegundos generamos LIPSS paralelas a la polarización mucho más profundas y mejor definidas que las generadas con pulsos de femtosegundos. Además, medimos una inhibición de la conductividad en las partes altas de las estructuras. Afirmamos que la causa de este cambio fue una pérdida de cristalinidad. También caracterizamos el cambio en la mojabilidad sin encontrar diferencias para las diferentes polarizaciones del haz. Para todas ellas, la muestra se volvió más hidrófila después de la irradiación. Creemos que esto se debe a cambios químicos causados por la oxidación por irradiación láser. Por otro lado, para los haces de vórtice óptico vemos LIPSS en forma de panel de abeja con períodos y profundidades similares a las otras estructuras.

Finalmente, irradiamos películas de $PC_{71}BM$ con haces vectoriales y de vórtice óptico de nanosegundos a 532 nm produciendo LIPSS paralelas a la polarización del láser de un período menor que los encontrados en P3HT y en un rango de fluencia mucho más estrecho. Sus características evolucionaron con los parámetros de irradiación igual que las estructuras encontradas en P3HT.

De estos resultados extraemos las siguientes conclusiones:

- **Conseguimos generar LIPSS en P3HT y $PC_{71}BM$ con formas complejas en un solo paso:** El uso de haces vectoriales permitió la creación de LIPSS con un patrón radial, concéntrico o espiral –siguiendo la polarización del haz.

- **Estas estructuras podrían aplicarse a la creación de nanocables con estas formas complejas:** La acusada disminución de la conductividad en la parte superior de las estructuras, respecto al efecto en su parte inferior, podría utilizarse para crear nanocables con estas geometrías.
- **Conseguimos generar LIPSS con forma de panal de abeja en un solo paso:** El uso de haces de vórtice ópticos permitió la creación de LIPSS con forma de panal de abeja. La diferente fase de los haces de vórtice óptico no debería afectar a las estructuras, por lo que creemos que su forma se debe la polarización circular del haz. Sin embargo, en otros materiales, las nanoestructuras que resultan de la irradiación circularmente polarizada son nanopuntos distribuidos uniformemente.

En cuanto a las futuras líneas de investigación, proponemos lo siguiente:

- **Investigar el origen de las LIPSS con forma de panal de abeja:** Para comprobar si esta forma está causada por la polarización circular del haz o la fase diferente de los haces de vórtice óptico, una posibilidad es irradiar P3HT y $PC_{71}BM$ con haces Gaussianos de nanosegundos con diferentes elipticidades y comprobar si podemos recrear estas estructuras en forma de panal.

3) Conclusiones metodológicas

Además de estas conclusiones científicas, desde un punto de vista metodológico, he aplicado y adquirido conocimientos avanzados sobre las siguientes técnicas durante el transcurso de esta tesis:

- **Procesado superficial de polímeros**: Se aprendió a procesar polímeros tanto en forma de películas delgadas como en *bulk*, utilizando haces Gaussianos, vectoriales y de vórtice óptico de femto- y nanosegundos en longitudes de onda que fueron desde el infrarrojo cercano hasta el ultravioleta.
- **Caracterización**: Se ha logrado familiarizarse con diferentes técnicas para caracterizar propiedades superficiales de los polímeros tanto antes como después de la irradiación. Específicamente, se aprendió a utilizar de manera autónoma AFM para su topografía y la técnica de la gota sésil para su mojabilidad.
- **Cálculo de su energía superficial:** Se aprendieron dos métodos diferentes para calcular diferentes contribuciones a la energía superficial a partir de mediciones de ángulo de contacto realizadas mediante la técnica de la gota sésil y a hacer una comparación crítica de los resultados obtenidos por cada método.

- **Simulaciones numéricas del campo eléctrico:** Se aprendió a utilizar el Módulo de Óptica de Ondas de COMSOL Multyphisics ™, un programa basado en Métodos de Elementos Finitos para simular el campo eléctrico en una película delgada de polímero depositada sobre un substrato de oro. He trabajado independientemente para entender qué aproximaciones y parámetros utilizar para obtener los resultados deseados.

En resumen, en esta tesis hemos estudiado cómo diferentes parámetros afectan a la formación de LIPSS en películas delgadas de polímeros y la capacidad que tiene la formación de LIPSS para modificar las propiedades de las muestras. Como principal aportación de esta tesis, hemos identificado el **rol clave que el material y rugosidad del substrato y el espesor de la película delgada juegan en la formación de LIPSS en películas delgadas de polímeros con baja absorción lineal óptica depositados sobre diferentes sustratos, y hemos encontrado una explicación para esta importancia en la generación de una SSW en la interfaz substrato-película delgada. Además, hemos estudiado este rol en detalle con simulaciones numéricas.** En este sentido, creemos que hemos contribuido al avance de la comprensión de la formación de LIPSS en películas delgadas de polímeros utilizando pulsos de femtosegundos.

Colophon

This thesis has been funded by the Spanish Ministry of Universities (FPU17/01859).

VNiVERSiDAD
D SALAMANCA
CAMPUS DE EXCELENCIA INTERNACIONAL

Formación y caracterización de micro- y nanoestructuras superficiales en polímeros y nanocompuestos poliméricos preparadas mediante irradiación con láseres pulsados de nano- y femtosegundos

Javier Prada Rodrigo

Salamanca, Mayo 2023.

Tesis entregada para optar al grado de
Doctor por la Universidad de Salamanca
dentro del Programa de Doctorado en Física Aplicada y Tecnología

Codirigida por:
Esther Rebollar González (IQFR-CSIC)
Pablo Moreno Pedraz (ALF-USAL).

VNiVERSiDAD
D SALAMANCA
CAMPUS DE EXCELENCIA INTERNACIONAL

D. Pablo Moreno Pedraz, Catedrático de Ingeniería Mecánica de la Universidad de Salamanca y Dª. Esther Rebollar González, Investigadora del Instituto de Química Física Rocasolano (CSIC) CERTIFICAN:

Que la presente memoria, “Formation and characterization of surface micro- and nanostructures in polymers and polymeric nanocomposites prepared by irradiation with pulsed nano- and femtosecond lasers / Formación y caracterización de micro- y nanoestructuras superficiales en polímeros y nanocompuestos poliméricos preparadas mediante irradiación con láseres pulsados de nano- y femtosegundos” ha sido realizada bajo su dirección en el Departamento de Ingeniería Mecánica de la Universidad de Salamanca por D. JAVIER PRADA RODRIGO y constituye su Tesis Doctoral para optar al grado de Doctor por la Universidad de Salamanca dentro del Programa de Doctorado en Física Aplicada y Tecnología con Mención Internacional.

En Salamanca, a 3 de mayo de 2023.

MORENO
PEDRAZ PABLO
MANUEL -
07878086B

Firmado digitalmente
por MORENO PEDRAZ
PABLO MANUEL -
07878086B
Fecha: 2023.05.03
11:43:00 +02'00'

REBOLLAR
GONZALEZ
ESTHER - DNI
50866326D

Firmado
digitalmente por
REBOLLAR
GONZALEZ ESTHER -
DNI 50866326D
Fecha: 2023.05.03
11:16:59 +02'00'

D. Pablo Moreno Pedraz

Dª. Esther Rebollar González

Resumen

En este trabajo de tesis doctoral se estudió la formación de estructuras superficiales periódicas inducidas por láser (LIPSS, siglas del inglés *Laser Induced Periodic Surface Structures*) en polímeros y compuestos de matriz polimérica en forma de películas delgadas, ya sean autosoportadas o soportadas en diferentes substratos como son silicio, vidrio, acero, oro y poli(etileno tereftalato) (PET). Los polímeros y compuestos estudiados son PET, poli(trimetileno tereftalato) (PTT), un nanocomposite compuesto por PTT y nanotubos de disulfuro de wolframio (WS_2) (PTT-WS_2) y poli(3-hexiltiofeno) (P3HT).

En el caso de películas delgadas de PET depositadas sobre distintos substratos, las irradiamos con pulsos laser Gaussianos de femtosegundo en el infrarrojo (795 nm, 64 fs, 5 kHz) para estudiar la influencia del espesor de la película de polímero y el material y la rugosidad del substrato en la formación de LIPSS. Demostramos que el espesor condiciona la formación de LIPSS, de hecho, éstas no se formaron para películas con espesores mayores de 1300 nm. Además, la irradiación produjo LIPSS perpendiculares a la polarización del láser en muestras depositadas sobre substratos de oro de baja rugosidad, y LIPSS paralelas a la polarización en muestras sobre substratos de silicio o vidrio. Sin embargo, no aparecieron LIPSS en las muestras sobre substratos de PET, ni sobre oro de rugosidad alta, ni tampoco sobre acero de rugosidad alta. El periodo, que en general fue cercano a la longitud de onda del láser, y profundidad de las estructuras, medidos con microscopía de fuerzas atómicas (AFM), adquieren valores que están condicionados por el material del substrato y el espesor de la película delgada.

A partir de estos resultados, propusimos un mecanismo de formación adicional a los ya conocidos, que se activa debido a la excitación de una onda electromagnética superficial generada por dispersión (SSW) en la interfaz película delgada-substrato. El caso de las LIPSS formadas en polímeros sobre substratos de oro, las cuales aparecen orientadas en la dirección perpendicular a la esperada, decidimos estudiarlo más a fondo con la ayuda de simulaciones numéricas del campo eléctrico. La concordancia entre las simulaciones y las medidas experimentales nos llevó a postular que la SSW que activa el mecanismo de formación de LIPSS en este caso es un plasmón polaritón superficial (SPP).

Además del trabajo que acabamos de describir, también estudiamos el efecto de las LIPSS en la modificación de distintas propiedades de nuestras muestras.

En el caso de las películas autosoportadas de PTT y PTT-WS_2, las irradiamos con haces Gaussianos de femtosegundo en el ultravioleta (265 nm, 260 fs, 1 kHz), resultando en la

formación de LIPSS paralelas a la polarización con un periodo similar a la longitud de onda del láser. En las muestras con nanoaditivo la energía necesaria para la aparición de LIPSS fue ligeramente mayor, efecto que achacamos a su mayor porcentaje de cristalinidad y mayor disipación térmica. En cuanto al efecto de las LIPSS en las propiedades micromecánicas de las muestras, fue determinado con la técnica de mapeo nanomecánico cuantitativo de fuerza máxima (PF-QNM) y fue similar para ambos materiales. El módulo de Young se mantuvo constante, pero las fuerzas de adhesión disminuyeron aproximadamente en un factor cuatro tras el nanoestructurado, lo que atribuimos a un cambio en la química superficial. Respecto a la mojabilidad, la caracterizamos utilizando la técnica de la gota sésil para medir el ángulo de contacto del agua, glicerol y aceite de parafina en las dos muestras. En ambas muestras la mojabilidad aumentó con la formación de LIPSS y la energía superficial total permaneció constante. Sin embargo, su componente polar negativa aumentó considerablemente. También achacamos este fenómeno a un cambio en la química superficial.

Por otro lado, irradiamos películas delgadas de PET depositadas sobre distintos substratos con haces vectoriales de femtosegundo en el visible (515 nm, 180 fs, 3 kHz). La irradiación con haces vectoriales sobre películas delgadas de PET provocó la formación de LIPSS paralelas a la polarización en las muestras depositadas sobre substratos de silicio o de vidrio consiguiendo estructuras en forma de radios de bicicleta, anillos concéntricos y en espiral. En cuanto a las muestras depositadas sobre substratos de oro, aparecieron estructuras perpendiculares a la polarización del láser, pero demasiado desordenadas para poder llamarlas LIPSS.

También utilizamos estos haces para irradiar P3HT, consiguiendo LIPSS con las mismas direcciones paralelas a la polarización del láser. Además, utilizamos haces vectoriales y de vórtice óptico de nanosegundo en el visible (532 nm, 5 ns, 20 Hz), induciendo la formación de LIPSS en el mismo rango que se reportó previamente para haces Gaussianos con la misma longitud de onda. Esto permitió la generación de estructuras circulares, radiales y espirales. Medimos el cambio en la conductividad encontrando una disminución muy acusada en la parte superior de las estructuras en comparación con lo que ocurre en la parte inferior. Este cambio fue causado por una pérdida de cristalinidad. También caracterizamos el cambio en la mojabilidad utilizando el método de la gota sésil para medir el ángulo de contacto del agua antes y después de la irradiación. No encontramos diferencias para las diferentes polarizaciones del haz. Para todas ellas, la muestra se volvió más hidrófila después de la irradiación. Explicamos este fenómeno teniendo en cuenta los cambios químicos causados por la oxidación inducida por la irradiación láser.

Finalmente, irradiamos películas delgadas de (6,6)fenil-C_{71}-ácido butírico metil ester ($PC_{71}BM$) con esos mismos haces de nanosegundo produciendo LIPSS paralelas a la polarización del láser de un período menor que las encontradas en P3HT y en un rango de fluencia mucho más estrecho. Sus periodos y profundidades evolucionaron con los parámetros de irradiación igual que las estructuras encontradas en P3HT.

Contenido

Capítulo 1

Introducción

En esta tesis doctoral investigamos las estructuras superficiales periódicas inducidas por láser (LIPSS) generadas con diferentes tipos de láser en varios materiales poliméricos. Estudiamos el papel de los materiales en la formación de LIPSS, es decir, el impacto que tienen sus propiedades ópticas y si el procesamiento láser se realiza en el material en *bulk* o en una película delgada depositada sobre diferentes substratos. Además, utilizamos tres tipos de configuración de la sección del haz láser, a saber, haces Gaussianos, vectoriales y de vórtice óptico, para producir nanoestructuras con diferentes características.

En esta sección, presentamos los antecedentes teóricos y el estado del arte en este campo de investigación. Posteriormente, discutiremos las propiedades de los polímeros relevantes para nuestros estudios, así como los polímeros funcionales y las formas de dar funcionalidad a los polímeros. Posteriormente, entraremos en detalle en los métodos de micro- y nanoestructurado de superficies, centrándonos principalmente en los métodos láser. Entre ellos, el más relevante en esta investigación es la generación de LIPSS, por lo que presentamos las ventajas, historia y estado del arte de esta técnica. Finalmente, presentamos la estructura de esta tesis.

1.1. Conceptos generales sobre materiales poliméricos

Un polímero es una macromolécula hecha de unidades más pequeñas repetidas, llamadas monómeros, a través de enlaces covalentes [1–3]. El proceso químico por el cual los monómeros se unen para formar un polímero se llama polimerización [1].

El número de monómeros en un polímero se ve afectado por eventos aleatorios en el proceso de polimerización [1,2]. Por lo tanto, los productos de polimerización no pueden tener un peso molecular definido. Para lidiar con esto, se necesita un tratamiento estadístico, que calcule un peso molecular característico. Los pesos moleculares característicos más utilizados son el peso molecular medio en número (M_{n}) y el peso molecular medio en peso (M_{w}) (véase la Figura 1.1)

[1–3] . Suponiendo un número de moléculas N_i para cada peso molecular M_i con un peso total asociado a ese peso molecular $W_\mathrm{i} = N_\mathrm{i} \cdot M_\mathrm{i}$, podemos definir M_n como:

$$M_\mathrm{n} = \sum N_\mathrm{i} M_\mathrm{i} \,/ \sum N_\mathrm{i} \tag{1.1}$$

y M_w como:

$$M_\mathrm{w} = \sum W_\mathrm{i} M_\mathrm{i} \,/ \sum W_\mathrm{i} = \sum N_\mathrm{i} M_\mathrm{i}^2 \,/ \sum N_\mathrm{i}\, M_\mathrm{i} \tag{1.2}$$

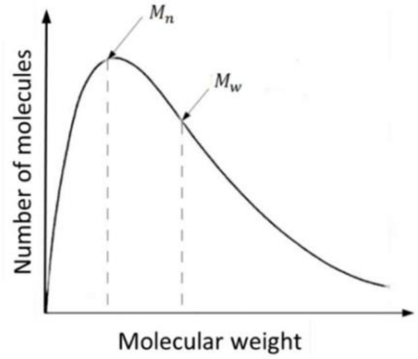

Figura 1.1. *Distribución típica de los pesos moleculares de un polímero. Figura modificada de [4].*

Otra propiedad importante de los polímeros es su estructura molecular. Según ella, los polímeros se clasifican como amorfos o semicristalinos [1–3]. Un polímero amorfo tiene sus cadenas aleatoriamente distribuidas, y uno semicristalino tiene regiones desorganizadas y regiones organizadas. En la práctica, es imposible encontrar un polímero completamente cristalino, solo polímeros semicristalinos con diferentes grados de cristalinidad [1,2]. La organización jerárquica de los átomos en polímeros semicristalinos se muestra en la Figura 1.2.

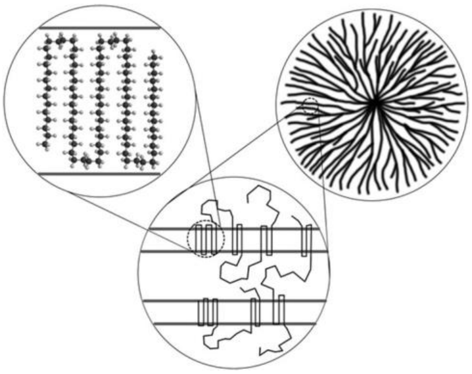

Figura 1. 2. *Estructura jerárquica de un polímero semicristalino [5].*

En nuestro trabajo, la temperatura a la cual las cadenas poliméricas puedan fluir es un parámetro relevante, ya que utilizaremos un proceso predominantemente térmico para nanoestructurar las muestras poliméricas. Para los polímeros amorfos, esa temperatura se llama temperatura de transición vítrea (T_g) [1,2]. Su valor es específico de cada polímero y depende de múltiples factores como el peso molecular y las interacciones químicas. En cuanto a los polímeros semicristalinos, sus regiones amorfas podrán fluir a T_g, pero sus regiones cristalinas necesitarán una temperatura más alta para romper la estructura cristalina. Esta temperatura se denomina temperatura de fusión (T_m) [2,3].

Los polímeros por sí mismos pueden tener propiedades únicas interesantes que a menudo están determinadas por la presencia de grupos funcionales en su estructura química [6]. Además, es posible dar a los polímeros una funcionalidad adicional con estrategias como incluir nanoaditivos en una matriz polimérica para crear un nanocomposite [7,8] o crear micro- y nanoestructuras en la superficie del polímero [9,10]. En este trabajo, investigamos principalmente este último método y lo aplicamos a un polímero semiconductor, concretamente, poli(3-hexiltiofeno) (P3HT), como representante de polímeros funcionales; a un nanocomposite: poli(trimetileno tereftalato) (PTT) dopado con nanotubos de disulfuro de tungsteno (WS_2) (PTT-WS_2); y a un polímero básico: poli(etileno tereftalato) (PET).

1.1.1. Polímeros semiconductores

Los polímeros se han considerado tradicionalmente materiales aislantes. Sin embargo, algunos polímeros como P3HT, poli(2,5-bis(3-tetradeciltiofeno-2-yl)tieno[3,2-b]tiofeno) (PBTTT) y poli(p-fenileno vinileno) (PPV) son intrínsecamente conductores debido a su estructura molecular. Todos ellos tienen o bien enlaces conjugados, es decir, enlaces simples y dobles alternos a lo largo de la columna vertebral del polímero, o están compuestos de anillos aromáticos unidos por enlaces simples carbono-carbono [11]. La conductividad de los polímeros conjugados se debe a la deslocalización de electrones π que actúan como la banda de conducción en un metal [11]. Por lo tanto, se ve afectada por la regioregularidad del polímero ya que la disposición de los átomos en cada monómero debe ser la misma para mantener las cadenas de enlaces alternos ininterrumpidas [12]. El nombre utilizado para esta "banda de conducción" es Orbital Molecular Desocupado Más Bajo (LUMO, del inglés *Lowest Unoccupied Molecular Orbital*) y la "banda de valencia" correspondiente se llama Orbital Molecular Ocupado Más Alto (HOMO, del inglés *Highest Occupied Molecular Orbital*). La diferencia en los niveles de energía HOMO-LUMO es el equivalente al GAP en un semiconductor [11]. Además de esta conductividad intrínseca, el dopaje químico y la alineación mecánica de las cadenas poliméricas pueden aumentar la conductividad de un polímero en muchos órdenes de magnitud [11].

El interés en el estudio de polímeros semiconductores ha aumentado debido a sus aplicaciones potenciales en electrónica como el uso de PBTTT en transistores de efecto de campo [13], el de PPV en LED poliméricos [14] y el de P3HT en el ámbito de los dispositivos fotovoltaicos como absorbente de luz y/o material donador de electrones [15].

1.1.2. Nanocomposites

Los nanocomposites se crean introduciendo un porcentaje de un nanomaterial, llamado aditivo, en una matriz polimérica. Los nanomateriales tienen excelentes propiedades mecánicas, eléctricas y térmicas que pueden transmitirse parcialmente al nanomaterial incluso para proporciones de nanomaterial a matriz polimérica inferiores al 1%. Sus propiedades se pueden adaptar modificando los dos materiales, la difusión del aditivo en la matriz y el porcentaje de aditivo introducido [16]. Estas propiedades han popularizado su uso en biomateriales [17], recubrimientos protectores [18], tecnología de película delgada [19] y muchos otros:

- Biomateriales para la regeneración del tejido óseo [17]: se utiliza una amplia gama de matrices poliméricas biocompatibles como quitosano, colágeno, celulosa, polietilenglicol, poli(ácido láctico) y poliuretano. Con respecto a los aditivos, la nano-hidroxiapatita [20], la nano-zirconia [21], la nano-sílice [22], las nanopartículas de plata [23], el dióxido de nano-titanio [24] y el óxido de grafeno [25] se emplean con frecuencia para conseguir propiedades tales como una gran área de superficie, resistencia mecánica mejorada, estabilidad, adhesión celular mejorada, proliferación y diferenciación celular.
- Recubrimientos protectores [18]: dado el gran número de propiedades diferentes que pueden tener los nanocomposites, es posible diseñar diferentes sistemas para diferentes aplicaciones. Algunos ejemplos son la nano-sílice en una matriz de poli(metacrilato de metilo) (PMMA), utilizada para materiales anticorrosivos [26] y nanotubos de halloysita en una matriz epoxi, utilizada como material ignífugo [27].
- Tecnología de película delgada [19]: se han investigado matrices de poliamida con una multitud de aditivos diferentes, como nanopartículas de zeolita, nano-sílice, nanopartículas de Ag y nanotubos de carbono para el filtrado de agua.

1.2. Micro- y nanoestructurado superficial de polímeros

El nanoestructurado superficial es una estrategia común, que consiste en cambiar la superficie de un material en la nanoescala para mejorar algunas de sus propiedades mecánicas, químicas o de cualquier otro tipo. En los polímeros, esta estrategia es útil para mejorar sus propiedades mecánicas superficiales o para dar al material una funcionalidad añadida [9,10], en algunos casos imitando a la naturaleza y creando las llamadas superficies biomiméticas [28]. Algunos ejemplos de sus aplicaciones son:

- Mojabilidad: La creación de nanoestructuras en una superficie puede diseñarse para crear superficies superhidrófilas o superhidrófobas, por ejemplo, para proporcionar superficies autolimpiables [29]. El control de la mojabilidad en un sentido más amplio puede aplicarse a cualquier líquido y tiene aplicaciones en biomateriales como por ejemplo para el control de la absorción de proteínas [9].
- Antibacteriano: Las superficies nanoestructuradas con características con un tamaño más pequeño que las bacterias evitan su proliferación, ya sea porque disminuye la adherencia, o porque las nanoestructuras perforan la bacteria, matándola [30,31].
- Crecimiento celular: Crear superficies con características en la escala del tamaño de las células puede mejorar el crecimiento celular. Además, este crecimiento puede ser guiado a través de un diseño adecuado de las nanoestructuras [32]. Esta estrategia se ha aplicado en campos como la implantología dental [33].
- Tribología: El nanoestructurado de una superficie reduce el área de contacto y por lo tanto las propiedades de adhesión y fricción [34].
- Fotovoltaica orgánica: Los electrones y los huecos se generan en la interfaz donante-aceptor. Por lo tanto, aumentar el área de esta interfaz mejoraría el rendimiento del dispositivo. Esto se puede hacer sin incrementar el tamaño del dispositivo aumentando la rugosidad de la interfaz. Además, las nanoestructuras superficiales también pueden mejorar la absorción de luz como resultado de la dispersión y la excitación de un plasmón superficial [35].
- Sensores: De la misma manera que mejoran el rendimiento fotovoltaico, las nanoestructuras pueden aumentar la señal de los sensores debido a los efectos de confinamiento del campo [36] o debido al aumento del área de superficie [37].

Teniendo en cuenta lo diferentes que son todas estas aplicaciones, existe un interés en desarrollar las técnicas de nanoestructurado adecuadas para cada aplicación. Actualmente, las técnicas más comunes para el nanoestructurado superficial son las técnicas litográficas [38,39]. Estas técnicas tienen la ventaja de una alta reproducibilidad y bajo coste, pero generalmente son técnicas complejas de muchos pasos y requieren acceso a una instalación de atmósfera controlada, como una sala limpia. Además, su resolución, área nanoestructurada y versatilidad son bastante limitadas. Por estas razones, las técnicas de procesado láser [40–43] han ido desarrollándose como una alternativa.

1.3. Estructurado superficial láser de polímeros

Las técnicas de procesado láser aprovechan la capacidad del láser para concentrar con precisión la energía en un área muy pequeña. Se dividen en dos grupos:

- Enfoques *bottom-up*: se basan en el depósito de una cantidad controlada de material sobre un substrato hasta que se crea la estructura deseada. Algunos ejemplos son la transferencia directa inducida por láser (LIFT, del inglés *Laser Induced Forward Transfer*) [40], útil para depositar una capa delgada de un material sobre un substrato transparente, y la evaporación por láser pulsado asistida por matriz (MAPLE, del inglés *Matrix Assisted Pulsed Laser Evaporation*) [44], que utiliza la mediación de un disolvente para transferir eficientemente materiales blandos a un substrato. Además, existen técnicas derivadas de ellas, para casos especiales, como la Escritura Directa MAPLE [44] —para materiales sensibles a la elevación de temperatura— y la Imagen Térmica Inducida por Láser (LITI, del inglés *Laser Induced Thermal Imaging*) [44] —para aplicaciones microelectrónicas plásticas.
- Enfoques *top-down*: Parten de un material en *bulk* y eliminan o reorganizan partes de éste para crear la estructura deseada. Algunos ejemplos son la Ablación Láser [42,45], que utiliza el láser directamente para eliminar el material, y la Litografía de Interferencia Láser (LIL, del inglés *Laser Interference Lithography*) [41], que utiliza el patrón de interferencia de dos o más haces láser para eliminar el material, creando micro y nanoestructuras. La técnica que estudiamos en esta tesis —LIPSS—, es también una técnica *top-down*. Las LIPSS son ondulaciones periódicas que se forman al irradiar un material con un láser en un rango de intensidad particular. Esta técnica puede crear nanoestructuras con períodos desde cientos de nanómetros a varias micras y profundidades desde menos de diez nanómetros hasta varios cientos. Sus principales ventajas son una gran área de procesado, simplicidad de operación y que,

comparada con otras técnicas, no requiere grandes equipos [46–48]. Discutiremos este método en detalle en la próxima sección.

1.3.1. Estructuras superficiales periódicas inducidas por láser

Las estructuras superficiales periódicas inducidas por láser son ondulaciones periódicas que se forman al irradiar un material con un láser en un rango de intensidad particular. Fueron descubiertas por Birnbaum [49] en el fondo de un cráter de ablación. Sipe *et al*. [50–52] las explicaron como resultado de la interferencia de la onda incidente con una onda dispersada en superficie, que en el caso de los metales puede ser un Polaritón de Plasmón Superficial (SPP, del inglés *Surface Plasmon Polariton*), lo que resulta en un aumento no homogéneo de la temperatura en la superficie del material. Incluso encontraron una fórmula para su período ($\varLambda$):

$$\varLambda = \frac{}{\mathrm{n_{eff}} \pm \mathrm{sin0}} \tag{1.3}$$

donde λ es la longitud de onda del láser, θ su ángulo de incidencia y n_{eff} el índice de refracción efectivo en una región cerca de la superficie, llamada región *selvedge* [53].

Desde entonces, se ha descrito la formación de LIPSS para pulsos láser con diferentes duraciones, desde ns [54], pasando por ps [55], hasta fs [56], en todo tipo de materiales [57–60], con una dirección que es paralela o perpendicular a la polarización del láser, dependiendo del material. Además, se han desarrollado estrategias que permiten el nanoestructurado de grandes áreas con alta regularidad y velocidad [61–63], así como métodos para usar LIPSS para crear diferentes nanoestructuras como redes de difracción lineales, rejillas y matrices de nanopuntos [54]. Las modificaciones fisicoquímicas producidas en el proceso de formación de LIPSS también se han estudiado utilizando diferentes métodos [64–67].

La técnica para generar LIPSS con pulsos láser de femtosegundo ofrece ventajas relacionadas con las características particulares de la interacción láser-materia en este régimen de tiempo. A saber, la absorción óptica lineal del material es menos crítica, y el tiempo de interacción es más corto que los tiempos de relajación térmica, dando como resultado una zona afectada térmicamente mucho menor [68], lo que permite un mejor control de la zona nanoestructurada por la irradiación. Sin embargo, esta técnica aún no se entiende completamente. Bonse *et al.* [69] adaptaron la teoría de Sipe para considerar los cambios en el índice de refracción debidos a la intensidad del láser, siguiendo el modelo de Drude, pero no se pudo explicar la formación de LIPSS en su totalidad.

En particular, cuando se utilizan pulsos de femtosegundos existen dos tipos de LIPSS: las anteriormente descritas LIPSS con un período dado por la ec. 1.3, llamadas LIPSS de baja frecuencia espacial (LSFL, del inglés *Low Spatial Frequency LIPSS*), y las llamadas LIPSS de alta frecuencia espacial (HSFL, del inglés *High Spatial Frequency LIPSS*), con periodos inferiores a la mitad de la longitud de onda del láser. Dependiendo del material, las HSFL pueden aparecer paralelas o perpendiculares a la polarización del láser (ver Tabla 1.1). Aunque esta clasificación no ha sido ampliamente adoptada, Bonse *et al.* las subdividieron en dos tipos [46]: las HSFL tipo 1, a menudo vistas en dieléctricos y semiconductores, con un período de solo unas pocas decenas de nanómetros y una profundidad que puede alcanzar los cientos de nanómetros; y HSFL tipo 2, a menudo vistas en metales, con períodos de unos pocos cientos de nanómetros y profundidades de solo unas pocas decenas de nanómetros.

Tabla 1.1. *Orientación y período de las HSFL encontradas en diferentes materiales.*

Material	**Orientación**	**Período (Λ)**	**Referencia**
Si	Paralelo	$\Lambda \leq 0.25\,\lambda$	[70]
Sílice fundida	Perpendicular	$\Lambda \leq 0.25\,\lambda$	[71]
Cuarzo	Perpendicular	$\Lambda \leq 0.21\,\lambda$	[71]
Ti	Paralelo	$0.08 \leq \Lambda / \lambda \leq 0.12$	[72]
TiN	Perpendicular	$\Lambda \leq 0.16\,\lambda$	[73]
Acero (800H)	Paralelo	$0.15 \leq \Lambda / \lambda \leq 0.24$	[74]
InP	Perpendicular	$\Lambda \leq 0.24\,\lambda$	[75]
Diamante	Paralelo	$\Lambda \leq 0{,}26\,\lambda$	[76]
ZnO	Perpendicular	$0.25 \leq \Lambda / \lambda \leq 0.35$	[75,77]
ZnSe	Paralelo	$\Lambda \sim \lambda / 2n$	[78]
Zafiro	Perpendicular	$\Lambda \leq 0.34\,\lambda$	[75]

El mecanismo de formación de las HSFL sigue siendo controvertido hoy en día [79]. Se han propuesto nuevos modelos teóricos para explicar estos fenómenos, incluyendo un modelo basado en la autoorganización a partir de altas inestabilidades electrostáticas originadas por el láser [80], uno basado en la hidrodinámica de películas delgadas [81], otro basado en el análisis de una excitación electrónica cuando se crea plasma de corta duración [82,83] u otro modelo que utiliza métodos de diferencias finitas en el dominio para resolver las ecuaciones diferenciales de Maxwell para materiales lineales, isótropos, dispersivos y sin pérdidas magnéticas [84]. Además, se ha reportado para semiconductores y metales [85] la aparición de otro tipo de estructuras más grandes, tanto en profundidad como en período, a mayores fluencias y número de pulsos que LSFL y HSFL [85]. El alcance de esta tesis es casi exclusivamente el estudio de LSFL, por lo que a partir de ahora nos referiremos a ellas como LIPSS.

Para pulsos de ns y fs, las LIPSS en polímeros en *bulk* aparecen paralelas a la polarización. Pueden formarse no sólo debido a la eliminación de material [86], sino también, para fluencias más bajas, debido a una reorganización del material [47,56]. Para que ocurra este reordenamiento, el polímero debe calentarse por encima de una temperatura a la que sus cadenas poliméricas puedan fluir. Como se discutió en la Sección 1.1, esta temperatura es T_g para polímeros amorfos y T_m para polímeros cristalinos [4,87].

La influencia de los parámetros del láser en la formación de LIPSS se ha estudiado extensamente tanto para láseres de ns como de fs mostrando comportamientos similares [69,88,89]. Estos estudios demostraron que el período y la profundidad de las LIPSS están influenciados no sólo por la longitud de onda y el material (como se muestra en la ec. 1.3) sino también por la intensidad y el número de pulsos utilizados. En general, tanto la profundidad como el período de las estructuras crecen con la fluencia hasta estancarse. Tienen la misma relación con el número de pulsos, lo que se atribuye a efectos de incubación [47,90–92].

Además, dado que las estructuras son paralelas a la polarización, el tipo de haz que utilizamos puede cambiar la dirección de las estructuras. Exploraremos esto usando haces Gaussianos, vectoriales y de vórtice óptico.

1.3.1.1. Tipos de haces para la formación de LIPSS

Cualquier haz puede ser representado por ec. 1.4.

$$\vec{E}(\vec{r},t) = \vec{A}(\vec{r},t)e^{i\,(\vec{\ },\ )} \tag{1.4}$$

donde $\vec{E}$ es el campo eléctrico, $\vec{r}$ es el vector de posición, t es el tiempo, el argumento de la exponencial ϕ es el estado de oscilación del campo eléctrico, llamado fase, el módulo de $\vec{A}$ es la amplitud del campo eléctrico, y su dirección es la dirección del campo eléctrico, que, tomando su dependencia con $\vec{r}$ y t en cuenta, da la llamada polarización del haz. El conjunto de los puntos donde la fase es constante se llama frente de onda. Para ondas armónicas planas polarizadas linealmente [93], es decir, ondas con una sola frecuencia (*f*), amplitud constante, con una dirección del campo eléctrico independiente de $\vec{r}$ y t, y un frente de onda plano, esa ecuación se convierte en ec. 1.5.

$$\vec{E}(\vec{r},t) = \vec{A}\, e^{\mathrm{i}(\text{-}\vec{k}\cdot\vec{\ }\text{-w}\ +\ \ 0)} \tag{1.5}$$

donde $\omega = 2\pi f$ es la frecuencia radial, $\vec{k}$ es el vector de onda, su módulo $k = \frac{\mathrm{wn}}{\mathrm{e}} = \frac{2\mathrm{rrn}}{\ }$ el número de ondas, su dirección es la dirección de propagación de la onda, n es el índice de refracción, c es la velocidad de la luz en el vacío, y ϕ_0 es la fase inicial a $t = 0$ y $\vec{r} = 0$.

Haces Gaussianos

Los haces láser generalmente pueden ser aproximados por haces Gaussianos [94]. El campo puede ser representado por la ec. 1.6, si está polarizado linealmente, siendo z la dirección de propagación y x la dirección de polarización, poniendo el origen de coordenadas en el punto donde el radio del haz es mínimo.

$$\vec{E}(\rho,z,t) = A_{0}\vec{u}_{\mathrm{x}}\, \frac{\mathrm{w}_0}{\mathrm{w(z)}}\, e^{-\frac{\mathrm{p}^2}{\mathrm{(z)}^2}}\, e^{\mathrm{i}\left(\mathrm{k\,z+k}\frac{\mathrm{p}^2}{2\mathrm{R(z)}}-\mathrm{lf;(z)\text{-}w}\ \right)} \tag{1.6}$$

donde A_0 es la amplitud máxima del campo eléctrico, w_0 es el radio mínimo del haz llamado cintura del haz, $w(z) = w_0 \mathrm{J}\overline{1 + \left(\frac{\mathrm{z}}{\mathrm{z_R}}\right)^2}$ es el radio del haz, $z_{\mathrm{R}} = \frac{\mathrm{rrw}_0^2\mathrm{n}}{\ }$ es la distancia a lo largo de la dirección de propagación desde la cintura del haz hasta el punto en el que se duplica el área del haz, llamado rango de Rayleigh $(w(z_{\mathrm{R}}) = \sqrt{2}\, w_0)$, $R(z) = \frac{\mathrm{z}^2+\mathrm{z}^2_{\mathrm{R}}}{\mathrm{z}}$ es el radio de curvatura del frente de onda, $\rho = \mathrm{j}\overline{x^2 + y^2}$ es la coordenada cilíndrica del radio, $\psi(z) = arctan\left(\frac{\mathrm{z}}{\mathrm{z_R}}\right)$ es la diferencia de fase adquirida por el haz alrededor de la región focal, llamada fase de Gouy, y $\vec{u}_{\mathrm{x}}$ es el vector unitario en la dirección x.

Haces Vectoriales

Los haces vectoriales [95], también llamados haces con espín, son haces donde la fase se comporta como la de un haz Gaussiano, pero la polarización varía con el acimut $\beta = arctan\left(\frac{\mathrm{y}}{\mathrm{x}}\right)$. Esta variación en la polarización fuerza un cero en intensidad en el centro del haz para evitar una singularidad, dándoles un perfil espacial de intensidad anular que puede ser aproximado por el polinomio de Laguerre-Gauss LG_{0l} [96]. Una propiedad importante de estos haces es su carga topológica l, definida como el número de rotaciones en la variación azimutal de la polarización. Un haz vectorial que se propaga en la dirección z puede describirse mediante la ec. 1.7:

$$\vec{E} = A_0\, LG_{0l}(x,y)\, e^{\text{-iw}}\ \left(cos\,(|l|\beta)\,\vec{u}_{\mathrm{x}} - sin(|l|\beta)\,\vec{u}_{\mathrm{y}}\right) \tag{1.7}$$

donde $\vec{u}_y$ es el vector unitario en la dirección y.

Estos haces se han utilizado para crear nanoestructuras complejas en metales [97], semiconductores [98] y dieléctricos [99].

Haces de vórtice óptico

Los haces de vórtice óptico [100], también conocidos como haces con momento angular orbital, son haces con el mismo perfil espacial de intensidad que los haces vectoriales, pero su polarización es circular y espacialmente constante, y su fase varía acimutalmente. Estos haces también tienen una propiedad importante llamada carga topológica l, pero aquí se define como el número de rotaciones en la variación azimutal de la fase.

Un haz de vórtice que se propaga en la dirección z puede describirse mediante la ec. 1.8:

$$\vec{E} = A_0 \; LG_{0l}(x, y) \; e^{-\mathrm{iw}} \; cos(|l|\beta) \; (\vec{u}_{\mathrm{x}} + e^{\mathrm{irr}/2}\vec{u}_{\mathrm{y}}) \tag{1.8}$$

Estos haces se han utilizado para crear nanoestructuras complejas en materiales como el silicio [101] y en aleaciones metálicas [102]. En cuanto a los polímeros, se han utilizado para crear microestructuras complejas por ablación en azo-polímeros [103].

Mostramos las principales características de los haces Gaussianos, vectoriales y de vórtice óptico en la Figura 1.3.

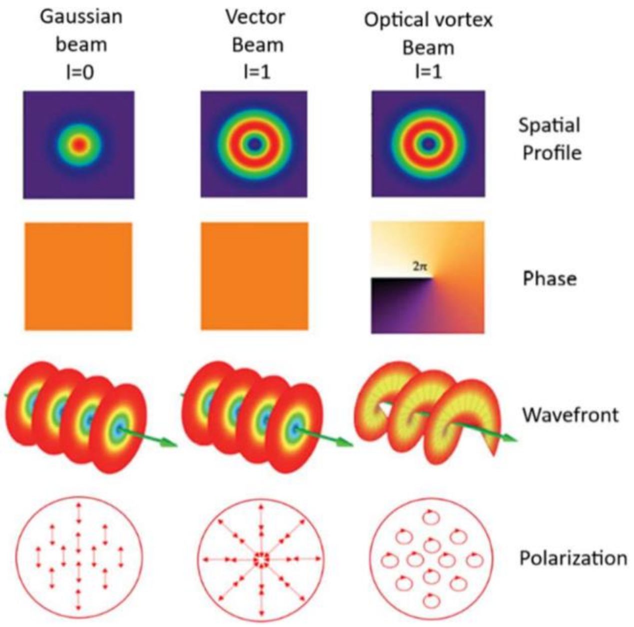

Figura 1.3. *Características de los haces Gaussianos, vectoriales y de vórtice óptico. (Imagen modificada, crédito: E-karimi, Creative Commons Attribution-Share Alike 3.0 unported).*

1.3.1.2. LIPSS en películas delgadas

Ha habido un creciente interés en la investigación de LIPSS en películas delgadas de diferentes materiales debido a sus posibles aplicaciones [47,56,104–108]. Para la formación de LIPSS, debemos tener en cuenta consideraciones adicionales, como la influencia de las diferentes propiedades del substrato y del espesor de la película. Cui *et al*. [107] reportaron que la conductividad térmica del substrato afecta al umbral de formación de LIPSS en la película delgada de polímero que lo cubre, y vincularon la organización de las LIPSS al espesor de la película de polímero. Además, Nürberger *et al*. [108] observaron un cambio en la orientación de las LIPSS formadas en un sistema multicapa de SiO_2/Si variando el espesor del SiO_2 dieléctrico sobre el substrato semiconductor de Si. Lo explicaron como una competencia entre dos mecanismos, el SPP excitado en la frontera película delgada-substrato, que produciría LIPSS perpendiculares a la polarización del láser, y la onda superficial dispersada excitada en la superficie de la película delgada de óxido, lo que resultaría en la generación de LIPSS paralelas a la polarización. Además, algunos trabajos recientes en los que se forman LIPSS en la superficie de películas delgadas de materiales dieléctricos tienen un interés notable, como es el caso de algunos óxidos en los que se forman LSFL sin ninguna interfaz plasmónica [59,109–112]. En cuanto a las películas delgadas de polímero, hay estudios que muestran la influencia del material del substrato en la generación de LIPSS para pulsos de nanosegundos y femtosegundos UV [91,107], donde las diferentes propiedades de transferencia de calor del substrato cambian el rango de fluencia para la formación de LIPSS. Además, otros trabajos que utilizan pulsos de femtosegundos en el infrarrojo cercano [113] revelaron que la formación de LIPSS solo ocurrió para algunos tipos de substratos.

1.3.1.3. Plasmones Polaritones Superficiales y formación de LIPSS

Como hemos reportado brevemente en las últimas secciones, para muestras metálicas, la interferencia de la onda incidente con un SPP excitado en la superficie de la muestra es el mecanismo que desencadena la formación de LIPSS y Nürberger *et al*. [108] propusieron el SPP como uno de los mecanismos que contribuyen a la formación de LIPSS en una película delgada de SiO_2 depositada sobre Si, un semiconductor. Puesto que estamos estudiando películas delgadas de polímeros depositados sobre diferentes substratos, algunos de los cuales son metálicos y semiconductores, vale la pena discutir el SPP y sus propiedades con más detalle.

SPP es una onda dispersa superficial que puede ser excitada en la interfaz entre un metal y un dieléctrico [114]. La solución de las ecuaciones de Maxwell para las condiciones geométricas de la excitación de SPP da como resultado una onda evanescente magnética transversal (TM). Para una interfaz plana en $y = 0$, se puede elegir el eje x para que el campo SPP se describa mediante la ec. 1.9:

$$E_{\mathrm{d,m}} = (E_{\mathrm{x}}, E_{\mathrm{yd,ym}}, 0)\, exp(-k_{\mathrm{yd,ym}} y)\, exp\,[i(k_{\mathrm{SPP}} x - \omega t)] \tag{1.9}$$

donde $k_{\mathrm{SPP}} = \frac{\mathrm{w}}{\mathrm{e}} \mathbf{J} \overline{\frac{\mathrm{E_d E_m}}{\mathrm{E_d + E_m}}}$ es el módulo del vector de onda del SPP para interfaces planas y medios con espesor mucho mayor que la distancia de penetración del SPP, ε es la permitividad eléctrica, los subíndices d y m corresponden al dieléctrico y el metal respectivamente y $k^2_{\mathrm{yd,ym}} = k^2_{\mathrm{SPP}} - \varepsilon_{\mathrm{d,m}} \left(\frac{\mathrm{w}}{\mathrm{e}}\right)^2$ y $E_{\mathrm{yd,ym}} = i \frac{\mathrm{k_{SPP}}}{\mathrm{k_{yd,ym}}} E_{\mathrm{x}}$.

Las propiedades relevantes para nuestro caso son el período espacial Λ y la longitud de penetración en el metal P_{m} y en el dieléctrico P_{d}. El período espacial se define como es habitual, y la longitud de penetración se define como la distancia a la interfaz a la que la amplitud del campo SPP decae $1/e$ veces. Estas propiedades se pueden obtener del módulo del vector de onda k_{SPP} como [114]:

$$\Lambda = 2\pi/k_{\mathrm{SPP}} \quad ; \quad P_{\mathrm{d}} = 1/Re(k_{\mathrm{yd}}) \quad ; \quad P_{\mathrm{m}} = 1/Re(k_{\mathrm{ym}}) \tag{1.10}$$

SPP es una onda TM, por lo tanto, la dirección de su vector de onda es paralela a la proyección de la polarización del láser en la interfaz. Como se ve en la definición de k_{SPP}, ya que $\varepsilon_{\mathrm{d}} > 1$ y $Re(\varepsilon_{\mathrm{m}}) < 0$, el módulo del vector de onda del SPP es mayor que el de la luz incidente (ω/c), por lo que para excitar SPP necesitamos aumentar este vector de onda. Hay muchas configuraciones de irradiación para lograr esto que se pueden encontrar en la bibliografía [115]. En este trabajo, los SPP deberían poder excitarse como resultado de la dispersión debido a la rugosidad del substrato.

En cuanto a la influencia de los diferentes parámetros sobre el SPP, existen trabajos teóricos sobre la influencia de las propiedades de una película delgada depositada sobre un substrato y el SPP generado. Según la teoría [116], el espesor de la película delgada cambia el vector de onda SPP y, por lo tanto, el periodo LIPSS, siguiendo la ec. 1.11:

$$e^{-4\mathrm{k_{tf}d}} = \frac{\mathrm{k_{tf}/E_{tf} + k_s/E_s}}{\mathrm{k_{tf}/E_{tf} - k_s/E_s}} \, \frac{\mathrm{k_{tf}/E_{tf} + k_{air}/E_{air}}}{\mathrm{k_{tf}/E_{tf} - k_{air}/E_{air}}} \tag{1.11}$$

donde k es el módulo del vector de onda y los subíndices $tf,\ s$ y air se refieren a la película delgada, el substrato y el aire respectivamente. Como se puede ver en [116], para películas de pequeño espesor, ec. 1.11 se puede aproximar como:

$$k_{\mathrm{SPP-}} = k_{\mathrm{SPP}} + k_{\boxed{?}} + k_{\boxed{?}} \tag{1.12}$$

con k_a y k_b:

$$k_a = \frac{2rr}{}\left(\frac{E_{tf}-E_{air}}{E_{tf}}\right)\left(\frac{E_{air}Re(E_s)}{E_{air}+R\ (E_s)}\right)^2 \left(\frac{E_{tf}-R\ (E_s)}{E_{air}-Re(E_s)}\right)\left(-Re(\varepsilon_s)\varepsilon_{ai}\ \right)^{-\frac{1}{2}}\left(\frac{2rr}{}d\right) \tag{1.13}$$

$$k_b = k_a \frac{1 \quad k_a}{2\ Re(k_{SPP})}\left(\frac{2(2E_{air}^2-E_{tf}^2)}{E_{air}(E_{air}-E_{tf})}+\frac{Re(E_s)+E_{air}}{-E_{air}}\right)-\frac{1}{2}\frac{/m(E_s)}{Re(E_s)} \tag{1.14}$$

En cuanto al efecto de la rugosidad, también hay estudios sobre su influencia en la formación de SPP [117–120] y su impacto en las propiedades de las LIPSS [121]. Estos estudios se centran en la influencia de dos parámetros de rugosidad. La rugosidad cuadrática media (R_q),

$$R_q = \left[\frac{1}{LA}\int_0^L\int_0^A Z(x,y)^2dx\,dy\right]^{1/2} \tag{1.15}$$

siendo $Z(x, y)$ la función de altura de la superficie, da una indicación de la altura o profundidad de los picos y valles de la superficie; y la longitud de autocorrelación (σ), definida como la distancia horizontal a la que la función de autocorrelación (ec. 1.16) disminuye a 0.2 más rápidamente, lo que da una indicación de la anchura de los picos y valles de la superficie.

$$ACF(t_x,t_y) = \frac{\int_0^L\int_0^A Z(x,y)Z((x-\ _x),(y-\ _y))dxdy}{\int_0^L\int_0^A Z(x,y)Z(x,y)dxdy} \tag{1.16}$$

Para obtener más información sobre su definición matemática, se puede consultar la referencia [122].

Volviendo al asunto que nos ocupa, en el apéndice de la referencia [117], se demostró que para $\varepsilon_s = \varepsilon_s + i\ \varepsilon_{si}$ con $|\varepsilon_s\ | \gg |\varepsilon_{si}|$, R_q y σ causan un cambio en el vector de onda del SPP, que, siempre que R_q sea mucho menor que la longitud de onda del láser incidente, sigue la ec. 1.17:

$$\Delta k_{SPP} = \frac{R_q^2 Cl^2}{2}\frac{IE_{sr}E_{tf}I^{1/2}}{(E_{sr}+E_{tf})^2}e^{-k_{SPP}^2Cl^2/4}F(k_{SPP}, k, \sigma) \tag{1.17}$$

aquí $F(k_{SPP},\ k,\ \sigma)$ es una función independiente de R_q. De la ec. 1.17 y la ec. 1.10 se deduce que el período y la longitud de penetración del SPP disminuyen monótonamente con R_q y tienen una dependencia más compleja con σ.

Es trivial mostrar la importancia del material del substrato en sí, ya que el SPP solo se puede generar en interfaces metal-dieléctrico, y sus propiedades están fuertemente influenciadas por la permitividad eléctrica de los materiales en ambos lados de la interfaz [114].

1.4. Estructura de la tesis

Esta tesis se estructura en siete capítulos. En este primer capítulo, hemos introducido los antecedentes teóricos y el estado del arte en este campo de estudio.

En el Capítulo 2, describiremos las propiedades de los materiales con los que trabajamos y los métodos para preparar nuestras muestras, así como los diferentes esquemas de irradiación y técnicas de caracterización utilizados para cada muestra. Por último, explicaremos los métodos de simulación numérica utilizados para comprender mejor los cambios en algunas de las muestras después de la irradiación.

En los capítulos del 3 al 6, mostraremos los resultados de nuestros experimentos, así como una discusión de estos resultados. En el Capítulo 3, exploraremos la formación de LIPSS en películas delgadas de PET de diferente espesor sobre diferentes substratos. En el Capítulo 4, estudiaremos el mecanismo de formación de LIPSS en las muestras con substratos de oro con la ayuda de simulaciones numéricas. En el Capítulo 5, entraremos en la caracterización de las propiedades de las LIPSS que pueden ser interesantes para potenciales aplicaciones, como son el cambio en las propiedades micromecánicas, topografía, energía superficial y mojabilidad inducida por la formación de LIPSS en el nanocomposite PTT-WS_2. En el Capítulo 6, se estudian los cambios en la conductividad después de generar LIPSS con haces vectoriales en P3HT y (6,6)fenil C_{71} ácido butírico metil ester ($PC_{71}BM$).

Finalmente, en el Capítulo 7, resumiremos los principales resultados de esta tesis y las posibles líneas para futuras investigaciones.

1.5. Referencias

[1] C.A. Harper, Modern Plastics Handbook, McGraw-Hill, 2000. https://www.accessengineeringlibrary.com/content/book/9780070267145 (accessed March 31, 2020).

[2] J.M.G. Cowie, V. (Valeria) Arrighi, Polymers Chemistry and Physics of Modern Materials, Third Edition., CRC Press, 2007.

[3] W. Hu, Polymer physics: A molecular approach, 1st ed., Springer Vienna, 2013. https://doi.org/10.1007/978-3-7091-0670-9.

[4] G. Strobl, The physics of polymers: Concepts for understanding their structures and behavior, 3rd ed., Springer Berlin Heidelberg, 2007. https://doi.org/10.1007/978-3-540-68411-4.

[5] S.T. Milner, Polymer crystal-melt interfaces and nucleation in polyethylene, Soft Matter. 7 (2011) 2909–2917. https://doi.org/10.1039/c0sm00070a.

[6] K. Wang, K. Amin, Z. An, Z. Cai, H. Chen, H. Chen, Y. Dong, X. Feng, W. Fu, J. Gu, Y. Han, D. Hu, R. Hu, D. Huang, F. Huang, F. Huang, Y. Huang, J. Jin, X. Jin, Q. Li, T. Li, Z. Li, Z. Li, J. Liu, J. Liu, S. Liu, H. Peng, A. Qin, X. Qing, Y. Shen, J. Shi, X. Sun, B. Tong, B. Wang, H. Wang, L. Wang, S. Wang, Z. Wei, T. Xie, C. Xu, H. Xu, Z.K. Xu, B. Yang, Y. Yu, X. Zeng, X. Zhan, G. Zhang, J. Zhang, M.Q. Zhang, X.Z. Zhang, X. Zhang, Y. Zhang, Y. Zhang, C. Zhao, W. Zhao, Y. Zhou, Z. Zhou, J. Zhu, X. Zhu, B.Z. Tang, Advanced functional polymer materials, Materials Chemistry Frontiers 4 (2020) 1803–1915. https://doi.org/10.1039/D0QM00025F.

[7] G. Mittal, V. Dhand, K.Y. Rhee, S.J. Park, W.R. Lee, A review on carbon nanotubes and graphene as fillers in reinforced polymer nanocomposites, Journal of Industrial and Engineering Chemistry 21 (2015) 11–25. https://doi.org/10.1016/J.JIEC.2014.03.022.

[8] S. Paszkiewicz, A. Szymczyk, R. Pilawka, B. Przybyszewski, A. Czulak, Z. Rosłaniec, Improved Thermal Conductivity of Poly(trimethylene terephthalate- *block* -poly(tetramethylene oxide) Based Nanocomposites Containing Hybrid Single-Walled Carbon Nanotubes/Graphene Nanoplatelets Fillers, Advances in Polymer Technology 36 (2017) 236–242. https://doi.org/10.1002/adv.21611.

[9] I. Firkowska-Boden, X. Zhang, K.D. Jandt, Controlling Protein Adsorption through Nanostructured Polymeric Surfaces, Advanced Healthcare Materials 7 (2018) 1700995. https://doi.org/10.1002/ADHM.201700995.

[10] J.C. Arango, L.O. Williams, A. Shi, A. Singh, E.K. Nava, R. v. Fisher, J.A. Garfield, S.A. Claridge, Nanostructured Surface Functionalization of Polyacrylamide Hydrogels Below the Length Scale of Hydrogel Heterogeneity, ACS Applied Materials & Interfaces 14 (2022) 43937–43945. https://doi.org/10.1021/acsami.2c12034.

[11] M.C. Scharber, N.S. Sariciftci, Low Band Gap Conjugated Semiconducting Polymers, Advanced Materials Technology 6 (2021) 2000857. https://doi.org/10.1002/admt.202000857.

[12] B. de Boer, A. Facchetti, Semiconducting polymeric materials, Polymer Reviews 48 (2008) 423–431. https://doi.org/10.1080/15583720802231718.

[13] I. McCulloch, M. Heeney, C. Bailey, K. Genevicius, I. MacDonald, M. Shkunov, D. Sparrowe, S. Tierney, R. Wagner, W. Zhang, M.L. Chabinyc, R.J. Kline, M.D. McGehee, M.F. Toney, Liquid-crystalline semiconducting polymers with high charge-carrier mobility, Nature Materials 5 (2006) 328–333. https://doi.org/10.1038/nmat1612.

[14] M.T. Bernius, M. Inbasekaran, J. O'brien, W. Wu, Progress with Light-Emitting Polymers, Advanced Materials 12 (2000) 1737–1750. https://doi.org/10.1002/1521-4095.

[15] K. Xian, Y. Liu, J. Liu, J. Yu, Y. Xing, Z. Peng, K. Zhou, M. Gao, W. Zhao, G. Lu, J. Zhang, J. Hou, Y. Geng, L. Ye, Delicate crystallinity control enables high-efficiency P3HT organic photovoltaic cells, Journal of Materials Chemistry A 10 (2022) 3418–3429. https://doi.org/10.1039/D1TA10161G.

[16] F. Hussain, M. Hojjati, M. Okamoto, R.E. Gorga, Review article: Polymer-matrix nanocomposites, processing, manufacturing, and application: An overview, Journal of Composite Materials 40 (2006) 1511–1575. https://doi.org/10.1177/0021998306067321.

[17] A. Bharadwaz, A.C. Jayasuriya, Recent trends in the application of widely used natural and synthetic polymer nanocomposites in bone tissue regeneration, Materials Science and Engineering: C 110 (2020) 110698. https://doi.org/10.1016/J.MSEC.2020.110698.

[18] C.I. Idumah, C.M. Obele, E.O. Emmanuel, A. Hassan, Recently Emerging Nanotechnological Advancements in Polymer Nanocomposite Coatings for Anti-corrosion, Anti-fouling and Self-healing, Surfaces and Interfaces 21 (2020) 100734. https://doi.org/10.1016/j.surfin.2020.100734.

[19] Z. Yang, P.F. Sun, X. Li, B. Gan, L. Wang, X. Song, H.D. Park, C.Y. Tang, A Critical Review on Thin-Film Nanocomposite Membranes with Interlayered Structure: Mechanisms, Recent Developments, and Environmental Applications, Environmental Science & Technology 54 (2020) 15563–15583. https://doi.org/10.1021/acs.est.0c05377.

[20] W. Bonfield, M.D. Grynpas, A.E. Tully, J. Bowman, J. Abram, Hydroxyapatite reinforced polyethylene — a mechanically compatible implant material for bone replacement, Biomaterials 2 (1981) 185–186. https://doi.org/10.1016/0142-9612(81)90050-8.

[21] B. Gaihre, A.C. Jayasuriya, Comparative investigation of porous nano-hydroxyapaptite/chitosan, nano-zirconia/chitosan and novel nano-calcium zirconate/chitosan composite scaffolds for their potential applications in bone regeneration, Materials Science and Engineering: C 91 (2018) 330–339. https://doi.org/10.1016/J.MSEC.2018.05.060.

[22] M. Mehrasa, M.A. Asadollahi, K. Ghaedi, H. Salehi, A. Arpanaei, Electrospun aligned PLGA and PLGA/gelatin nanofibers embedded with silica nanoparticles for tissue engineering, International Journal of Biological Macromolecules 79 (2015) 687–695. https://doi.org/10.1016/J.IJBIOMAC.2015.05.050.

[23] A. Hasan, G. Waibhaw, V. Saxena, L.M. Pandey, Nano-biocomposite scaffolds of chitosan, carboxymethyl cellulose and silver nanoparticle modified cellulose nanowhiskers for bone tissue engineering applications, International Journal of Biological Macromolecules 111 (2018) 923–934. https://doi.org/10.1016/J.IJBIOMAC.2018.01.089.

[24] Z. Chen, Y. Wang, T. Ba, Y. Li, J. Pu, T. Chen, Y. Song, Y. Gu, Q. Qian, J. Yang, G. Jia, Genotoxic evaluation of titanium dioxide nanoparticles in vivo and in vitro, Toxicology Letters 226 (2014) 314–319. https://doi.org/10.1016/J.TOXLET.2014.02.020.

[25] W. Shao, J. He, F. Sang, Q. Wang, L. Chen, S. Cui, B. Ding, Enhanced bone formation in electrospun poly(l-lactic-co-glycolic acid)–tussah silk fibroin ultrafine nanofiber scaffolds incorporated with graphene oxide, Materials Science and Engineering: C 62 (2016) 823–834. https://doi.org/10.1016/J.MSEC.2016.01.078.

[26] N. Saba, M. Jawaid, O.Y. Alothman, M.T. Paridah, A. Hassan, Recent advances in epoxy resin, natural fiber-reinforced epoxy composites and their applications, Journal of Reinforced Plastics and Composites. 35 (2015) 447–470. https://doi.org/10.1177/0731684415618459.

[27] N. Misra, V. Kumar, J. Bahadur, S. Bhattacharya, S. Mazumder, L. Varshney, Layered silicate-polymer nanocomposite coatings via radiation curing process for flame retardant applications, Progress in Organic Coatings 77 (2014) 1443–1451. https://doi.org/10.1016/J.PORGCOAT.2014.04.027.

[28] E. Stratakis, J. Bonse, J. Heitz, J. Siegel, G.D. Tsibidis, E. Skoulas, A. Papadopoulos, A. Mimidis, A.C. Joel, P. Comanns, J. Krüger, C. Florian, Y. Fuentes-Edfuf, J. Solis, W. Baumgartner, Laser

engineering of biomimetic surfaces, Materials Science and Engineering: R: Reports 141 (2020) 100562. https://doi.org/10.1016/J.MSER.2020.100562.

[29] S. K. Samal, S. Mohanty, S.K. Nayak, eds., Superhydrophobic Polymer Coatings, Elsevier, 2019. https://doi.org/10.1016/c2018-0-00746-x.

[30] D.P. Linklater, V.A. Baulin, S. Juodkazis, R.J. Crawford, P. Stoodley, E.P. Ivanova, Mechano-bactericidal actions of nanostructured surfaces, Nature Reviews Microbiology 19 (2021) 8–22. https://doi.org/10.1038/s41579-020-0414-z.

[31] A.M. Richter, G. Buchberger, D. Stifter, J. Duchoslav, A. Hertwig, J. Bonse, J. Heitz, K. Schwibbert, Spatial period of laser-induced surface nanoripples on pet determines escherichia coli repellence, Nanomaterials 11 (2021) 3000. https://doi.org/10.3390/NANO11113000/S1.

[32] E. Rebollar, I. Frischauf, M. Olbrich, T. Peterbauer, S. Hering, J. Preiner, P. Hinterdorfer, C. Romanin, J. Heitz, Proliferation of aligned mammalian cells on laser-nanostructured polystyrene, Biomaterials 29 (2008) 1796–1806. https://doi.org/10.1016/J.BIOMATERIALS.2007.12.039.

[33] R. Rasouli, A. Barhoum, H. Uludag, A review of nanostructured surfaces and materials for dental implants: Surface coating, patterning and functionalization for improved performance, Biomaterials Science 6 (2018) 1312–1338. https://doi.org/10.1039/c8bm00021b.

[34] P. Lan, E.E. Nunez, A.A. Polycarpou, Advanced Polymeric Coatings and Their Applications: Green Tribology, in: S. Hashmi, I.A. Choudhury (Eds.), Encyclopedia of Renewable and Sustainable Materials, Elsevier, 2020: pp. 345–358. https://doi.org/10.1016/b978-0-12-803581-8.11466-3.

[35] T. Putnin, S. Nootchanat, C. Lertvachirapaiboon, K. Shinbo, K. Kato, K. Ounnunkad, A. Baba, Effect of Micro/Nanostructured P3HT:PCBM Surfaces on the Performance of Organic Photovoltaic Devices, Molecular Crystals and Liquid Crystals 688 (2019) 89–97. https://doi.org/10.1080/15421406.2019.1651073.

[36] R.A. Surmenev, R. V. Chernozem, I.O. Pariy, M.A. Surmeneva, A review on piezo- and pyroelectric responses of flexible nano- and micropatterned polymer surfaces for biomedical sensing and energy harvesting applications, Nano Energy 79 (2021) 105442. https://doi.org/10.1016/j.nanoen.2020.105442.

[37] E.D. Diebold, N.H. Mack, S.K. Doom, E. Mazur, Femtosecond Laser-Nanostructured substrates for Surface-Enhanced Raman scattering, Langmuir 25 (2009) 1790–1794. https://doi.org/10.1021/la803357q.

[38] M.A. Rose, J.J. Bowen, S.A. Morin, Emergent Soft Lithographic Tools for the Fabrication of Functional Polymeric Microstructures, ChemPhysChem 20 (2019) 909–925. https://doi.org/10.1002/CPHC.201801140.

[39] L.M. Cox, A.M. Martinez, A.K. Blevins, N. Sowan, Y. Ding, C.N. Bowman, Nanoimprint lithography: Emergent materials and methods of actuation, Nano Today 31 (2020) 100838. https://doi.org/10.1016/J.NANTOD.2019.100838.

[40] B. Thomas, A.P. Alloncle, P. Delaporte, M. Sentis, S. Sanaur, M. Barret, P. Collot, Experimental investigations of laser-induced forward transfer process of organic thin films, Applied Surface Science 254 (2007) 1206–1210. https://doi.org/10.1016/J.APSUSC.2007.09.042.

[41] F. Yu, P. Li, H. Shen, S. Mathur, C.-M. Lehr, U. Bakowsky, F. Mücklich, Laser interference lithography as a new and efficient technique for micropatterning of biopolymer surface, Biomaterials 26 (2005) 2307–2312. https://doi.org/10.1016/J.BIOMATERIALS.2004.07.021.

[42] S. Lazare, V. Tokarev, A. Sionkowska, M. Wiśniewski, Surface foaming of collagen, chitosan and other biopolymer films by KrF excimer laser ablation in the photomechanical regime, Applied Physics A 81 (2005) 465–470. https://doi.org/10.1007/s00339-005-3260-y.

[43] M. Sirajuddin, P.J. Reddy, Pyroelectric behaviour of laser-evaporated poly(vinyl fluoride) films, Thin Solid Films 124 (1985) 149–154. https://doi.org/10.1016/0040-6090(85)90257-3.

[44] A.P. Caricato, A. Luches, Applications of the matrix-assisted pulsed laser evaporation method for the deposition of organic, biological and nanoparticle thin films: a review, Applied Physics A 2011 105:3 105 (2011) 565–582. https://doi.org/10.1007/S00339-011-6600-0.

[45] P.E. Dyer, Excimer laser polymer ablation: twenty years on, Applied Physics A 77 (2003) 167–173. https://doi.org/10.1007/S00339-003-2137-1.

[46] J. Bonse, S. Hohm, S. V. Kirner, A. Rosenfeld, J. Kruger, Laser-Induced Periodic Surface Structures- A Scientific Evergreen, IEEE Journal on Selected Topics in Quantum Electronics 23 (2017) 9000615. https://doi.org/10.1109/JSTQE.2016.2614183.

[47] E. Rebollar, M. Castillejo, T.A. Ezquerra, Laser induced periodic surface structures on polymer films: From fundamentals to applications, European Polymer Journal 73 (2015) 162–174. https://doi.org/10.1016/j.eurpolymj.2015.10.012.

[48] J. Bonse, S. v Kirner, S. Höhm, N. Epperlein, D. Spaltmann, A. Rosenfeld, J. Krüger, Applications of laser-induced periodic surface structures (LIPSS), in: U. Klotzbach, K. Washio, R. Kling (Eds.), Laser-Based Micro- and Nanoprocessing XI, SPIE, 2017: pp. 114–122. https://doi.org/10.1117/12.2250919.

[49] M. Birnbaum, Semiconductor Surface Damage Produced by Ruby Lasers, Journal of Applied Physics 36 (1965) 3688–3689. https://doi.org/10.1063/1.1703071.

[50] J.E. Sipe, J.F. Young, J.S. Preston, H.M. van Driel, Laser-induced periodic surface structure. I. Theory, Physical Reviews B 27 (1983) 1141–1154. https://doi.org/10.1103/PhysRevB.27.1141.

[51] J.F. Young, J.S. Preston, H.M. van Driel, J.E. Sipe, Laser induced periodic surface structure. II. Experiments on Ge, Si, Al and brass, Physical Review B 27 (1983) 1155–1172. https://doi.org/10.1103/PhysRevB.27.1155.

[52] J.F. Young, J.E. Sipe, H.M. van Driel, Laser-induced periodic surface structure. III. Fluence regimes, the role of feedback, and details of the induced topography in germanium, Physical Review B 30 (1984) 2001–2015. https://doi.org/10.1103/PhysRevB.30.2001.

[53] J.E. Sipe, Bulk-selvedge coupling theory for the optical properties of surfaces, Physical Review B 22 (1980) 1589–1599. https://doi.org/10.1103/PhysRevB.22.1589.

[54] E. Gutiérrez-Fernández, T.A. Ezquerra, A. Nogales, E. Rebollar, Straightforward patterning of functional polymers by sequential nanosecond pulsed laser irradiation, Nanomaterials 11 (2021). https://doi.org/10.3390/nano11051123.

[55] M. Mezera, M. van Drongelen, G.R.B.E. Römer, Laser-Induced Periodic Surface Structures (LIPSS) on Polymers Processed with Picosecond Laser Pulses, Journal of Laser Micro/Nanoengineering 13 (2018) 105–116. https://doi.org/10.2961/jlmn.2018.02.0010.

[56] E. Rebollar, J.R. Vázquez De Aldana, I. Martín-Fabiani, M. Hernández, D.R. Rueda, T.A. Ezquerra, C. Domingo, P. Moreno, M. Castillejo, Assessment of femtosecond laser induced periodic surface structures on polymer films, Physical Chemistry Chemical Physics 15 (2013) 11287–11298. https://doi.org/10.1039/c3cp51523k.

[57] S.I. Kudryashov, T. Pflug, N.I. Busleev, M. Olbrich, A. Horn, M.S. Kovalev, N.G. Stsepuro, Topological transition from deeply sub- to near-wavelength ripples during multi-shot mid-IR femtosecond laser exposure of a silicon surface, Optical Materials Express 11 (2021) 1. https://doi.org/10.1364/ome.412790.

[58] G.D. Tsibidis, E. Stratakis, Ionisation processes and laser induced periodic surface structures in dielectrics with mid-infrared femtosecond laser pulses, Scientific Reports 10 (2020). https://doi.org/10.1038/s41598-020-65613-w.

[59] C. Florian, J.L. Déziel, S. v. Kirner, J. Siegel, J. Bonse, The role of the laser-induced oxide layer in the formation of laser-induced periodic surface structures, Nanomaterials 10 (2020). https://doi.org/10.3390/nano10010147.

[60] O. Shavdina, H. Rabat, M. Vayer, A. Petit, C. Sinturel, N. Semmar, Polystyrene thin films nanostructuring by UV femtosecond laser beam: From one spot to large surface, Nanomaterials 11 (2021). https://doi.org/10.3390/nano11051060.

[61] A. San-Blas, M. Martinez-Calderon, E. Granados, M. Gómez-Aranzadi, A. Rodríguez, S.M. Olaizola, LIPSS manufacturing with regularity control through laser wavefront curvature, Surfaces and Interfaces 25 (2021) 101205. https://doi.org/10.1016/J.SURFIN.2021.101205.

[62] C. Kunz, S. Engel, F.A. Müller, S. Gräf, Large-Area Fabrication of Laser-Induced Periodic Surface Structures on Fused Silica Using Thin Gold Layers, Nanomaterials 10 (2020) 1187. https://doi.org/10.3390/NANO10061187.[63] J. Reif, C. Martens, S. Uhlig, M. Ratzke, O. Varlamova, S. Valette, S. Benayoun, On large area LIPSS coverage by multiple pulses, Applied Surface Science 336 (2015) 249–254. https://doi.org/10.1016/J.APSUSC.2014.11.153.

[63] J. Reif, C. Martens, S. Uhlig, M. Ratzke, O. Varlamova, S. Valette, S. Benayoun, On large area LIPSS coverage by multiple pulses, Applied Surface Science 336 (2015) 249–254. https://doi.org/10.1016/J.APSUSC.2014.11.153.

[64] E. Rebollar, S. Pérez, M. Hernández, C. Domingo, M. Martín, T.A. Ezquerra, J.P. García-Ruiz, M. Castillejo, Physicochemical modifications accompanying UV laser induced surface structures on poly(ethylene terephthalate) and their effect on adhesion of mesenchymal cells, Physical Chemistry Chemical Physics 16 (2014) 17551–17559. https://doi.org/10.1039/c4cp02434f.

[65] R.I. Rodríguez-Beltrán, D.E. Martínez-Tong, A. Reyes-Contreras, S. Paszkiewicz, A. Szymczyk, T.A. Ezquerra, P. Moreno, E. Rebollar, Laterally-resolved mechanical and tribological properties of laser-structured polymer nanocomposites, Polymer 168 (2019) 178–184. https://doi.org/10.1016/j.polymer.2019.02.034.

[66] S. Pérez, E. Rebollar, M. Oujja, M. Martín, M. Castillejo, Laser-induced periodic surface structuring of biopolymers, Applied Physics A 110 (2013) 683–690. https://doi.org/10.1007/s00339-012-7186-x.

[67] J. Prada-Rodrigo, R.I. Rodríguez-Beltrán, S. Paszkiewicz, A. Szymczyk, T.A. Ezquerra, P. Moreno, E. Rebollar, Laser-induced periodic surface structuring of poly(trimethylene terephthalate) films containing tungsten disulfide nanotubes, Polymers 12 (2020) 1090. https://doi.org/10.3390/POLYM12051090.

[68] B.N. Chichkov, C. Momma, S. Nolte, F. Von Alvensleben, A. Tünnermann, Femtosecond, picosecond and nanosecond laser ablation of solids, Applied Physics A 63 (1996) 109–115. https://doi.org/10.1007/BF01567637.

[69] J. Bonse, A. Rosenfeld, J. Krüger, On the role of surface plasmon polaritons in the formation of laser-induced periodic surface structures upon irradiation of silicon by femtosecond-laser pulses, Journal of Applied Physics 106 (2009) 104910. https://doi.org/10.1063/1.3261734.

[70] F. Costache, S. Kouteva-Arguirova, J. Reif, Sub-damage-threshold femtosecond laser ablation from crystalline Si: Surface nanostructures and phase transformation, Applied Physics A 79 (2004) 1429–1432. https://doi.org/10.1007/s00339-004-2803-y.

[71] S. Höhm, A. Rosenfeld, J. Krüger, J. Bonse, Femtosecond laser-induced periodic surface structures on silica, Journal of Applied Physics 112 (2012) 014901. https://doi.org/10.1063/1.4730902.

[72] J. Bonse, S. Höhm, A. Rosenfeld, J. Krüger, Sub-100-nm laser-induced periodic surface structures upon irradiation of titanium by Ti:sapphire femtosecond laser pulses in air, Applied Physics A 110 (2013) 547–551. https://doi.org/10.1007/s00339-012-7140-y.

[73] N. Yasumaru, K. Miyazaki, J. Kiuchi, Femtosecond-laser-induced nanostructure formed on hard thin films of TiN and DLC, Applied Physics A 76 (2003) 983–985. https://doi.org/10.1007/S00339-002-1979-2.

[74] B. Huis in ’t Veld, H. van der Veer, Initiation of femtosecond laser machined ripples in steel observed by scanning helium ion microscopy (SHIM), Journal of Laser Micro Nanoengineering 5 (2010) 28–34. https://doi.org/10.2961/JLMN.2010.01.0007.

[75] A. Borowiec, H.K. Haugen, Subwavelength ripple formation on the surfaces of compound semiconductors irradiated with femtosecond laser pulses, Applied Physics Letters 82 (2003) 4462. https://doi.org/10.1063/1.1586457.

[76] Q. Wu, Y. Ma, R. Fang, Y. Liao, Q. Yu, X. Chen, K. Wang, Femtosecond laser-induced periodic surface structure on diamond film, Applied Physics Letters 82 (2003) 1703–1705. https://doi.org/10.1063/1.1561581.

[77] D. Dufft, A. Rosenfeld, S.K. Das, R. Grunwald, J. Bonse, Femtosecond laser-induced periodic surface structures revisited: A comparative study on ZnO, Journal of Applied Physics 105 (2009) 034908. https://doi.org/10.1063/1.3074106.

[78] T.Q. Jia, H.X. Chen, M. Huang, F.L. Zhao, J.R. Qiu, R.X. Li, Z.Z. Xu, X.K. He, J. Zhang, H. Kuroda, Formation of nanogratings on the surface of a ZnSe crystal irradiated by femtosecond laser pulses, Physicl Review B 72 (2005) 125429. https://doi.org/10.1103/PhysRevB.72.125429.

[79] A. Sarracino, A.R. Ansari, B. Torralva, S. Yalisove, Sub-100 nm high spatial frequency periodic structures driven by femtosecond laser induced desorption in GaAs, Applied Physics Letters 118 (2021) 242106. https://doi.org/10.1063/5.0053037.

[80] O. Varlamova, J. Reif, S. Varlamov, M. Bestehorn, Self-organized Surface Patterns Originating from Laser-Induced Instability, in: S. Sakabe, C. Lienau, R. Grunwald (Eds.), Progress in Nonlinear Nano-Optics. Nano-Optics and Nanophotonics, Springer, Cham, 2015: pp. 3–29. https://doi.org/10.1007/978-3-319-12217-5_1.

[81] G.D. Tsibidis, C. Fotakis, E. Stratakis, From ripples to spikes: A hydrodynamical mechanism to interpret femtosecond laser-induced self-assembled structures, Physical Review B 92 (2015) 041405. https://doi.org/10.1103/PhysRevB.92.041405.

[82] R. Buividas, M. Mikutis, S. Juodkazis, Surface and bulk structuring of materials by ripples with long and short laser pulses: Recent advances, Progress in Quantum Electronics 38 (2014) 119–156. https://doi.org/10.1016/J.PQUANTELEC.2014.03.002.

[83] L. Wang, B. Bin Xu, X.W. Cao, Q.K. Li, W.J. Tian, Q.D. Chen, S. Juodkazis, H.B. Sun, Competition between subwavelength and deep-subwavelength structures ablated by ultrashort laser pulses, Optica 4 (2017) 637–642. https://doi.org/10.1364/OPTICA.4.000637.

[84] G.R.B.E. Römer, J.Z.P. Skolski, J.V. Oboňa, A.J. Huis In ’t Veld, Finite-difference time-domain modeling of laser-induced periodic surface structures, in: Physics Procedia, 2014: pp. 1325–1333. https://doi.org/10.1016/j.phpro.2014.08.058.

[85] G.D. Tsibidis, E. Skoulas, A. Papadopoulos, E. Stratakis, Convection roll-driven generation of supra-wavelength periodic surface structures on dielectrics upon irradiation with femtosecond pulsed lasers, Physical Review B 94 (2016) 081305. https://doi.org/10.1103/PhysRevB.94.081305.

[86] J. Heitz, B. Reisinger, M. Fahrner, C. Romanin, J. Siegel, V. Svorcik, Laser-induced periodic surface structures (LIPSS) on polymer surfaces, in: International Conference on Transparent Optical Networks, 2012. https://doi.org/10.1109/ICTON.2012.6253723.

[87] I. Martín-Fabiani, M.-C. García-Gutiérrez, D.R. Rueda, A. Linares, J.J. Hernández, T.A. Ezquerra, M. Reynolds, Crystallization under One-Dimensional Confinement in Alumina Nanopores of Poly(trimethylene terephthalate) and Its Composites with Single Wall Carbon Nanotubes, ACS Applied Materials & Interfaces 5 (2013) 5324–5329. https://doi.org/10.1021/am401194p.

[88] M. Csete, Z. Bor, Laser-induced periodic surface structure formation on polyethylene-terephthalate, Applied Surface Science 133 (1998) 5–16. https://doi.org/10.1016/S0169-4332(98)00192-5.

[89] M. Hashida, Y. Ikuta, Y. Miyasaka, S. Tokita, S. Sakabe, Simple formula for the interspaces of periodic grating structures self-organized on metal surfaces by femtosecond laser ablation, ersApplied Physics Lett 102 (2013) 174106. https://doi.org/10.1063/1.4803940.

[90] M. Castillejo, T.A. Ezquerra, M. Martín, M. Oujja, S. Pérez, E. Rebollar, Laser nanostructuring of polymers: Ripples and applications, AIP Conference Procedings 1464 (2012) 372. https://doi.org/10.1063/1.4739891.

[91] E. Rebollar, T.A. Ezquerra, A. Nogales, Laser-induced periodic surface structures (Lipss) on polymer surfaces, in: Wrinkled Polymer Surfaces: Strategies, Methods and Applications, 2019: pp. 143–155. https://doi.org/10.1007/978-3-030-05123-5.

[92] I. Martín-Fabiani, E. Rebollar, S. Pérez, D.R. Rueda, M.C. García-Gutiérrez, A. Szymczyk, Z. Roslaniec, M. Castillejo, T.A. Ezquerra, Laser-Induced Periodic Surface Structures

Nanofabricated on Poly(trimethylene terephthalate) Spin-Coated Films, Langmuir 28 (2012) 7938–7945. https://doi.org/10.1021/la300833x.

[93] R. Freeman, J. King, G. Lafyatis, Essentials of Electricity and Magnetism, in: Electromagnetic Radiation, Oxford University Press, 2019: pp. 3–42. https://doi.org/10.1093/oso/9780198726500.003.0001.

[94] O. Svelto, Principles of lasers, 5th ed., Springer US, Milan, 2010. https://doi.org/10.1007/978-1-4419-1302-9.

[95] D.G. Hall, Vector-beam solutions of Maxwell's wave equation, Optics Letters 21 (1996) 9–11. https://doi.org/10.1364/OL.21.000009.

[96] Q. Zhan, Cylindrical vector beams: from mathematical concepts to applications, Advances in Optics and Photonics 1 (2009) 1–57. https://doi.org/10.1364/AOP.1.000001.

[97] O.J. Allegre, W. Perrie, S.P. Edwardson, G. Dearden, K.G. Watkins, Laser microprocessing of steel with radially and azimuthally polarized femtosecond vortex pulses, Journal of Optics 14 (2012) 085601. https://doi.org/10.1088/2040-8978/14/8/085601.

[98] J. JJ Nivas, E. Allahyari, F. Cardano, A. Rubano, R. Fittipaldi, A. Vecchione, D. Paparo, L. Marrucci, R. Bruzzese, S. Amoruso, Vector vortex beams generated by q-plates as a versatile route to direct fs laser surface structuring, Applied Surface Science 471 (2019) 1028–1033. https://doi.org/10.1016/j.apsusc.2018.12.091.

[99] A. Papadopoulos, E. Skoulas, G.D. Tsibidis, E. Stratakis, Formation of periodic surface structures on dielectrics after irradiation with laser beams of spatially variant polarisation: a comparative study, Applied Physics A 124 (2018) 1–12. https://doi.org/10.1007/S00339-018-1573-X.

[100] P. Coullet, L. Gil, F. Rocca, Optical vortices, Optics Communications 73 (1989) 403–408. https://doi.org/10.1016/0030-4018(89)90180-6.

[101] K.K. Anoop, A. Rubano, R. Fittipaldi, X. Wang, D. Paparo, A. Vecchione, L. Marrucci, R. Bruzzese, S. Amoruso, Femtosecond laser surface structuring of silicon using optical vortex beams generated by a q-plate, Applied Physics Letters 104 (2014) 241604. https://doi.org/10.1063/1.4884116.

[102] L.L. Ran, S.L. Qu, Z.Y. Guo, Surface mico-structures on amorphous alloys induced by vortex femtosecond laser pulses, Chinese Physics B 19 (2010) 034204. https://doi.org/10.1088/1674-1056/19/3/034204.

[103] A. Ambrosio, L. Marrucci, F. Borbone, A. Roviello, P. Maddalena, Light-induced spiral mass transport in azo-polymer films under vortex-beam illumination, Nature Communications 2012 3:1. 3 (2012) 1–9. https://doi.org/10.1038/ncomms1996.

[104] R. Santillan, A. Wong, P. Segovia, M. Camacho-Lopez, S. Camacho-Lopez, Femtosecond laser-induced periodic surface structures formation on bismuth thin films upon irradiation in ambient air, Optical Materials Express 10 (2020) 674. https://doi.org/10.1364/ome.384019.

[105] D.A. Belousov, K.A. Bronnikov, K.A. Okotrub, S.L. Mikerin, V.P. Korolkov, V.S. Terentyev, A. V. Dostovalov, Thermochemical laser-induced periodic surface structures formation by femtosecond laser on hf thin films in air and vacuum, Materials 14 (2021) 6714. https://doi.org/10.3390/ma14216714.

[106] S.M. Petrović, B. Gaković, D. Peruško, E. Stratakis, I. Bogdanović-Radović, M. Čekada, C. Fotakis, B. Jelenković, Femtosecond laser-induced periodic surface structure on the Ti-based nanolayered thin films, Journal of Applied Physics 114 (2013) 233108. https://doi.org/10.1063/1.4848016.

[107] J. Cui, A. Nogales, T.A. Ezquerra, E. Rebollar, Influence of substrate and film thickness on polymer LIPSS formation, Applied Surface Science 394 (2017) 125–131. https://doi.org/10.1016/j.apsusc.2016.10.045.

[108] P. Nürnberger, H.M. Reinhardt, H.C. Kim, E. Pfeifer, M. Kroll, S. Müller, F. Yang, N.A. Hampp, Orthogonally superimposed laser-induced periodic surface structures (LIPSS) upon nanosecond laser pulse irradiation of SiO 2 /Si layered systems, Applied Surface Science 425 (2017) 682–688. https://doi.org/10.1016/j.apsusc.2017.06.316.

[109] A. Talbi, C.T. Tameko, A. Stolz, E. Millon, C. Boulmer-Leborgne, N. Semmar, Nanostructuring of titanium oxide thin film by UV femtosecond laser beam: From one spot to large surfaces, Applied Surface Science 418 (2017) 425–429. https://doi.org/10.1016/J.APSUSC.2017.02.033.

[110] A. Talbi, P. Coddet, M. Tabbal, A.L. Thomann, E. Millon, A. Stolz, C. Boulmer-Leborgne, G.M. O'Connor, N. Semmar, Comparative study of laser induced periodic surface structures formed on pulsed laser deposited and magnetron sputtered titanium oxide films, Applied Surface Science 476 (2019) 303–307. https://doi.org/10.1016/J.APSUSC.2019.01.069.

[111] M. Zamfirescu, A. Dinescu, M. Danila, G. Socol, C. Radu, The role of the substrate material type in formation of laser induced periodical surface structures on ZnO thin films, Applied Surface Science 258 (2012) 9385–9388. https://doi.org/10.1016/J.APSUSC.2012.01.089.

[112] M. Hashida, Y. Miyasaka, Y. Ikuta, S. Tokita, S. Sakabe, Crystal structures on a copper thin film with a surface of periodic self-organized nanostructures induced by femtosecond laser pulses, Physical Review B 83 (2011) 235413. https://doi.org/10.1103/PhysRevB.83.235413.

[113] R.I.R. Beltrán, Nanoestructurado de composites de matriz polimérica y aditivos de base carbono con láseres pulsados de nano- y femtosegundos, Universidad de Salamanca, 2018. https://doi.org/10.14201/GREDOS.137359.

[114] A. v. Zayats, I.I. Smolyaninov, A.A. Maradudin, Nano-optics of surface plasmon polaritons, Physics Reports 408 (2005) 131–314. https://doi.org/10.1016/J.PHYSREP.2004.11.001.

[115] H. Raether, Surface Plasmons on Smooth and Rough Surfaces and on Gratings, in: Springer Tracts in Modern Physics, 1st ed., Springer, Berlin, 1988: pp. 58–70. https://doi.org/10.1007/BFb0048317.

[116] I. Pockrand, Surface plasma oscillations at silver surfaces with thin transparent and absorbing coatings, Surface Science 72 (1978) 577–588. https://doi.org/10.1016/0039-6028(78)90371-0.

[117] E. Fontana, R.H. Pantell, Characterization of multilayer rough surfaces by use of surface-plasmon spectroscopy, Physical Review B 37 (1988) 3164–3182. https://doi.org/10.1103/PhysRevB.37.3164.

[118] F. Toigo, A. Marvin, V. Celli, N.R. Hill, Optical properties of rough surfaces: General theory and the small roughness limit, Physical Review B 15 (1977) 5618–5626. https://doi.org/10.1103/PhysRevB.15.5618.

[119] S. Schröder, A. Duparré, L. Coriand, A. Tünnermann, D.H. Penalver, J.E. Harvey, Modeling of light scattering in different regimes of surface roughness, Optics Express 19 (2011) 9820. https://doi.org/10.1364/OE.19.009820.

[120] K. Arya, Z.B. Su, J.L. Birman, Localization of the Surface Plasmon Polariton Caused by Random Roughness and its Role in Surface-Enhanced Optical Phenomena, Physical Review Letters 54 (1985). https://doi.org/10.1103/PhysRevLett.54.1559.

[121] Y. Fuentes-Edfuf, J.A. Sánchez-Gil, C. Florian, V. Giannini, J. Solis, J. Siegel, Surface Plasmon Polaritons on Rough Metal Surfaces: Role in the Formation of Laser-Induced Periodic Surface Structures, ACS Omega 4 (2019) 6939–6946. https://doi.org/10.1021/acsomega.9b00546.

[122] P. Sahoo, Surface topography, in: J.P. Davim (Ed.), Tribology for Engineers, Woodhead Publishing, 2011: pp. 1–32. https://doi.org/10.1533/9780857091444.1.

Capítulo 7

Conclusiones

En resumen, en este trabajo primero estudiamos experimentalmente cómo diferentes parámetros afectan a la formación de LIPSS en películas delgadas de polímeros. Además, estudiamos el efecto de la formación de LIPSS en la modificación de las propiedades de las muestras caracterizando el cambio en las propiedades micromecánicas, topografía, mojabilidad, energía superficial, química superficial y conductividad de las muestras tras la irradiación.

1) Efecto del espesor de la película delgada y la rugosidad y el material del substrato en la formación de LIPSS en películas poliméricas delgadas con baja absorción lineal óptica

Irradiamos películas delgadas de PET de diferente espesor depositadas sobre diferentes substratos, con un láser de femtosegundo con una longitud de onda de 795 nm.

Como se ve en la Tabla 7.1, las LIPSS se generaron para películas delgadas, pero no para películas micrométricas. Las LIPSS también se generaron en muestras con substratos de silicio, oro y vidrio, pero no en muestras con substratos de acero, PET u oro de alta R_q. En cuanto a su dirección, las LIPSS aparecieron perpendiculares a la polarización del láser en las muestras con substratos de oro y paralelas a ella en las demás muestras. Además, en las muestras donde se generaron LIPSS, el espesor de la película delgada y el material del substrato afectaron al período y la profundidad de las estructuras.

El caso de las muestras sobre substratos de oro, para el que las LIPSS aparecieron en la dirección perpendicular a la que esperábamos, se estudió en más detalle con la ayuda de simulaciones numéricas del campo eléctrico. Mediante éstas, exploramos con más detalle el efecto del espesor de la película delgada y la rugosidad del substrato a la formación de LIPSS. Además, lo comparamos con el efecto teórico que tienen estos parámetros en los Plasmones Polaritones Superficiales (SPPs) y con nuestros resultados experimentales. Los resultados de nuestras simulaciones reprodujeron la teoría en su rango de aplicación. Además, usando nuestras simulaciones pudimos entender cualitativamente lo que sucede fuera de este rango. Las simulaciones también reprodujeron cualitativamente nuestros resultados experimentales.

Table 7.1. *Tipo de LIPSS, dirección respecto a la polarización del láser y rango de formación en cada muestra. "N.A" indica que las LIPSS no aparecieron en esa muestra.*

Substrato	**Espesor (nm)**	**Dirección de las LIPSS**	**Tipo de LIPSS**	**Fluencia (mJ/cm^2)**	**Número de pulsos**
Oro de baja R_q	90	⊥	LSFL	2.7-3.6	50k-100k
Oro de baja R_q	102	⊥	LSFL	4.0-6.3	50k-100k
Oro de baja R_q	150	⊥	LSFL	4.4-8.9	50k-100k
Oro de baja R_q	1300	N.A.	N.A.	N.A.	N.A.
Oro de baja R_q	16000	N.A.	N.A.	N.A.	N.A.
Silicio	79	∥	LSFL	21	10k-100k
Silicio	120	∥	LSFL	18-26	2k-100k
Silicio	16000	N.A.	N.A.	N.A.	N.A.
Vidrio	115	∥ y ⊥	LSFL y HSFL	44-73	1k-100k
Vidrio	205	∥	LSFL	44-63	1k-100k
Vidrio	16000	N.A.	N.A.	N.A.	N.A.
PET	243	N.A.	N.A.	N.A.	N.A.
PET	318	N.A.	N.A.	N.A.	N.A.
Acero	210	N.A.	N.A.	N.A.	N.A.
Acero	298	N.A.	N.A.	N.A.	N.A.
Oro de alta R_q	165	N.A.	N.A.	N.A.	N.A.

De estos resultados extraemos las siguientes conclusiones:

- **El material y la rugosidad del substrato y el espesor de la película delgada son parámetros clave en la formación de LIPSS:** Para pulsos de femtosegundos en películas delgadas de un polímero con baja absorción lineal óptica, no solo cambian el rango de formación de las LIPSS y sus características, sino que también pueden ser el factor que determine si se pueden generar LIPSS o no. En el caso del espesor de la película delgada, podemos aplicar esta conclusión a polímeros en *bulk* si los describimos como películas con un espesor muy alto. Es posible que las LIPSS no aparezcan en un polímero en *bulk* pero sí en películas delgadas del mismo polímero.

- **El mecanismo de formación de LIPSS en estas muestras se ve afectado por la excitación de una onda superficial generada por dispersión (SSW) en la interfaz substrato-película delgada:** Para pulsos de femtosegundos en películas delgadas de un polímero con baja absorción lineal óptica, esta SSW es más intensa que la SSW habitual excitada en la superficie de la muestra y es la razón detrás de la importancia del material y la rugosidad del substrato y el espesor de la película delgada en la formación de LIPSS. Teniendo en cuenta su influencia, podemos explicar todos nuestros resultados experimentales excepto los relacionados con la muestra más delgada sobre un substrato de vidrio. En esta muestra, tanto LSFL y HSFL aparecieron con períodos que no pudimos explicar por completo.
- **En el caso de muestras sobre substratos de oro, esta SSW es un SPP:** Las simulaciones numéricas del campo eléctrico mostraron la formación de SPP en la interfaz substrato-película delgada. Además, estas simulaciones reprodujeron cualitativamente nuestros resultados experimentales, lo que nos aseguró que en las muestras con sustratos de oro la SSW mencionada anteriormente es un SPP.
- **En el caso de muestras sobre sustratos de oro, el período de las LIPSS disminuye con el R_q del substrato y el espesor de la película delgada:** Usando simulaciones numéricas, exploramos con más detalle el efecto del espesor de la película delgada y la rugosidad del substrato y lo comparamos con la teoría sobre cómo estos parámetros afectan a los SPP, y con nuestros experimentos. Encontramos un buen acuerdo entre nuestras simulaciones y la teoría en su rango de aplicación.

En cuanto a las futuras líneas de investigación, proponemos lo siguiente:

- **Investigar el régimen de rugosidad del substrato y de espesor de la película que permite la formación de LIPSS:** Por cuestiones logísticas, en esta tesis sólo irradiamos muestras sobre substratos con rugosidad o muy baja o muy alta. En cuanto a espesor de la película, no irradiamos espesores entre 205 nm y 1300 nm. Aunque estudiamos casos intermedios con nuestras simulaciones numéricas, sería interesante intentar estudiarlas experimentalmente y ver si reproducimos los resultados de las simulaciones.
- **Investigar el rango de absorción lineal óptica en el que el SSW excitado en la interfaz substrato-película delgada influye en la formación de LIPSS:** La irradiación del mismo tipo de muestras con haces Gaussianos de femtosegundos, pero con diferentes longitudes de onda, nos permitiría explorar diferentes rangos de absorción lineal óptica

y definir el rango en el que debemos tener en cuenta esta SSW. El estudio podría hacerse para muestras sobre substratos de oro, ya que la diferencia de orientación sería la propiedad más fácil de monitorizar.

- **Investigar las estructuras que aparecieron en la muestra más delgada sobre un substrato de vidrio:** La irradiación de muestras con distintos espesores entre 100 y 200 nm podría ayudarnos a comprender el efecto del espesor de la película en la formación de distintas estructuras. Otra opción sería tratar de extender las simulaciones numéricas realizadas para muestras sobre substratos de oro a estas muestras y estudiar las diferencias en el campo eléctrico entre muestras con distintos espesores.

2) Estudio del efecto de la formación de LIPSS en la modificación de las propiedades de los materiales

Hemos estudiado la generación de LIPSS en películas autosoportadas de un nanocompuesto formado de una matriz de PTT dopada con nanotubos de WS_2. Además, hemos tratado de utilizar haces complejos para generar estructuras complejas en un solo paso, aplicando este método a películas delgadas de PET depositadas sobre diferentes substratos, así como a películas delgadas de P3HT y $PC_{71}BM$, dos semiconductores orgánicos con aplicaciones en células solares orgánicas, depositadas sobre Silicio dopado.

En cuanto a las muestras de PTT-WS_2, las irradiamos con haces Gaussianos de femtosegundos a 265 nm generando LIPSS. También estudiamos la generación de LIPSS en muestras de PTT para investigar el efecto del nanoaditivo. En ambas muestras las estructuras aparecieron paralelas a la polarización del láser con un período cercano a su longitud de onda. La presencia del nanoaditivo condujo a un aumento de la densidad de energía necesaria para desencadenar la formación de LIPSS. Explicamos esto como el efecto del mayor porcentaje de cristalización y disipación térmica del PTT-WS_2. Además, caracterizamos la mojabilidad y la energía superficial de las muestras. En ambas muestras, la mojabilidad aumentó con la formación de LIPSS, y la energía superficial total se mantuvo constante. Sin embargo, su componente polar negativa aumentó considerablemente. Esto se debió a la formación de especies hidrófilas polares, causadas por una reacción con el oxígeno en el aire, catalizada por la ionización y la alta temperatura de la superficie de la muestra mientras se producía la irradiación. Finalmente, utilizamos PF-QNM para caracterizar el cambio en las propiedades nanomecánicas de la superficie después de la irradiación. En ambas muestras, la formación de LIPSS no cambió notablemente el módulo de Young, pero indujo una disminución de la fuerza de adhesión en un factor de cuatro. Atribuimos este efecto al cambio de la química superficial. De estos resultados extraemos las siguientes conclusiones:

- **Las LIPSS se pueden utilizar para cambiar la topografía de estas muestras, dándoles una funcionalidad adicional, sin dañarlas:** Esta técnica no es ablativa y el módulo de Young de la muestra se mantuvo sin cambios tras la irradiación.
- **Los LIPSS permiten la creación de pequeñas zonas con nanoestructuras diferentes**: Gracias al alto control sobre el área irradiada, podríamos cambiar los parámetros de irradiación en diferentes áreas de una muestra, creando pequeñas zonas con nanoestructuras con diferentes periodos, profundidades y orientaciones.
- **El nanoestructurado superficial con LIPSS se puede utilizar en este nanocompuesto sin ningún demérito:** Exceptuando que se necesita un pequeño aumento en la intensidad de la irradiación, las LIPSS aparecieron con las mismas características en PTT y PTT-WS_2, y los cambios que provocaron en las propiedades superficiales de las muestras fueron muy similares.

También proponemos la siguiente línea de investigación:

- **Investigar la influencia del porcentaje de nanoaditivo y su orientación en la formación de LIPSS:** En nuestros experimentos, el porcentaje de nanoaditivo fue del 0,5% en peso y se distribuyó uniformemente en la matriz PTT con los nanotubos tomando orientaciones aleatorias. Sería interesante comprobar si el leve impacto (descrito anteriormente) que el nanoaditivo tuvo en la generación de LIPSS aumentaría si incrementamos este porcentaje o si los nanotubos estuvieran predominantemente orientados en una dirección.

En cuanto a las irradiaciones con haces complejos, irradiamos películas delgadas de PET sobre diferentes substratos con haces vectoriales de femtosegundos a una longitud de onda de 515 nm. Las LIPSS aparecieron paralelas a la polarización de los haces en muestras sobre substratos de silicio o vidrio. Sin embargo, en muestras sobre substratos de oro, aparecieron estructuras orientadas perpendiculares a la polarización, pero demasiado desordenadas para ser llamadas LIPSS.

De estos resultados se extrajeron las siguientes conclusiones.

- **Conseguimos generar LIPSS en PET con formas complejas utilizando un proceso de un solo paso:** Generamos estructuras en forma de radios de bicicleta, círculos concéntricos y espirales en un solo paso utilizando haces vectoriales de femtosegundos.

- **Hay diferencias en las LIPSS inducidas por haces Gaussianos y aquellas inducidas con haces vectoriales:** Las LIPSS aparecieron en un rango de fluencia y pulsos diferente y cambian de manera diferente con el espesor de las películas delgadas. Sin embargo, no estamos seguros de si las diferencias se deben a la diferencia en la longitud de onda (795 nm en un caso, 513 nm en el otro) y la tasa de repetición (5 kHz frente a 10 Hz-3 kHz) o son debidas al uso de haces vectoriales en lugar de haces Gaussianos.

En cuanto a las futuras líneas de investigación, proponemos la siguiente:

- **Investigar las diferencias entre las LIPSS inducidas por haces Gaussianos y las inducidas con haces vectoriales:** Para aislar el efecto del tipo de haz del de la longitud de onda de irradiación y la tasa de repetición, podríamos repetir el experimento con haces Gaussianos y vectoriales con las mismas longitudes de onda y tasas de repetición.

Con respecto al P3HT, utilizamos haces vectoriales de femtosegundos a una longitud de onda de 515 nm. Encontramos LIPSS paralelas a la polarización del haz. También utilizamos haces vectoriales y de vórtice óptico de nanosegundos a 532 nm. Utilizando haces vectoriales de nanosegundos generamos LIPSS paralelas a la polarización mucho más profundas y mejor definidas que las generadas con pulsos de femtosegundos. Además, medimos una inhibición de la conductividad en las partes altas de las estructuras. Afirmamos que la causa de este cambio fue una pérdida de cristalinidad. También caracterizamos el cambio en la mojabilidad sin encontrar diferencias para las diferentes polarizaciones del haz. Para todas ellas, la muestra se volvió más hidrófila después de la irradiación. Creemos que esto se debe a cambios químicos causados por la oxidación por irradiación láser. Por otro lado, para los haces de vórtice óptico vemos LIPSS en forma de panel de abeja con períodos y profundidades similares a las otras estructuras.

Finalmente, irradiamos películas de $PC_{71}BM$ con haces vectoriales y de vórtice óptico de nanosegundos a 532 nm produciendo LIPSS paralelas a la polarización del láser de un período menor que los encontrados en P3HT y en un rango de fluencia mucho más estrecho. Sus características evolucionaron con los parámetros de irradiación igual que las estructuras encontradas en P3HT.

De estos resultados extraemos las siguientes conclusiones:

- **Conseguimos generar LIPSS en P3HT y $PC_{71}BM$ con formas complejas en un solo paso:** El uso de haces vectoriales permitió la creación de LIPSS con un patrón radial, concéntrico o espiral –siguiendo la polarización del haz.

- **Estas estructuras podrían aplicarse a la creación de nanocables con estas formas complejas:** La acusada disminución de la conductividad en la parte superior de las estructuras, respecto al efecto en su parte inferior, podría utilizarse para crear nanocables con estas geometrías.
- **Conseguimos generar LIPSS con forma de panal de abeja en un solo paso:** El uso de haces de vórtice ópticos permitió la creación de LIPSS con forma de panal de abeja. La diferente fase de los haces de vórtice óptico no debería afectar a las estructuras, por lo que creemos que su forma se debe la polarización circular del haz. Sin embargo, en otros materiales, las nanoestructuras que resultan de la irradiación circularmente polarizada son nanopuntos distribuidos uniformemente.

En cuanto a las futuras líneas de investigación, proponemos lo siguiente:

- **Investigar el origen de las LIPSS con forma de panal de abeja:** Para comprobar si esta forma está causada por la polarización circular del haz o la fase diferente de los haces de vórtice óptico, una posibilidad es irradiar P3HT y $PC_{71}BM$ con haces Gaussianos de nanosegundos con diferentes elipticidades y comprobar si podemos recrear estas estructuras en forma de panal.

3) Conclusiones metodológicas

Además de estas conclusiones científicas, desde un punto de vista metodológico, he aplicado y adquirido conocimientos avanzados sobre las siguientes técnicas durante el transcurso de esta tesis:

- **Procesado superficial de polímeros**: Se aprendió a procesar polímeros tanto en forma de películas delgadas como en *bulk*, utilizando haces Gaussianos, vectoriales y de vórtice óptico de femto- y nanosegundos en longitudes de onda que fueron desde el infrarrojo cercano hasta el ultravioleta.
- **Caracterización**: Se ha logrado familiarizarse con diferentes técnicas para caracterizar propiedades superficiales de los polímeros tanto antes como después de la irradiación. Específicamente, se aprendió a utilizar de manera autónoma AFM para su topografía y la técnica de la gota sésil para su mojabilidad.
- **Cálculo de su energía superficial:** Se aprendieron dos métodos diferentes para calcular diferentes contribuciones a la energía superficial a partir de mediciones de ángulo de contacto realizadas mediante la técnica de la gota sésil y a hacer una comparación crítica de los resultados obtenidos por cada método.

- **Simulaciones numéricas del campo eléctrico:** Se aprendió a utilizar el Módulo de Óptica de Ondas de COMSOL Multyphisics ™, un programa basado en Métodos de Elementos Finitos para simular el campo eléctrico en una película delgada de polímero depositada sobre un substrato de oro. He trabajado independientemente para entender qué aproximaciones y parámetros utilizar para obtener los resultados deseados.

En resumen, en esta tesis hemos estudiado cómo diferentes parámetros afectan a la formación de LIPSS en películas delgadas de polímeros y la capacidad que tiene la formación de LIPSS para modificar las propiedades de las muestras. Como principal aportación de esta tesis, hemos identificado el **rol clave que el material y rugosidad del substrato y el espesor de la película delgada juegan en la formación de LIPSS en películas delgadas de polímeros con baja absorción lineal óptica depositados sobre diferentes sustratos, y hemos encontrado una explicación para esta importancia en la generación de una SSW en la interfaz substrato-película delgada. Además, hemos estudiado este rol en detalle con simulaciones numéricas.** En este sentido, creemos que hemos contribuido al avance de la comprensión de la formación de LIPSS en películas delgadas de polímeros utilizando pulsos de femtosegundos.